Hyaluronan Mediated Motility Receptor Regulates Daughter Cell Size Control Pathways During Mitosis

by

Lin Mei

B.Sc., The University of British Columbia, 2016

A THESIS SUBMITTED IN PARTIAL FULFILLMENT OF
THE REQUIREMENTS FOR THE DEGREE OF

DOCTOR OF PHILOSOPHY

in

THE FACULTY OF GRADUATE AND POSTDOCTORAL STUDIES

(Experimental Medicine)

THE UNIVERSITY OF BRITISH COLUMBIA

(Vancouver)

November 2022

The following individuals certify that they have read, and recommend to the Faculty of Graduate and Postdoctoral Studies for acceptance, the dissertation entitled:

Hyaluronan mediated motility receptor regulates daughter cell size control pathways during mitosis

submitted by Lin Mei in partial fulfilment of the requirements for

the degree of Doctor of Philosophy

in Experimental Medicine

Examining Committee:

Christopher Maxwell, Associate Professor, Pediatrics, UBC

Supervisor

Michael Gold, Professor, Microbiology & Immunology, UBC

Supervisory Committee Member

Peter Stirling, Associate Professor, Medical Genetics, UBC

Supervisory Committee Member

Francis Lynn, Associate Professor, Surgery, UBC

University Examiner

Alexander G. Beristain, Associate Professor, Obstetrics & Gynaecology, UBC

University Examiner

Additional Supervisory Committee Members:

Kenji Sugioka, Assistant Professor, Zoology, UBC

Supervisory Committee Member

Abstract

During cell division, one mitotic cell generates two daughter cells. Molecular pathways that build, stabilize and orient the mitotic spindle are critical during cell division as the mitotic spindle ensures equal segregation of chromosomes and controls the size of the daughter cells. During anaphase, the spindle mid-zone signals the cleavage site, a site that defines the separation of the daughter cells in most animal cells. Under normal conditions, the spindle is centred in the dividing cell, leading to equal-sized daughter cells. However, daughter cells with different physical sizes can be generated due to an off-centre spindle during anaphase. Unequal-sized daughter cells differ in their relative amounts of cytoplasmic content, such as organelles, which can affect their survival, growth, and behavior.

Several mechanisms regulate daughter cell size in mitosis, including asymmetric cortical dynein pulling forces on the spindle and asymmetric membrane elongation at the cell surface. The Maxwell Lab revealed that the gene product hyaluronan mediated motility receptor (HMMR) plays an important role in the asymmetric cortical localization and activity of dynein, a pulling-force generating microtubule motor protein. Moreover, HMMR is a breast cancer susceptibility gene. My research now shows that HMMR also regulates asymmetric membrane elongation to control daughter cell size. My results reveal that HMMR-overexpressing cells display ectopic membrane elongation at anaphase as well as the ultimate loss of daughter cell size control; moreover, elevated HMMR expression correlates with activation of Aurora kinase A and mis-localization of components of the ARP2/3 complex, which potentially disrupts the stability of the cortex during mitosis.

Collectively, my research identifies a new role for HMMR in the regulation of cortical integrity and daughter cell sizes potentially through an Aurora kinase A-dependent control of

ARP2/3 complex localization to the mitotic spindle poles. The disruption of daughter cell size control mediated by elevated HMMR expression may contribute to heterogeneous cell size and genome instability that often occurs during tumorigenesis.

Lay Summary

Cell division is needed for animal development and proper tissue functioning. During most cell divisions, the parental cell gives rise to two equal-sized daughter cells that inherit identical genetic information. The control of daughter cell size during cell division relies on proper spindle positioning during anaphase. There are several mechanisms to maintain a centred mitotic spindle. However, some of these molecular mechanisms remain unclear. In this thesis, I identified a new pathway that controls daughter cell size during mitosis. When I disrupted this pathway, I uncovered consistent phenotypes in immortal cell lines, and primary samples taken from human donors or transgenic mice. My thesis provides new insight about mechanisms that control daughter cell sizes and may shed light on the process of tumorigenesis that is associated with defective cell division.

Preface

The following manuscript is associated with this thesis.

F. Mateo*, Z He*, L Mei*,(*co-first authors), G Ruiz de Garibay, C Herranz, N García, A Lorentzian, A Baigés, E Blommaert, A Gómez, O Mirallas, A Garrido-Utrilla, L Palomero, R Espín, AI Extremera, MT Soler Monsó, A Petit, R Li, J Brunet, K Chen, S Tan, C Eaves, C McCloskey, R Hakem, R Khokha, PF Lange, C Lázaro, CA Maxwell† and MA Pujana† († co-senior authors).
Modification of BRCA1-associated cancer risk by HMMR overexpression.
Nature Communications 2022 Apr 7;13(1):1895. doi:10.1038/s41467-022-29335-z

Following figures in this thesis have been published in the manuscript above:

Figure 3.1 to 3.4, 3.7 to 3.10, and 3.13 to 3.19 in Chapter 3.

Figures 4.3 to 4.8, and 4.10 in Chapter 4.

Figures 5.3, 5.5, and 5.9 presented in Chapter 5.

In association with Dr. Maxwell and committee members, I have designed the experiments. I completed the experiments and data analyses in this thesis, with the following exceptions:

- The immunoprecipitation-mass spectrometry experiments and analysis in Chapter 3 were performed by Dr. Jihong Jiang (Maxwell Lab) and Charlie Kuan, M.Sc. (Lange Lab) (BC Children's Hospital) as Figure 3.9.
- Lentiviruses with plasmids expressing eGFP and GFP-Aurora A used in Chapter 4 were provided by Dr. Zhengcheng He and Shanshan Wang (Maxwell Lab).
- Dr. Marisa Connell generated *Drosophila* lines expressing UAS-GFP-HMMR and UAS-Cherry-jupiter/UAS-HMMR. Dr. Connell generated the movies from which I quantified the percentage and size of blebbing neuroblasts in Chapter 5 as Figure 5.1.
- Dr. Francesca Mateo and Dr. Miquel Angel Pujana (Pujana Lab) shared paraffin embedded and frozen mouse mammary gland tissues for analysis in Chapter 5.

- Dr. Zhengcheng He (Maxwell Lab) helped with the isolation and single-cell suspension of the primary mammary epithelial cells from mouse. After lentivirus transduction to express EGFP or EGFP-Cre, Dr. Zhengcheng He sorted the GFP-positive cells 24 hours post-transduction in Chapter 5.
- Dr. Zhengcheng He (Maxwell Lab) helped with the gene editing design using CRISPR-Cas9 and Prime editing for rs299290 in Chapter 5.
- The primary mammary luminal progenitor cells were isolated and sorted by Dr. Connie Eaves' laboratory (BC Cancer) in Chapter 5.
- Dr. Zhengcheng He (Maxwell Lab) cultured and obtained movies of the primary mammary luminal progenitor cells in Chapter 5 as Figure 5.10A.

Samples obtained from human donors and animal models were obtained and manipulated following the approved protocols listed:

- Mammary tissues from donors with consent were processed according to the University of British Columbia Research Ethics Board (reference H19-04034).
- Animal experiments regarding the *BLG-Cre Trp53*$^{+/-}$ *Brca1*$^{fl/fl}$ *HMMR*$^{Tg/Tg}$ mice were conducted in the University of Barcelona-Bellvitge animal facility with the permission of the IDIBELL University of Barcelona-Bellvitge Ethics Committee, according to the Generalitat de Catalunya license authority (reference 9774) .

Table of Contents

Lists of Tables

List of Figures

List of Abbreviations

ABP	Actin-binding proteins
ADPKD	Autosomal dominant polycystic kidney disease
AdPROM	Affinity-directed protein missile
aGFP	Anti-GFP
AKI	Aurora A inhibitor
ALK5	TGFβ type I receptor kinase
APC/C	Anaphase-promoting complex/cyclosome
Arl13b	ADP-ribosylation factor-like protein 13B
ARPC1B	Actin-related protein 2/3 complex subunit 1B
ARPC2	Actin-related protein 2/3 complex subunit 2
ARPC3	Actin-related protein 2/3 complex subunit 3
ARPC4	Actin-related protein 2/3 complex subunit 4
ARPC5	Actin-related protein 2/3 complex subunit 5
ARPKD	Autosomal recessive polycystic kidney disease
ARP2	Actin-related protein 2
ARP3	Actin-related protein 3
ATP	Adenosine triphosphate
ATPase	Adenosine triphosphatease
AURKA	Aurora kinase A
AURKB	Aurora kinase B
BARD1	BRCA1 associated RING domain 1
BC	Basal cell
BLG	Beta-lactoglobulin
BRCA1	Breast cancer 1, early onset protein
BSA	Bovine serum albumin
BUB1	Mitotic checkpoint serine/threonine-protein kinase
bZip	Basic leucine zipper
Cas9	CRISPR-associated protein 9
CCNB1	G2/mitotic-specific cyclin-B1
CCNG1	Cyclin G1
CD48	Cluster of Differentiation 48
CD68	Cluster of Differentiation 68
cDNA	Complimentary DNA
cGAS	Cyclic GMP-AMP Synthase
CHICA	Protein FAM83D
CK1α	Casein kinase 1α
CNS	Central nervous system
CRISPR	Clustered regularly interspaced short palindromic repeats
D box	Destruction box

Da	Dalton
DAPI	4', 6-diamidino-2-phenylindole
DHC	Dynein heavy chain
DMEM	Dulbecco's modified Eagle medium
DMSO	Dimethyl sulfoxide
DNA	Deoxyribonucleic acid
Dox	Doxycycline
DTT	Dithiothreitol
DYNLL1	Dynein light chain 1
EB1	End binding protein 1
ECM	Extracellular matrix
EDTA	Ethylenediaminetetraacetic acid
Eg5	Kinesin-5
EGF	Epidermal growth factor
eGFP	Enhanced green fluorescent protein
EpCAM	Epithelial cell adhesion molecule
ESC	Embryonic stem cell
EtOH	Ethyl alcohol
F4/80	EGF-like module-containing mucin-like hormone receptor-like 1
FACs	Fluorescence-activated cell sorting
F-actin	Filamentous actin
FBS	Fetal bovine serum
G-actin	Globular actin monomer
GAPDH	Glyceraldehyde 3-phosphate dehydrogenase
GENT2	Gene Expression database of Normal and Tumour tissues 2
GFP	Green fluorescent protein
GMC	Ganglion mother cell
gRNA	Guide RNA
GTEx	Genotype-Tissue Expression project
GTP	Guanine triphosphate
HA	Hyaluronan
HABP	Hyaluronan-binding protein fraction
HEPES	4-(2-hydroxyethyl)-1-piperazineethanesulfonic acid
hMLH1dn	Human mutL homolog1 dominant negative
HMMR/Hmmr	Hyaluronan mediated motility receptor (gene)
HMMR	Hyaluronan mediated motility receptor (protein)
HPA	Human Protein Atlas
HRP	Horseradish peroxidase
H&E	Hematoxylin & eosin
IAA	Indole-3-acetic acid

IC50	Half maximal inhibitory concentration
IF	Immunofluorescence
IVT	*In vitro* transcription
KD	Knockdown
kDa	Kilodaltons
Ki67	Antigen KI-67
KO	Knockout
LB	Luria-Bertani
LC	Luminal cell
LGN	G-protein signaling modulator 2
LP	Luminal progenitor
MAT2B	Methionine adenosyltransferase 2B
MCM2	Minichromosome Maintenance Complex Component 2
MEC	Mammary epithelial cell
MEF	Mouse embryonic fibroblast
Mira	Miranda
MLH1dn	Dominant negative of a DNA mismatch repair gene MLH1
MO	Morpholino oligomer
MYO18A	Myosin 18A
ngRNA	Nicking guide RNA
NEBD	Nuclear envelope breakdown
NEK	NIMA-related protein kinase
Neo	Neomycin selection
NF-κB	Nuclear factor kappa B
NMII	Non-muscle myosin II
NMIIa	Non-muscle myosin IIa
NMIIb	Non-muscle myosin IIb
NMIIc	Non-muscle myosin IIc
NP	Neuroepithelial progenitor
NPF	Nucleation promoting factor
NUDCD2	NudC domain-containing protein 2
NuMA	Nuclear mitotic apparatus protein
Opti-MEM	Reduced-Serum Medium (Minimal Essential Medium)
PAM	Protospacer adjacent motif
PBS	Phosphate buffered saline
PBS	Primer binding site
PC	Polycystin
PCNA	Proliferating cell nuclear antigen
PCNT	Pericentrin
PCP	Planar cell polarity

PCR	Polymerase chain reaction
PE	Prime editor
pegRNA	Prime editing guide RNA
PFA	Paraformaldehyde
PLA	Proximity Ligation Assay
PLK1	Polo-like kinase 1
PKD	Polycystic kidney disease
PP1	Protein phosphatase 1
PX458	PSpCas9(BB)-2A-GFP
Ran	RAs-related Nuclear protein
RFP	Red fluorescent protein
RHAMM	Receptor for hyaluronan mediated motility
RNA	Ribonucleic acid
RNA-seq	RNA sequencing
rpm	Revolutions per minute
RTT	Reverse transcription templates
siRNA	Small interfering ribonucleic acid
SAC	Spindle assembly checkpoint
SAF	Spindle assembly factor
SC	Stromal cell
SEM	Standard error of mean
SD	Standard deviation
SDS	Sodium dodecyl sulfate
smFISH	Single-molecule fluorescent *in situ* hybridization
SNP	Single nucleotide polymorphism
ssDNA	Single-stranded DNA
STING	Stimulator of Interferon Genes
STLC	(+)-S-Trityl-L-cysteine
TAM	Tumor-associated macrophages
TFA	Trifluoroacetic acid
TPM	Transcripts per million
TPX2	Targeting protein for Xklp2
VCAM	Vascular cell adhesion protein 1
VHL	Von Hippel-Lindau
WASP	Wiskott-Aldrich syndrome protein
WB	Western blot
WDS	WISH/DIP/SPIN90
WT	Wild type
γTuRC	γ-tubulin ring complex

Acknowledgements

This project was made possible with the help and support from many people. First, I would like to thank my supervisor, Dr. Chris Maxwell for the guidance and support he provided. I would also like to thank my supervisory committee, Dr. Michael Gold, Dr. Peter Stirling and Dr. Kenji Sugioka, for their valuable time and advice on my research study. Moreover, I would like to thank the past and present members of the Maxwell Lab who have taught and trained me for doing different types of experiments and trouble-shooting skills, especially Dr. Helen Chen, Dr. Jihong Jiang, Dr. Marisa Connell and Dr. Zhengcheng He. Also, I appreciate the help from my other labmates Dr. Tony Chu, Maria Guo, Alyssa Wang, and BCCHR trainees for the fun talks we had during lunchtime. I enjoyed the collaboration experience with Dr. Miguel Angel Pujana's lab and Dr. Gopal Sapkota's lab during my graduate school. In addition, I would like to thank my previous supervisors Dr. Alice Mui, Dr. Sylvia Cheung, and Dr. Shirin Kalyan. I have learnt a lot from them.

Lastly, I would like to thank my grandparents and parents for their support and understanding all these years. Without their unconditional love, I would not be able to face all the difficulties and challenges in my life.

Dedication

This work is dedicated to my parents, grandparents and my lovely little Pomeranian PP for their care, support and expectations.

Chapter 1: Introduction

Proper tissue development relies on the ability of stem cells to undergo symmetric or asymmetric cell divisions (Morrison and Kimble, 2006). For example, neurogenesis is a process where neural stem and progenitor cells generate neurons (Sun and Hevner, 2014). In vertebrates, neurogenesis takes place throughout the neural tube during the development of the central nervous system (CNS) (Taverna *et al.*, 2014). Subsequent processes include neuronal migration and differentiation, the formation of dendrites and axons, and the development of neuronal connectivity (Kriegstein and Noctor, 2004). During cortical neurogenesis, cortical stem and progenitor cells undergo different modes of cell division to generate different cell types, which are categorized based on the location of mitosis, cell polarity and the capacity to proliferate of the produced daughter cells (Taverna *et al.*, 2014).

Cortical stem cell and progenitor cells can undergo either symmetric or asymmetric cell division, which gives rise to different types of daughter cells (Habib and Acebrón, 2022). Symmetric proliferative, symmetric consumptive, asymmetric self-renewing, and asymmetric consumptive are the four modes of cell division that occur during neurogenesis (Taverna *et al.*, 2014). In symmetric proliferative division, the two daughter cells generated from a division are identical to the mother cell. In symmetric consumptive division, the mother cell generates two identical daughter cells that are different from the mother cell. During asymmetric self-renewing division, one daughter cell is identical to the mother cell while the other daughter cell is phenotypically or functionally different. Asymmetric consumptive division results in two daughter cells that are distinct from each other and from the mother cell. Since asymmetric cell division results in uneven distribution of polarized factors, the daughter cells can behave differently and have different cell fates. Thus, while each cell division must ensure the equal

segregation of genetic information (chromosomes), the two daughter cells can differ in their acquisition of non-genetic information and/or their environmental context, each of which can have dramatic consequences on the ultimate phenotype or function of that daughter cell.

1.1 Mitosis

Humans begin as a single zygote cell that develops through mitosis. During these development and growth stages, mitosis increases the number of cells and produces specialized cells that must ultimately perform different functions. During adulthood, mitosis maintains and replaces cells in order to support tissue function in the organism. Consequently, cell division is a tightly regulated process where a parental cell gives rise to two daughter cells inheriting identical genetic material. In order to ensure the stable segregation of chromosomes, more than 800 proteins are known to contribute to the formation and regulation of the mitotic spindle (Sauer *et al.*, 2005).

1.1.1 Stages of mitosis and mechanisms of chromosome alignment and segregation

Mitosis begins with prophase, a stage where chromosomes condense within the nucleus while at the same time microtubules nucleate at the centrosomes (Walczak *et al.*, 2010). When the cell enters prometaphase, the nuclear envelope breaks down (NEBD) and microtubules attach to the chromosomes through kinetochores. 'The dance of chromosomes' is also initiated at prometaphase where chromosomes can migrate towards or away from the spindle pole. This chromosome movement eventually leads to metaphase, which is defined by the alignment of chromosomes at the spindle equator to form the metaphase plate. When the cell passes the metaphase checkpoint, sister chromatid cohesion is cleaved, and the cell enters anaphase. During

anaphase, sister chromatids are pulled toward opposite spindle poles in order to evenly distribute the genetic material into both daughter cells. Next, the chromosomes decondense and a nuclear envelope reforms around the two nuclei in telophase. During cytokinesis, ingression of the cell membrane between the two nuclei forms the midbody and two daughter cells are produced, following the abscission of the midbody.

1.1.2 Anaphase spindle position determines daughter cell size

During late anaphase, the spindle midzone between the separating chromosomes sends signals to determine the site of cleavage between the two daughter cells (Burgess and Chang, 2005). Consequently, the two daughter cells often inherit equal volumes of cytoplasm. However, cytoplasmic factors, including polarized cell-fate determinants, and extrinsic niche signals can be distributed evenly or unevenly to the daughter cells through symmetric and asymmetric cell division, respectively (Kiyomitsu, 2015). Spindle orientation affects the distribution of polarized factors in the mitotic cell and these polarized factors play a role in the fate of the two daughter cells (Tzur *et al.*, 2009; Kiyomitsu, 2015) (Figure 1.1).

Mitotic spindle position also determines the physical size of the two daughter cells. The spindle is positioned at the cell centre in most vertebrate cell divisions, which gives rise to two equal-sized daughter cells. For example, mouse skin lymphoblasts undergo symmetric cell division where the difference in cell volume between the two daughter cells is usually less than 10 percent (Tzur *et al.*, 2009; Sung *et al.*, 2013). Yet, some cells displace the mitotic spindle to generate unequal-sized daughters, including in the early embryo of *Caenorhabditis elegans* and *Drosophila* neuroblasts (Kiyomitsu, 2015).

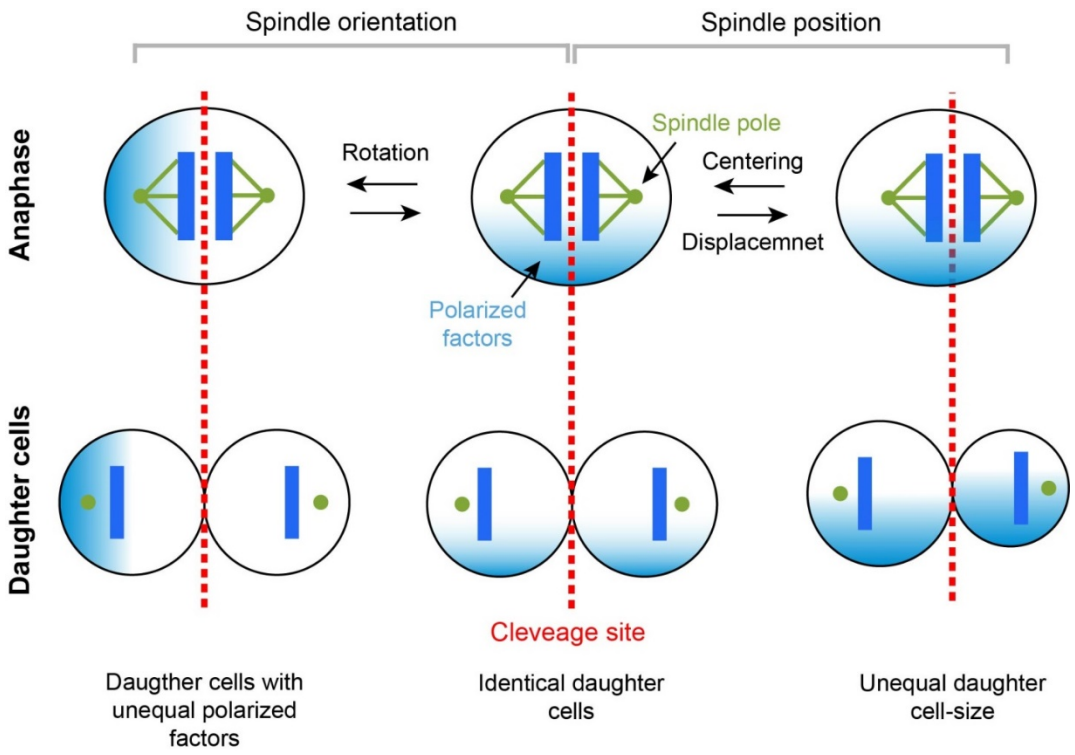

Figure 1.1 Different spindle position and orientation that affect daughter cells.

The spindle mid-zone signal (red dashed line) defines the cleavage site to generate two daughter cells. Spindle orientation determines the distribution of polarized factors (blue shaded areas) in the daughter cells, including asymmetric (left) and symmetric distributions (middle and right). Spindle position also affects daughter cell size. For example, an off-centre spindle in anaphase leads to unequal-sized daughter cells (right). Figure adapted from (Kiyomitsu, 2015).

Daughter cell size can determine cell function and behavior, which further regulates tissue architecture (Sung *et al.*, 2013). For example, different daughter cell sizes indicate different relative amounts of cytoplasmic components, molecules and organelles (Dalton and Carroll, 2013). Unequal daughter cell size may have an effect on nucleus formation during early interphase, leading to differences in the relative volumes of the nucleus and cytoplasm that is preserved in the cell cycle (Hara and Kimura, 2011). Moreover, changes of cell size can affect the rate of nuclear import and export (Brownlee and Heald, 2019). Finally, the growth behavior of large and small cells after cell division is different (Tzur *et al.*, 2009). Therefore, the correct

regulation of daughter cell sizes is an essential determinant of cellular phenotypes and tissue function.

1.2 Spindle positioning mechanisms

Unlike the metaphase checkpoint, which functions to ensure proper chromosome segregation (London and Biggins, 2014), there is no known checkpoint to safeguard spindle position (Kiyomitsu, 2015). However, several mechanisms work together to correct spindle positioning and control daughter cell size, including asymmetric cortical dynein pulling forces and asymmetric membrane elongation (Figure 1.2A).

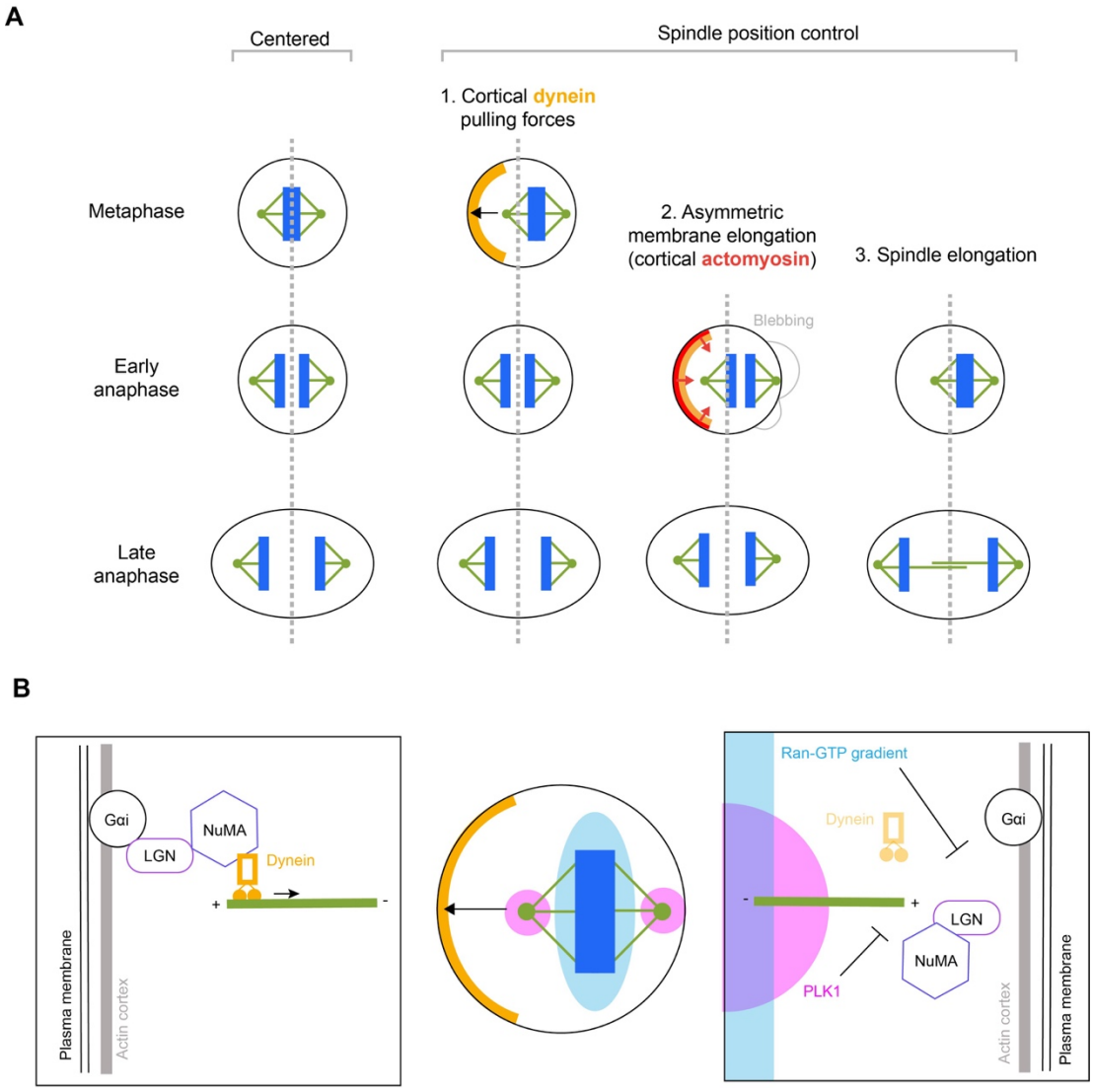

Figure 1.2 Mechanisms that regulate spindle positioning during mitosis.

A) Figure adapted from (Kiyomitsu, 2015). Most vertebrate cell divisions result in a centred metaphase spindle, which results in a centred anaphase spindle and spindle mid-zone (left). However, some metaphase spindles are off-centre and, thus, undergo positioning control mechanisms (right):
(1) During metaphase and early anaphase, asymmetric cortical dynein pulling forces (yellow) act on an off-centre spindle to correct and maintain its position till late anaphase.
(2) An off-centre spindle in early anaphase activates asymmetric membrane elongation, where asymmetrically localized actomyosin (red) contracts one polar side of the membrane to generate a cytosolic flow that leads to expansion/blebbing on the opposite polar side.
(3) Spindles can also elongate during anaphase until the spindle is correctly centred.

B) During metaphase, NuMA-LGN-Gαi at the actin rich cell cortex recruits dynein, which pulls on spindle microtubules. When the spindle pole approaches the cortex, chromosome-derived Ran-GTP gradient attenuates the interaction between LGN-NuMA and Gαi whereas PLK1 at spindle pole downregulates the interaction between LGN-NuMA and dynein.

1.2.1 Asymmetric cortical dynein forces correct spindle position prior to metaphase

Multiple mechanisms work together to regulate spindle position during mitosis. A well-described mechanism during prometaphase is cortical pulling forces on astral microtubules (those microtubules that extend from the spindle poles to the cell cortex) generated by dynein minus end-directed microtubule-based motor complexes, which control both spindle orientation and spindle positioning (Morin and Bellaïche, 2011; McNally, 2013) (Figure 1.2).

Dynein contains a dynein heavy chain (DHC) and other non-catalytic subunits, which form a complex with dynactin to regulate cortical dynein motor activity (Kardon and Vale, 2009). In vertebrates, the recruitment of dynein to the cell cortex depends on the localization of nuclear mitotic apparatus protein (NuMA)/G-protein signaling modulator 2 (LGN)/Gαi complex at the cell cortex (McNally, 2013). These cortical dynein complexes, located at opposing sides of the dividing cell, essentially play 'tug-of-war' on spindle microtubules to establish a centred and oriented mitotic spindle.

In a cell with a centred spindle in metaphase, the spindle position is often maintained until late anaphase as the cell divides symmetrically (Kiyomitsu, 2015). In the case of a mis-positioned metaphase spindle, however, dynein is stripped from the cortex closest to the mis-positioned pole and asymmetrically localized dynein at the far side of the cell cortex generates pulling forces that centre the spindle (Figure 1.2B) (Kiyomitsu and Cheeseman, 2012). The localization of dynein complexes at the cortex is controlled by a chromosome-derived Ran-GTP gradient that reduces cortical complexes of NuMA-LGN and Gαi when the metaphase chromosomes are close to the cell cortex at one pole (Kiyomitsu and Cheeseman, 2012, 2013). In parallel, polo-like kinase 1 (PLK1), which is localized at the spindle pole, provides signals that lead to the disassociation of the NuMA-LGN complex from dynein-dynactin (Kiyomitsu and

Cheeseman, 2012). During anaphase, an additional pool of NuMA is recruited by 4.1G/R to the cell cortex and acts synergistically with the LGN pathway (Kiyomitsu and Cheeseman, 2013). Cortical dynein is also regulated by a complex of hyaluronan mediated motility receptor (HMMR)-CHICA-dynein light chain 1 (DYNLL1), which binds microtubules and creates a gradient of DYNLL1 around the spindle pole (Dunsch *et al.*, 2012). DYNLL1 binds dynein to inhibit its interaction with adaptors and thus reduces the amount of cortical dynein (Dunsch *et al.*, 2012). Moreover, HMMR plays an important role in PLK1-Ran-GTP axis: PLK1-phosphorylated HMMR localizes Ran-GTP to the spindle poles, where Ran-GTP regulates cortical localization of NuMA-LGN (Kiyomitsu and Cheeseman, 2012; Connell *et al.*, 2017). Because HMMR contributes to the cortical dynein localization needed to orient and position the mitotic spindle, HMMR-silenced cells exhibit abnormally rotating spindle and decreased PLK1 activity at kinetochores and spindle poles (Chen *et al.*, 2014; Connell *et al.*, 2017).

1.2.2 Asymmetric membrane elongation corrects daughter cell size during anaphase

Although cortical dynein forces during metaphase and anaphase contribute to spindle positioning, a portion of HeLa cells still show an off-centre spindle in late anaphase, which requires another spindle positioning mechanism to fix the problem (Kiyomitsu and Cheeseman, 2013). An off-centre spindle in late anaphase is corrected by asymmetric membrane elongation, where the polar cell cortex that is closer to the spindle expands asymmetrically to alter the site of cleavage relative to the cell size (Kiyomitsu, 2015) (Figure 1.2). This rapid process generates a cytosolic flow that: (1) pushes on the spindle requiring cortical dynein to stabilize one spindle pole, and (2) expands the cell membrane (Kiyomitsu, 2015). Moreover, the sudden membrane elongation is not due to the production of new membrane, but is mediated by remodeling of pre-

existing cell cortex (Kiyomitsu and Cheeseman, 2013). During anaphase, actomyosin not only contributes to the formation of the contractile ring, but also localizes at the cell cortex to generate actomyosin-based contractile forces on the plasma membrane (Kiyomitsu, 2015).

Asymmetric cortical actomyosin produces stronger contractile forces on the cortex at one pole of the cell to destabilize the cell shape and generate asymmetric membrane elongation at the opposite side (Kiyomitsu, 2015). Asymmetric localization of cortical factors may play a role in this process. For example, anillin, a cortical scaffold protein that regulates myosin II, is removed from the cortex by chromosome-derived Ran-GTP (Kiyomitsu, 2015; Beaudet *et al.*, 2017). Depletion of anillin using small interfering ribonucleic acid (siRNA) induced premature membrane blebbing in metaphase and enlarged membrane blebs in anaphase (Kiyomitsu and Cheeseman, 2013). Although a Ran-GTP gradient plays a key role in regulating this second spindle positioning system, cortical actomyosin may also be regulated during mitosis by other pathways. A third mechanism to position the mitotic spindle relies on the full extension of the spindle such that it reaches both sides of the cell cortex and the spindle becomes centred spontaneously (Kiyomitsu, 2015; Garzon-Coral *et al.*, 2016) (Figure 1.2).

1.3 Mechanism of membrane blebbing

Membrane blebbing of cells is a phenomenon described in multiple processes including apoptosis, cell division, cell motility and cell spreading (Bereiter-Hahn *et al.*, 1990; Hickson *et al.*, 2006; Ridley, 2015; Zhang *et al.*, 2018). A dense actin network form the actin cortex that is connected to the plasma membrane and the coupling of the actin cortex with membrane provides mechanical rigidity to prevent bleb formation (Peukes and Betz, 2014). Actomyosin at the cortex induces contractile forces to generate hydrostatic pressure that pushes against the plasma

membrane (Tinevez *et al.*, 2009; Peukes and Betz, 2014). When the hydrostatic pressure is in balance with the rigidity of the actin cortex, no bleb forms (Peukes and Betz, 2014). However, this balance of force is broken when the plasma membrane decouples from the actin cortex or the actin cortex ruptures (Charras, 2008; Peukes and Betz, 2014). As a result, the hydrostatic pressure pushes outward on the membrane, forming a bleb (Figure 1.3).

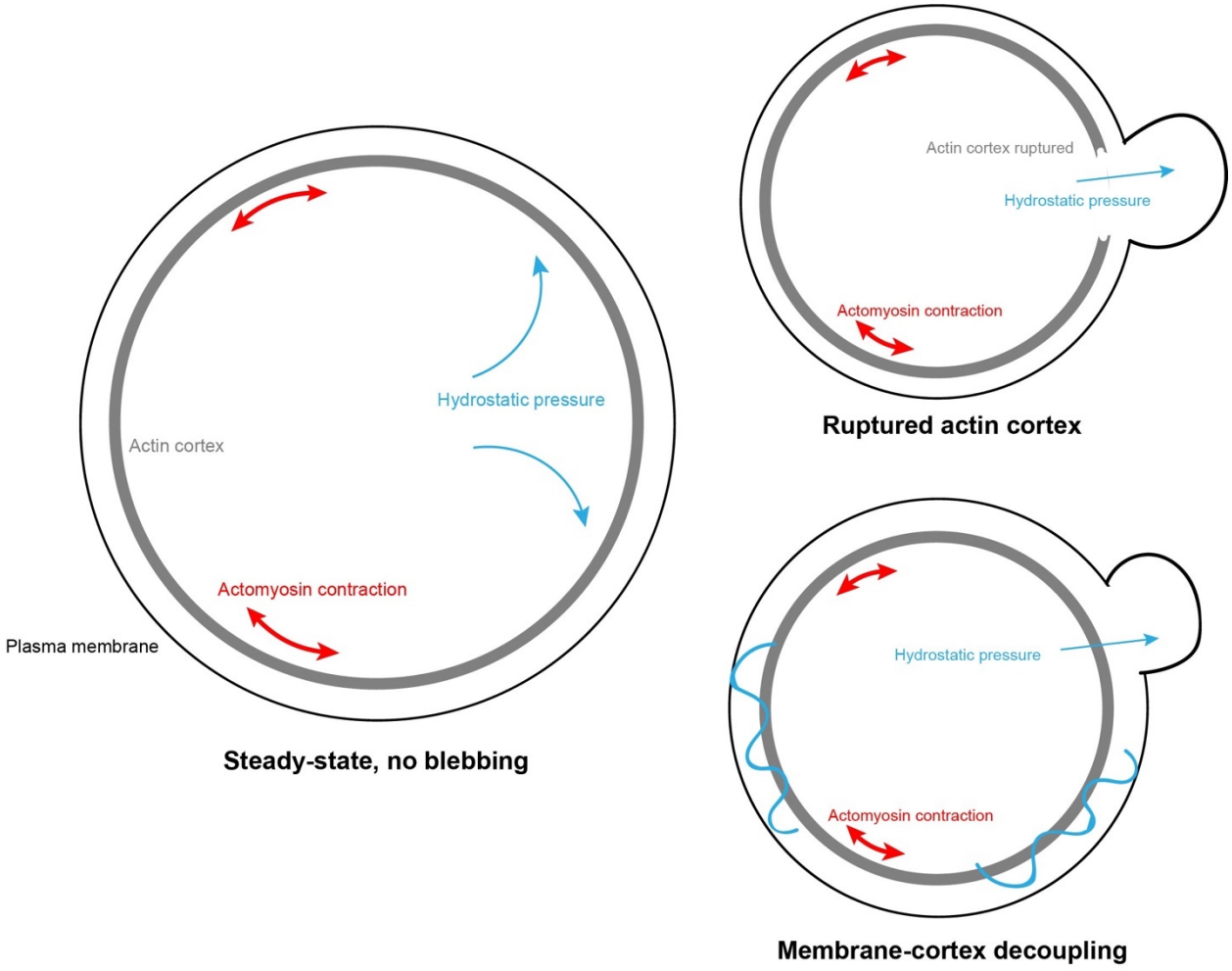

Figure 1.3 Mechanism of membrane blebbing
At steady-state, there is a balance between actin cortex rigidity and hydrostatic pressure generated by actomyosin contraction forces. However, when the actin cortex ruptures, hydrostatic pressure pushes against the membrane and form a bleb. Similarly, actomyosin can drive intracellular pressure that delaminates membrane from the actin cortex, resulting in the formation of a bleb.

1.4 Aurora kinase A regulates mitotic spindle assembly and integrity

Several kinase families are important regulators of cell division, including aurora kinases, cyclin-dependent kinases, polo-like kinases and NIMA-related protein kinases (NEKs). Aurora kinase A (Aurora A, AURKA), is an important mitotic kinase that regulates centrosome maturation and bipolar spindle assembly (Marumoto *et al.*, 2005). Chapter 4 discusses a potential daughter cell size control mechanism involving Aurora A. Thus, I will provide a brief review of Aurora A in this section.

1.4.1 A brief introduction to the discovery, structure, subcellular localization and expression of Aurora A

Aurora A was identified in *Drosophila* as *aurora.* Mutations of the *aurora* gene impedes centrosome separation, leading to a monopolar microtubule aster that was phenotypically similar to Aurora Borealis (Glover *et al.*, 1995). In vertebrates, Aurora A is a serine/threonine kinase that regulates centrosome maturation and separation and the formation of bipolar spindles (Giet and Prigent, 1999; Carmena *et al.*, 2009).

Aurora kinases consist of two main components: a regulatory domain that resides in the N-terminus and a catalytic C-terminal domain (Dodson *et al.*, 2010). The N-terminus of the kinase family varies whereas the catalytic C-terminal is highly conserved with greater than 70% sequence homology between Aurora A and Aurora B (Carmena *et al.*, 2009). Degradation of Aurora A is regulated by ubiquitination through several degradation motifs: the D-box, A-box and KEN-box (Castro *et al.*, 2002; Crane *et al.*, 2004). Activation of Aurora A depends on interactions with cofactors through the catalytic domain, followed by a conformational change in the kinase domain that facilitates autophosphorylation of Threonine 288 in the T-loop (Bayliss *et*

al., 2003; Eyers *et al.*, 2003, 2005; Hirota *et al.*, 2003; Satinover *et al.*, 2004; Carmena *et al.*, 2009; Dodson and Bayliss, 2012). Protein phosphatase 1 (PP1) inactivates Aurora A by dephosphorylating T288 (Katayama *et al.*, 2001). Also, protein phosphatase 6 dephosphorylates TPX2 bound Aurora A at T288 to control mitotic spindle formation (Zeng *et al.*, 2010).

During interphase, Aurora A localizes to both the nucleus and the centrosome (Rannou *et al.*, 2008), but is found only on the centrosomes in G2 phase (Bischoff *et al.*, 1998; Lens *et al.*, 2010). In mitotic cells, Aurora A stays on the spindle poles and decorates the spindle fibers (Bischoff *et al.*, 1998).

Expression of Aurora A is cell-cycle dependent with peak expression from late G2 to metaphase (Katayama *et al.*, 2004). Upon onset of mitotic exit, Aurora A is degraded through the anaphase promoting complex/cyclosome (APC/C) (Castro *et al.*, 2002; Crane *et al.*, 2004; Giubettini *et al.*, 2011). Analysis of mRNA revealed that the level of Aurora A expression is high in thymus, testis and fetal liver, and low in lymph nodes, bone marrow and spleen (Bischoff *et al.*, 1998).

1.4.2 The role of Aurora A during cell division

Aurora A is a critical regulator of cell division that phosphorylates multiple substrates in different phases of the cell cycle. In late G2 phase, Aurora A is activated by the LIM protein, Ajuba, and this activation is essential for the activation of cyclin B1-Cdk1 and entry into mitosis (Hirota *et al.*, 2003). Aurora A also facilitates the nuclear localization of cyclin B by phosphorylating CDC25B at the G2-M transition to drive mitotic entry (Cazales *et al.*, 2005). Active Aurora A promotes the phosphorylation and recruitment of spindle assembly factors

(SAFs) to the centrosome (Berdnik and Knoblich, 2002; Giet *et al.*, 2002; Terada *et al.*, 2003; Barros *et al.*, 2005; Kinoshita *et al.*, 2005; Mori *et al.*, 2007).

As cells enter prophase, Aurora A induces centrosome separation (Glover *et al.*, 1995; Roghi *et al.*, 1998; Giet *et al.*, 1999). After NEBD, Aurora A autophosphorylation on T288 is promoted by TPX2 (Bayliss *et al.*, 2003; Eyers *et al.*, 2003; Tsai *et al.*, 2003; Xu *et al.*, 2011; Dodson and Bayliss, 2012). TPX2 binding also stabilizes active Aurora A by inducing a conformational change that prevents dephosphorylation (Bayliss *et al.*, 2003; Eyers *et al.*, 2003; Tsai *et al.*, 2003; Satinover *et al.*, 2004), and localizes the kinase to the spindle poles (Kufer *et al.*, 2002; De Luca *et al.*, 2006; Giubettini *et al.*, 2011). The TPX2-mediated spindle pole localization of Aurora A depends on HMMR (Groen *et al.*, 2004; Maxwell *et al.*, 2005; Chen *et al.*, 2014; Scrofani *et al.*, 2015).

Active Aurora A induces microtubule nucleation and assembly through recruitment of SAFs to the centrosomes (Berdnik and Knoblich, 2002; Giet *et al.*, 2002; Terada *et al.*, 2003; Barros *et al.*, 2005; Kinoshita *et al.*, 2005; Mori *et al.*, 2007). Moreover, Aurora A phosphorylates breast cancer 1 (BRCA1) to inactivate the E3 ubiquitin ligase complex, BRCA1-BRCA1 associated ring domain protein 1 (BARD1), and this inactivation stabilizes SAFs (Sankaran *et al.*, 2005, 2006, 2007; Pujana *et al.*, 2007). In *C. elegans* zygotes, Aurora A (AIR-1 in *C. elegans*) concentrates around the spindle poles to inhibit local actomyosin contractile activity at the proximal cortex, inducing cortical flows to break symmetry (Zhao *et al.*, 2019). Thus, Aurora A may also regulate cytoplasmic flow during mitosis by inhibiting cortical actomyosin activity in vertebrate cells. In conclusion, Aurora A is involved in multiple mitotic processes, which highlights the importance of active Aurora A at the proper intracellular location and time.

1.5 Hyaluronan mediated motility receptor (HMMR) participates in spindle assembly, stability and positioning pathways

Hyaluronan-mediated motility receptor (HMMR also known as RHAMM) is a non-motor spindle assembly factor that associates with microtubules and is critical to mitotic spindle structure (Assmann *et al.*, 1999; Maxwell *et al.*, 2003; Chen *et al.*, 2014). While historically HMMR is identified as a hyaluronan binding protein, several lines of evidence regarding *HMMR* gene and protein structure, protein function and gene location through evolution suggest that HMMR is an evolutionarily conserved intracellular protein that regulates homeostasis, mitosis and meiosis regulator (He *et al.*, 2020).

1.5.1 A brief history of HMMR

Hyaluronan (HA) is a linear polysaccharide found in the extracellular matrix (ECM) that acts as a signaling molecule that binds cell-surface receptors (Lee and Spicer, 2000). HMMR was first purified from mouse NIH-3T3 cells, and mouse sarcoma virus transformed 3T3 cells, as part of a multi-component hyaluronan-binding protein (HABP) fraction (Turley *et al.*, 1987). HABP was found to be composed of three bands showed by sodium dodecyl sulfate (SDS)-gel electrophoresis: 70 kilodaltons (kDa), 66 kDa and 56 kDa (Turley *et al.*, 1987). A few years later, an antibody binding the 56 kDa component of the HABP was found to block the locomotion of 10T1/2 cell (Turley *et al.*, 1991). The complimentary deoxyribonucleic acid (cDNA) of the 56 kDa HABP was cloned from 3T3 cells and antibodies raised against this protein were shown to inhibit *ras*-regulated locomotion, which led to the gene product being given the name Receptor for Hyaluronan-Mediated Motility (RHAMM also known as HMMR) (Hardwick *et al.*, 1992). The gene product binds via ionic interactions with HA or heparin *in vitro*, and the key domains

for this interaction are located in the C-terminus, at amino acids 636-646 and amino acids 658-667 (Yang *et al.*, 1993, 1994). These two basic HA-binding motifs were later found to lie within the highly basic leucine zipper motif (bZIP), which is needed to localize the protein to the centrosome. We now know that murine HMMR runs at 95 kDa (Hofmann *et al.*, 1998b; Fieber *et al.*, 1999), which is not consistent with the 56 kDa component of the HABP.

Much of the work that defined murine HMMR as a HA binding gene product was performed with truncated variants, including the RHAMM1 variant (exon 6-18 without exon 8), RHAMM2 variant (exons 10-18), and the RHAMM1v4 variant (exons 6-18) (Hardwick *et al.*, 1992; Entwistle *et al.*, 1995; Hall *et al.*, 1995). RHAMM1v4 is commonly found in *ras*-transformed cells (Entwistle *et al.*, 1995; Hall *et al.*, 1995) as a 73 kDa protein containing exon 4 (which is now known to be exon 8 in full-length HMMR). Later, in mice, full-length HMMR was found to be a 95 kDa protein encoded by the complete *Hmmr* gene that consists of 18 exons (Hofmann *et al.*, 1998b; Fieber *et al.*, 1999). In mice, full-length HMMR is expressed in many organs with the highest expression levels in spleen, thymus and testes (Fieber *et al.*, 1999).

In humans, full-length HMMR was identified by using murine RHAMM2 cDNA to screen the cDNA library of a human breast sample (Wang *et al.*, 1996). Human HMMR is an 84 kDa protein that consists of 725 amino acids (Wang *et al.*, 1996) (termed HMMR isoform a; HMMR isoform b lacks a single codon and consists of 724 aa). Two splice variants of human HMMR were identified: HMMR lacking exon 13 ($HMMR^{-exon13}$) and HMMR lacking exon 4 ($HMMR^{-exon4}$, also known as HMMR isoform c) (Assmann *et al.*, 1998; Wang *et al.*, 1998; Crainie *et al.*, 1999; Line *et al.*, 2002). $HMMR^{-exon13}$ is found in breast cancer carcinoma and multiple myeloma (Wang *et al.*, 1998; Crainie *et al.*, 1999) whereas $HMMR^{-exon4}$ is present in

many cancer tissues, such as myeloma, breast and colorectal cancers (Assmann *et al.*, 1998; Crainie *et al.*, 1999; Line *et al.*, 2002).

Although HMMR was initially considered to be a cell surface receptor, studies show that HMMR exhibits intracellular localization and function (Assmann *et al.*, 1998; Hofmann *et al.*, 1998b; Fieber *et al.*, 1999). Antibodies against murine full-length HMMR revealed that HMMR is localized intracellularly instead of at the cell surface (Hofmann *et al.*, 1998b). Because HMMR co-localizes with and interacts with microtubules and actin filaments (Assmann *et al.*, 1999), the gene product has also been referred to as intracellular hyaluronic acid binding protein (IHABP) (Assmann *et al.*, 1998; Hofmann *et al.*, 1998b; Fieber *et al.*, 1999).

1.5.2 Structural domains of HMMR

In humans, HMMR is encoded by *HMMR*, a gene located at 5q33.2-qter (Spicer *et al.*, 1995). The HMMR gene product consists of three major regions: 1) a basic N-terminal region containing the microtubule-interacting exon 4 (Assmann *et al.*, 1999); 2) a coiled-coil stalk ranging from aa 69-681 that may be a dimerization domain; and 3) a highly conserved, C-terminal basic leucine zipper (bZIP) motif (Maxwell *et al.*, 2003) (Figure 1.3).

Figure 1.4 Structural domains of HMMR.
HMMR is predicted to be a largely coiled-coil (blue) protein with microtubule binding domain (green) at the N-terminus and a centrosome targeting bZip motif (orange) at the C-terminus. Exon4 (amino acids 91-107) is not only a splice variant but also a microtubule-binding domain. Threonine 703 is a substrate of the mitotic kinases Aurora A and/or PLK1.

The N-terminal domain in HMMR binds directly to microtubules (Assmann et al., 1999) whereas the C-terminus can interact with microtubules indirectly through dynein (Maxwell *et al.*, 2003; Chen *et al.*, 2014). Thus, HMMR can potentially crosslink microtubules (Chen *et al.*, 2014). The C-terminal motif of HMMR contains a centrosome-targeting motif and is required for TPX2 localization, proper spindle assembly and spindle integrity (Maxwell *et al.*, 2003; Chen *et al.*, 2014). A CHICA-interacting region is located within the stalk region in HMMR (aa 365-546) (Dunsch *et al.*, 2012). Although the function remains unclear, a calcium-dependent calmodulin binding domain is found at aa 574-602 in HMMR (Assmann *et al.*, 1998). In addition, PLK1 (Grosstessner-Hain *et al.*, 2011) and Aurora A (Maxwell *et al.*, 2011) recognize and phosphorylate T703, a site that is C-terminal to the bZIP motif.

1.5.3 Expression and intracellular functions of HMMR

The first *Hmmr* mutant mice were generated by deleting exons 8-16 of *Hmmr* gene ($Hmmr^{-exon8-16}$) in embryonic stem cells (Tolg *et al.*, 2003). $Hmmr^{-exon8-16}$ mice did not display obvious developmental defects at birth with respect to size and gross anatomy (Tolg *et al.*, 2003). $Hmmr^{-exon8-16}$ mice generally lived up to 2 years, similar to wild type (WT) mice (Tolg *et al.*, 2003). However, neonates of homozygous mating were reduced in number indicating a possible defect in fertility (Tolg *et al.*, 2003).

A different HMMR mutant ($Hmmr^{m/m}$) mouse model was generated by inserting a neomycin cassette that contains stop codons between exon 10 and 11 of *Hmmr*, resulting in a gene product lacking the C-terminus (Li *et al.*, 2015). These $Hmmr^{m/m}$ mice also survived and did not display detectable differences in appearance compared to WT mice (Li *et al.*, 2015). However, $Hmmr^{m/m}$ females exhibited hypofertility, which became more serious as they aged (Li

et al., 2015). Moreover, *Hmmr*$^{m/m}$ neuroprogenitor cells displayed metaphase spindle rotation more frequently than WT cells and this spindle abnormality correlated with transient megalencephaly, a developmental defect of the brain (Li *et al.*, 2017).

Another HMMR knockout (KO) mouse model (*Hmmr*$^{tm1a/tm1a}$) was generated in the Maxwell lab through the insertion of the *lacZ* gene after exon 2 of *Hmmr* to disrupt HMMR expression (Connell *et al.*, 2017). *Hmmr*$^{tm1a/tm1a}$ mice (*Hmmr* KO) had a very low survival rate compared to their wild-type (WT) littermates, with only 20% of *Hmmr* KO newborns surviving after two days (Connell *et al.*, 2017). *Hmmr* KO mice were smaller than their WT littermates (Connell *et al.*, 2017). Moreover, a shrinkage of seminiferous tubules and increased apoptosis in the testes were observed in *Hmmr* KO mice (Connell *et al.*, 2017). Finally, the brain size of *Hmmr* KO mice showed large variation, including both microcephaly and megalencephaly (Connell *et al.*, 2017).

The brains in *Hmmr* KO neonatal mice had a reduced cortical area and enlarged ventricles, which were associated with mis-oriented cell division of the neuroepithelial progenitors (NPs) (Connell *et al.*, 2017). In WT E14.5 embryos, HMMR localized to the spindle microtubules that oriented along the ventricle surface whereas, in *Hmmr* KO embryos, HMMR was lost and only up to 66.6% of NPs had spindles lining within 30 degrees of the ventricle surface (Connell *et al.*, 2017). Similarly, *Xenopus laevis* embryos injected with *Hmmr* morpholino oligomers (MO), which silence HMMR expression during development, showed defects during neural tube closure, consequently leading to narrowed forebrains, loss of hemispheric separation, and smaller olfactory bulbs (Prager *et al.*, 2017). It is likely that *Hmmr* KO mice presented more severe defects than those observed in *Hmmr*$^{-exon8-16}$ mice and *Hmmr*$^{m/m}$ mice because insertion of lacZ after exon 2 produced a more complete knockout whereas the

other two gene disruption strategies result in the expression of truncated versions of HMMR with some functionality.

Taken together, three animal models for *Hmmr/hmmr* KO or mutation demonstrate defects in neurodevelopment associated with neuroprogenitor cell division as well as deficits in fertility, which is expected given the heightened expression of HMMR in human testis and reproductive tissues.

1.5.4 HMMR regulates Aurora A and Polo-like kinase 1

HMMR is an intracellular protein that binds to interphase microtubules and accumulates at centrosomes to play important roles in mitosis (Assmann *et al.*, 1999; Maxwell *et al.*, 2003). During prophase, HMMR is located at the microtubules between the two asters as well as directly at the asters (Maxwell *et al.*, 2003). When the cell enters prometaphase, HMMR becomes concentrated at the spindle pole and along the spindle microtubules (Maxwell *et al.*, 2003). In the Ran-GTP-dependent microtubule nucleation pathway, Ran-GTP induces the interaction of HMMR and TPX2, an activator of Aurora A (Groen *et al.*, 2004; Chen *et al.*, 2014; Scrofani *et al.*, 2015) (Figure 1.4). HMMR recruits TPX2 to the sites of microtubule assembly to activate Aurora A (Chen *et al.*, 2014). Active Aurora A then recruits downstream substrates to the site of microtubule assembly (Macurek *et al.*, 2008).

HMMR-silenced cells showed a significant increase in mitotic spindle defects including disorganized spindles and multipolar spindles, as well as delayed mitotic kinetics in terms of both bipolar spindle assembly and completion of mitosis (Chen *et al.*, 2014). In addition, HMMR-silenced cells undergo mitotic spindle rotation (Chen *et al.*, 2014). HMMR-depleted cells also display reduced microtubule nucleation at non-centrosomal sites as well as lower

TPX2 abundance due to increased proteasome-mediated degradation (Chen *et al.*, 2014). In these HMMR-silenced cells, inhibition of the proteasome restored TPX2 abundance but did not rescue Aurora A activity because TPX2 was still not properly localized to the spindle poles in the absence of HMMR (Chen *et al.*, 2014). In general, HMMR affects Aurora A activity through the regulation of the localization and abundance of TPX2.

HMMR also affects PLK1 activity. HMMR promotes PLK1 activity at mitotic spindle poles, which stabilizes astral microtubules and localizes Ran to mitotic spindle poles (Connell *et al.*, 2017). HMMR-silenced cells exhibit decreased PLK1 activity at kinetochores (Chen *et al.*, 2014; Connell *et al.*, 2017). In addition, PLK1 may reciprocally regulate HMMR that mitotic phosphoproteome analysis identifies HMMR-threonine 703 as a potential substrate of PLK1 (Nousiainen *et al.*, 2006).

1.5.5 HMMR regulates the Ran-GTP pathway

HMMR is involved in the Ran-GTP-importin A pathway where HMMR localizes Ran-GTP to the spindle pole and Ran-GTP activates spindle assembly factors (SAFs), such as NuMA and TPX2, by releasing the SAFs from importin α/β (Joukov *et al.*, 2006; Connell *et al.*, 2017).

HeLa cells with overexpression of green fluorescent protein (GFP) -tagged HMMR (GFP-HMMR) require more time to complete the spindle checkpoint and to complete mitosis. However, GFP-HMMR overexpression does not affect TPX2 and p-Aurora A localization at the mitotic spindle poles although a significant proportion of the GFP-HMMR expressing cells display off-centred spindles (Connell *et al.*, 2017). Moreover, in GFP-HMMR overexpressing cells, Ran-GTP localized not only on the spindle pole but also ectopically along mitotic spindles while cortical NuMA localization was completely lost (Connell *et al.*, 2017) (Figure 1.4). Ran-

GTP regulates cortical dynein and asymmetric localization of actomyosin (as discussed in section 1.3.1 and 1.3.2). Thus, the aberrant expression of GFP-HMMR may also disturb these two pathways through the ectopic localization of Ran-GTP at mitotic spindles.

1.5.6 HMMR controls dynein and kinesin motor activities during mitosis

During mitosis, dynein is critical for maintaining proper spindle orientation and position (Maxwell *et al.*, 2003; Dunsch *et al.*, 2012; Kiyomitsu and Cheeseman, 2012; Kiyomitsu, 2015). Dynein molecular motors and kinesin molecular motors move along microtubules towards the minus ends and positive ends, respectively (Kardon and Vale, 2009). HMMR regulates these activities; for example, through a DYNLL1-CHICA-HMMR complex, HMMR contributes to asymmetric cortical dynein localization during cell division (Dunsch *et al.*, 2012). The CHICA-HMMR complex binds to the mitotic spindle and, through the C-terminus of CHICA, recruits DYNLL1, a regulator that can remove dynein for the cell cortex to generate a gradient of DYNLL1 around the spindle poles (Dunsch *et al.*, 2012). As the spindle pole approaches the cell cortex during cell division, the gradient around the spindle pole downregulates cortical dynein through the action of DYNLL1 (Dunsch *et al.*, 2012) (Figure 1.4). Moreover, HMMR affects cortical dynein localization indirectly through PLK1 activity and Ran-GTP localization at the spindle poles (Chen *et al.*, 2014; Connell *et al.*, 2017). Thus, HMMR modifies localization of dynein at cell cortex during cell division.

HMMR also regulates a plus-end directed molecular motor, kinesin Eg5. The metaphase spindle is stabilized by forces generated by the plus-end-directed kinesin motor kinesin-5 (Eg5), which slides antiparallel microtubules outward, and the minus-end-directed kinesin-14, which slides antiparallel microtubules inward (Ou and Scholey, 2022). Eg5 is a key kinesin that is

found near centrosomes and regulates centrosome separation in prophase (Eibes *et al.*, 2018). Cortical dynein together with Eg5, generate the outward movement of spindle elongation by pulling and pushing forces, respectively (Ou and Scholey, 2022).

Centrosomes are critical for spindle assembly and the separation of the centrosomes leads to formation of the two spindle poles during mitosis (Eibes *et al.*, 2018). *Xenopus* HMMR (also known as XRHAMM) regulates centrosome separation by controlling centrosomal localization of TPX2, which is important for the organization of the microtubule aster and the localization of Eg5 (Eibes *et al.*, 2018). The binding of TPX2 inhibits Eg5 activity, reducing outward-directed forces (Chen *et al.*, 2018). Therefore, the balance between the outward- and inward-directed forces was disrupted in HMMR-silenced cells and can result in activation of spindle assembly checkpoint (SAC), which is activated when kinetochores are not properly attached to microtubule (Chen *et al.*, 2018; Lara-Gonzalez *et al.*, 2021).

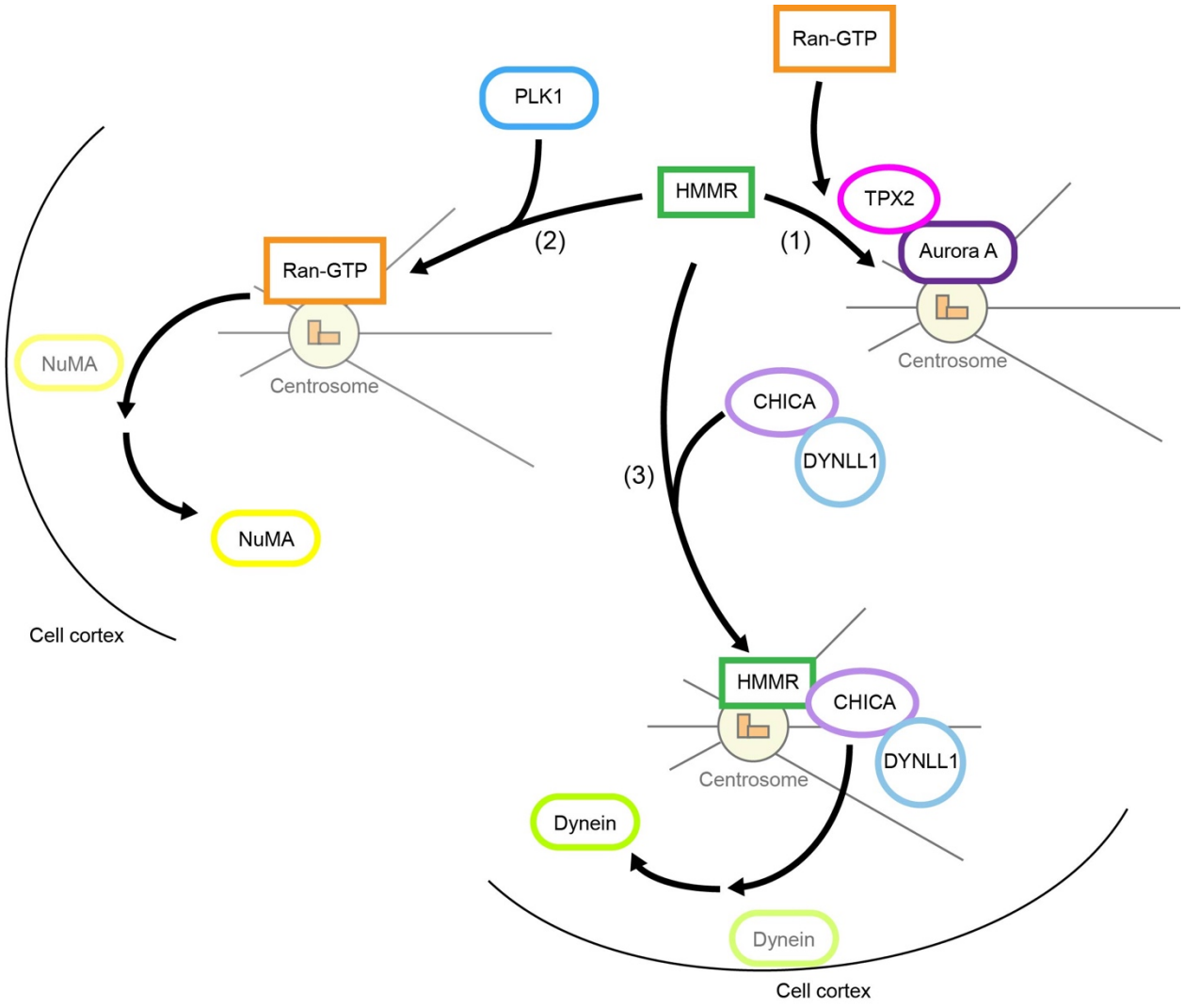

Figure 1.5 HMMR mediated pathways during mitosis.

1) Ran-GTP induces the interaction between HMMR and TPX2. HMMR recruits TPX2 to the mitotic spindle, where TPX2 activates and stabilizes Aurora A.
2) HMMR facilitates centrosomal localization of Ran-GTP in a PLK1-dependent manner, which may affect cortical NuMA retention.
3) HMMR-CHICA-DYNLL1 complex localizes to the mitotic spindle to regulate cortical dynein.

1.5.7 BRCA1-BARD1 and the anaphase promoting complex/cyclosome (APC/C) regulate the degradation of HMMR

During anaphase and telophase, HMMR localizes to the spindle midzone (Maxwell, 2003). During mitotic exit, HMMR is degraded during anaphase by both the ubiquitin ligase anaphase-promoting complex/cyclosome (APC/C) (Song and Rape, 2010) and the E3 ubiquitin ligase complex BRCA1/BARD1 during anaphase (Pujana *et al.*, 2007). APC/C recognizes the destruction (D) box, KEN box, and TEK box in the C-terminal domain of HMMR (Song and Rape, 2010). Moreover, in *Xenopus*, the proper degradation of HMMR by BRCA1/BARD1 maintains an adequate level of TPX2 and ensures proper spindle assembly and integrity (Joukov *et al.*, 2006). Loss of BRCA1 leads to aberrant localization of TPX2 and disrupts spindle integrity (Groen *et al.*, 2004; Joukov *et al.*, 2006). Finally, *HMMR* is a breast cancer susceptibility gene and *HMMR* haplotypes, which are associated with either elevated or reduced *HMMR* germline expression, affect the risk of breast cancer development in *BRCA1* mutation carriers (Pujana *et al.*, 2007; Blanco *et al.*, 2015).

1.5.8 HMMR and cancer

The level of HMMR is generally low in most tissues. In proliferative tissues, for example in spleen, thymus, testis and placenta, HMMR expression is elevated (Fieber *et al.*, 1999; Connell *et al.*, 2017). Breast cancer development is associated with *HMMR* haplotype tagging single nucleotide polymorphisms (htSNPs) that correlate with either HMMR overexpression or HMMR downregulation, implying any aberrant HMMR expression level can affect tumorigenesis (Pujana *et al.*, 2007).

HMMR overexpression affects disease progression and survival in multiple types of tumors (Wang *et al.*, 1998; Yamada *et al.*, 1999; Li *et al.*, 2000; Rein *et al.*, 2003; Even-Ram *et al.*, 2007; Gust *et al.*, 2009; Shigeishi *et al.*, 2014). In addition, high HMMR expression correlates with poor prognosis in many cancer types, for example in breast, stomach, endometrial prostate, colorectal cancers and multiple myeloma (Li *et al.*, 2000; Assmann *et al.*, 2001; Maxwell *et al.*, 2004; Zlobec *et al.*, 2008; Gust *et al.*, 2009). Moreover, the long noncoding RNA (lncRNA), HMMR antisense RNA I (HMMR-AS1), stabilizes HMMR levels and regulates tumorigenesis progression (Liu *et al.*, 2016; Li *et al.*, 2018). Yet, low HMMR expression is also associated with poor survival in other cancers, such as peripheral nerve sheath tumors and seminomas (Mantripragada *et al.*, 2008; Mohan *et al.*, 2013; Li *et al.*, 2015). In addition, the expression of a splice variant of HMMR that lacks exon 4 ($HMMR^{-exon4}$) is elevated in a variety of cancers (He *et al.*, 2020). The N-terminal exon 4 of HMMR encodes a part of the microtubule-binding domain and expression of $HMMR^{-exon4}$ can induce the growth of pancreatic islet tumors as well as its metastasis (Assmann *et al.*, 1999; Maxwell *et al.*, 2003; Du *et al.*, 2011).

Multiple complexes or pathways regulate HMMR expression in cells, such as TP53, the Hippo pathway, APC/C and BRCA1-BARD1 activity (Pujana *et al.*, 2007; Sohr and Engeland, 2008; Song and Rape, 2010; Wang *et al.*, 2013). Aberrant HMMR expression, either overexpression or depletion, may disrupt microtubule-based processes during mitosis and promote tumorigenesis. Thus, the association between HMMR and tumorigenesis is likely multifactorial. Increased proliferation (and high HMMR expression) correlates with poor prognosis. Conversely, abnormally low HMMR expression, or expression of an isoform that may lose normal function (-exon 4), is associated with genome instability and correlates with poor prognosis.

1.6 Actin binding proteins and mitosis

The actin cytoskeleton is the major constituent of the cell cortex and plays an essential role during mitosis to facilitate cell rounding, strengthen the cell cortex and cytokinesis (Kunda and Baum, 2009; Kelkar *et al.*, 2020). Actin filaments and myosin II contribute to normal spindle assembly and positioning by separating and positioning the centrosomes in early cell division (Rosenblatt *et al.*, 2004). Moreover, asymmetric cortical actomyosin in anaphase generates membrane blebs rapidly to re-adjust the cellular boundary (Kiyomitsu, 2015). Finally, during cytokinesis, actomyosin at the cleavage furrows generates the contractile ring to cleave the daughter cells (Heng and Koh, 2010). HMMR also interacts with filamentous actin (F-actin) by immunofluorescence and co-sedimentation assay (Assmann *et al.*, 1999). Although the actin-binding motif in HMMR and how HMMR regulates the actin network requires further investigations, HMMR is similar to tropomyosin, an actin-binding protein (ABP), with respect to sequence and predicted structure (Ayscough, 1998; Assmann *et al.*, 1999).

The molecular control of the actin network is important for multiple mitotic stages. For example, the overexpression of cofilin, a protein that depolymerizes actin, results in G1 phase arrest (Lee and Keng, 2005). Also, aggregation of F-actin occurs around chromosomes in cells with disrupted actin-related protein 2/3 (ARP2/3) complex (Heng and Koh, 2010). In addition, actomyosin generates force that contributes to chromosome segregation (Heng and Koh, 2010). Therefore, actin dynamics and remodeling are critical to mitosis and these processes are regulated by a group of ABPs that control F-actin assembly and disassembly, stability, actin bundling, and cross-linking (Winder and Ayscough, 2005).

1.6.1 Non-muscle myosin IIa (NMIIa/MYH9) during cell division

There are three isoforms of non-muscle myosin II (NMII): NMIIa (MYH9), NMIIb (MYH10), and NMIIc (MYH14) (Ouderkirk and Krendel, 2014). All three NMII isoforms localize to the cell cortex (Biro *et al.*, 2013; Maliga *et al.*, 2013; Beach *et al.*, 2014).

NMIIa is encoded by the gene *MYH9* (Ma and Adelstein, 2014; Shutova and Svitkina, 2018). NMIIa filaments can cluster with disordered actin filaments to form actin-NMII networks for large-scale contractions during cell migration and cytokinesis (Svitkina *et al.*, 1997; Baird *et al.*, 2017; Spira *et al.*, 2017). NMIIa plays a major role in junction assembly, cell rear retraction and remodeling of extracellular matrix (Even-Ram *et al.*, 2007; Smutny *et al.*, 2010; Liu *et al.*, 2014). Similar to other NMII paralogs, NMIIa is involved in contraction forces during cytokinesis (Beach and Egelhoff, 2009).

NMII is important for bleb formation and the regulation of cell shape (Shutova and Svitkina, 2018). Ectopic expression of NMIIa induces membrane blebbing while NMIIa knockdown (KD) in MCF-7 cells reduces the percentage of cells that form multiple blebs (Dey *et al.*, 2017). Generally, NMIIa contributes mainly to rapid and strong contractile forces during multiple cellular processes due to its high adenosine triphosphatease (ATPase) rate compared to NMIIb and NMIIc (Shutova and Svitkina, 2018). In addition, NMIIa drives the retraction of membrane bleb during cytokinesis (Taneja and Burnette, 2019).

1.6.2 Non-muscle myosin IIb (NMIIb/MYH10) in cell division

Non-muscle myosin IIB (NMIIb) is a component of the actomyosin contractile ring that is established at the cleavage furrow (Roy *et al.*, 2016). The adenosine triphosphate (ATP)-

dependent interaction between NMIIb and actin filaments promotes sliding of the filaments and generates tension forces (Vicente-Manzanares *et al.*, 2009).

Besides a role in contractile ring formation, NMIIb also contributes to cortical stability during mitosis (Ma *et al.*, 2012). NMIIb-silenced COS-7 cells exhibit a fluctuating cortical surface during cytokinesis (Ma *et al.*, 2012). NMIIb contributes to cortical force generation and this function does not rely on actin-sliding ability but rather on interactions with actin and the ability to produce tension on actin filaments (Ma *et al.*, 2012). In addition, *Xenopus* NMIIb was shown to bind anillin directly using affinity chromatography (Straight *et al.*, 2005) and anillin is a cortical scaffold protein that regulates myosin II during cell division (Kiyomitsu, 2015). Therefore, NMIIb plays a critical role in regulating actin structures and maintaining durable stresses and cytoskeleton stability during mitosis.

1.6.3 ARP2/3 complex during cell division

The ARP2/3 complex consists of seven subunits in total, including ARP2, ARP3, ARPC1, ARPC2, ARPC3, ARPC4, and ARPC5 (Goley and Welch, 2006). When activated, the ARP2/3 complex mimics an actin dimer to initiate actin nucleation by generating a branched actin filament (Rodnick-Smith *et al.*, 2016). ARP2/3 is usually inactive and becomes active in the presence of ATP, existing F-actin, globular actin monomers (G-actin) and nucleation promoting factors (NPFs) for example the WASP family proteins, WISH/DIP/SPIN90 (WDS)-family proteins and cortactin (Rodnick-Smith *et al.*, 2016; Gautreau *et al.*, 2022).

ARP2/3 activity regulates membrane bleb formation by modifying cortical actin organization (Severson *et al.*, 2002; Pollard and Borisy, 2003; Roh-Johnson and Goldstein, 2009; Bergert *et al.*, 2012; Bovellan *et al.*, 2014). The ARP2/3 complex is the major actin filament

regulator in lamellipodium and the inhibition of ARP2/3 complex activity by drugs, or siRNA treatment, can transform lamellipodium into membrane blebs in adherent carcinoma cells (Pollard and Borisy, 2003; Bergert *et al.*, 2012). Similar results were found in *C. elegans* in that depletion of ARP2/3 induces blebbing (Severson *et al.*, 2002; Roh-Johnson and Goldstein, 2009). During mitosis, ARP2/3 is also required for the formation of an amorphous actin cluster that revolves underneath the cell membrane (Mitsushima *et al.*, 2010). This unique mitotic actin cluster is due to rapid actin polymerization and depolymerization (Mitsushima *et al.*, 2010). Although the physiological function of the revolving actin cluster remains unclear, disrupted ARP2/3 complex activity resulted in a prolonged period from prometaphase to anaphase and more cells displays multiple nuclei due to aberrant cytokinesis (Moulding *et al.*, 2007).

Other subunits of the ARP2/3 complex have critical mitotic functions. For example, ARPC1B interacts with Aurora A and regulates G2/M progression (Molli *et al.*, 2010). Moreover, recent studies tracking ARPC2, as a marker for the ARP2/3 complex, have found a role for the ARP2/3 complex in the regulation of centrosomal actin (Farina *et al.*, 2019; Plessner *et al.*, 2019). It is intriguing to discover that ARPC2 dynamically localizes at the cortex and around centrosomes during cell division (Mitsushima *et al.*, 2010; Farina *et al.*, 2019; Plessner *et al.*, 2019). ARPC2 and ARPC4 form a dimer that serves as a structural backbone of the complex and the major surface for mother actin filament interaction (Gournier *et al.*, 2001; Robinson *et al.*, 2001; Rouiller *et al.*, 2008). Conditional depletion of ARPC2 in murine bone-marrow-derived macrophages results in loss of both the ARP2 and ARP3 subunits, suggesting absence of the complex as all 7 subunits are required for stability of the ARP2/3 complex (Rotty *et al.*, 2015). ARPC2$^{-/-}$ mammalian fibroblasts have less dynamic actin filaments compared to wild-type controls (Rotty *et al.*, 2015). Thus, ARPC2 localization may determine ARP2/3 complex

functions. Yet, it remains unclear how the ARP2/3 complex may affect other mitotic phases and whether spindle pole-localized proteins can regulate ARP2/3 complex activity at in order to regulate cytokinesis.

1.7 Rationale, hypothesis and significance of study

1.7.1 Summary of rationale, hypothesis and aims

During mitosis, HMMR interacts with TPX2, forming a ternary complex with dynein to maintain spindle integrity (Maxwell *et al.*, 2003; Groen *et al.*, 2004). TPX2 is a co-factor of Aurora A that is required for optimal kinase activity (Bayliss *et al.*, 2003; Dodson and Bayliss, 2012), and HMMR facilitates the correct localization of TPX2 and proper activation of Aurora A (Maxwell *et al.*, 2011; Chen *et al.*, 2014). Aurora A affects actin organization by regulating actin-regulating proteins such as ARP2/3 complex, cofilin and actomyosin components (Molli *et al.*, 2010; Ritchey and Chakrabarti, 2014; Zhao *et al.*, 2019). Regulated localization of actomyosin components at the cortex is critical for cell shape changes during mitosis and therefore determines daughter cell-size (Kiyomitsu, 2015). Collectively, these results suggest the elevated expression of HMMR, which correlates with tumorigenesis, may affect complexes at the cortex with downstream consequences on asymmetric membrane elongation, genome stability, and daughter cell-size control pathways.

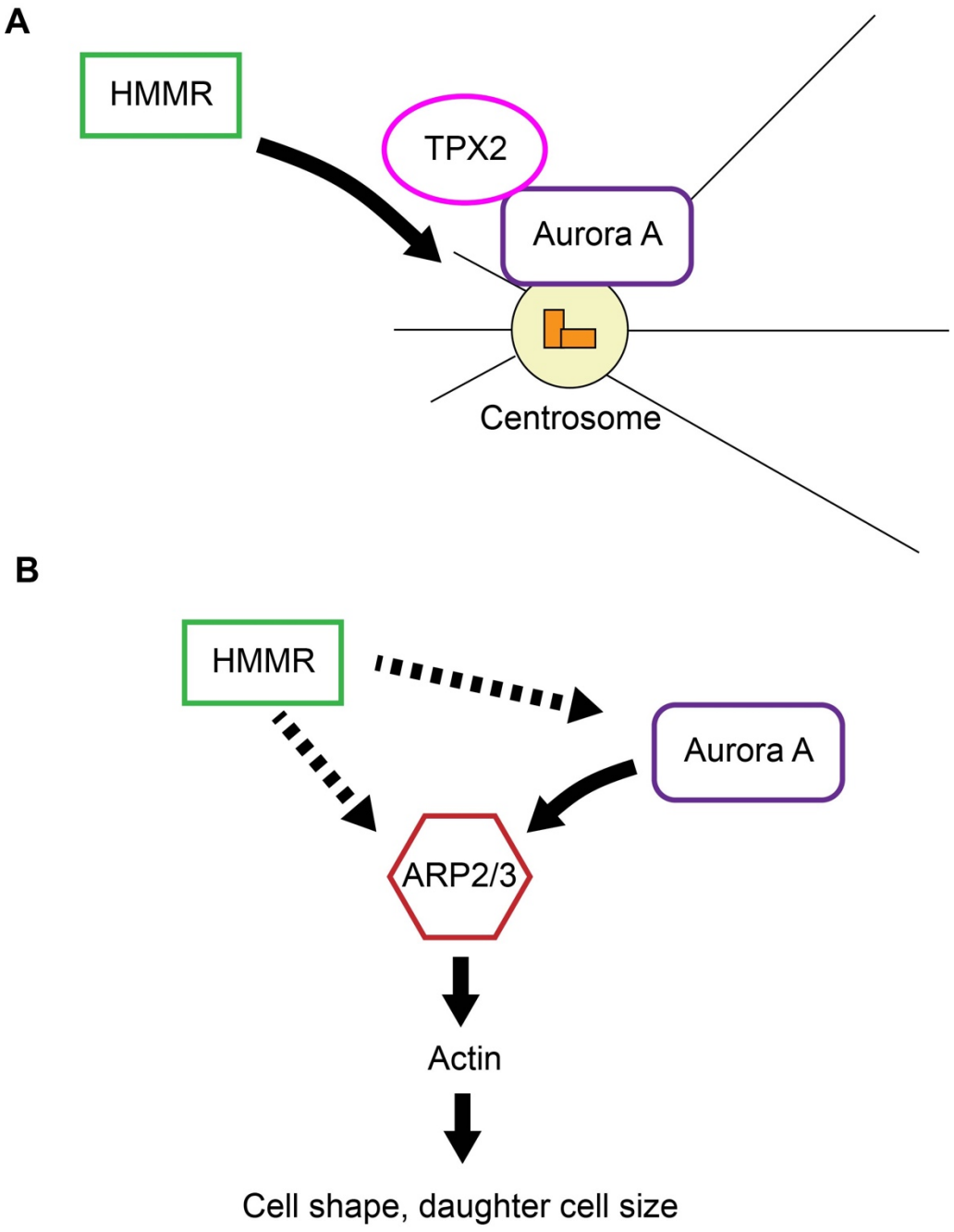

Figure 1.6 Potential HMMR-mediated pathway to regulate daughter cell size.

A) HMMR recruits TPX2 to the mitotic spindle and TPX2 promotes optimal Aurora A activity at spindle pole.

B) HMMR may regulate actin-binding proteins directly or indirectly through Aurora A during cell division to modify daughter cell size.

Hypothesis: HMMR regulates asymmetric membrane elongation and daughter cell size by modifying cortical actomyosin components during anaphase.

Aim 1. Investigate whether HMMR-overexpression affects membrane elongation and the control of daughter cell size during cell division.

Aim 2. Discover putative HMMR binding proteins that may regulate cortical stiffness and membrane blebbing during anaphase to elucidate potential HMMR-mediated kinase pathways that may govern daughter cell size.

Aim 3. Examine the effect of altered HMMR expression *in vivo, in situ* and *ex vivo* on phenotypes that relate to the control of daughter cell size.

1.7.2 Significance

Cell size affects cell behaviour (Fuse *et al.*, 2003; Ou *et al.*, 2010; Kiyomitsu and Cheeseman, 2013; Jankele *et al.*, 2021). Daughter cell size may also affect cell cycle and proliferation, due to altered ratio of nucleus and cytoplasm volume (Hara and Kimura, 2011); indeed, a difference of cell size in cancer is an cell-autonomous trait that may influence metastatic potential (Ginzberg *et al.*, 2015; Mu *et al.*, 2017). Thus, the control of daughter cell size is an essential homeostatic and tumor suppressive function. However, it is not known how asymmetric membrane elongation is regulated (Kiyomitsu, 2015). Findings from my study provide new insights into how the level of HMMR expression regulates anaphase spindle positioning and daughter cell size.

Chapter 2: Materials and methods

2.1 Isolation and culturing of human mammary epithelial cells (collaboration with the Eaves Lab, BC Cancer Research Center)

Mammary tissues were obtained from donors with consent and manipulated following approved protocols by the University of British Columbia Research Ethics Board (reference H19-04034). Human mammary epithelial cells were isolated from normal reduction mammoplasty tissues as described (Eirew *et al.*, 2008). Tissue was ground using scalpels followed by dissociation in DMEM/Ham's F12 media (1:1, STEMCELL Technologies) supplemented with 2% BSA (Gibco), 100 U/mL hyaluronidase (Sigma), and 300 U/mL collagenase (Sigma) at 37 ºC for 18 hours. The dissociated mammary organoids were then centrifuged at 80 x g for 4 minutes, suspended in 6% dimethyl sulfoxide (DMSO) in fetal bovine serum (FBS) and then cryopreserved in liquid nitrogen.

To obtain mammary epithelial cells, the cryopreserved mammary organoids were thawed and washed with 2% FBS in Hank's Balanced Salt Solution (HF), followed by dissociation in 5 mg/mL dispase (STEMCELL Technologies), 2.5 mg/mL trypsin with 1 mM ethylenediaminetetraacetic acid (EDTA) (STEMCELL Technologies) and 100 μg/mL DNase I (Sigma). Dissociated cells were then washed in HF and single cell suspension was achieved by passing the suspension through a 40 μm cell strainer. The single-cell suspension was first sorted by fluorescence-activated cell sorting (FACS) to obtain $DAPI^{-}CD45^{-}CD31^{-}$ cells, followed by purification based on epithelial cell adhesion molecule (EpCAM) and CD49f expression: $EpCAM^{low}CD49^{+}$ for basal cells (BCs), $EpCAM^{high}CD49^{+}$ for luminal progenitors (LPs), $EpCAM^{high}CD49^{-}$ for luminal cells (LCs) and $EpCAM^{-}CD49^{-}$ for stromal cells (SCs). Purified human mammary cells were cultured in 1:1 DMEM/F12 (STEMCELL Technologies)

supplemented with 5% FBS, 1 µg/mL insulin (Sigma), 0.5 µg/mL hydrocortisone (Sigma), 10 ng/mL EGF (Sigma) and 10 ng/mL cholera toxin (Sigma).

2.2 Generation of BLG-Cre *Trp53*$^{+/-}$ *Brca1*$^{fl/fl}$ *HMMR*$^{Tg/Tg}$ mice (collaboration with Pujana Lab, Spain)

All animal experiments were conducted in the University of Barcelona-Bellvitge animal facility, under the Generalitat de Catalunya license authority (reference 9774) and with the permission of the IDIBELL University of Barcelona-Bellvitge Ethics Committee. Homologous recombination in embryonic stem cells (ESCs) (genOway's custom development) was used to generate a mouse model with conditional expression of human HMMR gene. First, human HMMR cDNA and hGHpA signal were cloned into the genOway Rosa26 Quick KnockinTM targeting vector. A 5'-loxP-flanked STOP-neomycin selection (Neo) cassette is flanked by the Cre recombinase, thus activating the HMMR transgene controlled by the endogenous Rosa26 promoter upon recombination. Asc I restriction enzyme cut the targeting vector and ES cells were transfected with the linear construct by electroporation. Colonies were selected by G418, followed by PCR and Southern blot to screen for homologous recombination of 3' end of the targeting vector and 5' end of the Rosa 26 locus. The verified ES cells were injected into C57L/6J-recipient blastocytes, followed by implantation into pseudo-pregnant females for further development. The resulting chimeric males were mated with C57BL/6 wild-type females. Germline transmission of the knock-in allele in F1 mice was confirmed by polymerase chain reaction (PCR) analysis. F1 heterozygous offspring were crossed to produce F2 homozygous mice. F2 mice were then mated with the Trp53tm1Brd Brca1tm1Aash Tg(LGB-cre)74Acl/J mice, also known as BLG-Cre; Brca1F22-24/F22-24; Trp53+/- mice (The Jackson Laboratory, cat#

012620). Upon lactation, the BLG-Cre is active and leads to loss of Brca1 and human HMMR expression in mammary tissue.

2.3 Mouse tissue processing and paraffin embedding

Mouse tissues were freshly frozen or fixed in 4% formaldehyde in phosphate buffered saline (PBS), then embedded in paraffin. Tissues were sectioned at intervals of 4 μm. Sectioned tissues were deparaffinized prior to antigen-retrieval processing and sections were further processed for immunostaining as described in (Li *et al.*, 2015).

2.4 Generation and imaging of *Drosophila* neuroblasts expressing human HMMR (performed by Dr. Connell in Maxwell Lab, collaboration with Allan Lab, UBC)

This work was performed by Marisa Connell in the Maxwell Lab in collaboration with the Allan Lab (UBC). HMMR transgenic lines were generated by Genetic Services Inc. using site-specific insertion of attB vectors into the attP40 locus by phiC31-integrase. *D. melanogaster* were maintained on standard cornmeal-agar food at RT. For live imaging, larvae were grown at 25 °C. Embryos were collected at 25 °C for 15 hours. Second instar larval brains were dissected and mounted in Schneider's media supplemented with 10% FBS and 0.5 M ascorbic acid (Sigma). Images were taken at intervals of 12 seconds using a Perkin Elmer Ultraview VOX spinning disc confocal microscope and a Leica DMI6000 inverted microscope equipped with a Hamamatsu 9100-02 camera.

2.5 Cell culture

All cell lines were grown at 37°C in a 5% (v/v) CO_2 incubator.

2.5.1 Maintenance and propagation of HeLa cells and tet-on HeLa cells

HeLa cells were purchased from American Type Culture Collection (ATCC) and cultured in Dulbecco's modified eagle medium (DMEM, Thermo Fisher) with 10% fetal bovine serum (FBS, Invitrogen), 20 U/ ml penicillin (Invitrogen) and 20 ug/ ml streptomycin (Invitrogen).

Tetracycline-inducible (tet-on) HeLa cells were created and provided by the Pilarski laboratory (University of Alberta) (He *et al.*, 2017). Tet-on HeLa cells were cultured in DMEM with 10% tetracycline-free FBS (Clontech), 10 mM 4-(2-hydroxyethyl)-1-piperazineethanesulfonic acid (HEPES) (Invitrogen), 1 mM Na pyruvate (Invitrogen), 4 mL L-glutamax (Invitrogen), 200 µg/ ml hygromycin B (Invitrogen), and 200 µg/ ml Geneticin (Fisher). GFP-HMMR expression was induced with addition of 1 µg/ml doxycycline (Clontech). Expression of induced GFP-HMMR was visualized by fluorescence microscopy. Cells were passaged at 85% confluence and reseeded at 15-20% confluence.

2.5.2 Maintenance and propagation of MCF10A cells

MCF10A non-tumorigenic human mammary epithelial cells were purchased from ATCC. MCF10A-TUBA1B-RFP is a subline expressing Red Fluorescent protein (RFP)-tagged Tubulin α 1B that was purchased from Sigma-Aldrich (Cat# CLL1039). All sublines of MCF10A cells were cultured in DMEM/F12 (1:1) media supplemented with 5% horse serum, 20 U/ml penicillin (Invitrogen), 20 ug/ml streptomycin (Invitrogen), 20 ng/mL epidermal growth factor (EGF, Sigma), 0.5 µg/mL hydrocortisone (Sigma), 10 µg/mL insulin (Sigma), and 100 ng/mL cholera toxin (Sigma).

2.5.3 Cell synchronization

Mitotic HeLa cells were synchronized in mitosis (M) phase by treating cells with 200 ng/ml nocodazole (Sigma) for 16 hours. The cells were then washed and incubated in a proteasome inhibitor, 15 μM MG132 (Sigma), for 2 hours followed by collection. For G2/M phase synchronization, the cells were incubated in a CDK1 inhibitor, 10 μM RO-3306, for 16 hours and released for 2 hours with 15 μM MG132. For monopolar synchronization, the cells were incubated with an Eg5 inhibitor, 5 μM of (+)-S-Trityl-L-cysteine (Sigma), for 18 hours and mitotic exit was forced by the addition of 20 μM RO-3306 (Sigma) for 15 minutes.

2.6 siRNA transfection

HeLa cells were seeded at 70% confluence in 6-well plates and allowed to adhere overnight. Small interfering RNA (siRNA) sequences are listed in Table 2.1.

Table 2.1 siRNA sequences

siRNA	
siHMMR 3' UTR-A	Sense (S): 5' GAAAUAAGGACAAGCCUAAUU Antisense (AS): 5' PUUAGGCUUGUCCUUAUUUCUU
siHMMR 3' UTR-B	S: 5' GCAAAUACCUCCUCCCUAAUU AS: 5' UUAGGGAGGAGGUAUUUGCUU
siHMMR 5' UTR	S: 5' UGGCUUUCCAAUUGGCUAAUU AS: 5' PUUAGCCAAUUGGAAAGCCAUU

For transfection in one well, 2 µg siRNA construct was mixed with 200 µl jetPRIME buffer (VWR) and then mixed with 4.5 µl jetPRIME reagent (VWR) followed by a 12-minute incubation at room temperature. To each well, 200 µl of transfection mixture was added dropwise evenly onto the cells in the medium and the plate was gently rocked back and forth and side-to-side to mix. The cells were washed after 24 hours and reseeded in 6-well plates and 96-well plates for western blot analysis and live-cell imaging, respectively.

2.7 Lentivirus production

Lentiviruses with plasmids expressing eGFP and GFP-Aurora A were provided by Dr. Zhengcheng He and Shanshan Wang, respectively (Maxwell Lab). Lentiviral particles were made as described (He *et al.*, 2017). Briefly, HEK-293FT cells (Invitrogen) were cultured in 10% FBS/DMEM with a density of 4-4.5 million cells in a 10 cm plate. The cells were incubated overnight and 4 hours after replacing media, the cells were transfected with a mixture of 2.5 µg pMD2.G envelope plasmid, 7.5 µg psPAX2 packaging plasmid, 10 µg target shRNA plasmid and 87 µl calcium solution. The transfection cocktail was added to the plate dropwise. The transfected HEK-293FT cells were incubated in a lentiviral facility room for 12 to 15 hours. Next day morning, the transfected cells were cultured with fresh media and the cells were allowed to recover for 24 hours. Then, virus was collected in a polypropylene storage tube and stored at 4 °C. Fresh media was added to the plate again for a second collection after another 24 hours. The harvested virus was centrifuged at 1500 rpm to remove debris and the supernatant was passed through a 0.45 µm low protein binding Millipore filter into an ultracentrifuge tube (Beckman #326823). The tubes were centrifuged at 25,000 rpm for 100 minutes at 4 °C and resuspended in 70 µL PBS.

2.8 Lentivirus transduction

HeLa cells were seeded in 6 well plates to reach 80% confluency and media was refreshed four hours prior to lentiviral transduction. Cells were incubated with virus-containing media overnight. On the next day, media was replaced and transduction efficiency was examined by fluorescence microscopy.

2.9 Generation of rs299290 SNP in RFP-TubA1B MCF10A cells by gene editing

Several methods of gene editing were performed to generate rs299290 SNP in RFP-tubulin MCF10A cells, including clustered regularly interspaced short palindromic repeats (CRISPR) - CRISPR-associated protein 9 (Cas9), Prime editing and PRIME-Del.

2.9.1 CRISPR-Cas9

UCSC Genome Browser was used to select guide RNAs (gRNA) for CRISPR-Cas9 (Kent *et al.*, 2002). A single-stranded DNA (ssDNA) complementary to the targeted strand containing the PAM site was designed to include the gene editing changes as well as silent mutation to modify the original PAM site. The gRNA pair was ligated to BbsI restriction enzyme digested pSpCas9(BB)-2A-GFP (PX458) plasmid (Addgene #48138). The constructed plasmids were transformed into DH5α and incubated in ampicillin added agar plates at 37 °C overnight for selection. Three colonies were picked and cultured in LB/ampicillin media at 37 °C overnight, followed by plasmid extraction (Qiagen, #2706X4). Cloning results were confirmed by Sanger sequencing provided in the Center for Molecular Medicine and Therapeutics (CMMT). Lipofectamine™ 3000 Transfection Reagent (Invitrogen™, #L3000001) was used to transfect CRISPR-Cas9 plasmids and ssDNA. The prepared transfection reagent was added dropwise to

RFP-tub MCF10A cells in 6 well plate followed by overnight incubation at 37°C. GFP signal was verified for transfection efficiency using live-cell fluorescence microscopy.

2.9.2 Prime editing

The design of prime editing components, including primer binding sites (PBS), 3' reverse transcription templates (RTT), spacer/gRNA, and nicking gRNA (ngRNA) were selected from PrimeDesign web tool (Hsu *et al.*, 2021). The linker sequence for connecting 3'RTT and tevopreQ1 motif was calculated by pegLIT software developed by the Liu Lab (Nelson *et al.*, 2021). The spacer, 3'RTT and scaffold were ligated to Bsa1-HFv2 digested pU6-pegRNA-GG-Vector (Addgene #132777). The ngRNA of Prime editing was ligated into BsmBI digested BPK1520 plasmid (Addgene #65777). PE2 (Addgene, #169850) was initially used for Prime editing. Two plasmids encoding Prime editor max (PEmax) and hMLH1dn were purchased from Addgene (#178113, 178114) to increase Prime editing efficiency. The plasmids preparation, plasmid sequencing and transfection of plasmids were identical to that described in section 2.9.1.

For direct RNA delivery of Prime editing method, *in vitro* transcription (IVT) protocol was modified based on the protocol described in Supplementary Note S2 (Adikusuma *et al.*, 2021). To generate RNA from the constructed pegRNA plasmid, amplification of the linear target components was performed by PCR using Q5® Hot Start High-Fidelity 2X Master Mix (NEB, #M0494S). Amplification of pT7-PEmax and pT7-hMLH1dn was performed using the same PCR kit and IVT primers to correct T7 promoter inactivation. The resulting PCR product was confirmed by DNA gel electrophoresis prior to PCR purification (Qiagen, #28104). IVT was performed following protocol provided with HiScribe T7 High-Yield RNA Synthesis Kit (NEB, #E2040S). CleanCap AG (TriLink biotechnologies) was added for IVT of PEmax and hMLH1dn.

The resulting RNA was treated with DNase I (NEB, #M0303S). RNA from pegRNA plasmid was purified as described in RNA cleanup protocol (Qiagen, #74034). RNA transcribed from pT7-PEmax and pT7-hMLH1dn was purified using lithium chloride (Thermo Fisher Scientific, #AM9480). Synthetic RNA of ngRNA was ordered from Synthego and Clean Cap EGFP mRNA (TriLink biotechnologies, #L-7601)) was ordered as a positive control for nucleofection. Reconstituted and purified RNA was stored at -80°C.

Nucleofection was performed for RNA delivery. RFP-tub MCF10A cells were collected and counted so that 200,000 cells were resuspended in 5 µL Opti-MEM (Gibco) media. Cargo mix was made from 2 µg of hMLH1dn RNA, 1 µg in 0.5 µL of PEmax RNA, 90 pmol in 0.9 µL of pegRNA RNA, 60 pmol in 0.6 µL of ngRNA RNA. Cargo mix was added to the resuspended cells and 50 µL Opti-MEM was added following gentle mixing. The cell mixture was transferred to the electroporation cuvette (VWR, #89047-208) and placed in the Nucleofector™ Platform, using T-020 program. The treated cell mixture was transferred to a collagen-coated 24 well plate supplied with pre-warmed MCF10A media and incubated at 37°C overnight. After 24 hours, nucleofection efficiency was verified by examining EGFP signal from EGFP mRNA positive control. When the cells reached 90% confluency, cells were cloned by single-cell seeding.

2.9.3 PRIME-Del

PRIME-Del design was generated by an online tool (Choi *et al.*, 2022). Preparation of plasmids and plasmid transfection procedures were identical to that described in section 2.9.2.

2.9.4 Single-cell colony seeding and PCR analysis

Harvested cells after transfection were counted and manually seeded into 96 well plate to achieve single-cell seeding. The seeded cells were allowed to grow for about two weeks until 90% confluent. The single cell colonies were collected and split into 96 well and 24 well plates for storage and DNA extraction, respectively. Genomic DNA was extracted from these cell colonies (Qiagen, #69504) and PCR amplification around the target site was performed using Platinum™ Taq DNA polymerase (Invitrogen™, #15966005). DNA gel electrophoresis was performed prior to PCR purification and the target mutation was verified by Sanger sequencing.

2.10 Immunofluorescence and image acquisition

Cells were seeded on coverslips and fixed with ice-cold methanol for 3 minutes at -20 °C or with 4% paraformaldehyde at room temperature for 10 minutes, followed by ice-cold methanol fixation at -20 °C for 10 minutes. Cells were permeabilized with PBS-0.25% Triton X-100 (Sigma) for 20 minutes at room temperature. Fixed and permeabilized cells were washed with PBS and blocked in PBS with 0.1% Triton X-100 and 3% bovine serum albumin (BSA) for 1 hour at room temperature. Antibodies were diluted in PBS with 0.1% Triton X-100 and 3% BSA accordingly (Table 2.2).

Table 2.2 Primary antibody and chemical dilutions

Antibodies	Company	Catalog #	Host	Dilution
Anti-ARP3	Abcam	ab49671	Mouse	WB: 1:5000
Anti-ARPC2	Santa-Cruz	SC-515754	Mouse	IF: 1:200
Anti-Aurora A	Cell signalling	4718	Rabbit	IF: 1:1000
Anti-cGAS	Cell signalling	#15102	Rabbit	IF: 1:500
Anti-CHICA	Abcam	ab112899	Rabbit	WB: 1:500
Anti-EB1	Abcam	ab53358	Rat	IF: 1:1000
Anti-GAPDH	Proteintech	60004-1-Ig	Mouse	WB: 1:5000
Anti-GFP	Abcam	ab1218	Mouse	WB: 1:500, IF: 1:500
Anti-HMMR	Abcam	ab124729	Rabbit	WB: 1:1000, IP: 1:10, IF: 1:100
Anti-HMMR	Abcam	ab108339	Rabbit	WB: 1:1000
Anti-Lamin B1	Abcam	ab16048	Rabbit	IF: 1:1000
Anti-NF-kB p52	EMD Millipore	06-413	Rabbit	IF: 1:500
Anti-NMIIa	Abcam	ab55456	Mouse	IF: 1:500
Anti-NMIIb	Abcam	ab684	Mouse	IF: 1:50
Anti-NMIIb	Abcam	ab204358	Rabbit	WB: 1:250
Anti-PCNT	Abcam	ab28144	Mouse	IF: 1:1000
Anti-PCNT	Convance	PRB-433C	Rabbit	IF: 1:1000
Anti-phospho-Aurora A (T288)	Cell signalling	3079	Rabbit	IF: 1:1000
CellLight™ Actin-RFP	ThermoFisher	C10583		2 µl/10,000 cells
Hoechst 33342	Invitrogen	H3570		IF: 1:5000, live cell imaging: 1:1000

Coverslips were incubated with diluted antibodies for 3 to 4 hours at room temperature, followed by three PBS washes. The coverslips were then incubated with diluted secondary antibodies at room temperature for 1.5 hours. Cells were incubated in PBS with Hoechst dye for 15 minutes, followed by two PBS washes and a dH_2O wash prior to mounting. Coverslips were mounted using ProLong Gold Antifade Reagent (Invitrogen) and allowed to seal overnight at room temperature.

Fixed cells were imaged using the Olympus Fluoview FV10i confocal microscope with Fluoview software (Olympus). The images were taken using a 60X 1.2 NA oil objective as a stack of 5 optical sections with a spacing of 0.5 μm through the cell volume. The images were analyzed using ImageJ v1.46j (National Institute of Health) to generate maximum intensity projections of the fluorescence channels.

2.11 Proximity ligation assay (PLA)

Primary antibodies were conjugated to Red Oligo A or Red Oligo B (Duolink™ PLA Multicolor Probemaker Kit, Sigma-Aldrich) overnight according to the manual provided. Cells were fixed with ice-cold methanol for 3 minutes at -20°C, followed by permeabilization with PBS-0.25% Triton X-100 (Sigma-Aldrich) for 20 minutes at room temperature. Then, the cells were processed for PLA fluorescence imaging as described by Duolink® PLA Fluoresecence Protocol (Sigma-Aldrich) with steps including blocking, primary antibody incubation, probe incubation, ligation, amplification, final washes and mounting.

2.12 Live cell imaging

Cells were grown in Falcon plastic 96-well plates and stained with Hoechst for 5 minutes, followed by three PBS washes prior to imaging. The plate was mounted with a silicone gasket (Chamlide CMM) in a 37°C environmental chamber supplied with 5% CO_2 (Precision Control). The plates were imaged with an Olympus IX81 epifluorescence microscope (Olympus) and a cooled charge coupled device camera (CoolSNAP HQ2; Photometrics) controlled by the MetaMorph 7.5 software (Molecular Devices Inc.). Images were taken using a 40X or 20X 0.75 NA dry objective. For blebbing analysis, the interval between frames varied for each experiment as indicated.

2.13 Western blot and immunoprecipitation protocols

Cells were collected and washed with cold PBS once. Washed cells were lysed with 5-10 x 10^6 cells/ml in RIPA buffer (25 mM Tris, pH7.8, 150 mM NaCl, 0.1% SDS, 1.0% NP-40, 0.5% sodium deoxycholate) with protease inhibitor cocktail and PhosSTOP tablets that target a broad spectrum of proteases and phosphatases, respectively (Roche). For immunoprecipitation, the samples were standardized by cell count numbers. Cells were lysed in 0.5% NP-40 immunoprecipitation buffer (50 mM Tris-HCl, pH7.4, 150 mM NaCl, 1 mM EDTA, 0.5% NP-40) supplemented with protease inhibitors and phosphatase inhibitors (Roche). Cell lysates were rotated at 4°C for 30 minutes and passed through a 25-gauge needle for 15 times to homogenize. The lysates were centrifuged at 16,000 X g for 15 minutes at 4°C, followed by a BCA protein assay to determine the protein concentration.

For immunoprecipitation experiments, cell lysates were pre-cleared with protein A/G PLUS-Agarose beads (Santa Cruz) and rotated for 30 minutes at 4°C. Antibodies were added to

the pre-cleared lysates and rotated at 4°C overnight to bind the protein complex. Clean A/G PLUS-Agarose beads (Santa Cruz) were then added to the cell lysates and rotated at 4°C for 4 hours. Complex-bound beads were washed with lysis buffer three times. SDS-PAGE sample buffer was added to the sample and boiled at 95°C. The prepared samples were separated by SDS-PAGE, transferred to nitrocellulose, and blotted with primary antibodies, followed by secondary antibodies conjugated to horseradish peroxidase (HRP). The blotted membranes were treated with enhanced chemiluminescence (GE Healthcare) for imaging.

2.14 Immunoprecipitation-Mass spectrometry of protein complexes (collaboration with Lange Lab, BCCHR)

HeLa cells were synchronized with 200 ng/ ml nocodazole (Sigma-Aldrich) for 17 hours and 15 μM MG132 (Sigma) for 2 hours prior to collection. Cells were lysed at 5-10 × 10^6 cells/ml in immunoprecipitation buffer (50 mM Tris-HCl, pH7.4, 150 mM NaCl, 1 mM EDTA, 1% NP-40, 0.1% sodium deoxycholate in HPLC H_2O) supplemented with protease and phosphatase inhibitors (Roche), as described (Dunsch *et al.*, 2012). Cell lysates were collected by centrifugation at 16,000 X g for 10 min at 4˚C with the protein concentration was determined by the BCA protein assay kit (Thermo Fisher). Cell lysates were pre-cleared with protein A/G PLUS-Agarose beads (Sigma-Aldrich) for 30 min, followed by anti-HMMR antibody (ab124729) or rabbit IgG (Sigma-Aldrich 12-370) incubation at 4˚C on rotation for 24 hours. Then, protein A/G PLUS-Agarose beads were added and incubated for 22 hours at 4˚C on rotation. Isolated complexes with the beads were washed with lysis buffer three times and twice with PBS to remove detergent. The protein samples were eluted with 50 μl of 100 mM citric acid, pH 2.6 at

50˚C followed by centrifugation at 1300 rpm for 10 min. The supernatant was collected and 125 µl of 1 M HEPES, pH 8.5 was added to neutralize the sample.

Proteins were reduced by incubation with 5 µl of 200 mM dithiothreitol (DTT) at 37˚C for 1 hour and alkylated by incubating with 10 µl of 400 mM indole-3-acetic acid (IAA) for 1 hour in the dark, quenched by 10 µl of 200 mM DTT. Trypsin/Lys-C mix (Promega, Madison, WI) was added to the protein sample at a 1:100 enzyme to protein ratio at 37˚C for 16 hours. Reductive dimethylation was used for stable isotope labelling by adding formaldehyde and heavy formaldehyde ($C^{13}D_2O$) to IgG control and HMMR IP samples with a final concentration of 40 mM, followed by immediate addition and incubation with 20 mM sodium cyanoborohydride at 21˚C for 1 hour. The samples were combined and acidified to pH 2.5 by adding trifluoroacetic acid (TFA), followed by peptides purification with C18-STAGE tips as described (Rappsilber *et al.*, 2003).

The Easy nLC ultra-high-pressure LC system (Thermo Fisher Scientific) was coupled to a Q Exactive HF mass spectrometer with an EASY-Spray source to perform liquid chromatography tandem mass spectrometry analysis. For separation and injection, an EASY-Spray C18 column (Thermo Fisher Scientific, 50 cm long, 75 µm inner diameter) heated to 50˚C and dried stage-tip eluates suspended in 10 µl buffer A (0.1% FA) and 2 µl were used, respectively. Loading of the peptides was by a back pressure of 550 bar, followed by separation of peptides through a gradient of 3-25% buffer B (0.1% FA in 80% CAN) over 105 min, then 25-40% buffer B over 20 min at a flow rate of 300 nl/ min. The chromatography method terminates by increasing buffer B from 40 to 100% over 3 min followed by 100% buffer B for 12 min. The column was equilibrated with 11 µl buffer A before the next sample loading.

Acquired spectra were analysed by Proteome Discoverer software (Thermo Fisher Scientific, version 2.5) to search against the *Homo sapiens* reference proteome including isoforms, downloaded from the UniProt database (2017-07) (Bateman, 2019). The searches utilized a 1% false discovery rate-cut-off at peptide and protein level with modifications including: static modifications, +57.021 Daltons (Da) on C residue; variable modifications, +15.995 Da on M, and +28.031 or +34.063 on K; and peptide N terminus, +42.011 Da. A Student's t-test was used to determine the differential abundance in anti-HMMR versus rabbit IgG immunoprecipitates. Proteins commonly identified in affinity enrichment experiments were flagged based on information derived from the CRAPome (version 2.0) database (Mellacheruvu *et al.*, 2013).

2.15 Cytotoxicity assay

HeLa cells were seeded in 9 wells of the 96-well plate with 7 x 10^3 cells per well. Serial dilutions of each drug were added when cell density reached about 20 x 10^3 per well. After a 48-hour incubation, media was removed and 100 µl fresh media was added followed by 20 µl Assay Solution of the cell cytotoxicity assay kit (Abcam, ab112118). Cells were then incubated at 5% CO_2, 37℃ for 4 hours, protected from light. After a 4-hour incubation, absorbance change at 570 nm and 605 nm were monitored using a plate reader and the ratio of OD570 and OD605 was calculated for each dose treatment to generate an inhibitor curve.

2.16 Reagents and antibodies

Hoechst (Invitrogen) was used to stain the nucleus in live-cell imaging and immunofluorescence staining. Primary antibodies and their working concentrations are listed in

Table 2.2. Secondary antibodies were conjugated to HRP (Sigma) or to Alexa Fluor 488, 594, or 647, for western blot analysis and immunofluorescence labeling, respectively.

2.17 Statistics

Data were displayed in each figure as mean ± standard deviation (SD) or individual cell analysis from at least three experimental replicates, unless noted otherwise. Statistical analysis was performed using two-tailed Student's t-test (unpaired or paired) or one-way ANOVA as indicated in figures. When P-value was < 0.05, the results were considered significant. In specified figures, the data was analysed with ANOVA with Sidak's multiple comparisons test and P-value was multiplicity adjusted for each comparison with a family-wise significance and confidence levels of 0.05 (95% confidence interval).

Chapter 3: The consequence of HMMR overexpression and the effects on membrane elongation and the control of daughter cell size

3.1 Rationale and hypothesis

In symmetric cell division, the size difference between daughter cells is typically less than ten percent (Tzur *et al.*, 2009; Sung *et al.*, 2013) because dissimilar daughter cell sizes may affect the relative size of the nucleus, the cytoplasm and its content, and daughter cell function (Hara and Kimura, 2011; Dalton and Carroll, 2013). For instance, unequal daughter cell sizes with uneven distribution of cell-fate determinants can result from asymmetric cell divisions, which produce two daughter cells with different functions (Kiyomitsu, 2015)

During cell division in most vertebrate cells, the mitotic spindle is positioned at the centre of the cell in metaphase and the spindle position in anaphase determines the cell cleavage site, which defines the boundary of the emerging two daughter cells (Kiyomitsu, 2015). Vertebrate cells have compensatory mechanisms to correct off-centre mitotic spindles and prevent dissimilar daughter cell sizes.

At anaphase, an off-centre spindle will activate asymmetric membrane elongation, which is regulated by cortical actomyosin contractile forces, to induce blebbing on one side of the dividing cell cortex and correct the central position of the spindle (Kiyomitsu, 2015). Prior work from the Maxwell Lab found that the aberrant expression of GFP-HMMR in HeLa cells induces metaphase spindles that are frequently rotated or mis-positioned relative to control-treated groups (Connell *et al.*, 2017; He *et al.*, 2017). Therefore, I hypothesize that overexpression of GFP-HMMR may be sufficient to induce anaphase membrane blebbing, which is needed to correct daughter cell sizes that may result from off-centre mitotic spindles.

3.2 Results

3.2.1 HeLa cells that express GFP-HMMR are delayed in metaphase

HeLa cells that express GFP-HMMR and HeLa cells in which HMMR is silenced both induce abnormal spindle rotation phenotypes (Connell *et al.*, 2017). HMMR-silenced cells also delay their progression through mitosis (Chen *et al.*, 2014; Connell *et al.*, 2017). The kinetics of mitotic progression are not yet clear for cells induced to express GFP-HMMR, termed tet-on HeLa cells. So, I first measured the expression levels for both GFP-HMMR and endogenous HMMR in M-phase synchronized lysates collected from parental HeLa cells and tet-on HeLa cells grown in the absence (-dox) or presence (+dox) of doxycycline (Figure 3.1). Although I observed some leaky expression of GFP-HMMR in tet-on HeLa cells (-dox), the endogenous HMMR level was lower in these cells (Figure 3.1). Thus, the total level of HMMR expressed in tet-on HeLa cells (-dox) was similar to the level in control HeLa cells. For tet-on HeLa cells (+dox), induced GFP-HMMR expression approximately doubled the levels of HMMR in lysates relative to those from parental cells or tet-on HeLa cells (-dox) (Figure 3.1 table).

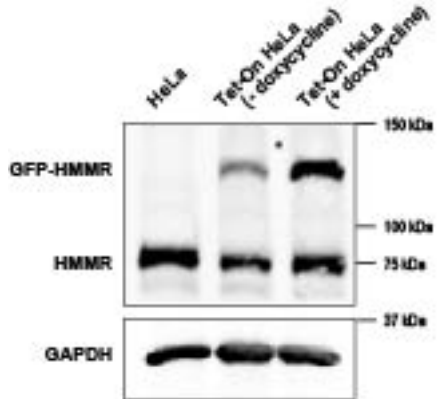

Analysis of immunoblot signal intensity (AU)

Protein \ Cell	HeLa	Tet-On HeLa (-dox)	Tet-On HeLa (+dox)
GFP-HMMR	n/a	338.9	1642.7
HMMR	1052.3	691.7	836.6
Total	1052.3	1030.6	2379.3

Figure 3.1 HMMR expression in parental and tet-on HeLa cells.
Tet-on HeLa cells were treated with doxycycline (or water) for 24 hours to induce GFP-HMMR overexpression. Cells were synchronized at M phase with nocodazole and MG132, lysed, and HMMR expression was measured by Western blot with Licor imaging. Equal loading was verified by GAPDH level. Signal intensity of arbitrary values were quantified and tabulated. This experiment is representative of 2 independent experiments.

To characterize the kinetics of mitotic progression for GFP-HMMR overexpressing cells, I induced tet-on HeLa cells through treatment with doxycycline for 24 hours, or water as a control (-dox). I then tracked mitosis using time-lapse microscopy of cells counterstained with Hoechst dye. I defined metaphase duration as the time required to transition from chromosome alignment to the separation of sister chromatids (Figure 3.2A). I defined anaphase duration as the time required to progress from chromosome segregation to cleavage furrow formation and I defined telophase duration as the time required from the end of anaphase until chromosome decondensation (Figure 3.2B,C). Using these definitions, I measured the kinetics of the various mitotic stages. I found no significant difference in the duration of anaphase or telophase among the three treatment groups (not shown). However, I found that GFP-HMMR overexpressing tet-on HeLa cells (+dox) remained in metaphase longer than control-treated HeLa cells (Figure 3.2A,B). I determined that the metaphase duration in control and non-induced tet-on HeLa cells (-dox) was 27 ± 12.7 minutes and 33 ± 19.5 minutes, respectively. The time spent in metaphase was increased to 42 ± 28.8 minutes in GFP-HMMR overexpressing tet-on HeLa cells (+dox). Moreover, I found that GFP-HMMR overexpressing tet-on HeLa cells (+dox) frequently had mis-oriented spindles during metaphase (Figure 3.2C), which is consistent with the published literature from the Maxwell Lab (He *et al.*, 2017).

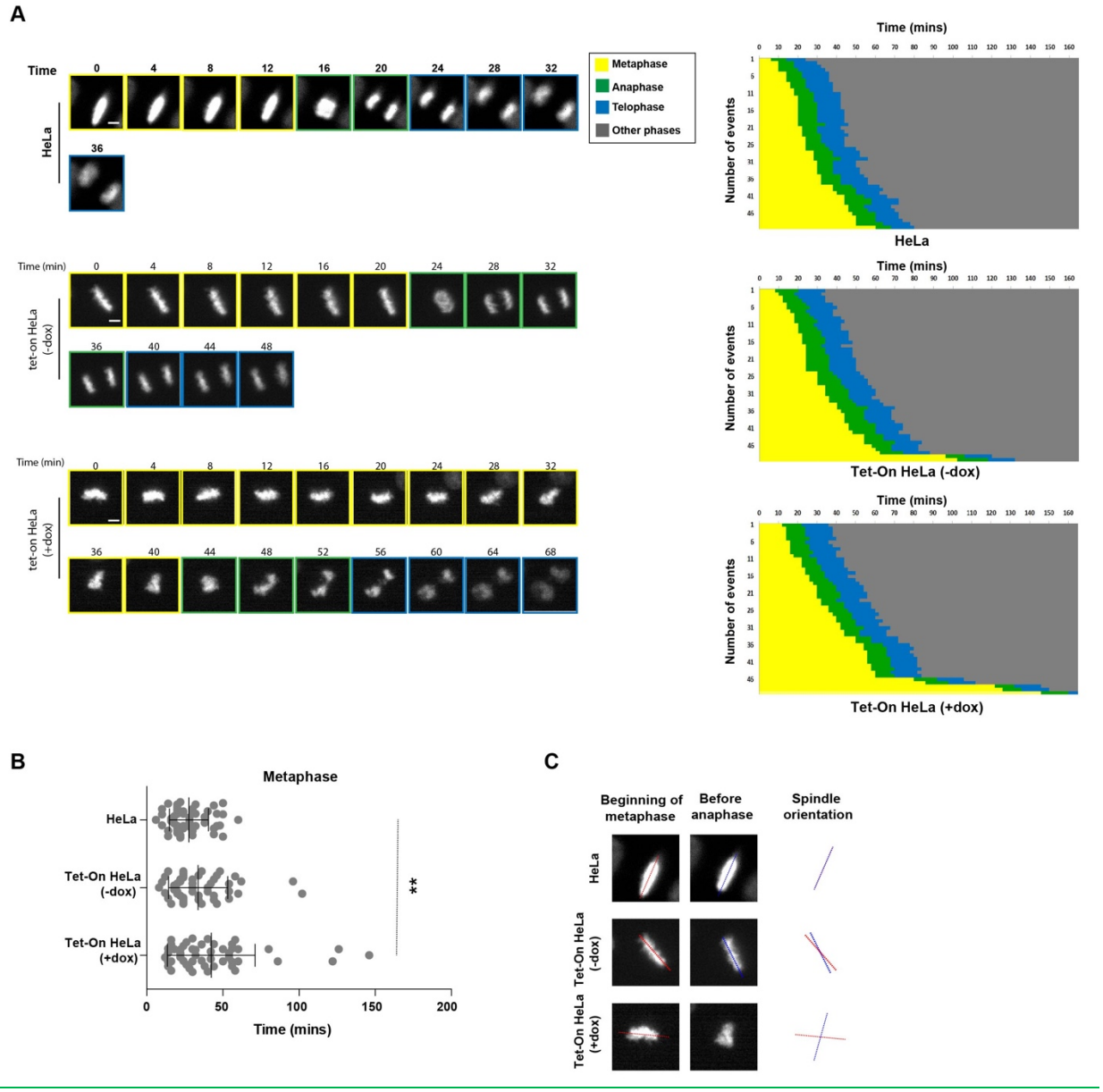

Figure 3.2 GFP-HMMR expression delays metaphase and induces rotated spindles.

A) Images of mitotic progression for HeLa cells, tet-on HeLa cells (-dox), and tet-on HeLa cells (+dox) tracked by time-lapse microscopy. Mitotic phases are color-coded and the mitotic kinetics of 50 cells per condition is tabulated. Scale bar=5 μm.

B) Quantitation of metaphase duration of HeLa cells or tet-on HeLa cells (-dox), and tet-on HeLa cells (+dox) tracked by time-lapse microscopy (Mean ± S.D., n=50 cells, 2 experiments, **P=0.0034, one-way ANOVA).

C) Illustration of spindle angle rotation during metaphase. Orientation of condensed chromosomes at the beginning of metaphase is indicated by a red dashed line and the orientation of condensed chromosomes before anaphase is indicated by a blue dashed line.

3.2.2 Anaphase membrane blebbing is common in GFP-HMMR-overexpressing cells

A mis-oriented or mis-positioned mitotic spindle during cell division can stimulate asymmetric membrane blebbing (Kiyomitsu, 2015). To assess this phenotype, I treated tet-on HeLa cells with doxycycline, or water (-dox), for 24 hours and I then imaged mitotic cells using time-lapse microscopy (Figure 3.3A). I quantified the percentage of cells that had membrane blebs during anaphase for each experiment. In non-induced tet-on HeLa cells (-dox) and parental cells, I found no or very few membrane blebs during anaphase; however, I found that GFP-HMMR overexpressing tet-on HeLa cells (+dox) displayed a significantly higher occurrence of membrane blebbing events with various sizes (Figure 3.3B). I also observed mis-oriented and constantly moving spindles in GFP-HMMR overexpressing tet-on HeLa cells (+dox), and this phenotype correlated with a higher frequency of membrane elongation.

It is also important to note that the phenotype of blebbing was dramatically different between control HeLa cells and GFP-HMMR overexpressing tet-on HeLa cells (+dox). Indeed, GFP-HMMR overexpressing tet-on HeLa cells often displayed either multiple small cortical spikes (Figure 3.3A +dox cell#1) or very prominent membrane elongations (Figure 3.3A +dox cell#2).

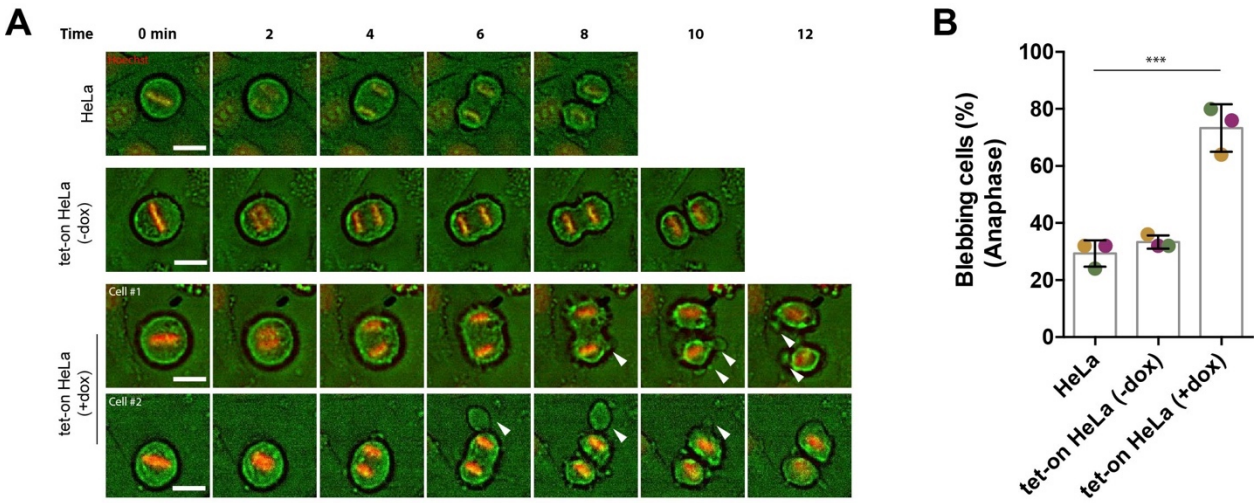

Figure 3.3 GFP-HMMR-overexpressing HeLa cells present frequent and large membrane blebs during anaphase.

A) Living parental HeLa cells or tet-on HeLa cells were pre-treated with water (-dox) or doxycycline (+dox) for 24 hours and mitotic cells were followed by time-lapse microscopy. Images were taken at 1 frame per minute. Membrane blebbing events are highlighted with white arrowheads (Green channel = Transmitted light 50%; Red channel = Hoechst). Scale bar =20 μm.

B) Quantification of anaphase membrane blebbing events in parental HeLa cells, tet-on HeLa cells (-dox), or tet-on HeLa cells (+dox). Means from individual experiments are colour-coded and displayed along with Mean ± SD (n=3 experiments, ***P=0.0001, one-way ANOVA).

3.2.3 Daughter cell size control is altered in GFP-HMMR-overexpressing cells

I next quantified daughter cell sizes when cells entered late cytokinesis (Figure 3.4A) in order to investigate if the increased frequency of anaphase blebbing correlated with a loss of daughter cell size control. Indeed, I observed dramatic alterations in daughter cell size ratios in GFP-HMMR overexpressing tet-on HeLa cells (+dox). That is, the induction of asymmetric membrane elongation in these cells did not normalize the daughter cell size ratio (Figure 3.4B). I then separately analyzed cells as those that did (+) or did not (-) undergo asymmetric membrane elongation. I observed no significant difference between daughter cell-size ratio resulted from cells with and without anaphase blebbing in control groups (Figure 3.4B). As well, I found that the process of asymmetric membrane elongation was not correlated with a normalization of daughter cell sizes in GFP-HMMR overexpressing tet-on HeLa cells (+dox). In fact, daughter cell size differences were actually larger in GFP-HMMR overexpressing tet-on HeLa cells (+dox) that exhibited membrane blebbing events.

In conclusion, I observed a significant increase in membrane blebbing events in GFP-HMMR overexpressing tet-on HeLa cells (+dox), which is predicted by the elevated frequency of mis-oriented or rotating spindles that I also observed in these cells. However, the induction of anaphase membrane blebbing events in GFP-HMMR overexpressing tet-on HeLa cells (+dox) was not accompanied by a normalization of the daughter cell size ratio suggesting anaphase membrane elongation under this condition may not be regulated properly.

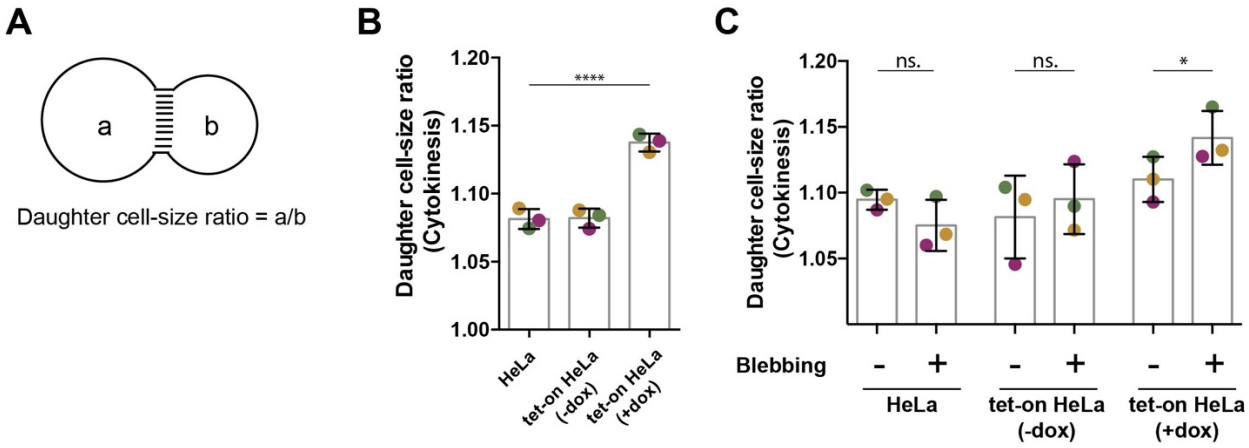

Figure 3.4 Daughter cell size control is altered in GFP-HMMR-overexpressing HeLa cells.

A) Daughter cell size ratio was calculated as the area of the bigger daughter cell divided by the area of the smaller daughter cell during cytokinesis.

B) Quantification of average daughter cell size ratio of HeLa cells, tet-on HeLa cells (-dox) and induced tet-on HeLa cells (+dox) (Mean ± SD, n=3 experiments, individual experiments are colour-coded, ****P<0.0001, one-way ANOVA).

C) Quantification of average daughter cell size ratio of HeLa cells, tet-on HeLa cells (-dox) and induced tet-on HeLa cells (+dox) with and without anaphase membrane blebs (Mean ± SD n=3 experiments, individual experiments are colour-coded, P=0.12 (HeLa), P=0.72 (tet-on HeLa (-dox)), *P=0.023 (tet-on HeLa (+dox)), paired t-test).

3.2.4 Induced membrane elongation is phenotypically different in GFP-HMMR-overexpressing HeLa cells

Anaphase membrane blebbing frequency was increased in GFP-HMMR overexpressing tet-on HeLa cells (+dox) compared with control-treated cells and the appearance of blebs was distinct from control groups. To measure the difference in blebbing observed between groups, I quantified the size of the largest anaphase membrane bleb relative to the cell size at the same time point (Figure 3.5A). I found that GFP-HMMR overexpressing tet-on HeLa cells (+dox) displayed phenotypically distinct membrane blebbing events, which were of various sizes, whereas the size of blebs in control-treated cells (~2% of total size) were relatively consistent across treatments (Figure 3.5B). In GFP-HMMR overexpressing tet-on HeLa cells (+dox), I found the size of membrane elongation was pronounced and averaged 5-fold larger than those observed in control-treated sub-line.

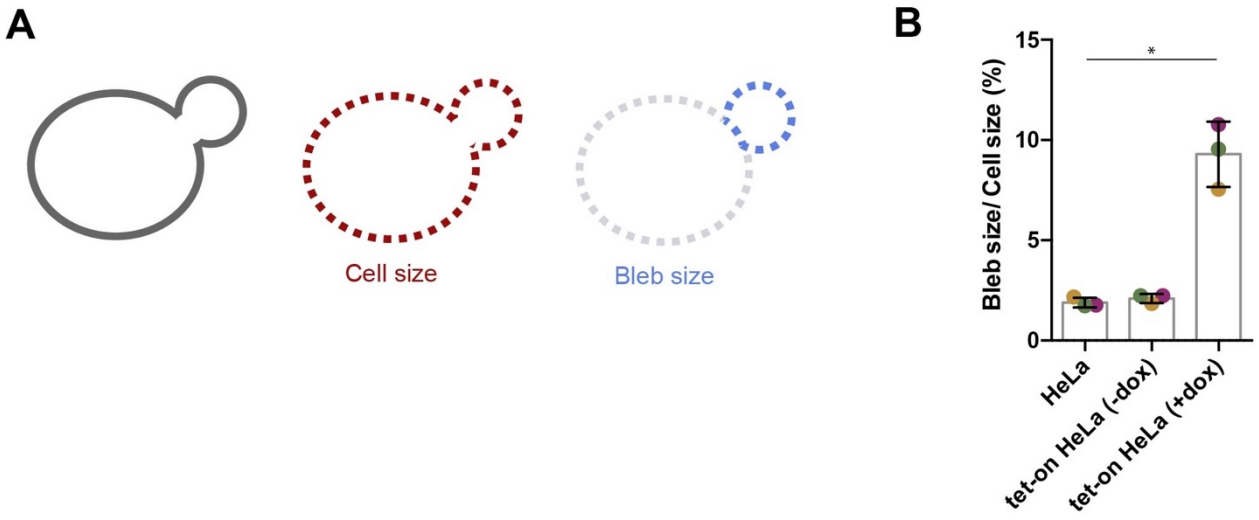

Figure 3.5 GFP-HMMR-overexpressing cells present with pronounced membrane blebbing events during anaphase.

A) Membrane bleb size was quantified by measuring the size of the largest bleb that occurred. Bleb size was then divided by the cell size measured at the same time during anaphase.

B) Bleb size in HeLa, tet-on HeLa (-dox), tet-on HeLa (+dox cells) (Mean ± SD, n= 3 experiments, individual experiments are colour-coded, *P=0.016, one-way ANOVA).

Taken together, my findings indicate that expression of GFP-HMMR delays mitotic progression, mis-orients mitotic spindles, and induces an asymmetric membrane elongation pathway during anaphase. However, the asymmetric membrane elongation pathway is not able to correct daughter cell size control. Importantly, the phenotype of blebbing is very distinct in GFP-HMMR overexpressing tet-on HeLa cells (+dox), with average bleb sizes five times larger than those observed under control conditions. The appearance of large protrusions on the cell cortex is likely related to cortical stability (Roh-Johnson and Goldstein, 2009; Bovellan *et al.*, 2014), which suggests that overexpression of GFP-HMMR may directly reduce cortical contractility.

3.2.5 Global inhibition of membrane blebbing does not reduce daughter cell size difference in GFP-HMMR overexpressing cells

To examine if a reduction of membrane blebbing can improve daughter cell size control, I treated GFP-HMMR overexpressing tet-on HeLa cells (+dox) with blebbistatin, an inhibitor of non-muscle myosin II (NMII) that prevents membrane blebbing globally (Straight *et al.*, 2003; Kovács *et al.*, 2004; Roman *et al.*, 2018). As I did not want to significantly alter mitotic progression, I first determined the half maximal inhibitory concentration (IC50) of blebbistatin and titrated that dose down between 50-fold to about 10,000-fold for live cell imaging experiments (Figure 3.6A). I measured an IC50 dose of 36.16 μM (Figure 3.6B). I also observed a significantly decreased frequency of anaphase membrane blebbing as the concentration of drug increased from 0.005 μM to 1 μM (Figure 3.6B). Although membrane blebbing was significantly reduced in these blebbistatin-treated cells, the daughter cell size ratio did not change significantly (Figure 3.6C). However, drug-mediated correction of the abnormal membrane elongation phenotypes may recover some but not all daughter cell sizes in GFP-HMMR overexpressing tet-

on HeLa cells (+dox) because inhibition of blebbing prevented large tension forces in anaphase but did not rescue spindle position that was affected by other HMMR-mediated pathways.

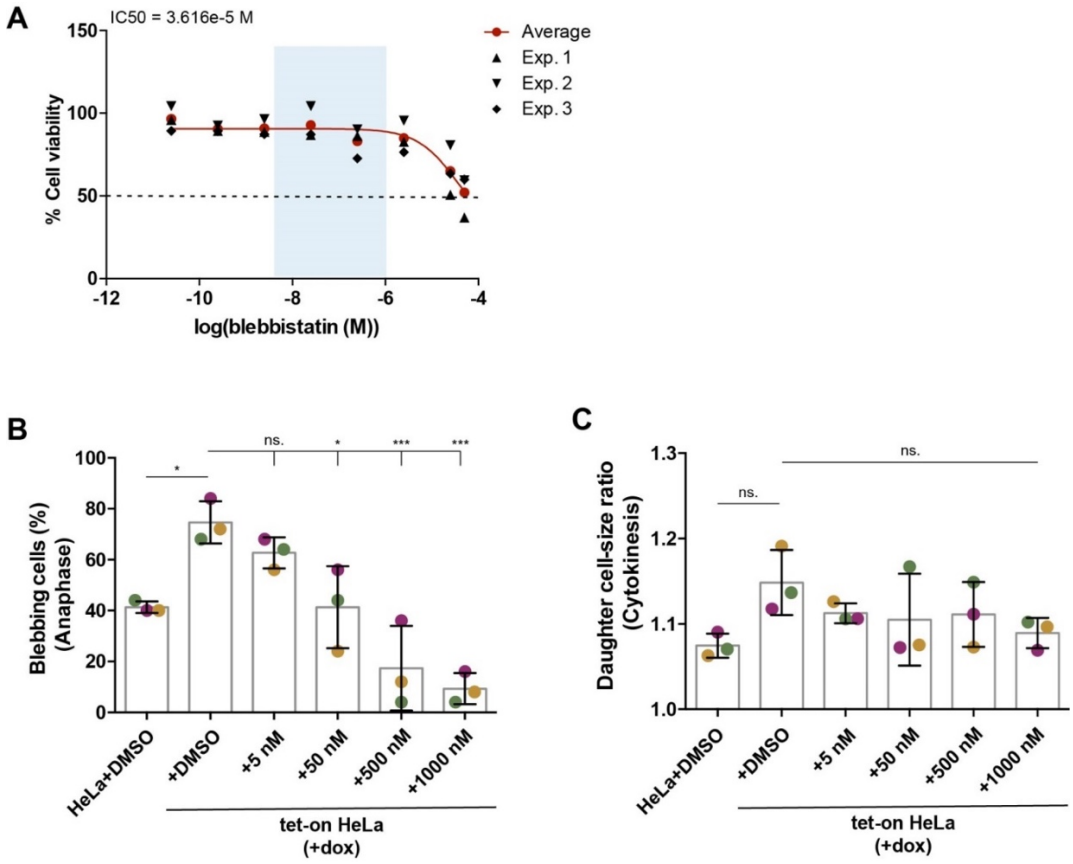

Figure 3.6 Global reduction of membrane blebs does not rescue daughter cell size control.

A) Viability of HeLa cells treated for 48 hours with graded doses of blebbistatin to inhibit myosin II activity. Shaded blue area indicates the sub-lethal doses selected for phenotype screening (n=3 experiments). The curve fitting (red line) used Dose-response – Inhibition, equation: log(inhibitor) vs. response model of Prism 6. Equation used was Y=Bottom value + (Top value –Bottom value)/(1+10^((X-LogIC50))).

B) Frequency of anaphase blebbing in parental cells (+vehicle) or tet-on HeLa cells (+dox) treated with different doses of blebbistatin (Mean ± SD, n= 3 experiments, colour-coded, *P=0.037 (HeLa+DMSO vs. tet-on HeLa +DMSO), P=0.96 (tet-on HeLa+DMSO vs. tet-on HeLa+5 nM), *P=0.037 (tet-on HeLa+DMSO vs. tet-on HeLa +50 nM), ***P=0.004 (tet-on HeLa+DMSO vs. tet-on HeLa +500 nM), ***P=0.001 (tet-on HeLa+DMSO vs. tet-on HeLa+1000 nM), one-way ANOVA with Sidak's multiple comparisons test).

C) Daughter cell size ratio in parental cells (+vehicle) or tet-on HeLa cells (+dox) treated with different doses of blebbistatin (Mean ± SD, n= 3 experiments, colour-coded, P=0.23 (HeLa+DMSO vs. tet-on HeLa+DMSO), P=0.97 (tet-on HeLa+DMSO vs. tet-on HeLa+5 nM), P=0.89 (tet-on HeLa +DMSO vs. tet-on HeLa +50 nM), P=0.96 (tet-on HeLa +DMSO vs. tet-on HeLa+500 nM), P=0.52 (tet-on HeLa+DMSO vs. tet-on HeLa+1000 nM), one-way ANOVA with Sidak's multiple comparisons test).

3.2.6 GFP-HMMR overexpressing HeLa cells show frequent chromosome mis-segregation

Uncontrolled blebbing during cell division can introduce cortical tension and induce shape instability (Tinevez *et al.*, 2009; Sedzinski *et al.*, 2011). To mechanistically connect membrane blebbing with chromosome segregation defects, I followed mitosis with live-cell imaging and incorporated RFP-actin to observe cortical actin organization during blebbing and Hoechst to track chromosome movements (Figure 3.7A). To examine if cell behavior in the presence of RFP-actin was consistent with untreated cells, I measured blebbing frequency, daughter cell-size ratio and bleb size, which showed similar results as in previous sections (Figure 3.7B-D). Importantly, cortical RFP-actin localization was not evenly distributed with cells having unstable shape changes during mitosis in GFP-HMMR overexpressing cells (Figure 3.7E). In cells with unstable shape changes (green arrow), I observed abnormal cytokinesis with a high frequency of lagging or bridging chromosomes (Figure 3.7E).

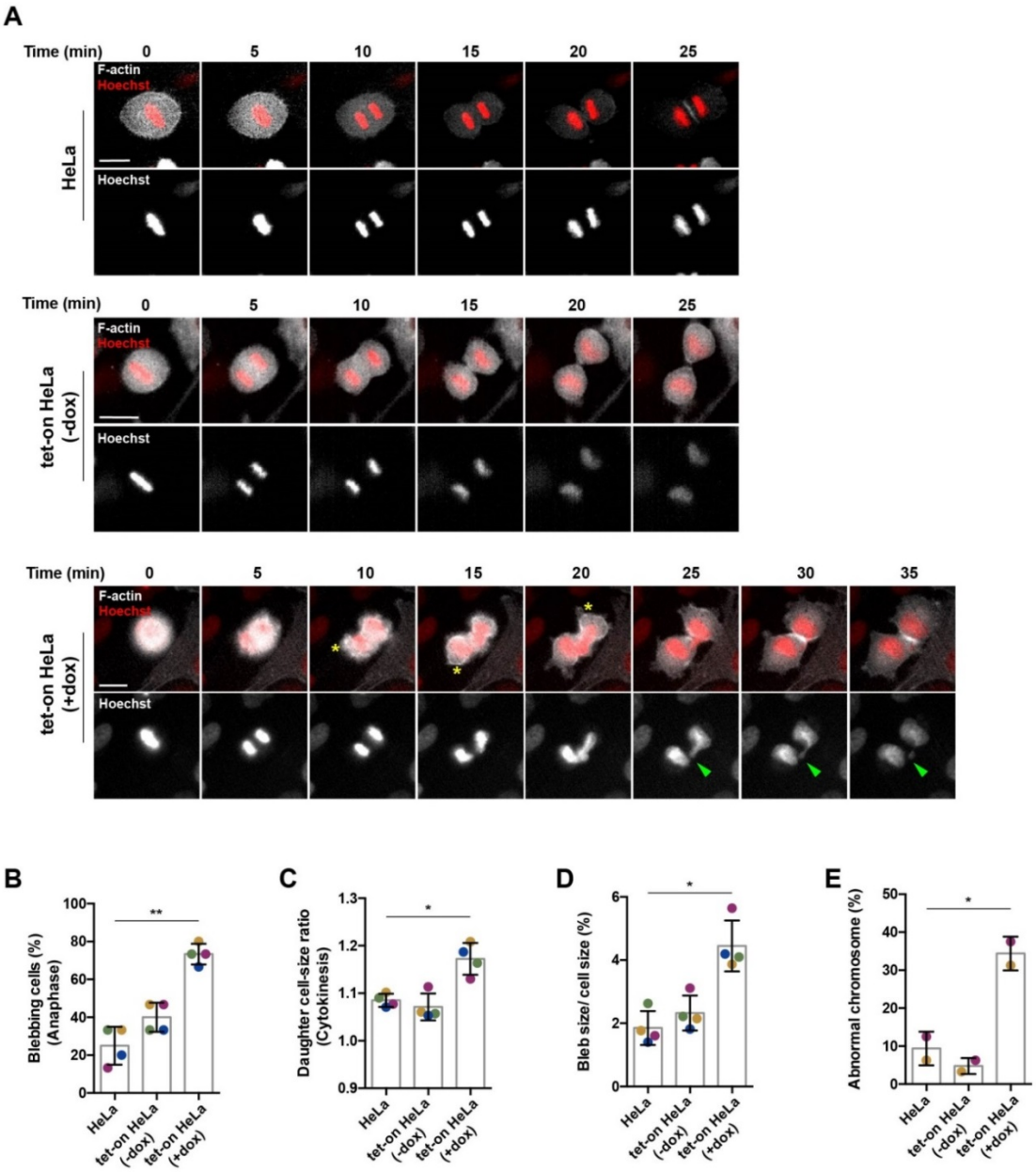

Figure 3.7 GFP-HMMR overexpressing cells show higher chromosome mis-segregation.

A) Parental HeLa cells or tet-on HeLa cells pre-treated with water (-dox) or doxycycline (+dox) for 24 hours were incubated overnight with CellLight™ Actin-RFP. Mitotic cells were followed with images taken every 5 minutes. Membrane blebbing events and lagging chromosomes are highlighted with a yellow asterisk or a green arrowhead, respectively (White channel = Actin RFP; Red channel = DAPI). Scale bar=10 μm.

B) Quantitative analysis of anaphase membrane blebbing in parental HeLa cells, tet-on HeLa cells (-dox), or induced tet-on HeLa cells (+dox) (Mean ± SD, n=4 experiments, colour-coded, **P=0.0055, one-way ANOVA).

C) Quantitative analysis of average daughter cell size ratio of parental HeLa cells, tet-on HeLa cells (-dox), or induced tet-on HeLa cells (+dox) (Mean ± SD, n=4 experiments, colour-coded, *P=0.029, one-way ANOVA).

D) Bleb size in parental HeLa cells, tet-on HeLa cells (-dox), or tet-on HeLa cells (+dox) (Mean ± SD, n=4 experiments, colour-coded, *P=0.014, one-way ANOVA).
E) Quantification of the percentage of abnormal mitotic chromosome phenotypes, including lagging or bridging chromosomes, observed in parental HeLa cells, tet-on HeLa cells (-dox), or tet-on HeLa cells (+dox) (Mean ± SD, n=2 experiments, *P=0.037, one-way ANOVA).

3.2.7 GFP-HMMR overexpressing cells demonstrate interphase genome instability

Lagging and bridging chromosomes during mitosis can lead to the formation of micronuclei (Thompson and Compton, 2011). Therefore, I measured several phenotypes related to interphase genome instability, including the frequency of nucleus budding and the presence of a micronucleus.

In fixed samples, I used immunofluorescence to detect HMMR and confirm its elevated expression in tet-on HeLa cells (+dox) after 24 hours of induction (Figure 3.8A). Then, I investigated the proportion of cells showing nucleus budding and micronuclei through immunofluorescence detection of the nuclear envelop protein Lamin B (Funkhouser *et al.*, 2013) and cyclic GMP-AMP synthase (cGAS), which frequently localizes to a micronucleus (Mackenzie *et al.*, 2017; Khoo and Chen, 2018; Liu *et al.*, 2018) (Figure 3.8B, C). Compared to control-treated cells, I observed a significantly higher proportion of GFP-HMMR overexpressing tet-on HeLa cells (+dox) with nucleus budding and micronuclei with associated cGAS (Figure 3.8B, C). Because the activation of the cGAS and stimulator of interferon genes (STING) pathway induces nuclear translocation of p52-RELB as part of the non-canonical NF-κB signaling (Bakhoum *et al.*, 2018; Hou *et al.*, 2018), I performed immunofluorescence analysis to evaluate the intensity signal of p52 in the nucleus versus cytoplasm (Figure 3.8D). I found a significantly higher level of p52 in the nucleus in GFP-HMMR overexpressing tet-on HeLa cells (+dox), which is consistent with the activation of the cGAS-STING pathway.

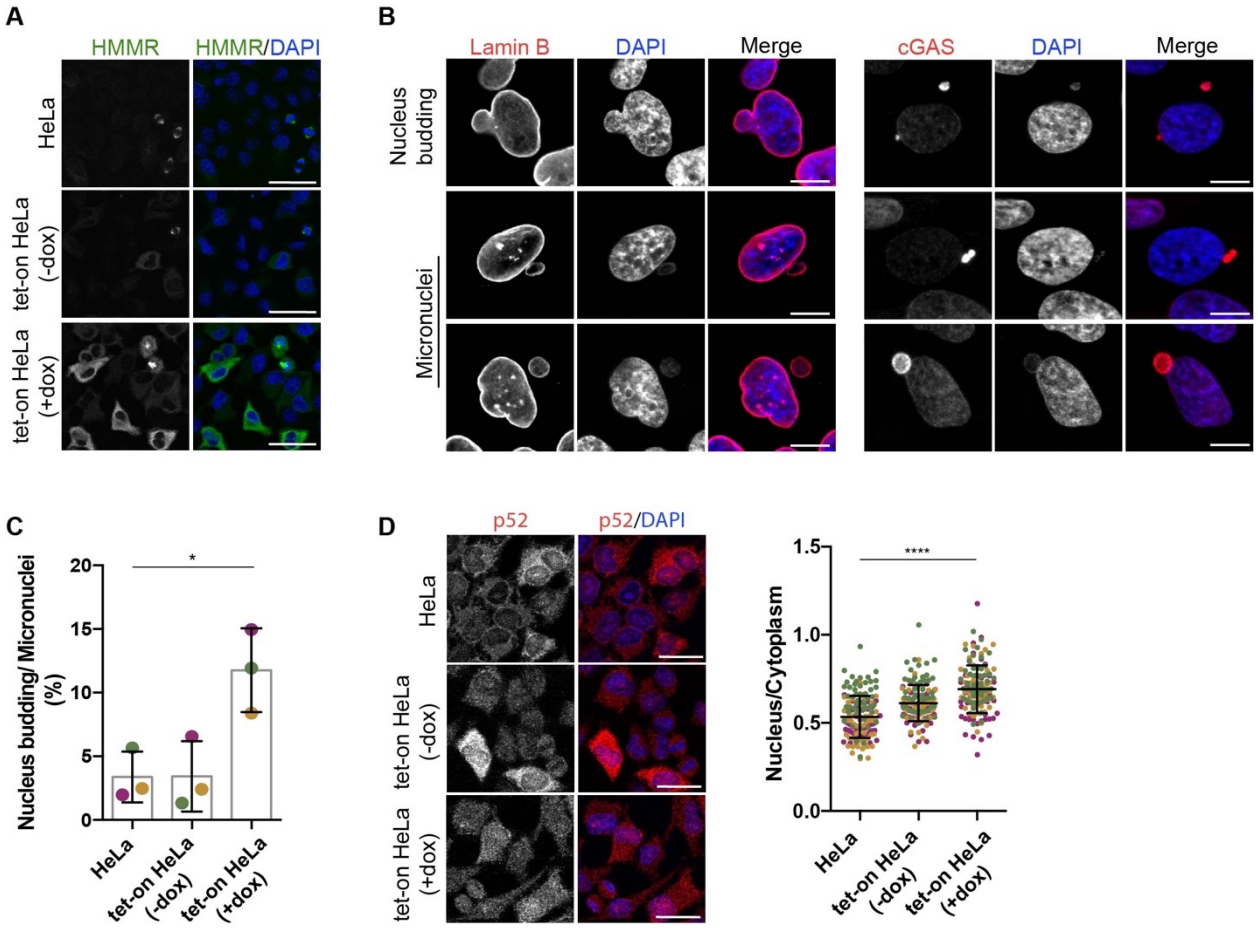

Figure 3.8 GFP-HMMR overexpressing cells present with a higher frequency of nucleus budding and micronuclei.

A) Immunofluorescence analysis of HMMR in parental HeLa cells, tet-on HeLa cells (-dox) and tet-on HeLa cells (+dox). Scale bar = 50 μm.

B) Immunofluorescence analysis of Lamin B or cGAS in parental HeLa cells, tet-on HeLa cells (-dox) and tet-on HeLa cells (+dox). Scale bar = 10 μm.

C) Quantification of the percentage of cells with micronuclei or budding nucleus, including nucleus budding and micronuclei, in parental HeLa cells, tet-on HeLa cells (-dox), and tet-on HeLa cells (+dox) (Mean ± SD, n=3 experiments, colour-coded, *P=0.0144, one-way ANOVA).

D) Immunofluorescence detection and localization of p52 in parental HeLa cells, tet-on HeLa cells (-dox), and tet-on HeLa cells (+dox). Scale bar = 30 μm. Quantitative analysis of p52 nucleus localization was determined as the intensity of p52 in the nucleus relative to the intensity in the cytoplasm (Mean ± SD, n=150 cells per group, ****P<0.0001, one-way ANOVA).

In conclusion, GFP-HMMR overexpressing tet-on HeLa cells mis-segregated chromosomes and displayed markers of genome instability including an active cGAS-STING

pathway. As an active cGAS-STING pathway has been linked with pro-inflammatory signaling that can be either growth suppressive or stimulatory (Mackenzie *et al.*, 2017; Khoo and Chen, 2018; Liu *et al.*, 2018), this result may provide a mechanistic link between HMMR overexpression and tumorigenesis.

3.2.8 HMMR potentially interacts with a set of actin-binding proteins during mitosis

HMMR is a non-motor mitotic spindle assembly factor that alters mitotic kinase and motor protein activities by localizing regulatory proteins for these enzymes, including TPX2, CHICA/FAM83D, or DYNLL1, to the spindle and spindle poles (Dunsch *et al.*, 2012; Chen *et al.*, 2014; Connell *et al.*, 2017; Li *et al.*, 2017; Fulcher *et al.*, 2019). To discover new partner proteins for HMMR in mitotic cells, the Maxwell and Lange Labs performed anti-HMMR immunoprecipitation-mass spectrometry (IP-MS) analysis on M-phase synchronized HeLa cell lysates. HeLa cells were synchronized to M-phase with 200 ng/ml nocodazole and lysed. HMMR complexes were immunoprecipitated using anti-HMMR antibody (Abcam; ab124729) and mass-spectrometry was performed on the immunoprecipitated proteins by Dr. Philipp Lange and Charlie Kuan at the BC Children's Hospital Research Institute.

Mass spectrometry analysis of HMMR immunoprecipitates identified known HMMR partner proteins, including DYNLL1, CHICA and calmodulin (highlighted in red) (Figure 3.9). The HMMR immunoprecipitate was also found to contain a set of actin-binding proteins, including: myosin 18A (MYO18A), non-muscle myosin IIb (NMIIb/MYH10) and actin-related protein 3 (ARP3/ACTR3) (highlighted in blue, Figure 3.9), a well as non-muscle myosin IIa (NMIIa/MYH9), vimentin, and tropomyosin (processed data deposited in MassIVE, MSV000088870) (Mateo, He, Mei *et al.*, 2022). Many of these putative interactors are actin-

regulating proteins that are known to affect actomyosin structures (Charras, 2008; Murrell *et al.*, 2015; Sorce *et al.*, 2015; Beaudet *et al.*, 2017; Agarwal and Zaidel-Bar, 2019). Thus, it is possible that overexpressed GFP-HMMR directly localize actin-regulating proteins to the spindle to reduce their retention at the cortex and augment bleb size and frequency.

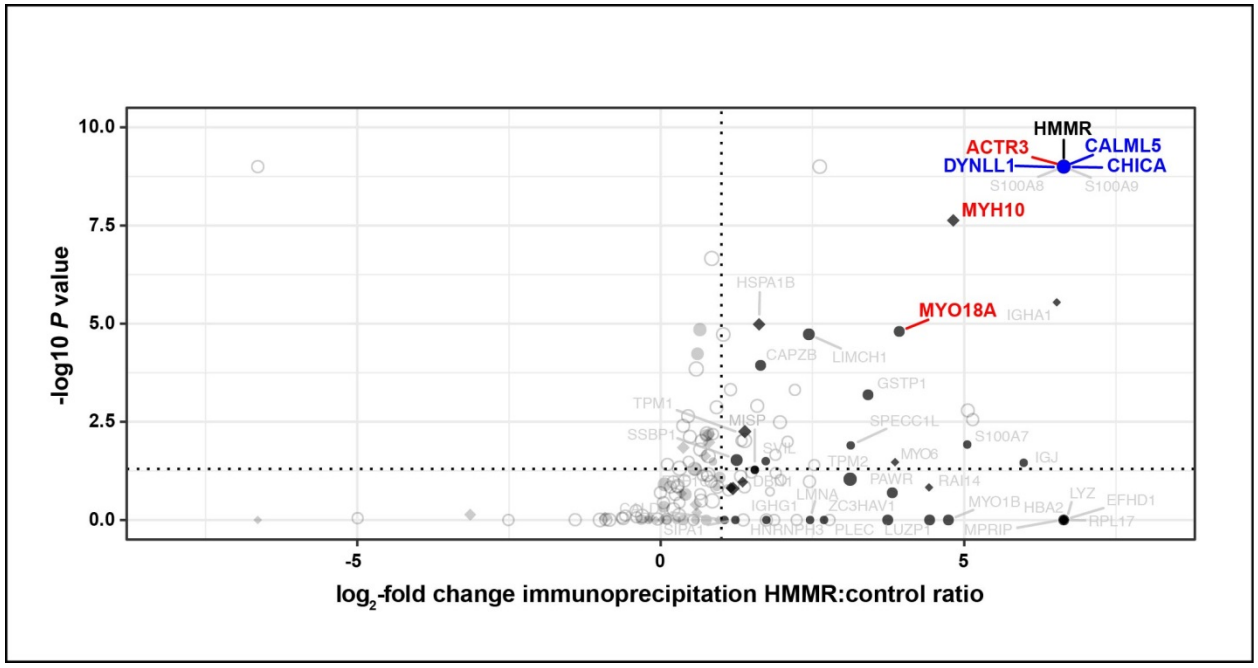

Figure 3.9 HMMR interactome during mitosis.
Mass spectrometry analysis of proteins co-precipitated from mitotic HeLa lysates with antibodies targeting HMMR or control immunoglobulin (log_2-fold change in HMMR:control ratio). Known HMMR-binding partners are highlighted in blue and actin-binding proteins (ARP3 (ACTR3), MYH10, and MYO18A) are highlighted in red. The plot shows the $-log_{10}$ two-sided Student's *t*-test normal *p* values against log_2 fold-change of HMMR versus control immunoglobulin IP results. The vertical and horizontal dashed lines indicate $p < 0.05$ and log_2 fold-change > 1, respectively. The symbols indicate the frequency at which proteins were found in the interaction screens as listed in the CRAPOME database (circle: rare interactor; open circle: common interactor; diamond: not listed in database); protein names in blue, red, and grey indicate known HMMR interactors, potential interactors (this study), and additional proteins found moderately to strongly enriched, respectively; and symbol size was proportional to the number of replicas a protein was identified in (n = 2 experiments; 2 replicates/condition). Mass-spectrometry analysis was performed by Dr. Philipp Lange and Charlie Kuan.

3.2.9 Recruitment of the ARP2/3 complex to the spindle pole may not be through a direct interaction with HMMR

The result of IP-MS analysis suggests that HMMR interacts with ARP2/3 complex components during mitosis, which potentially alters ARP2/3 complex localization. To confirm the interaction between HMMR and ARP2/3 complex, I synchronized HeLa cells at different stages of mitosis, using several methods, prior to cell lysis. I then performed immunoprecipitation (IP) using anti-HMMR antibody and detected target proteins using immunoblot analysis.

I first synchronized HeLa cells in M phase using nocodazole to prevent the formation of a mitotic spindle, followed by a treatment with the proteasome inhibitor MG132 to prevent mitotic exit. The synchronized cells were then lysed and subjected to IP incubation. Western blot analysis confirmed depletion of HMMR from lysates following incubation with anti-HMMR antibodies (post-IP fraction). The post-IP fractions also showed co-depletion of CHICA, a published HMMR interactor (Figure 3.10A); consistently, HMMR and CHICA were robustly detected in the anti-HMMR immunoprecipitates (IP:HMMR) (Figure 3.10A). However, ARP3 and NMIIb were not detected in the HMMR IP from M phase synchronized lysates, indicating that the level of co-precipitated protein, if any, was below the limit for detection.

The process of asymmetric membrane elongation is temporally restricted to anaphase. So, I then performed an alternative method of synchronization to enrich for cells in anaphase. I first treated parental HeLa cells with S-trityl-L-cysteine (STLC), an Eg5 motor inhibitor to prevent centrosome separation, followed by the Cdk1 inhibitor RO-3306 to stabilize microtubule-kinetochore attachments and forced to exit mitosis (Figure 3.10B). I used immunofluorescence analysis of the same batch of cells to confirm the synchronization enriched for anaphase cells

(not shown). I then performed a similar IP experiment and I used the post-IP fraction to confirm HMMR pull-down and I confirmed the positive control interaction with CHICA (Figure 3.10B). It is important to note that the post-IP fractions revealed less complete depletion of HMMR from these lysates and, as a consequence, little co-depletion of CHICA was apparent. Still, HMMR and CHICA were readily detected in the IP:HMMR fraction (Figure 3.10B). However, ARP3 was once again not detected in the IP:HMMR fraction (Figure 3.10B).

As I observed abnormal cortical instability in GFP-HMMR overexpressing tet-on HeLa cells (+dox), this suggested that a putative HMMR-ARP3 interaction may be more readily detected using this experimental model. Thus, I induced GFP-HMMR overexpression prior to metaphase synchronization using the CDK1 inhibitor RO-3306, which blocks cells in G2 phase. I released cells from the proteasome inhibitor MG132 for two hours, to again arrest cells at metaphase. I then performed a similar IP experiment and I used the post-IP fraction to confirm HMMR pull-down and performed experiments using two anti-HMMR antibodies (Abcam, ab124729, ab108339). I confirmed the positive control interaction with CHICA (Figure 3.10C,D). Again, the post-IP fractions showed the depletion of HMMR and GFP-HMMR was incomplete, which is likely due to the elevated levels of HMMR expression in these cells (Figure 3.10C,D). However, I did observe robust detection of GFP-HMMR and HMMR in the IP:HMMR fraction. Similarly, CHICA was depleted from the post-IP HMMR fraction and was robustly detected in the IP:HMMR fraction (Figure 3.10C,D). However, ARP3 was not similarly depleted and detected in the IP:HMMR fraction. I did observe a possible depletion of NMIIb from the post-IP HMMR fraction but its detection in the IP:HMMR fraction was obscured. Moreover, I repeated the IP experiment using anti-GFP antibody and I observed similar results (Figure 3.10E). Also, it is worth mentioning the GFP-IP was not robust. Thus, I conclude that a significant proportion of

ARP3 does not interact with HMMR in a manner that is detectable through western blot analysis, although it was implicated in our prior IP-MS analysis.

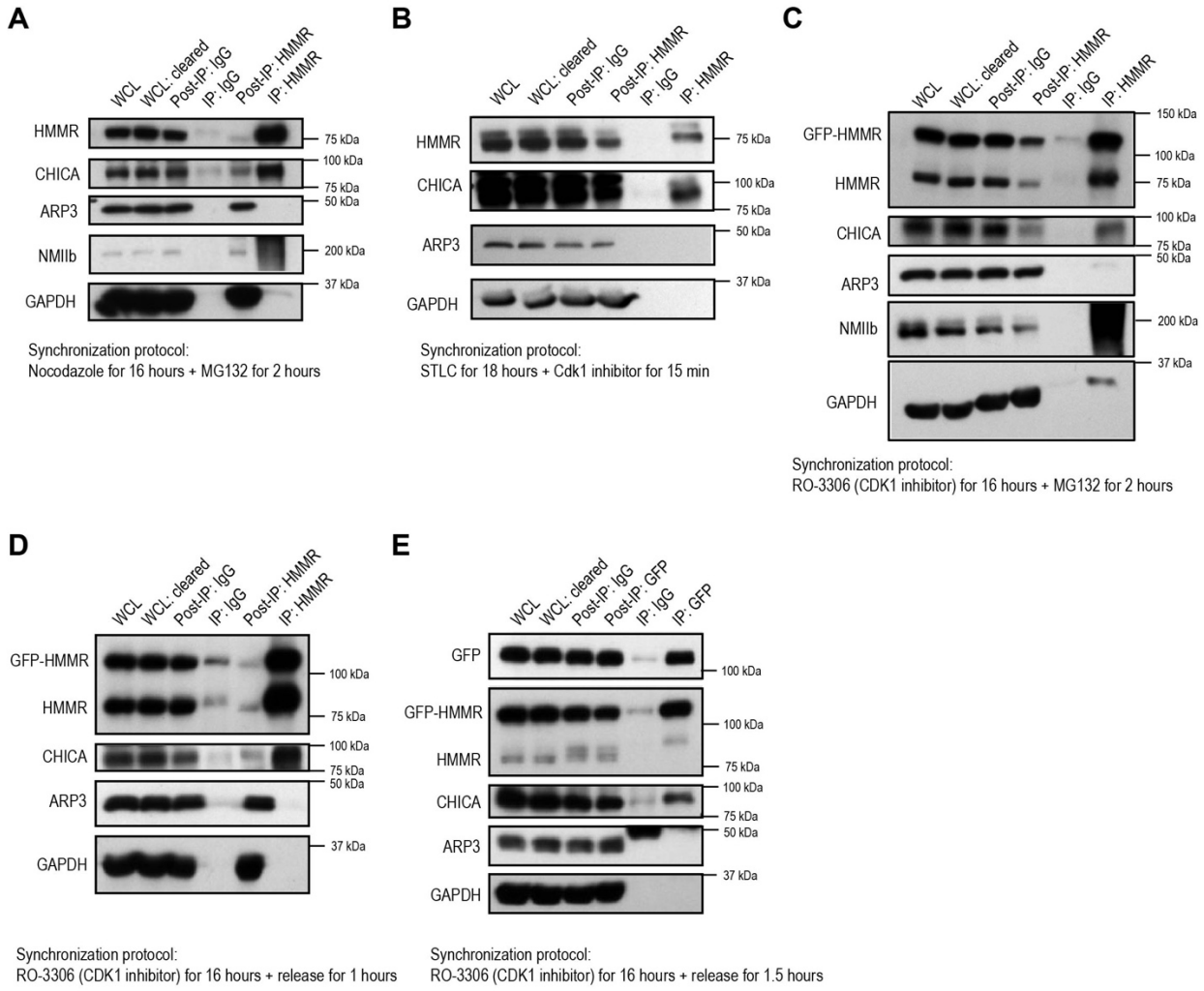

Figure 3.10 Immunoblots for HMMR immunoprecipitation from synchronized populations of HeLa or GFP-HMMR overexpressing tet-on HeLa cells (+dox).

A) Immunoprecipitation of HMMR from nocodazole and MG132-synchronized, M-phase HeLa cell lysates using an IgG control antibody or an anti-HMMR antibody. Co-precipitation of CHICA was a positive control. Co-precipitation of ARP3 was not detected. GAPDH was probed for equal loading and negative control.

B) Immunoprecipitation of HMMR from STLC and RO-3306 synchronized, M-phase populations of HeLa cell lysates with an IgG control antibody or an anti-GFP antibody. Co-precipitation of CHICA was a positive control. Co-precipitation of ARP3 was not detected. GAPDH was probed for equal loading and negative control.

C) Immunoprecipitation of HMMR from RO-3306 and MG132 synchronized, M-phase GFP-HMMR induced tet-on HeLa cell (+dox) lysates with an IgG control antibody or an anti-HMMR antibody. Co-precipitation of CHICA was a positive control. Co-precipitation of ARP3 was not detected. GAPDH was probed for equal loading and negative control.
D) Immunoprecipitation of HMMR from RO-3306 synchronized, M-phase GFP-HMMR induced tet-on HeLa cell (+dox) lysates with an IgG control antibody or an anti-HMMR antibody that targets C-terminus (ab108339). Co-precipitation of CHICA was a positive control. Co-precipitation of ARP3 was not detected. GAPDH was probed for equal loading and negative control.
E) Immunoprecipitation of GFP from RO-3306 synchronized, M-phase GFP-HMMR induced tet-on HeLa cell (+dox) lysates with an IgG control antibody or an anti-GFP antibody. Co-precipitation of CHICA was a positive control. Co-precipitation of ARP3 was not detected. GAPDH was probed for equal loading and negative control.

Proximity ligation assay (PLA) is a much more sensitive method to detect the physical proximity of two proteins within 40 nm of each other (Alam, 2018). However, PLA requires significant optimization in order to be confident in putative positive or negative results. Thus, I used immunofluorescence analysis to optimize the working conditions for the antibodies to detect the localization and expression level of proteins-of-interest in the HeLa cell lines at metaphase (Figure 3.11).

For my PLA analysis, I included three controls for detection of an interaction with HMMR in mitotic cells. First, I detected the proximity of GFP with HMMR in the GFP-HMMR overexpressing tet-on HeLa cells (+dox). For this pairing, I first confirmed the anti-GFP antibody signal was specific for HMMR overexpressing tet-on HeLa cells (+dox) and the localization was as expected for GFP-HMMR (Figure 3.12). Second, I detected the proximity of well-defined HMMR interactor proteins: CHICA and TPX2 (Dunsch *et al.*, 2012; Chen *et al.*, 2018). For these pairings, I confirmed the predicted localization of HMMR, TPX2 and CHICA to spindle microtubules (Kufer *et al.*, 2002; Marumoto *et al.*, 2005; Dunsch *et al.*, 2012). Third, I detected the spatial localization of putative PLA interactions with HMMR. So, I optimized the

detection of mitotic spindle poles, using a pericentrin antibody, and spindle microtubules, using a beta tubulin (TUBB) antibody. Finally, I optimized the working conditions for the detection of ARPC2, a component of the ARP2/3 complex. As expected, I observed cortical localization for ARPC2 in metaphase control-treated cells; provocatively, however, the localization of ARPC2 was dramatically altered in HMMR-overexpressing tet-on HeLa (+dox) cells, where it accumulated at mitotic spindles rather than the cell cortex.

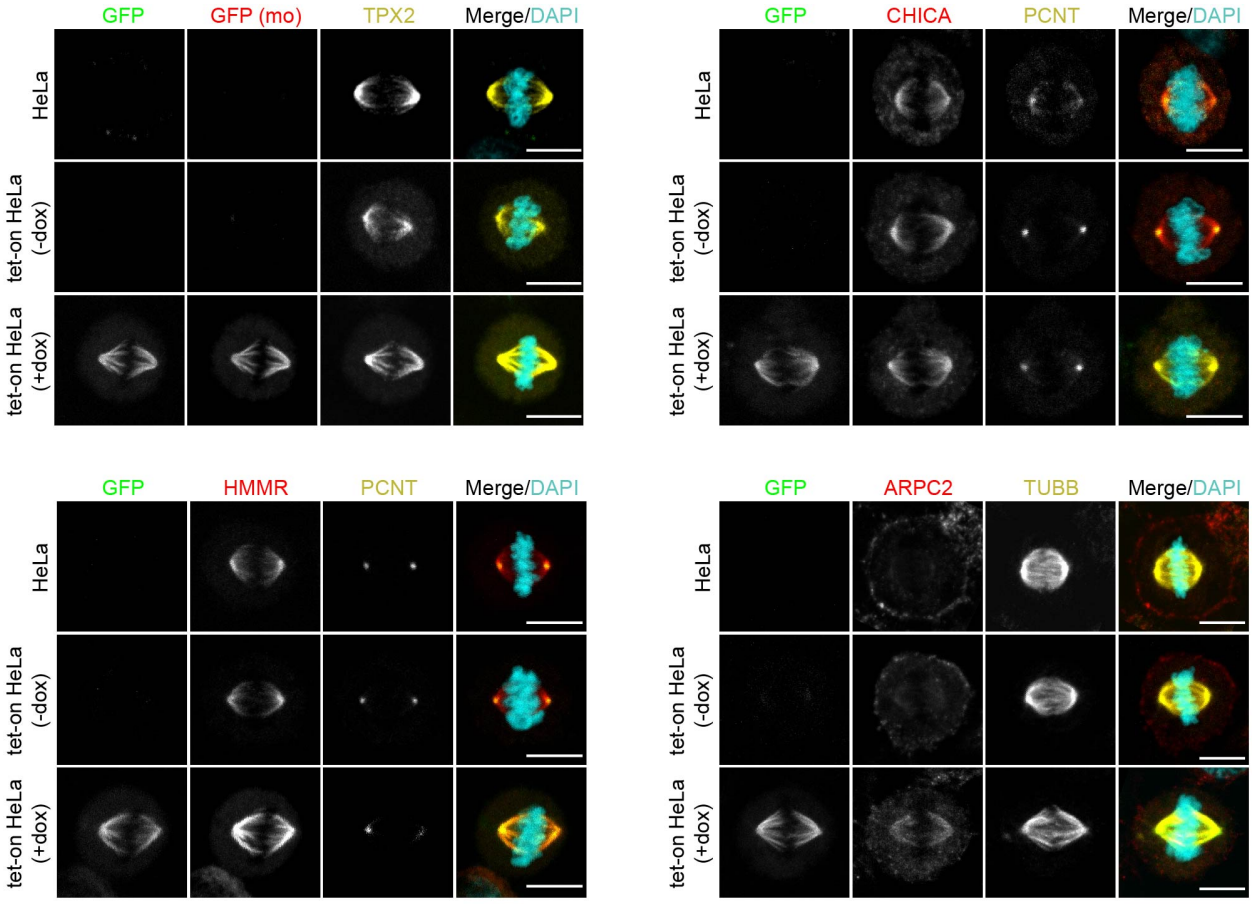

Figure 3.11 Localization of proteins of interest for PLA analysis in metaphase HeLa, tet-on HeLa cells (-dox), or GFP-HMMR overexpressing tet-on HeLa cells (+dox).
Localization of antibodies to be used in the proximity ligation assay in parental HeLa cells, tet-on HeLa cells (-dox) and tet-on HeLa cells (+dox). Scale bar = 10 µm.

After I optimized the working condition for each antibody, I performed a series of PLA in different combinations. First, I verified that I could detect a PLA signal between GFP and HMMR (Figure 3.12). As expected, I observed few PLA foci in parental HeLa cells and tet-on HeLa cells (-dox) at metaphase. Moreover, a strong PLA signal was detected at mitotic spindles in GFP-HMMR overexpressing tet-on HeLa cells (+dox). It is worth noting that a significant amount of PLA foci was also detected in the cytoplasm and the PLA signal between GFP and HMMR did not clearly match the spindle-localized GFP channel.

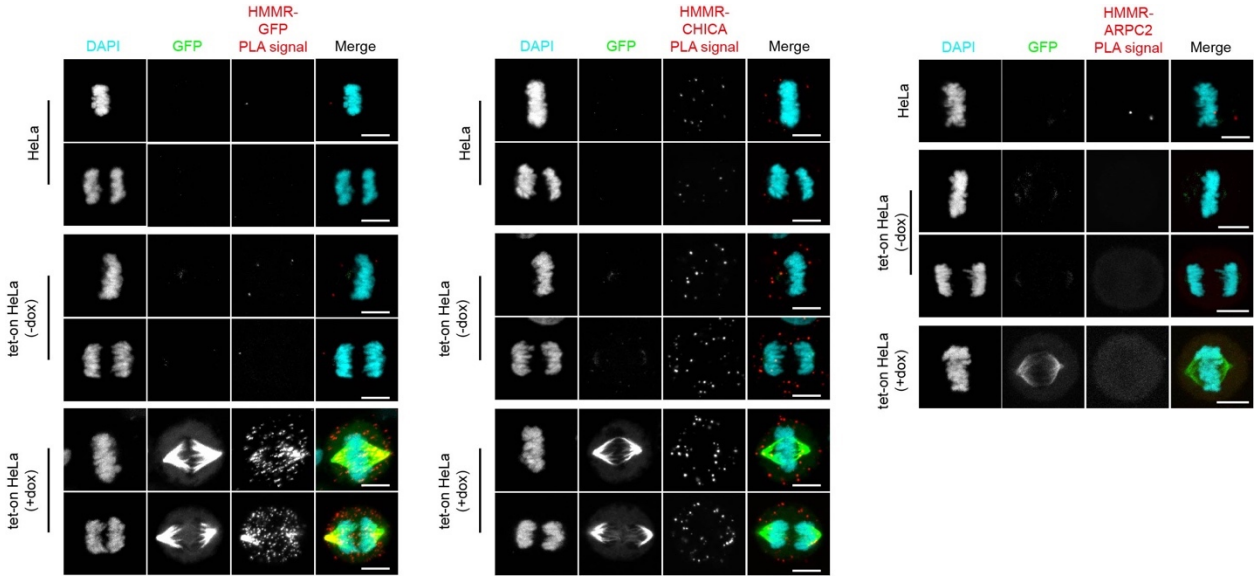

Figure 3.12 Proximity ligation assay probing HMMR, CHICA, and ARPC2 interaction. Proximity ligation assay to detect interactions between HMMR-GFP, HMMR-CHICA and HMMR-ARPC2. Scale bar = 10 μm.

I next tested the PLA using a combination of CHICA and HMMR antibodies. Surprisingly, I observed few PLA foci in metaphase cells, and while I detected more positive foci in GFP-HMMR overexpressing tet-on HeLa cells (+dox), the PLA foci did not localize to the spindle as expected. I observed similar results using a combination of ARPC2 and HMMR antibodies.

3.2.10 Cortical ARP2/3 complex localization is altered in GFP-HMMR overexpressing cells

ARPC2 (p34-ARC) is a component of the ARP2/3 complex that has recently been shown to locate transiently to the mitotic spindle pole as cells enter anaphase (Farina *et al.*, 2019) at a time when the mitotic membrane expands. Inhibition of ARP3 induces membrane blebbing in both cell and animal models (Roh-Johnson and Goldstein, 2009; Bergert *et al.*, 2012; Beckham *et al.*, 2014). Thus, I queried whether the pronounced membrane blebbing observed in GFP-HMMR overexpressing tet-on HeLa cells (+dox) correlated with disturbed localization of ARPC2.

In section 3.2.9, I observed different localization of ARPC2 between parental HeLa cells, tet-on HeLa cells (-dox) and GFP-HMMR overexpressing tet-on HeLa cells (+dox). Here, I investigated the localization of this component of the ARP2/3 complex in anaphase cells using a method described (Beaudet *et al.*, 2017; Farina *et al.*, 2019). Consistent with other studies, I found a significant amount of ARPC2 localized to the cortex in anaphase HeLa cells (Figure 3.13A). Although not completely lost, this cortical enrichment of ARPC2 was dampened in anaphase GFP-HMMR overexpressing tet-on HeLa cells (+dox) (Figure 3.13B,C). Instead, ARPC2 appeared to co-localize with GFP-HMMR on the spindle fibers; this change in localization was easily visualized through line profiles of signal intensities (Figure 3.13B). Therefore, I measured the intensity of ARPC2 localized at the cell cortex, or co-localized at GFP-HMMR positive mitotic spindles, in anaphase cells. My measurements confirmed loss of ARPC2 at the cortex and a significant augmented localization of ARPC2 to the spindle pole area in anaphase GFP-HMMR overexpressing tet-on HeLa cells (+dox) (Figure 3.13D), without concurrent alterations in the total abundance of ARPC2 (Figure 3.13E).

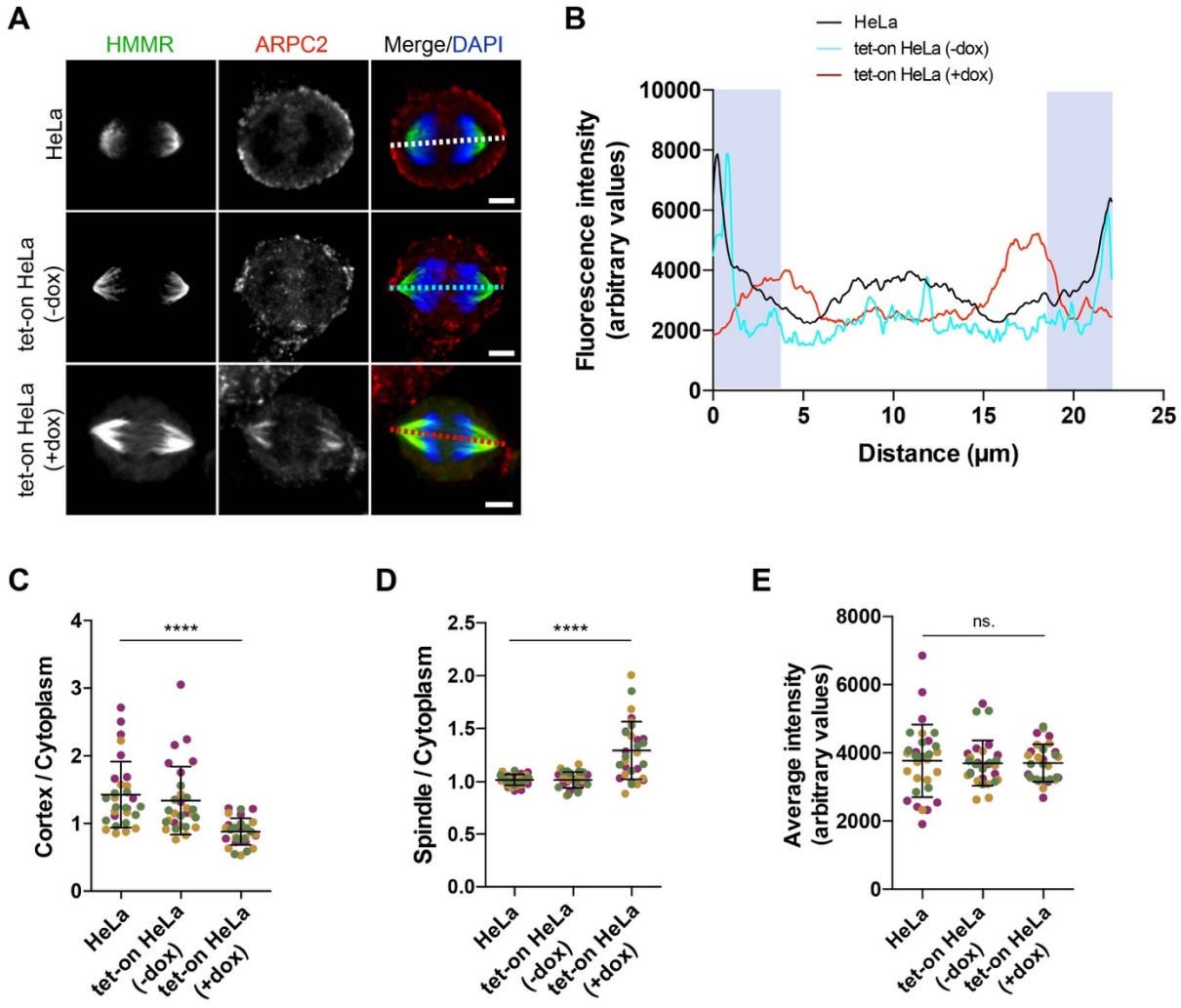

Figure 3.13 Cortical localization of ARP2/3 is lost in GFP-HMMR-overexpressing cells.

A) Immunofluorescence analysis of HMMR and ARPC2 in anaphase cells. Scale bar = 5 µm. White and red dash lines indicate the measurement of plot profile in panel B.

B) A plot profile measuring fluorescence intensity across the cells shown by the dash lines in panel A. The blue shaded areas are marks for 3 µm from the cortex.

C) Cortical ARPC2 enrichment in anaphase cells. The diagram presents the ratio of the average of the highest fluorescence intensity in the blue shaded areas divided by the highest fluorescence reading in the non-shaded area shown in panel B (Mean ± SD, n=40 cells per group, ****P<0.0001, one-way ANOVA).

D) ARPC2 spindle enrichment in anaphase cells was measured as the intensity of ARPC2 overlapped with HMMR at the spindle poles. Ratio was calculated using mean intensity (Integrated Intensity/Area) (Mean ± SD, n=30 cells per group, ****P<0.0001, one-way ANOVA).

E) Total abundance of ARPC2 in anaphase cells (Mean ± SD, n=30 cells per group, colour-coded, ns., P=0.93, one-way ANOVA).

3.2.11 Cortical localization of NMII is not altered in GFP-HMMR overexpressing cells

NMIIa (MYH9) and NMIIb (MYH10) are ABPs that are associated with cortical integrity and inhibited by blebbistatin, and which regulate progression through mitosis and mitotic cell shape (Beach and Egelhoff, 2009; Badirou *et al.*, 2014; Bovellan *et al.*, 2014; Roy *et al.*, 2016; Dey *et al.*, 2017; Shutova and Svitkina, 2018; Smith *et al.*, 2018; Chikina *et al.*, 2019; Svitkina, 2020). So, in addition to the localization of ARPC2, I also investigated the localization of NMIIa and NMIIb. However, my immunofluorescence analysis revealed that the subcellular and cortical localization of NMIIa (Fig. 3.14) and NMIIb (Figure 3.15) were not significantly altered in anaphase GFP-HMMR overexpressing tet-on HeLa cells (+dox). Therefore, the ectopic mis-localization of ARPC2 that I observed in anaphase GFP-HMMR overexpressing tet-on HeLa cells (+dox) does not appear to be a general disturbance of the localization of ABPs but rather a specific mis-localization of a key component of the ARP2/3 complex.

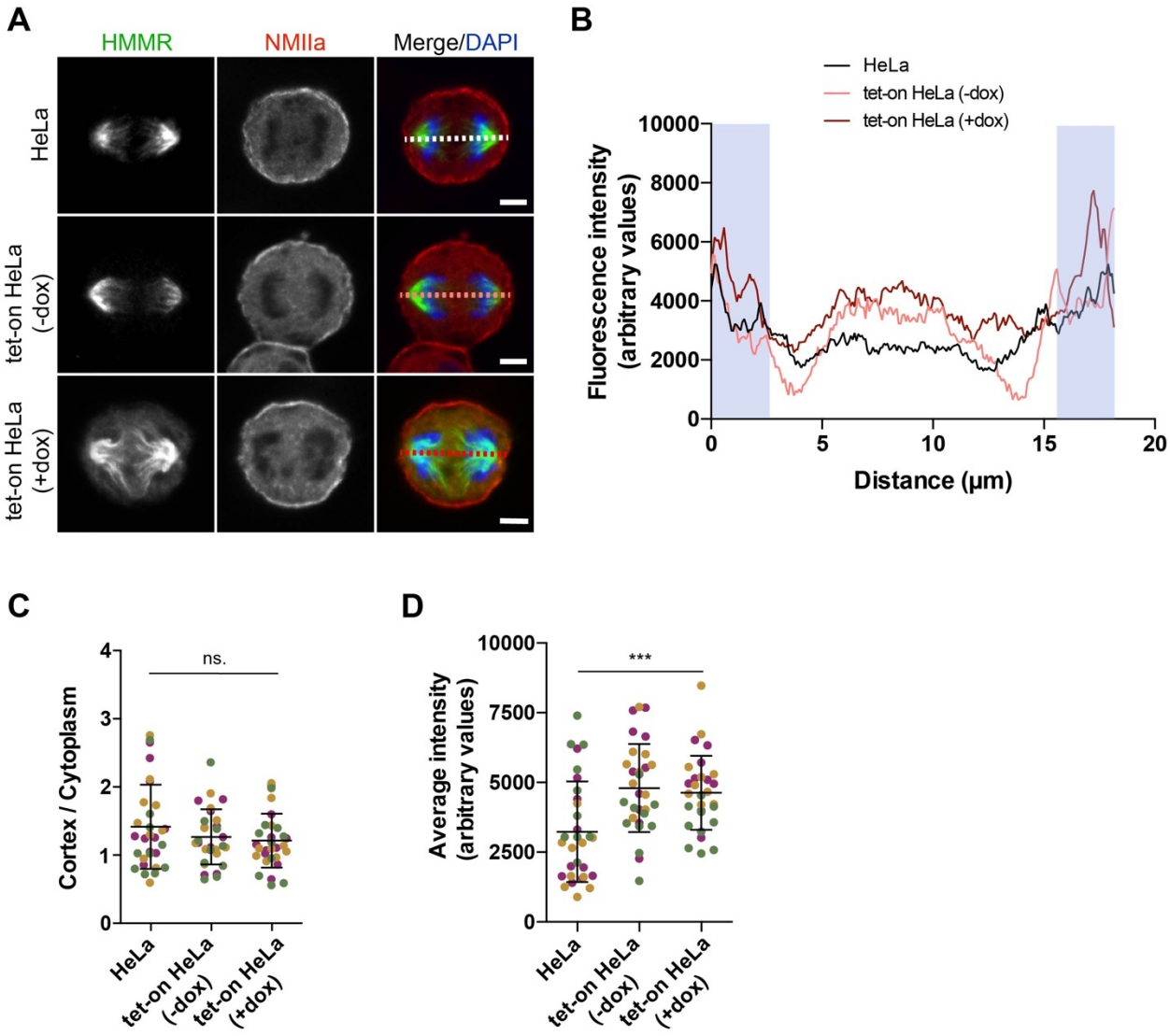

Figure 3.14 Subcellular localization of NMIIa does not change in the presence of GFP-HMMR overexpression.

A) Immunofluorescence analysis of GFP-HMMR overexpressing anaphase cells and control-treated anaphase cells probing for HMMR and NMIIa. Scale bar = 5 μm. White, pink and red dash lines in the middle column indicate the measurement of plot profile in panel B.

B) A plot profile measuring fluorescence intensity across the anaphase cells shown by the dash lines in panel A. The blue shaded areas are marks for 3 μm from the cortex.

C) Quantitation of cortical NMIIa enrichment in anaphase cells. The diagram presents the ratio of the average of the highest fluorescence intensity in the blue shaded areas divided by the highest fluorescence reading in the non-shaded area shown in panel B (Mean ± SD, n=30 cells per group, ns., P=0.25, one-way ANOVA).

D) Quantitation of the total abundance of NMIIa in anaphase cells (Mean ± SD, n=30 cells per group, ***P=0.0003, one-way ANOVA).

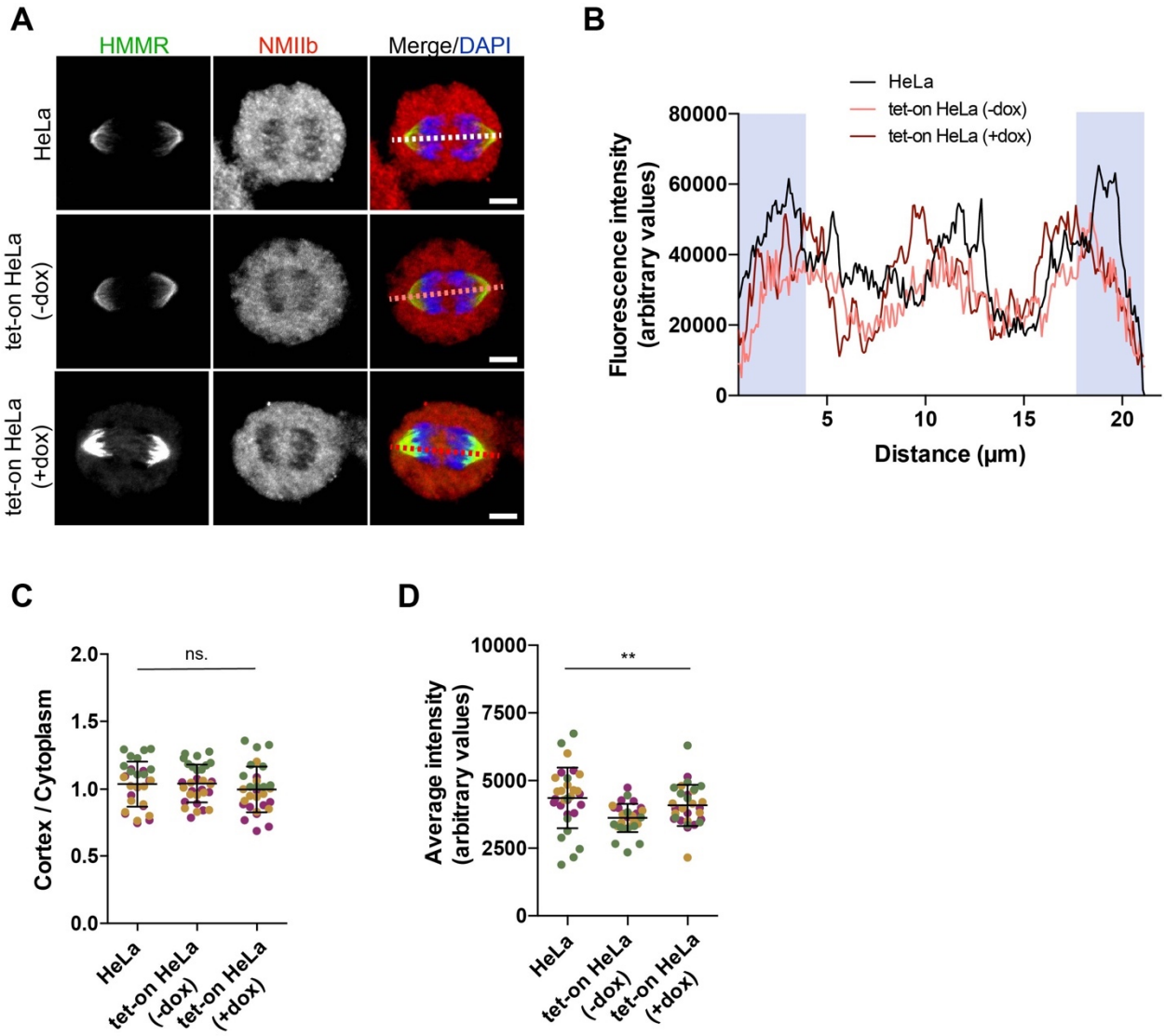

Figure 3.15 Cortical NMIIb is not affected in GFP-HMMR-overexpressing anaphase cells.

A) Immunofluorescence analysis of HMMR and NMIIb in anaphase cells. Scale bar = 5 µm. White and red dash lines in the middle column indicate the plot profile in panel B.

B) A plot profile measuring fluorescence intensity across the cells shown by the dash lines in panel A. The blue shaded areas are marks for 3 µm from the cortex.

C) Cortical NMIIb enrichment in anaphase cells presenting the ratio of the average of the highest fluorescence intensity in the blue shaded areas divided by the highest intensity in the non-shaded area shown in panel B (Mean ± SD, n=30 cells per group, ns., P=0.50, one-way ANOVA).

D) Abundance of NMIIb in GFP-HMMR overexpressing cells and control cells (Mean ± SD, n=30 cells per group, **P=0.0038, one-way ANOVA).

3.2.12 Mis-localization of ARP2/3 complex begins as cells enter mitosis

Although most ARP2/3 localizes to the cortex during cell division, a small pool of ARP2/3 also accumulates at the centrosomes in anaphase, which induces the formation of centrosomal actin filaments to facilitate mitotic exit (Bompard *et al.*, 2008; Mitsushima *et al.*, 2010; Sun *et al.*, 2011; Bovellan *et al.*, 2014; Farina *et al.*, 2019). Centrosomal localization of ARP2/3 is regulated temporally and only occurs when cells enter anaphase (Farina *et al.*, 2019). However, I found that the ARP2/3 complex component ARPC2 localized to the metaphase spindle in GFP-HMMR overexpressing tet-on HeLa cells (+dox) (Figure 3.11), suggesting HMMR may modify the localization of the ARP2/3 complex during cell division.

As a first step to understand a putative relationship between elevated HMMR expression and ARPC2 localization, I performed immunofluorescence analysis to track ARPC2 localization in each mitotic phase, as indicated by chromosome compaction and structure. In cells during interphase, I noted a trend towards augmented microtubule density at TUBB-positive and GFP-HMMR-positive centrosomes and a potential trend towards augmented localization of ARPC2 to these GFP-HMMR positive centrosomes in GFP-HMMR overexpressing tet-on HeLa cells (+dox) (Figure 3.16A); I observed an increase in ARPC2 level at centrosomes in prophase cells (Figure 3.16B). When cells proceeded to prometaphase, a significant amount of ARPC2 concentrated at spindle poles in GFP-HMMR overexpressing tet-on HeLa cells (+dox) (Figure 3.16C), whereas ARPC2 was largely retained in proximity to the cortex in control-treated prometaphase cells.

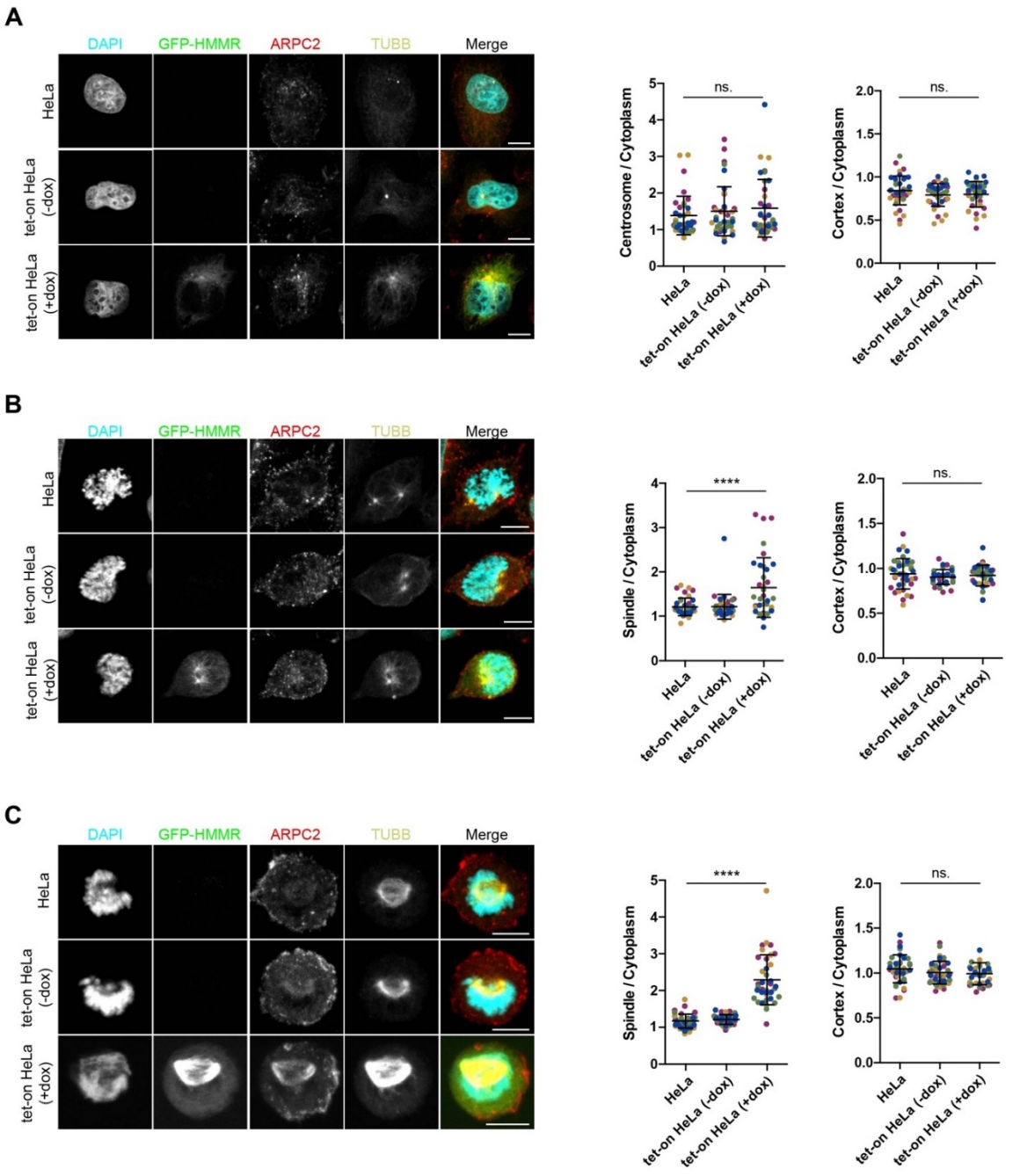

Figure 3.16 ARPC2 is mis-localized in GFP-HMMR overexpressing cells during mitosis.

A) Localization of ARPC2 and intensity at centrosomes or the cell cortex in interphase. Scale bar=10 µm. Mean ± SD n=40 (HeLa), 40 (-dox), 38 (+dox) cells, P=0.42 (centrosome), 0.25 (cortical), one-way ANOVA). Cortical ARPC2 intensity was calculated by measuring the intensity of ARPC2 within an area ~2 µm underneath the cell membrane.

B) Localization of ARPC2 and intensity at centrosomes or the cell cortex in prophase. Scale bar=10 µm. Mean ± SD, n=40 (HeLa), 40 (-dox), 35 (+dox) cells, ****P<0.0001 (spindle), P=0.4621 (cortical), one-way ANOVA).

C) Localization of ARPC2 at centrosomes during prometaphase. Scale bar=10 μm. ARPC2 intensity at the centrosome or the cell cortex in prometaphase cells (Mean ± SD, n=40 (HeLa), 39 (-dox), 38 (+dox) cells, ****P<0.0001 (spindle), P=0.19 (cortical), one-way ANOVA).

3.2.13 Accumulation of ARP2/3 complex at centrosomes normally occurs in anaphase

I then used immunofluorescence to confirm the published localization of ARPC2 and HMMR at the spindle pole in prometaphase cells and in cells forced to exit mitosis. I treated parental HeLa cells with 5 μM STLC for 18 hours to arrest them at prometaphase, and then I forced mitotic exit by the subsequent addition of 20 μM Cdk1 inhibitor, RO-3306, as described by Farina *et al.* (2019). Consistent with published findings, ARPC2 was not observed at spindle poles in cells arrested at prometaphase (Figure 3.17A). However, a small pool of ARPC2 accumulated around the spindle pole upon mitotic exit (Figure 3.17A).

To confirm the temporally-controlled spindle pole localization of ARPC2, I used pericentrin to demarcate centrosomes and I quantified the centrosome-localized relative to the cytoplasm-localized ARPC2 intensity. These analyses confirm that ARPC2 concentrated at the spindle pole during forced mitotic exit but not in prometaphase (Figure 3.17B).

As cortical ARP2/3 complexes may directly affect membrane blebbing, and cortical localization may be inversely linked to spindle pole intensity, I quantified ARPC2 intensity at the spindle pole relative to the cortex. The thickness of the cell cortex ranges from 0.2 μm to 1.0 μm depending on cell type and cell cycle status (Salbreux et al., 2012; Clark et al., 2013; Chugh et al., 2017). So, I manually defined the cortex area as ~2 μm underneath the membrane (Figure 3.17C). The ARPC2 intensity level I measured was consistent with that observed by Farina *et al.* (Farina *et al.*, 2019). Using these parameters, I observed a significant increase in ARPC2 intensity at centrosomes and a reduction at the cortex as cells exit mitosis (Figure 3.17D,E).

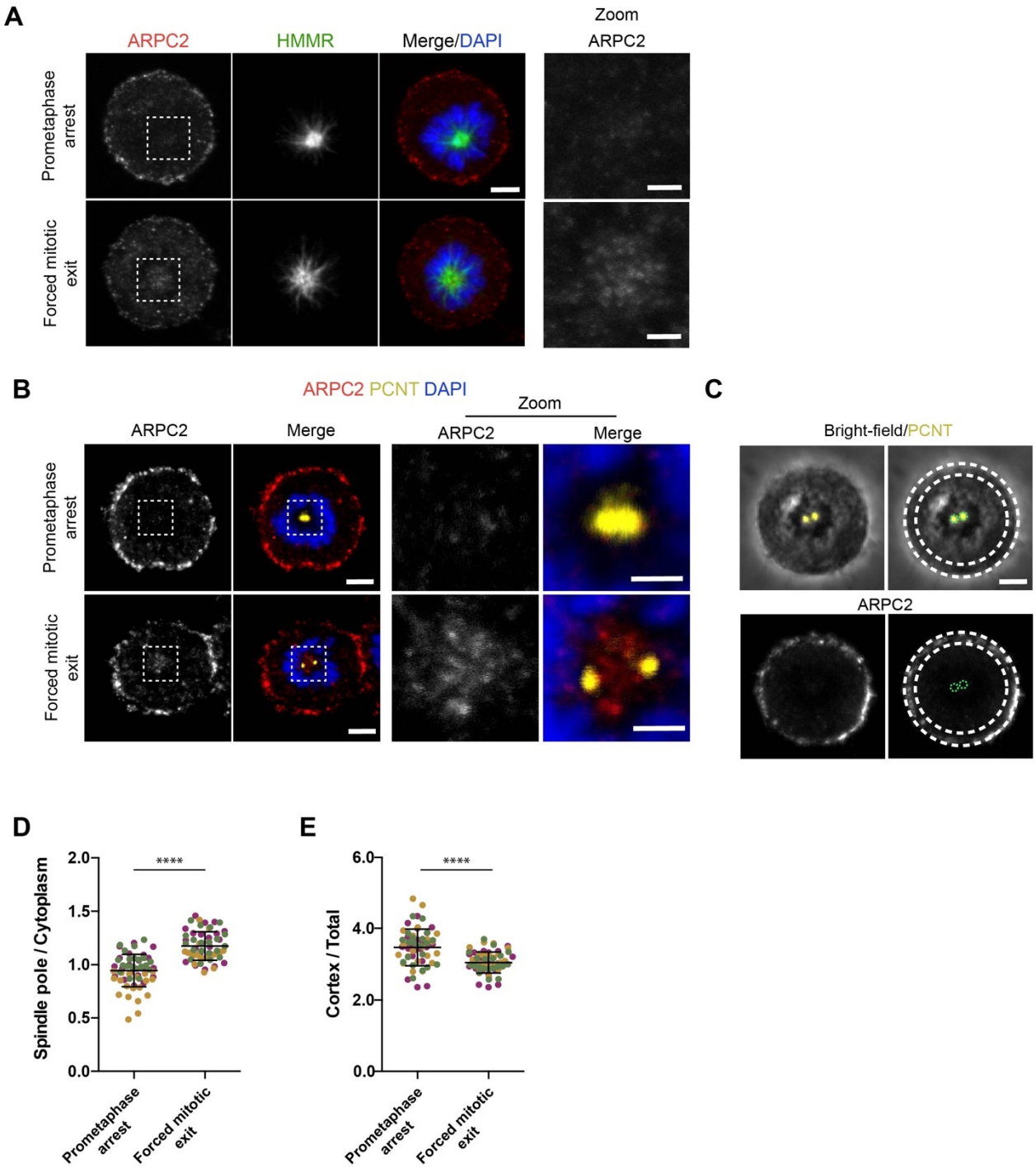

Figure 3.17 ARP2/3 and HMMR both localize to the spindle pole during forced mitotic exit.

A) Immunofluorescence analysis of ARPC2 and HMMR in HeLa cells arrested at prometaphase or forced to exit mitosis. Scale bar = 5 μm and for zoom = 2 μm.

B) Immunofluorescence analysis of ARPC2 and pericentrin in HeLa cells arrested at prometaphase or forced to exit mitosis. Scale bar = 5 μm and for zoom = 2 μm.

C) Spindle pole localized intensity measured in an area defined by pericentrin (green lines) and cortical intensity measured within an area ~2 μm underneath the cell membrane (white lines).

D) Spindle pole intensity for ARP2/3 complexes at prometaphase and anaphase. Experiments are colour coded. Mean ± SD, n=60 cells per group, ****P<0.0001, paired t-test).
E) Cortical intensity for ARP2/3 complexes at prometaphase and forced mitotic exit. Colour coded. Mean ± SD, n=60 cells per group, ****P<0.0001, paired t-test).

3.2.14 Centrosomal recruitment of ARPC2 is altered in GFP-HMMR-overexpressing cells

To measure centrosome recruitment of ARPC2 in GFP-HMMR overexpressing tet-on HeLa cells (+dox), I performed immunofluorescence analysis similar to that in section 3.13. First, I quantified spindle pole recruitment as well as cortical retention of ARPC2 in tet-on HeLa cells (-dox). The localization of ARPC2 in tet-on HeLa cells (-dox) showed a similar pattern as observed in parental HeLa cells. That is, cells forced to exit mitosis showed ARPC2 at the spindle poles but this localization was not apparent at prometaphase (Figure 3.18A). Moreover, the increased localization at the spindle pole during forced mitotic exit was observed concurrent with a reduced localization to the cell cortex (Figure 3.18B,C).

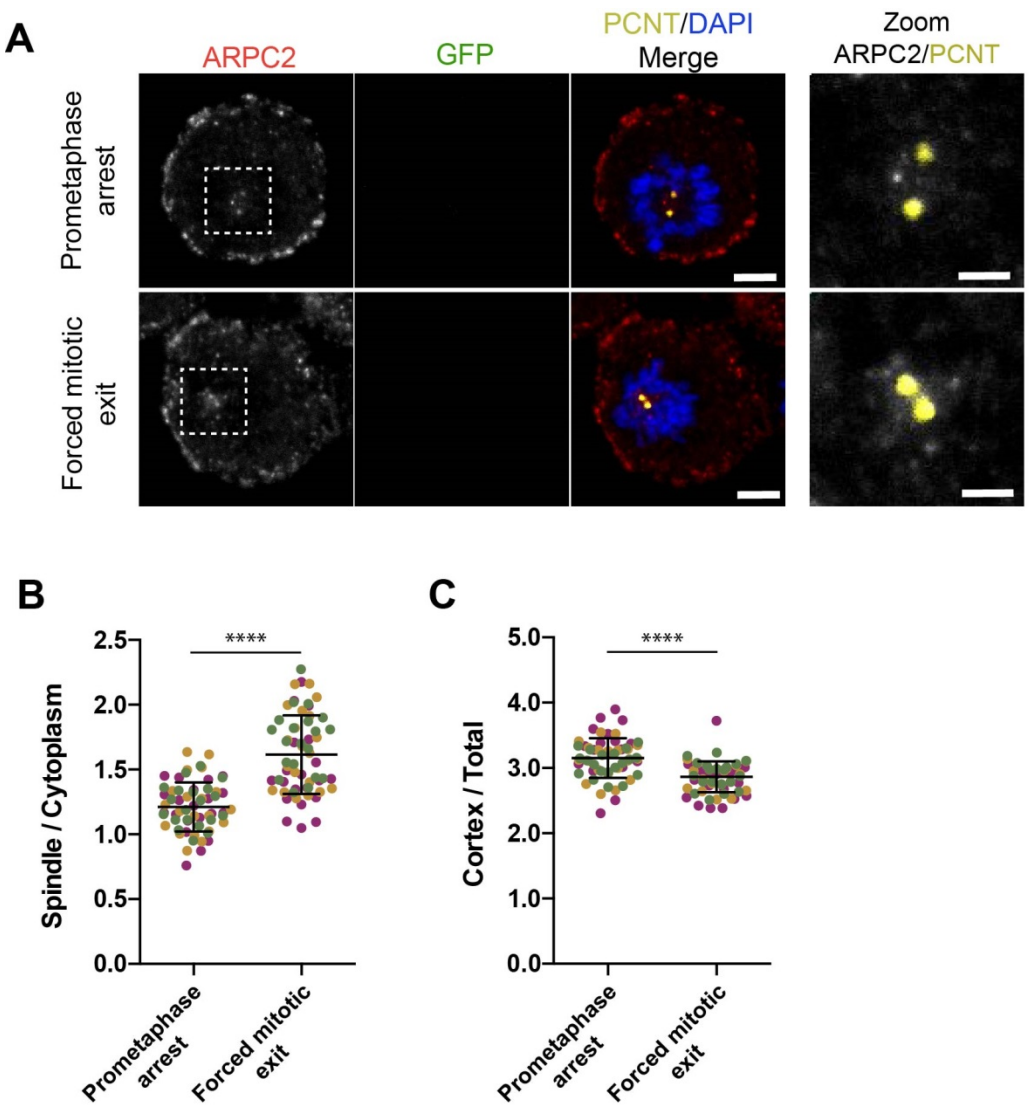

Figure 3.18 Spindle pole recruitment and cortical retention of ARP2/3 in non-induced tet-on HeLa cells display similar trend as those observed in control HeLa cells.

A) Tet-on HeLa cells (-dox) were arrested at prometaphase using STLC at 5 µM for 18 hours and forced to exit mitosis by the addition of 20 µM RO-3306 for 5 min. Cells were probed for ARPC2 and HMMR. Scale bar = 5 µm and for zoom = 2 µm.

B) Spindle pole intensity of ARP2/3 complexes at prometaphase and anaphase in tet-on HeLa cells (-dox) (Mean ± SD, n=60 cells per group, ****P<0.0001, paired t-test).

C) Cortical intensity of ARP2/3 complexes at prometaphase and forced mitotic exit in tet-on HeLa cells (-dox) (Mean ± SD, n=60 cells per group, ****P<0.0001, paired t-test).

In GFP-HMMR overexpressing tet-on HeLa cells (+dox), however, ARPC2 localized at the spindle pole in prometaphase cells prior to forced mitotic exit (Figure 3.19A). Moreover, the spindle pole intensity of ARPC2 in GFP-HMMR-overexpressing cells was higher than that observed in control cells undergoing forced mitotic exit. The ratio of ARPC2 intensity at spindle versus cortex, and the cortical ARPC2 intensity remained unchanged between prometaphase and forced mitotic exit (Figure 3.19B,C). This result indicates that the ARP2/3 complex is ectopically recruited to the spindle pole before anaphase onset in HeLa cells expressing GFP-HMMR.

Taken together, my findings indicate that the recruitment of ARPC2, a component of the ARP2/3 complex, is elevated at mitotic spindle poles in cells expressing GFP-HMMR and this localization correlates with reduced ARPC2 localization at the cell cortex. Although I observed a slight decrease of cortical ARPC2 localization in HMMR-silenced HeLa cells, it does not appear that HMMR depletion affects ARPC2 localization at cortex significantly (Figure 3.20). Thus, cortical integrity might be perturbed in GFP-HMMR-overexpressing cells compared with that in control cells not only in anaphase but also during prometaphase, which may expedite the membrane blebbing events that occur in late metaphase and anaphase.

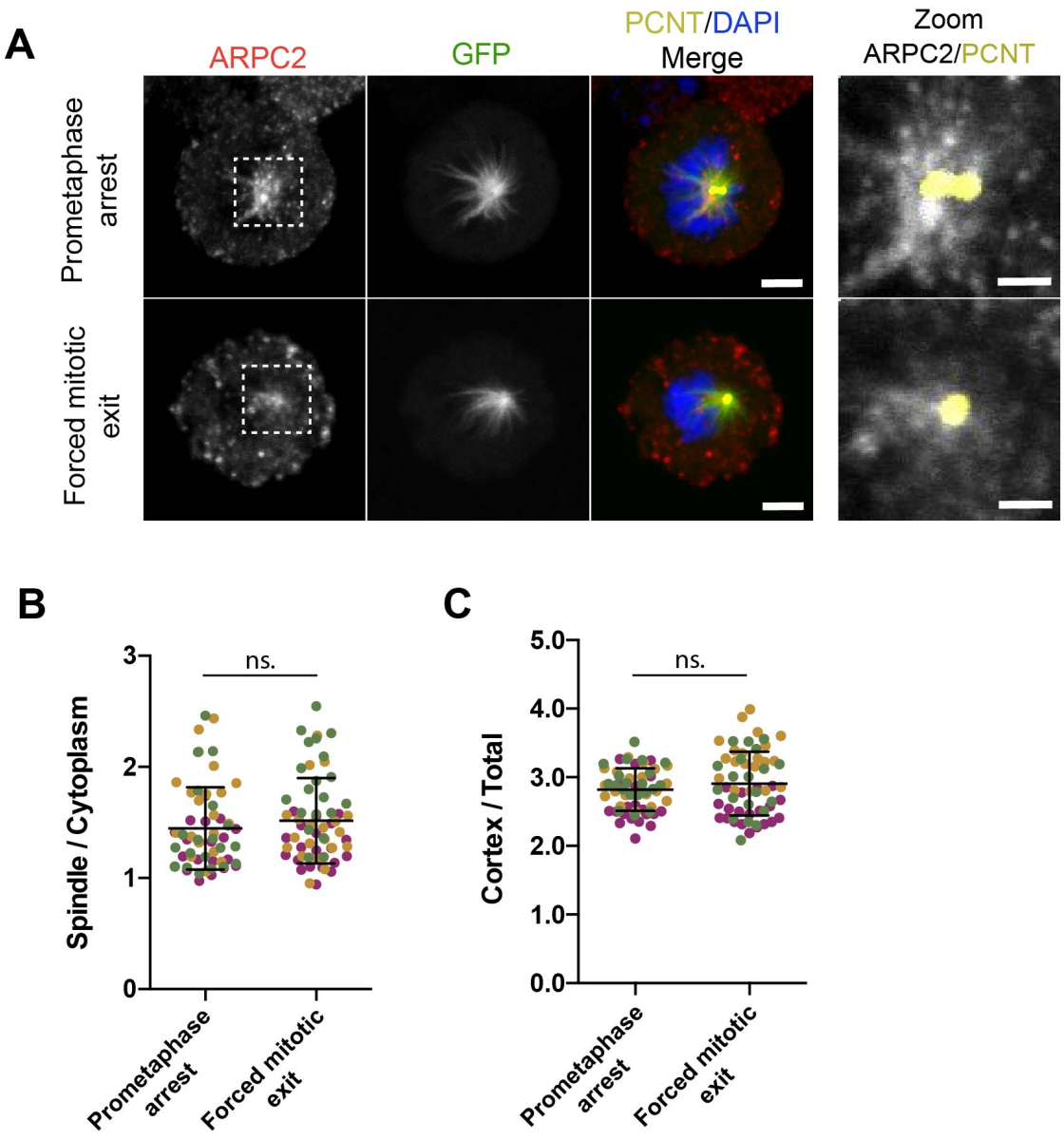

Figure 3.19 ARP2/3 abnormally accumulates at the centrosomes prior to anaphase onset in GFP-HMMR-overexpressing HeLa cells.

A) Tet-on HeLa cells (+dox) were arrested at prometaphase using STLC at 5 µM for 18 hours and forced to exit mitosis by the addition of 20 µM RO-3306 for 5 min. Cells were probed for ARPC2 and HMMR. Scale bar = 5 µm and for zoom = 2 µm.

B) Spindle pole intensity of ARP2/3 complexes at prometaphase and anaphase in tet-on HeLa cells (+dox) (Mean ± SD, n=60 cells per group, P=0.32, paired t-test).

C) Cortical intensity of ARP2/3 complexes at prometaphase and forced mitotic exit in tet-on HeLa cells (+dox) (Mean ± SD, n=60 cells per group, P=0.19, paired t-test).

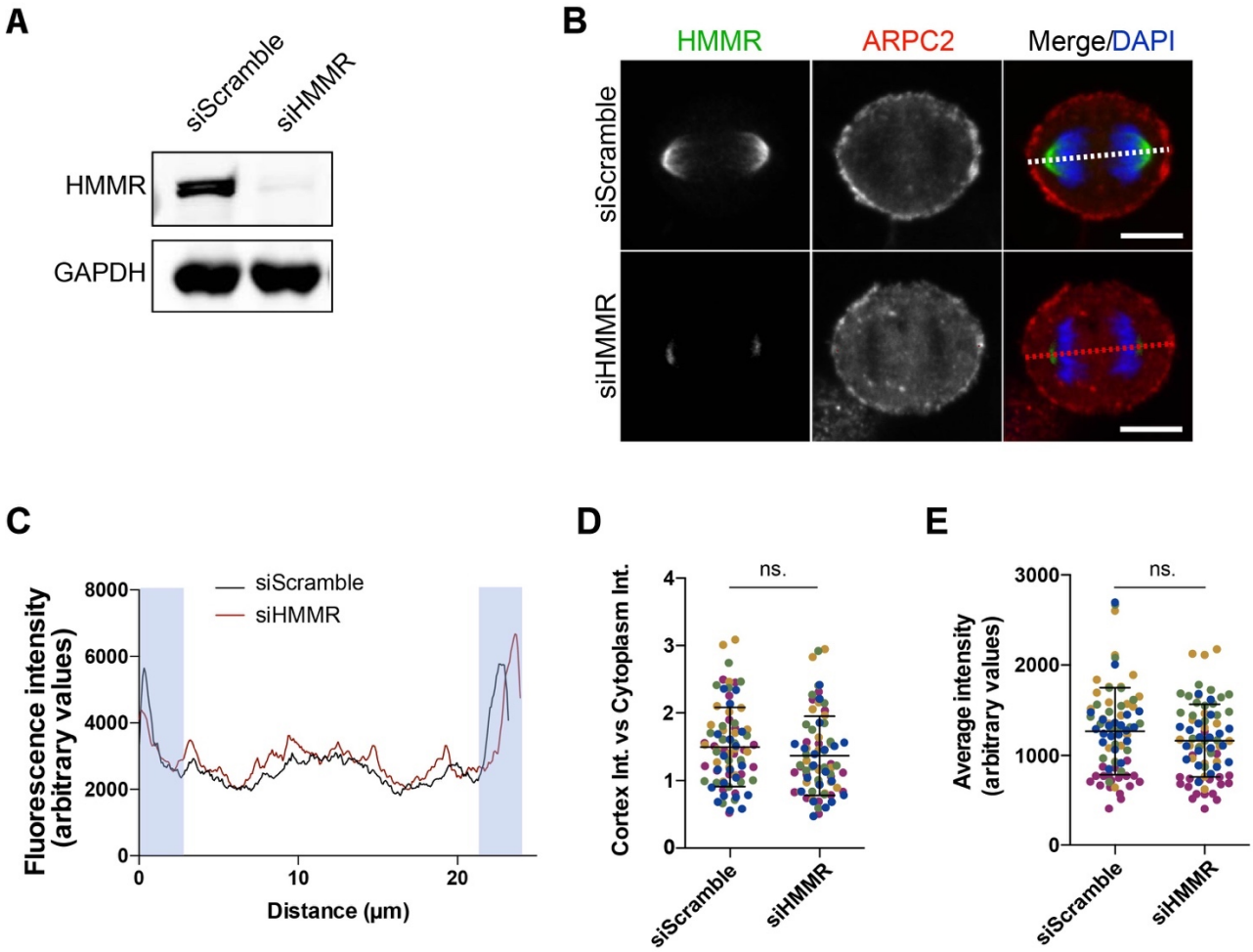

Figure 3.20 HMMR depletion does not affect cortical enrichment of the ARP2/3 complex.

A) HeLa cells were transfected with scrambled siRNA (siScramble) or siRNA targeting *HMMR* (siHMMR). HMMR expression was quantified by western blot analysis at 72 hours post transfection. GAPDH served as a loading control.

B) Immunofluorescence analysis of HMMR and ARPC2 in anaphase HeLa cells. Scale bar = 10 µm. White and red dash lines indicate the measurement of plot profile in panel B.

C) A plot profile measuring fluorescence intensity across anaphase cells, as shown by the dash lines in panel A. The blue shaded areas are marks for 3 µm from the cortex.

D) Cortical ARPC2 enrichment in anaphase cells. The diagram presents the ratio of the highest fluorescence intensity in the blue shaded areas divided by the highest fluorescence reading in the non-shaded area shown in panel B (Mean ± SD, n= 80 cells per group, P=0.16, unpaired t-test).

E) Total abundance of ARPC2 in anaphase cells (Mean ± SD, n= 80 cells per group, P=0.14, unpaired t-test).

3.3 Key findings

1. GFP-HMMR overexpression prolongs metaphase and results in rotating mitotic spindles.
2. GFP-HMMR overexpression induces unique and pronounced, but ineffective, asymmetric membrane elongation events.
3. GFP-HMMR overexpressing cells show higher probability of nucleus budding and micronuclei.
4. HMMR potentially interacts with a group of actin-binding proteins during mitosis.
5. The ARP2/3 complex component ARPC2, but not NMIIa or NMIIb, is mis-localized to the centrosome and mitotic spindle in GFP-HMMR overexpressing cells when cells enter mitosis, with a concurrent reduction at the mitotic cell cortex.

3.4 Discussion

Mitotic spindle position in anaphase determines the cellular boundary during cytokinesis and defines the cleavage site connecting the two daughter cells and thus daughter cell size (Kiyomitsu, 2015). The size difference between the daughter cells affects their cytoplasmic content, division frequency, nucleus formation, and even the behaviour of the cells (Fuse *et al.*, 2003; Tzur *et al.*, 2009; Ou *et al.*, 2010; Hara and Kimura, 2011; Dalton and Carroll, 2013; Kiyomitsu and Cheeseman, 2013; Sung *et al.*, 2013).

Mitotic spindle position is regulated by two main pathways: cortical dynein pulling forces that centre the spindle and asymmetric membrane elongation that corrects the cell boundary (Kiyomitsu, 2015). HMMR is involved in the regulation of cortical dynein localization directly through the localization of CHICA-DYNLL1 and indirectly through the centrosomal localization of Ran-GTP (Dunsch *et al.*, 2012; Kiyomitsu, 2015; Connell *et al.*, 2017). In both HMMR-

silenced and GFP-HMMR overexpressing cells, the mitotic spindle is mis-positioned more frequently than in control-treated cells and cortical dynein pulling forces are disrupted (Connell *et al.*, 2017). Yet, it remained unclear whether asymmetric membrane elongation is activated more frequently in response to off-centre spindles and if the size of daughter cells is affected in these cell models.

In this chapter, I measured the percentage of cells showing membrane blebbing events in anaphase and daughter cell size differences in HMMR overexpressing cells. I found that asymmetric membrane elongation was activated frequently in GFP-HMMR-overexpressing HeLa cells. Connell *et al* (2017) found that both HMMR-silenced and GFP-HMMR-overexpressing HeLa cells displayed off-centre spindles in metaphase (Connell *et al.*, 2017). Consistent with this result, I also find that GFP-HMMR-overexpressing cells spent a longer time in metaphase, which resembled mitotic phenotypes observed in HMMR-silenced cells (Chen *et al.*, 2014; Connell *et al.*, 2017). Since asymmetric membrane elongation is activated to normalize daughter cell size in mitotic cells with off-centre spindles, I analysed daughter cell sizes in these cell models. I found that daughter cell size control was defective in GFP-HMMR-overexpressing cells. While the elevated frequency of asymmetric membrane elongation events may simply reflect the elevated frequency of off-centre spindles in GFP-HMMR overexpressing cells, another possibility is that asymmetric membrane elongation was prompted by disrupted cortical integrity.

In order to determine if asymmetric membrane elongation improved daughter cell size control, I categorized daughter cell size ratios according to cells with and without blebbing events. While control treated cells showed consistent daughter cell-size ratios with and without blebbing, these ratios were altered with GFP-HMMR overexpression. In fact, asymmetric

membrane elongation not only failed to correct size ratios but also appeared to aggravate daughter cell size differences. Indeed, the bleb size observed in GFP-HMMR-overexpressing cells was phenotypically distinct from those observed in control-treated cells. This is quite surprising given that asymmetric membrane elongation is a tightly regulated and dynamic process that regulates cortical tension and stability in a temporally-controlled manner (Charras *et al.*, 2006; Bovellan *et al.*, 2014; Kiyomitsu, 2015). Consistent with an underlying fundamental defect, I found that simply reducing blebbing events, through treatments with blebbistatin, was not sufficient to rescue daughter cell size ratios in HeLa cells overexpressing GFP-HMMR.

I also observed abnormal chromosome segregation and elevated indicators of genome instability, which can also be induced by changes to cortical tension and improper blebbing in late anaphase (Pacquelet *et al.*, 2019). The population of GFP-HMMR overexpressing cells also displayed an elevated frequency of cGAS positive interphase cells and nuclear p52, an indicator of active NF-kB signalling. Such pro-inflammatory STING-IRF3-type I IFN signalling could result in inflammation-driven carcinogenesis (Khoo and Chen, 2018; Liu *et al.*, 2018; Ng *et al.*, 2018), and provide a mechanism for HMMR associated cancer progression.

Cortical actin and actin-binding proteins determine cortical stability and cell shape during cell division (Bovellan *et al.*, 2014). We identified a set of actin-binding proteins as potential binding partners of HMMR using IP-Mass spectrometry, including ARP3, a component of ARP2/3 complex. However, I was not able to confirm these putative interactions using immunoprecipitation followed by immunoblot analysis. It is probable that MS is more sensitive than immunoblot analysis for the detection of HMMR interacting peptides/proteins. It is also probable that an interaction between HMMR and components of the ARP2/3 complex would be spatially and temporally restricted to the centrosome/spindle pole during late metaphase or

anaphase. For this reason, I undertook multiple synchronization protocols to optimally collect cells at the metaphase-anaphase transition, but I was unable to confirm the interactions.

I undertook experiments using an additional method to detect potential interactions with HMMR, termed PLA. To achieve the optimal PLA results, the antibody used must have a concentration of 1 mg/mL in an amine-free buffer (Millipore Sigma, DUO96010). Although anti-GFP and anti-HMMR antibodies met the optimal requirement, the antibodies targeting CHICA and ARPC2 did not; this may partially explain my inability to confirm the positive control HMMR-CHICA interaction via PLA, thereby reducing confidence in the negative result for HMMR-ARPC2. Therefore, I cannot discount a potential interaction between HMMR and ARP2/3 complex, which was identified by IP-MS, as mass spectrometry can detect small amounts of proteins whereas western blot may require a larger amount for a detectable signal (Vasilescu and Figeys, 2006). Moreover, my PLA results are complicated by non-optimal antibody concentrations. Further experiments are needed to confirm or exclude a potential interaction between the ARP2/3 complex and HMMR, which is likely to be both spatially restricted to the spindle pole (a relatively small amount of ARP2/3) and temporally restricted to anaphase (a relatively brief period during mitosis). It is also plausible that HMMR and ARP2/3 complex components belong to the same multiprotein complex in a time sensitive manner.

As cells enter mitosis, a significant amount of ARP2/3 complex localizes to the cell cortex (Mitsushima *et al.*, 2010; Sun *et al.*, 2011; Bovellan *et al.*, 2014) and this activity is needed to maintain cortical stability and tension (Severson *et al.*, 2002; Roh-Johnson and Goldstein, 2009; Bergert *et al.*, 2012; Beckham *et al.*, 2014; Bovellan *et al.*, 2014) and prevent membrane protrusions forming due to cytosolic flow occurring in the cell (Sheetz and Dai, 1996; Paluch *et al.*, 2005, 2006; Wu *et al.*, 2013; Beckham *et al.*, 2014). My work indicates that

augmented HMMR abundance disturbs cortical stability and tension through the abnormal recruitment of the ARP2/3 complex to prophase and prometaphase centrosomes (peaks at prometaphase) and spindle microtubules, a process that is normally restricted to anaphase to facilitate mitosis exit (Farina *et al.*, 2019). Cortical intensity of ARP2/3 complex from interphase to prometaphase was not significantly different in bipolar spindle cells but more obvious in STLC-synchronized monopolar spindle cells. This may be due to the fact that as cells enter mitosis, ARP2/3 complex is remodelled from lamellipodia to facilitate the change of cell shape (Bovellan *et al.*, 2014; Rosa *et al.*, 2015; Farina *et al.*, 2019). Quantitative analysis of bipolar spindle cells might include the actin cytoskeleton transition to cell rounding whereas STLC-synchronized cells were rounded. Since asymmetric membrane elongation and centrosomal localization of ARP2/3 complex both occur during anaphase, and inhibition or depletion of ARP3 induces membrane blebbing or bleb-like protrusions (Severson *et al.*, 2002; Roh-Johnson and Goldstein, 2009; Bergert *et al.*, 2012; Beckham *et al.*, 2014; Bovellan *et al.*, 2014; Kiyomitsu, 2015; Farina *et al.*, 2019), it is possible that the directed localization of ARP2/3 complex away from the cortex to the spindle pole leads to thinner polar cortex so that asymmetric membrane elongation can be promoted quickly when the spindle is off-centre. However, in GFP-HMMR-overexpressing cells, the spindle accumulation of ARPC2 is abnormally promoted, via a potential direct interaction or another biochemical pathway (see Chapter 4), resulting in a less stable cortex that is prone to membrane blebbing events.

Caveats – In this study, I used GFP-HMMR inducible tet-on HeLa cells as a model for HMMR overexpression. With tetracycline induction for 24 hours, GFP-HMMR was expressed at a 1:1 ratio with endogenous HMMR. However, the non-induced tet-on HeLa cells also expressed

a low level of GFP-HMMR, although it appears that these cells express slightly lower level of endogenous HMMR so that the total amount of HMMR was similar to that of control HeLa cells (Figure 3.1A). Also, I repeated experiments using live cell imaging to analyze blebbing frequency and daughter cell size ratio in HeLa cells (+dox) and there was no difference between the results of HeLa cells (+dH2O) and HeLa cells (+dox) (not shown). However, the caveat regarding the control is that I only tested this set for blebbing frequency and daughter cell-size analysis but not for other experiments.

Inter- and intra-experimental variation in expression is one potential caveat associated with this system. To minimize this variation, I standardized the passage of cells that I used (parental and tet-on HeLa cells within 15 passages) and I standardized the doxycycline that I used (each newly thawed tube of doxycycline was used for no longer than two months). Within each experiment, I selected cells that showed a consistent level of GFP-HMMR overexpression for analysis by immunofluorescence.

HeLa cells are a standard experimental model for the study of mitosis, as these cells have predictable doubling time and are relatively amenable to different experimental manipulations, including drug treatments, frequent imaging and tetracycline-induction. Since membrane blebbing can be induced when cells are stressed, high tolerance to manipulations allow more accurate analysis of anaphase membrane blebbing (Gores *et al.*, 1990; Lane *et al.*, 2005; Charras *et al.*, 2008; Zhang *et al.*, 2018). However, HeLa cells are near tetraploid with extensive genomic rearrangements and a high level of aneuploidy and instability (Adey *et al.*, 2013; Landry *et al.*, 2013). In addition, p53 is absent in HeLa cells (Scheffner *et al.*, 1990; Berglind *et al.*, 2008) and p53 suppresses the expression and oncogenic activity of Aurora A (Chen *et al.*, 2002; Wu *et al.*, 2012). A significant caveat is that the findings from this chapter are limited to one cancer cell

line and, therefore, may represent responses that are not generalizable to non-cancerous cell lines or primary cells and tissues. Importantly, I address this significant caveat in Chapter 5.

A final important caveat associated with these findings is that the tet-on HeLa experimental model system expresses HMMR tagged with GFP. The benefit of this is the ability to track in real-time the expression levels of the tagged protein. Importantly, GFP-HMMR has been shown to localize similar to endogenous HMMR and GFP-HMMR expression has been shown to rescue functions in HMMR siRNA-treated cells (Chen *et al.*, 2014). Nevertheless, I cannot exclude the potential that GFP expression alters the phenotypes of interest and the expression levels of GFP-HMMR are clearly not physiological. To address the latter two points, I also examined these phenotypes in several *in vivo*, *in situ* and *ex vivo* models without GFP-tagging in Chapter 5.

Future studies – Future experiments can utilize alternative ways to manipulate HMMR expression to examine the effects on ARP2/3 complex localization as well as daughter cell-size related phenotypes. For example, the use of affinity-directed protein missile (AdPROM) technologies is an effective targeted proteolytic method based on the ubiquitin proteosome system (Fulcher *et al.*, 2016, 2017). The AdPROM system includes a cameloid anti-GFP (aGFP) nanobody fused to the von Hippel-Lindau (VHL) protein which recruits GFP-tagged proteins to the CUL2 E3 ubiquitin ligase and facilitates degradation by the proteasome (Fulcher *et al.*, 2016, 2017). This system would allow for the regulated expression of GFP-HMMR, with or without aGFP-VHL, to toggle between overexpression and no overexpression. With this technique, I expect to observe a significant rescue of ARP2/3 complex localization, reduced blebbing frequency and equal daughter cell-size.

Although I focused my work on the confirmation of putative HMMR-ABP interactions, the mass spectrometry analysis also identified a set of S100 proteins, including S100A7, S100A8, S100A9 and S100A10, within the mitotic HMMR immunoprecipitates. Future studies may focus on the confirmation of these putative interactions and their possible effects on proinflammatory signalling, similar to my hypothesis that GFP-HMMR induces proinflammatory cGAS-positive micronuclei in tet-on HeLa cells (+dox). A S1008/9 heterodimer was first identified as immunogenic protein released by phagocytes (Ghavami *et al.*, 2009). On the other hand, primary tumours release soluble factors that promote expression of S100A8 and S100A9 (Rafii and Lyden, 2006). S100A8/9 can induce cancer cell proliferation and facilitate invasion and adhesion of malignant cells (Ghavami *et al.*, 2009). Similar to cGAS-STING, S100A8/9 shows anti-tumorigenic effects but can also be tumour-promoting, which depends on the concentration (Ichikawa *et al.*, 2011; Mondet *et al.*, 2021). Intracellular S100A8/9 promotes the activity of phosphatase 2A (PP2A) (Khammanivong *et al.*, 2013), which targets G2/M Cdc25C to inhibit cell division (Margolis *et al.*, 2006; Forester *et al.*, 2007). It is plausible that an interaction between HMMR and S100A8/9 during cell division can alter tumour microenvironmental changes that promote tumorigenesis.

Significance – In Chapter 3, my research shows that altered expression of HMMR dysregulates asymmetric membrane elongation and the control of daughter cell size. My results reveal that HMMR overexpressing cells display a higher percentage of cells with anaphase-specific membrane elongation as well as the ultimate loss of daughter cell size control. I find that elevated HMMR expression correlates with the mis-localization of components of the ARP2/3 complex, which potentially disrupts cortical stability during mitosis.

Chapter 4: HMMR regulates ARP2/3 complex localization through Aurora kinase A during mitosis

4.1 Rationale and hypothesis

Asymmetric membrane elongation depends on the cortical localization of actomyosin, a network formed by actin and myosin that generates contractile forces (Kiyomitsu, 2015). Actin-related proteins play a role in regulating the actomyosin structures by re-organizing actin (Yang *et al.*, 2012; Schell *et al.*, 2018). The proximity of the mitotic spindle, and the proteins which localize to the spindle poles (Kiyomitsu, 2015; Connell *et al.*, 2017), acts as a signaling cue to regulate protein retention and the composition of cortical proteins. For example, HMMR localizes to the spindle poles and regulates the centrosomal localization of Ran-GTP in a PLK1-dependent manner (Connell *et al.*, 2017). Ran-GTP at the spindle poles and chromosomes acts on anillin to modify cortical actomyosin (Kiyomitsu and Cheeseman, 2013; Kiyomitsu, 2015; Connell *et al.*, 2017). Similarly, PLK1 activity at the mitotic spindles is regulated by the levels of HMMR (Chen *et al.*, 2014; Connell *et al.*, 2017) as is the cortical retention of dynein via the HMMR-CHICA-DYNLL1 complex (Dunsch *et al.*, 2012; Kiyomitsu and Cheeseman, 2012, 2013; Connell *et al.*, 2017). HMMR-CHICA complexes also recruits casein kinase 1α (CK1α) to the spindle, which affects spindle orientation and mitotic progression (Fulcher *et al.*, 2019). Similarly, HMMR-TPX2 complexes at mitotic spindle poles control the local activity of Aurora kinase A (Kufer *et al.*, 2002; Chen *et al.*, 2014). Thus, I hypothesize that HMMR at the spindle has the potential to affect the activities of PLK1, Aurora A, or CK1α, which influence cortical actomyosin components and daughter cell size control during cell division.

4.2 Results

4.2.1 Mis-localization of the ARP2/3 complex is not correlated with cortactin localization

Cortactin is a class II nucleation-promoting factor that activates the ARP2/3 complex and binds to actin filaments (Schnoor *et al.*, 2018). To determine if ARP2/3 complex mis-localization during cell division is relevant to cortactin. I stained GFP-HMMR overexpressing cells with an antibody targeting cortactin and performed immunofluorescence analysis (Figure 4.1). If cortactin regulates ARP2/3 complex mis-localization in GFP-HMMR overexpressing tet-on HeLa cells (+ dox) cells, I expect to observe spindle/cortical ratio identical to that of ARP2/3 complex: spindle pole/cortical ratio is higher than control from prophase to anaphase (section 3.2.12, 3.2.14). Nevertheless, immunofluorescence analysis on prometaphase tet-on HeLa cells (+ dox) showed lower spindle pole/cortical ratio of cortactin and no significant difference during prophase. In metaphase and anaphase, the spindle/cortical ratio of cortactin was significantly higher in GFP-HMMR overexpressing tet-on HeLa cells (+ dox) cells. Unlike the higher spindle pole/cortical ratio of ARP2/3 complex that began at prophase, similar localization pattern of cortactin occurred later in metaphase. Therefore, I conclude that the mis-localization of the ARP2/3 complex in GFP-HMMR tet-on HeLa cells (+ dox) was not correlated with cortactin localization.

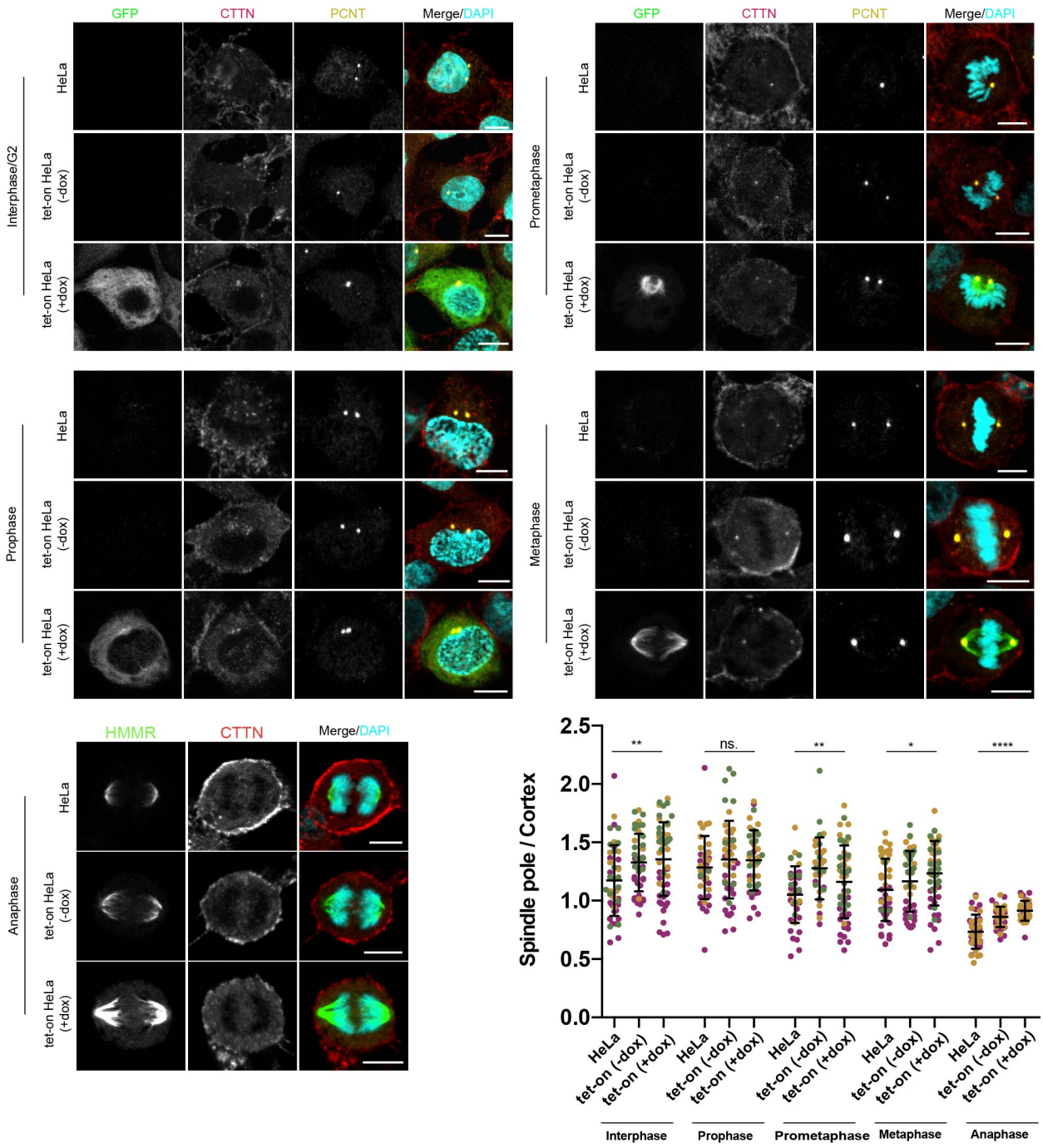

Figure 4.1 Cortical cortactin level is altered in GFP-HMMR overexpressing anaphase cells. Quantitative analysis of intracellular cortactin localization in HeLa, tet-on HeLa (-dox), tet-on HeLa (+dox) cells at interphase, prophase, prometaphase, metaphase and anaphase (Mean ± SD, Interphase: n=47 (HeLa), 42 (-dox), 53 (+dox) cells, **P=0.0053; Prophase: n=39 (HeLa), 49 (-dox), 41 (+dox) cells, P=0.5035; Prometaphase: n=40 (HeLa), 32 (-dox), 53 (+dox) cells, **P=0.0039; Metaphase: n=44 (HeLa), 47 (-dox), 52 (+dox) cells, *P=0.0363; Anaphase: n=40 (HeLa), 40 (-dox), 33 (+dox) cells, ****P<0.0001,one-way ANOVA). Scale bar = 10 μm.

4.2.2 Reduction of cortical ARP2/3 complex during anaphase is not due to the process of polar relaxation

The retention of cortical proteins that maintain cortex stability and cell shape can be affected by astral microtubules during anaphase and cytokinesis. Through a process termed polar or astral relaxation, astral microtubules extend to the polar cortex to send inhibitory signals that impede actomyosin-mediated contraction (Verma *et al.*, 2019; Chapa-Y-Lazo *et al.*, 2020). HMMR regulates the location of TPX2 and its activation of Aurora A, which controls mitotic microtubule assembly (Chen *et al.*, 2014). Thus, I hypothesized that GFP-HMMR overexpressing cells may have a higher density of astral microtubules, which may send premature signals to affect ARP2/3 complex localization.

To investigate the number of nucleation events of astral microtubules at the cortical area, I performed immunofluorescence analysis of end binding 1 (EB1), a protein that binds to the plus end of microtubules (Nehlig *et al.*, 2017). Specifically, I counted the number of EB1 foci around the cortex, which I defined as 2 μm from the cell boundary. However, I found that EB1 density was not elevated between control cells and GFP-HMMR overexpressing tet-on HeLa cells (+dox) in prophase or prometaphase (Figure 4.2A,B). On the contrary, EB1 density was significantly lower in metaphase and anaphase cells (Figure 4.2C,D). It is important to note that this significant reduction of astral microtubules in metaphase and anaphase occurs after the ectopic recruitment of ARPC2 to the spindle, which occurs during prophase in GFP-HMMR overexpressing tet-on HeLa cells (+dox). Thus, my observation of EB1 density implies that HMMR-overexpression does not lead to premature polar relaxation and further suggests the mis-localization of ARPC2 does not occur via microtubule dependent motors as astral microtubules are not reaching the cortex during metaphase and anaphase.

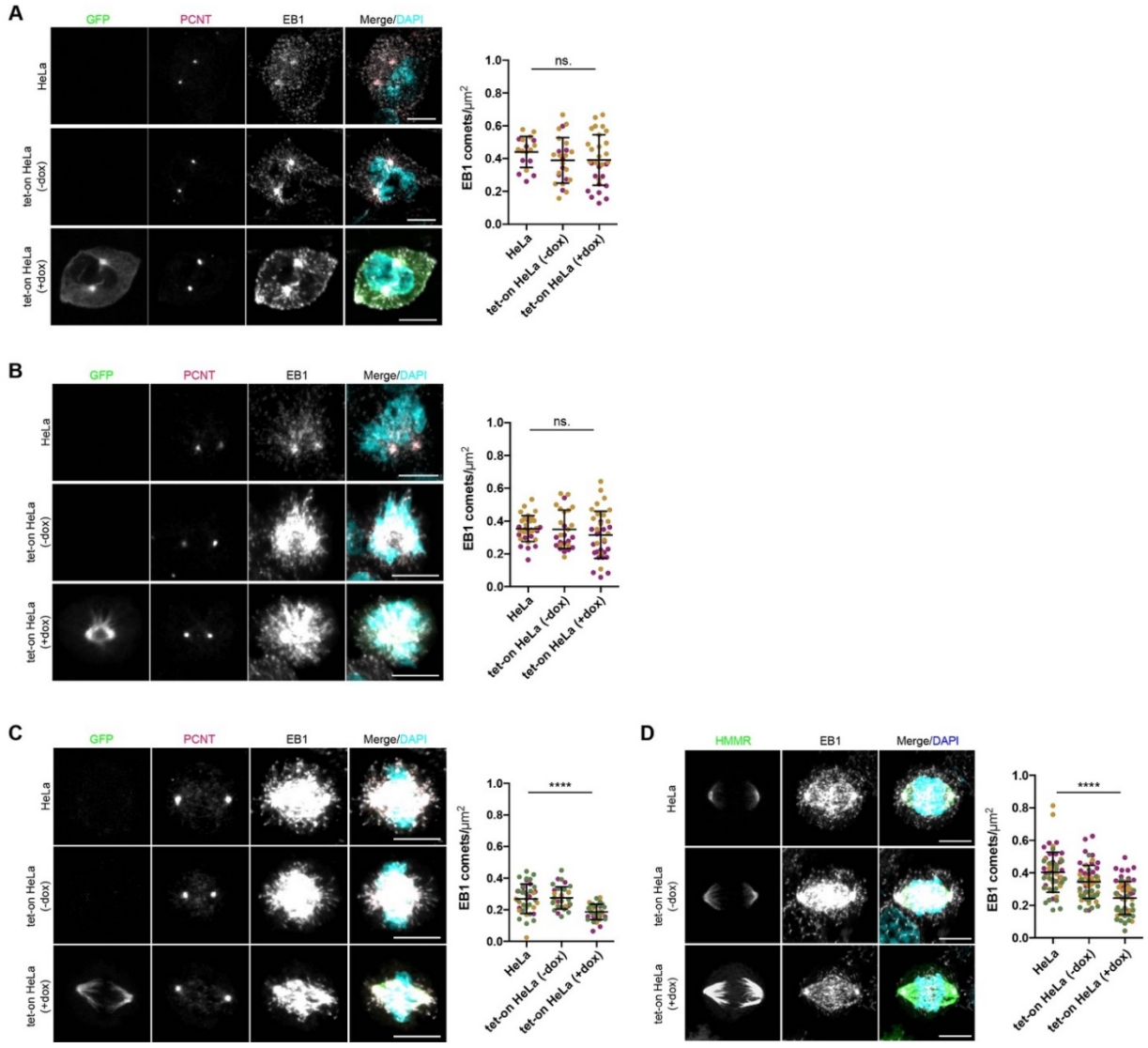

Figure 4.2 EB1 density at cortical area is reduced in metaphase and anaphase but not prophase or prometaphase.

A) Immunofluorescence analysis of EB1 in prophase parental HeLa cells, tet-on HeLa cells (-dox) and tet-on HeLa cells (+dox). Scale bar=10 μm. Cortical EB1 density was measured by the number of EB1 foci in an area ~2 μm underneath the cell membrane divided by the area (Mean ± SD, n=18 (HeLa), 25 (-dox), 30 (+dox) cells, P=0.40, one-way ANOVA).

B) Immunofluorescence analysis of EB1 in prometaphase parental HeLa cells, tet-on HeLa cells (-dox) and tet-on HeLa cells (+dox). Scale bar=10 μm. Cortical EB1 density (Mean ± SD, n=32 (HeLa), 27 (-dox), 36 (+dox) cells, P=0.3266, one-way ANOVA).

C) Immunofluorescence analysis of EB1 in metaphase parental HeLa cells, tet-on HeLa cells (-dox) and tet-on HeLa cells (+dox). Scale bar=10 μm. Cortical EB1 density (Mean ± SD, n=40 (HeLa), 33 (-dox), 35 (+dox) cells, ****P<0.0001, one-way ANOVA).

D) Immunofluorescence analysis of EB1 in anaphase parental HeLa cells, tet-on HeLa cells (-dox) and tet-on HeLa cells (+dox). Scale bar=10 μm. Cortical EB1 density (Mean ± SD, n=60 (HeLa), 60 (-dox), 60 (+dox) cells, ****P<0.0001, one-way ANOVA).

4.2.3 Inhibition of Aurora A rescues changes in daughter cell size control caused by HMMR overexpression

HMMR is a spindle assembly factor that maintains the structural integrity of the mitotic spindle (Maxwell et al. 2003). HMMR does not have enzymatic activity but functions to localize partner proteins (such as TPX2, FAM83D/CHICA, and BACH) to the spindle, which in turn regulates enzymatic activities, including kinases and molecular motors. For example, HMMR promotes the activity of several important kinases during mitosis, including Aurora A, PLK1 and CK1α (Chen *et al.*, 2014; Connell *et al.*, 2017; Fulcher *et al.*, 2019). Because my analysis of astral microtubules suggested that the mis-localization of ARPC2 may occur independent of motor activity along astral microtubules, I investigated the hypothesis that ectopic expression of GFP-HMMR augmented kinase activities to disturb the correct localization of ARPC2 during mitosis.

I postulated that the overexpression of GFP-HMMR may activate one or more related mitotic kinases to disturb the correct localization of the ARP2/3 complex. To test this hypothesis, I first performed a kinase inhibitor screen using small-molecule inhibitors for Aurora A (MNL8237), PLK1 (BI2536), and CK1α (D4476). In addition to these three kinases, I also included Aurora kinase B (Aurora B, AZD1152) as a related mitotic kinase that is not activated by HMMR (Chen *et al.*, 2018). Following exposure to graded doses of each inhibitor, I measured the frequency of membrane blebbing events and the daughter cell size ratio in GFP-HMMR overexpressing tet-on HeLa cells (+dox).

Each of the selected kinases control many pathways in cell division, affect cell cycle progression, and thus the inhibitors are cytostatic or cytotoxic. Thus, I first determined the dose response curve for each small-molecule inhibitor so that I could select a range of doses that

would not impact cell viability. I used a cytotoxicity assay (Abcam, ab112118) to examine the viability of HeLa cells 48 hours after exposure to different inhibitor doses. For MLN8237, I determined the IC50 dose to be ~41 nM. Because the MLN8237 dose response indicated that cell viability was not altered at doses less than 2.5 nM (6% of IC50) (Figure 4.3A), I performed ~2-fold dilutions from this dose for the following experiments (blue area, Figure 4.3A).

To determine whether the inhibition of Aurora A activity was sufficient to normalize daughter cell size control, I incubated GFP-HMMR-overexpressing tet-on HeLa cells (+dox) with the selected doses of Aurora A inhibitor (AKI), and mitotic cells were followed by time-lapse microscopy. Exposure to either 2.5 nM or 1.0 nM MLN8237 showed a decreasing trend of membrane blebbing events that occurred during anaphase (Figure 4.3B). Importantly, these sub-lethal doses of MLN8237 were also sufficient to rescue daughter cell size control in GFP-HMMR overexpressing tet-on HeLa cells (+dox) (Figure 4.3C). Other work in the Maxwell Lab found that 1 nM MLN8237 significantly reduced the intensity of endogenous active p-Aurora A (Thr288) at metaphase spindle poles in MCF10A cells (personal communication, Dr. Z. He, Maxwell Lab). Thus, low-dose AKI treatment is sufficient to dampen membrane blebbing events and recover control of daughter cell sizes in GFP-HMMR overexpressing tet-on HeLa cells (+dox).

In general, HMMR-overexpression may cause excess Aurora A kinase activity, which leads to frequent membrane blebbing and loss of daughter cell size control. Inhibition of Aurora A activity by low doses of AKIs can correct these phenotypes.

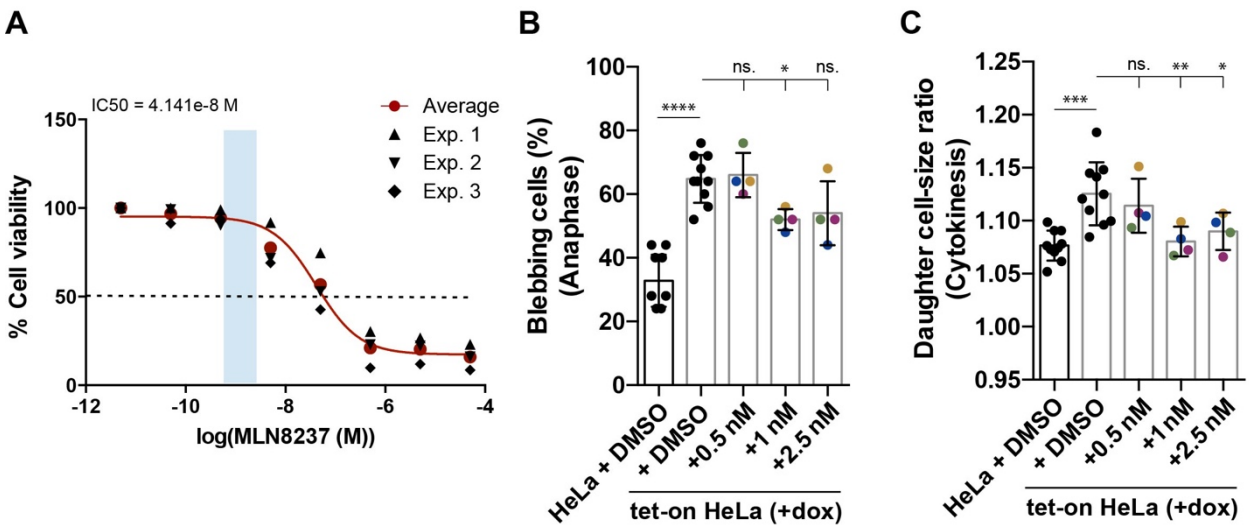

Figure 4.3 Inhibition of Aurora A rescues daughter cell size ratio in GFP-HMMR overexpressing HeLa cells.

A) HeLa cells were incubated with 8 titrated doses of Aurora A inhibitor (MLN8237) including a dimethyl sulfoxide (DMSO) control. Shaded blue area indicates the sub-lethal doses selected for following drug screening (n=3 experiments). Curve fitting used Dose-response – Inhibition, equation: log(inhibitor) vs. response model of Prism 6. Equation used was Y=Bottom value + (Top value –Bottom value)/(1+10^((X-LogIC50))).

B) Anaphase blebbing occurrence in GFP-HMMR-overexpressing tet-on HeLa cells (+dox) treated with Aurora A inhibitor (Mean ± SD, n=4 experiments, colour-coded, ****P<0.0001 (HeLa+DMSO vs. tet-on HeLa+DMSO), P=1.0 (tet-on HeLa+DMSO vs. tet-on HeLa+0.5 nM), *P=0.035 (tet-on HeLa+DMSO vs. tet-on HeLa+1 nM), P=0.095 (tet-on HeLa+DMSO vs. tet-on HeLa+2.5 nM), one-way ANOVA with Sidak's multiple comparisons test).

C) Daughter cell size ratio in GFP- HMMR-overexpressing tet-on HeLa cells (+dox) treated with Aurora A inhibitor (Mean ± SD, n=4 experiments, colour-coded, ***P=0.0001, (HeLa+DMSO vs. tet-on HeLa+DMSO), P=0.8678 (tet-on HeLa+DMSO vs. tet-on HeLa+0.5 nM), **P=0.0076 (tet-on HeLa+DMSO vs. tet-on HeLa+1 nM), *P=0.046 (tet-on HeLa+DMSO vs. tet-on HeLa+2.5 nM), one-way ANOVA with Sidak's multiple comparisons test).

4.2.4 Inhibition of Aurora B, PLK1, or CK1α do not significantly alter loss of daughter cell size control due to HMMR overexpression

To address the specificity of the effects I observed with AKI, I performed similar experiments using small-molecule inhibitors directed against PLK1 (BI2536) (Figure 4.4), CK1α (D4476) (Figure 4.5), or Aurora B (AZD1152) (Figure 4.6). I determined the following IC50 doses and sub-lethal effective doses that did not impact viability or cell cycle progression:

	BI2536 (PLK1)	D4476 (CK1α)	AZD1152 (Aurora B)
IC50	2.1 nM	35 μM	7 μM
Doses	0.3 nM, 0.1 nM, 0.05nM	15 μM, 5 μM, 1 μM	10 nM, 5 nM, 0.5 nM *

* The IC50 dose at 48 hours for AZD1152 (Aurora B) was 7 μM. But, the essential need for Aurora B during the metaphase checkpoint resulted in metaphase arrest for cells treated with doses 1000-fold below the IC50 dose.

Next, I treated the cells with the sublethal doses for each inhibitor and utilized live-cell microscopy to track cell division, as described previously. Cells treated with the highest dose of PLK1 (0.3 nM) and CK1α (15 μM) showed a tendency of decreasing in both blebbing frequency and daughter cell size ratio. However, it is worth noting that cells treated with doses above these concentrations did not undergo proper cell division. Overall, neither the frequency of blebbing nor the daughter cell size ratio measured in GFP-HMMR overexpressing tet-on HeLa cells (+dox) were significantly reduced with sublethal inhibition of PLK1 or CK1α (Figures 4.4 to 4.6). Although daughter cell size ratios changed slightly with inhibition of Aurora B, the responses were not dose-dependent; moreover, inhibition of Aurora B did not significantly alter blebbing frequency.

In conclusion, inhibition of Aurora A in a sublethal range, but not other similarly tested mitotic kinase inhibitors, was sufficient to rescue daughter cell size control in cells with GFP-HMMR overexpression.

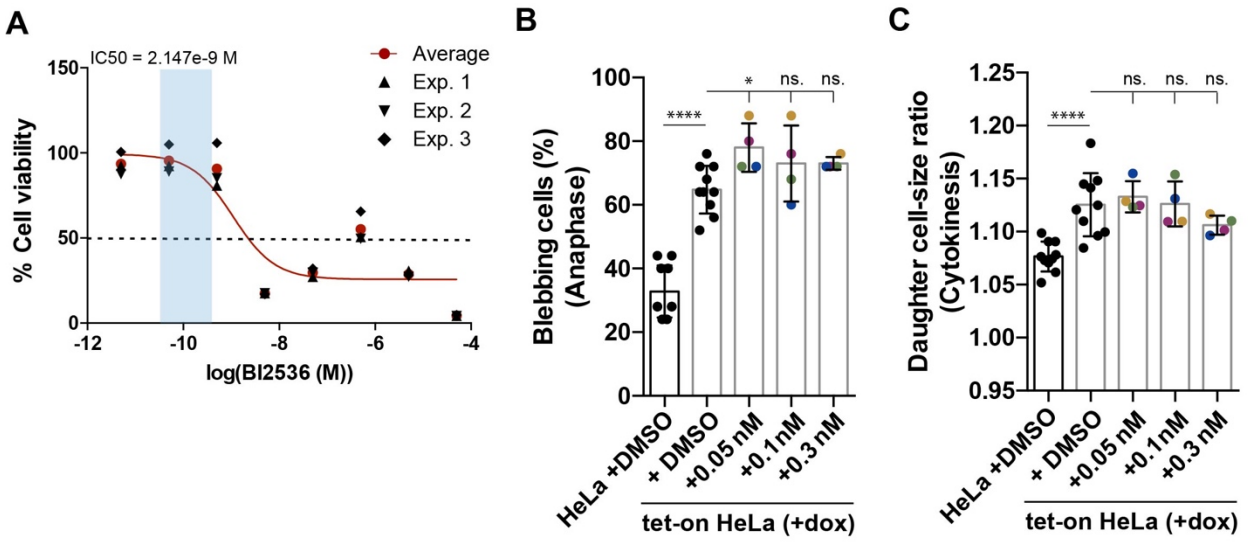

Figure 4.4 Inhibition of PLK1 does not affect daughter cell size ratio in GFP-HMMR-overexpressing HeLa cells.

A) HeLa cells were incubated with 8 titrated doses of PLK1 inhibitor (BI2536) including a DMSO control. Shaded blue area indicates the sub-lethal doses selected for following drug screening (n=3 experiments). Curve fitting used Dose-response – Inhibition, equation: log(inhibitor) vs. response model of Prism 6. Equation used was Y=Bottom value + (Top value –Bottom value)/(1+10^((X-LogIC50))).

B) Anaphase blebbing frequency in GFP-HMMR overexpressing tet-on HeLa cells (+dox) treated with Plk1 inhibitor (Mean ± SD, n=4 experiments, colour-coded, ****P<0.0001, (HeLa+DMSO vs. tet-on HeLa+DMSO), *P=0.037 (tet-on HeLa+DMSO vs. tet-on HeLa+0.05 nM), P=0.33 (tet-on HeLa+DMSO vs. tet-on HeLa+0.1 nM), P=0.33 (tet-on HeLa+DMSO vs. tet-on HeLa+0.3 nM), one-way ANOVA with Sidak's multiple comparisons test).

C) Daughter cell size ratio in GFP-HMMR overexpressing tet-on HeLa cells (+dox) treated with Plk1 inhibitor (Mean ± SD, n=4 experiments, colour-coded, ****P<0.0001 (HeLa+DMSO vs. tet-on HeLa+DMSO), P=0.96 (tet-on HeLa+DMSO vs. tet-on HeLa+0.05 nM), P=1.0 (tet-on HeLa+DMSO vs. tet-on HeLa+0.1 nM), P=0.44 (tet-on HeLa+DMSO vs. tet-on HeLa+0.3 nM), one-way ANOVA with Sidak's multiple comparisons test).

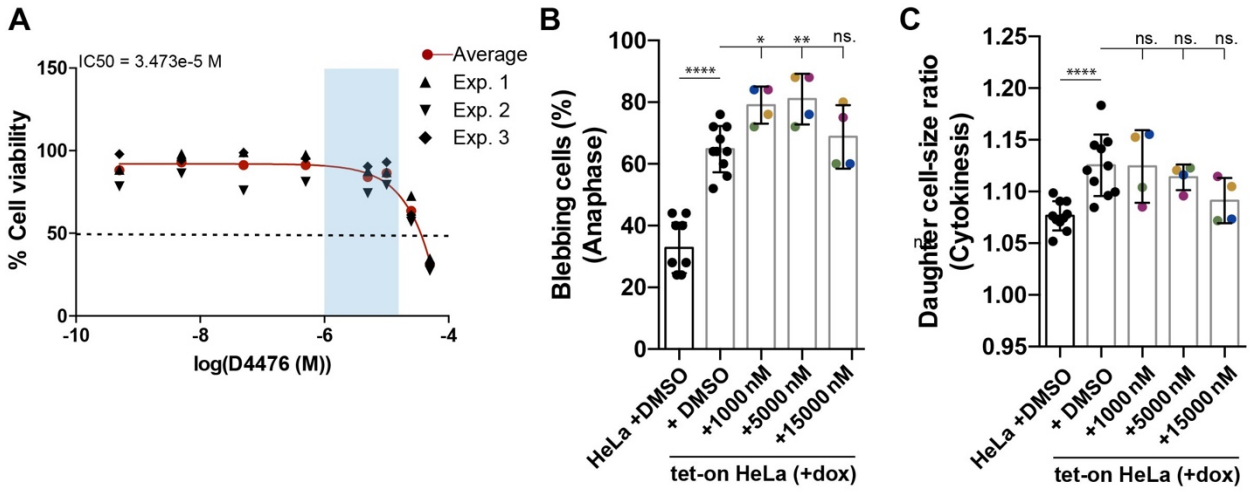

Figure 4.5 Inhibition of CK1α does not affect daughter cell size ratio in GFP-HMMR-overexpressing HeLa cells.

A) HeLa cells were incubated with 8 titrated doses of CK1α inhibitor (D4476) including a DMSO control. Shaded blue area indicates the sub-lethal doses selected for following drug screening (n=3 experiments). Curve fitting used Dose-response – Inhibition, equation: log(inhibitor) vs. response model of Prism 6. Equation used was Y=Bottom value + (Top value –Bottom value)/(1+10^((X-LogIC50))).

B) Anaphase blebbing frequency in GFP-HMMR overexpressing tet-on HeLa cells (+dox) treated with CK1α inhibitor (Mean ± SD, n=4 experiments, colour-coded, ****P<0.0001 (HeLa+DMSO vs. tet-on HeLa+DMSO), *P=0.023 (tet-on HeLa+DMSO vs. tet-on HeLa+1000 nM), **P=0.0081 (tet-on HeLa+DMSO vs. tet-on HeLa+5000 nM), P=0.88 (tet-on HeLa+DMSO vs. tet-on HeLa+15000 nM), one-way ANOVA with Sidak's multiple comparisons test).

C) Daughter cell size ratio in GFP-HMMR overexpressing tet-on HeLa cells (+dox) treated with CK1α inhibitor (Mean ± SD, n=4 experiments, colour-coded, ****P<0.0001 (HeLa+DMSO vs. tet-on HeLa+DMSO), P=1.0 (tet-on HeLa+DMSO vs. tet-on HeLa+1000 nM), P=0.89 (tet-on HeLa+DMSO vs. tet-on HeLa+5000 nM), P=0.086 (tet-on HeLa+DMSO vs. tet-on HeLa+15000 nM), one-way ANOVA with Sidak's multiple comparisons test).

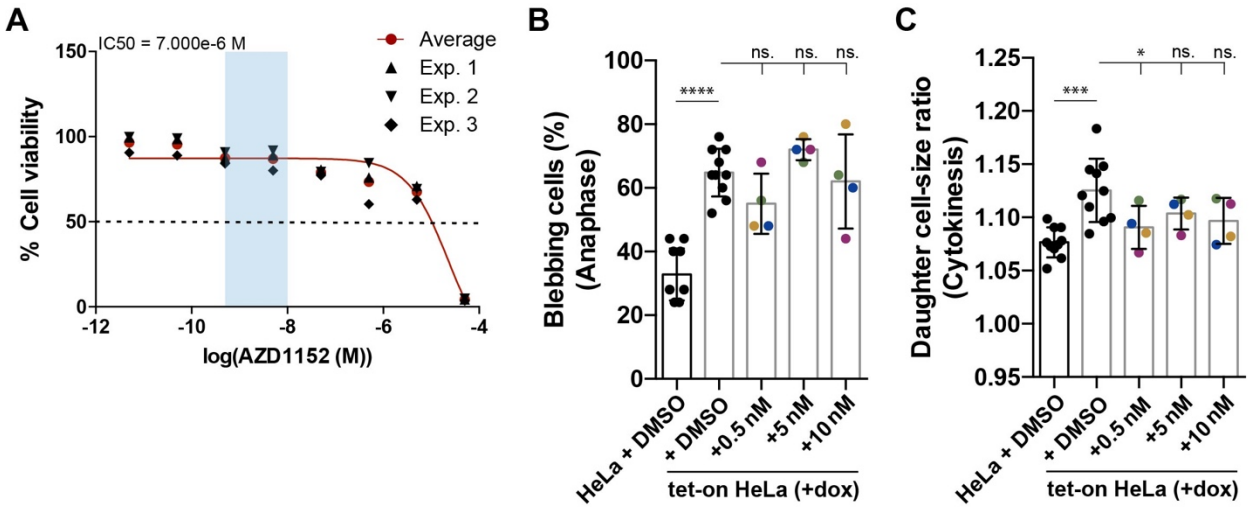

Figure 4.6 Inhibition of Aurora B shows no effect on daughter cell size ratio in GFP-HMMR-overexpressing HeLa cells.

A) HeLa cells were incubated with 8 titrated doses of Aurora B inhibitor (AZD1152) including a DMSO control. Shaded blue area indicates the sub-lethal doses selected for following drug screening (n=3 experiments). Curve fitting used Dose-response – Inhibition, equation: log(inhibitor) vs. response model of Prism 6. Equation used was Y=Bottom value + (Top value –Bottom value)/(1+10^((X-LogIC50))).

B) Anaphase blebbing frequency in GFP-HMMR overexpressing tet-on HeLa cells (+dox) treated with Aurora B inhibitor (Mean ± SD, n=4 experiments, colour-coded, ****P<0.0001 (HeLa+DMSO vs. tet-on HeLa+DMSO), P=0.2482 (tet-on HeLa+DMSO vs. tet-on HeLa+0.5 nM), P=0.5372 (tet-on HeLa+DMSO vs. tet-on HeLa+5 nM), P=0.9725 (tet-on HeLa+DMSO vs. tet-on HeLa+10 nM), one-way ANOVA with Sidak's multiple comparisons test).

C) Daughter cell size ratio in GFP-HMMR overexpressing tet-on HeLa cells (+dox) treated with Aurora B inhibitor (Mean ± SD, n=4 experiments, colour-coded, ***P=0.0001 (HeLa+DMSO vs. tet-on HeLa+DMSO), *P=0.0493 (tet-on HeLa+DMSO vs. tet-on HeLa+0.5 nM), P=0.3633 (tet-on HeLa+DMSO vs. tet-on HeLa+5 nM), P=0.1373 (tet-on HeLa+DMSO vs. tet-on HeLa+10 nM), one-way ANOVA with Sidak's multiple comparisons test).

4.2.5 Phosphorylated Aurora A is higher at centrosomes in GFP-HMMR overexpressing cells entering prometaphase

Inhibition of Aurora A at 2% of IC50 dose partially rescued blebbing frequency and daughter cell-size ratio in GFP-HMMR overexpressing tet-on HeLa cells (+dox). Moreover, HMMR activates TPX2-Aurora A complexes at the spindle (Groen *et al.*, 2004; Chen *et al.*, 2014; Scrofani *et al.*, 2015). During cell division, HMMR localizes and stabilizes TPX2 to the sites of microtubule assembly (Chen *et al.*, 2014). TPX2 is a co-factor of Aurora A which is required for optimal Aurora A kinase activity (Bayliss *et al.*, 2003; Dodson and Bayliss, 2012). Therefore, I hypothesized that active Aurora A may be elevated at mitotic centrosomes in GFP-HMMR overexpressing tet-on HeLa cells (+dox).

I performed immunofluorescence analysis of phosphorylated Aurora A over different phases of mitosis (Figure 4.7A) using confocal microscopy to acquire images at 0.5 μm stacks with total of 5 slices and measuring maximum intensity projections. My analysis revealed the level of phosphorylated Aurora A at centrosomes was higher in GFP-HMMR overexpressing tet-on HeLa cells (+dox). During prometaphase and metaphase (Figure 4.7B) which coincides with the aberrant accumulation of ARP2/3 complex at spindle poles examined in section 3.2.12. Therefore, it is plausible that GFP-HMMR overexpression mediated hyperactivity of Aurora A mis-localizes ARP2/3 complex during prometaphase, affecting subsequent localization of the ARP2/3 complex, leading to changes in cortical stability.

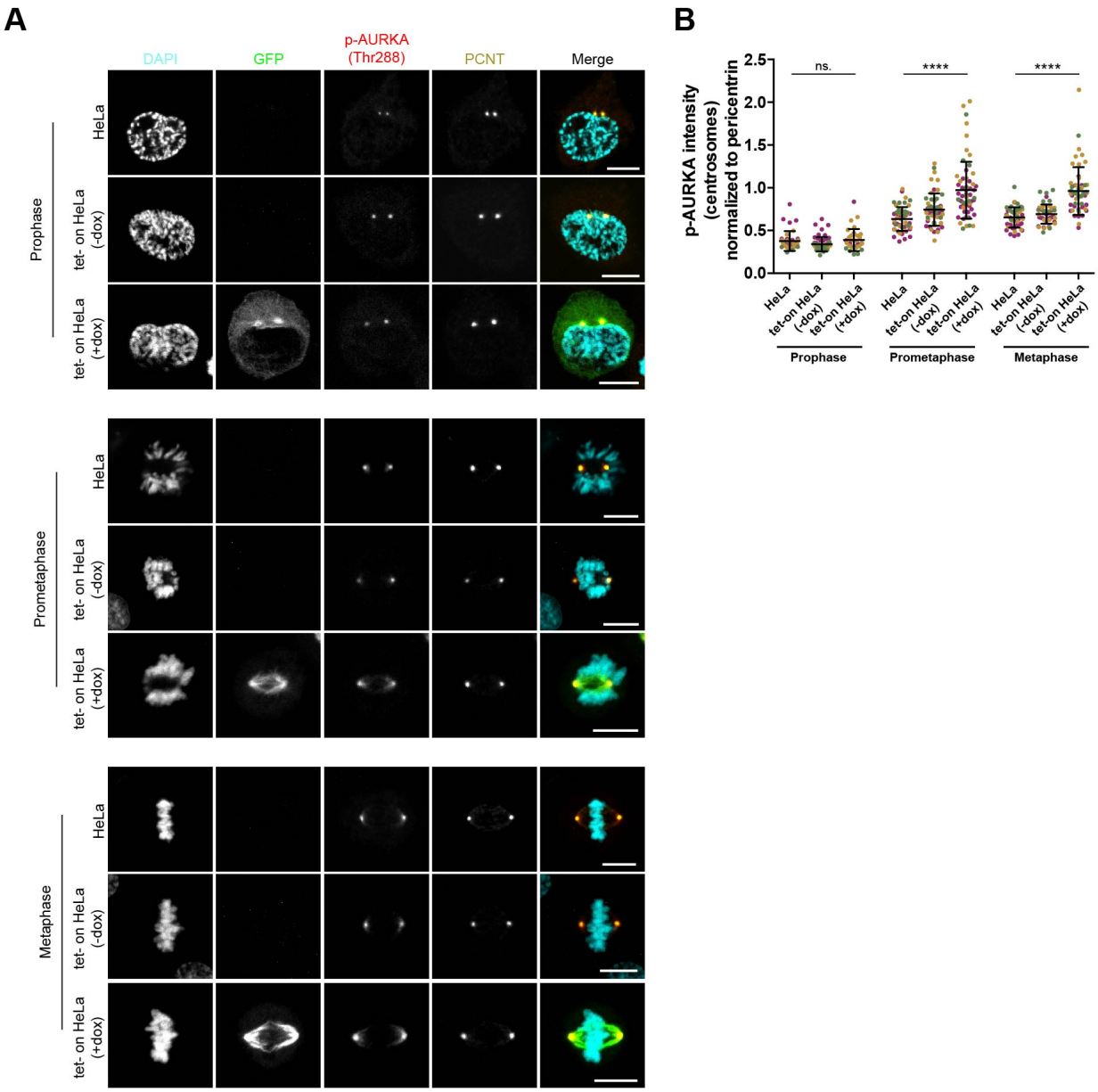

Figure 4.7 Phosphorylated Aurora A level at centrosomes is higher during prometaphase in GFP-HMMR overexpressing HeLa cells.

A) Immunofluorescence analysis p-Aurora A (T288) in parental HeLa cells, tet-on HeLa cells (-dox) and tet-on HeLa cells (+dox) at prophase, prometaphase, and metaphase. Centrosomes were marked by anti-pericentrin antibody. Scale bar = 10 µm**.**

B) Level of phosphorylated Aurora A at centrosomes during different mitotic phases. Centrosomes were marked by anti-pericentrin antibody (Mean ± SD, Prophase: n= 37 (HeLa), 54 (-dox), 33 (+dox) cells, P=0.0870; Prometaphase: n= 55 (HeLa), 54 (-dox), 62 (+dox) cells, ****P<0.0001; Metaphase: n= 55 (HeLa), 54 (-dox), 51 (+dox) cells, ****P<0.0001, one-way ANOVA).

Next, I also used immunofluorescence analysis to confirm the inhibitory effect of 1 nM MLN8237 during prometaphase and anaphase. I examined these stages as the ARP2/3 complex abnormally accumulates at spindle poles during prometaphase and asymmetric membrane blebbing occurs during anaphase. I treated parental HeLa and GFP-HMMR overexpressing tet-on HeLa cells (+dox) with DMSO or 1.0 nM MLN8237 for two hours before fixation for immunofluorescence analysis (Figure 4.8). My measurement of fluorescence intensity indicated that the levels of phosphorylated Aurora A at centrosomes was reduced with 1 nM MLN8237 treatment in both prometaphase and anaphase by about 40%.

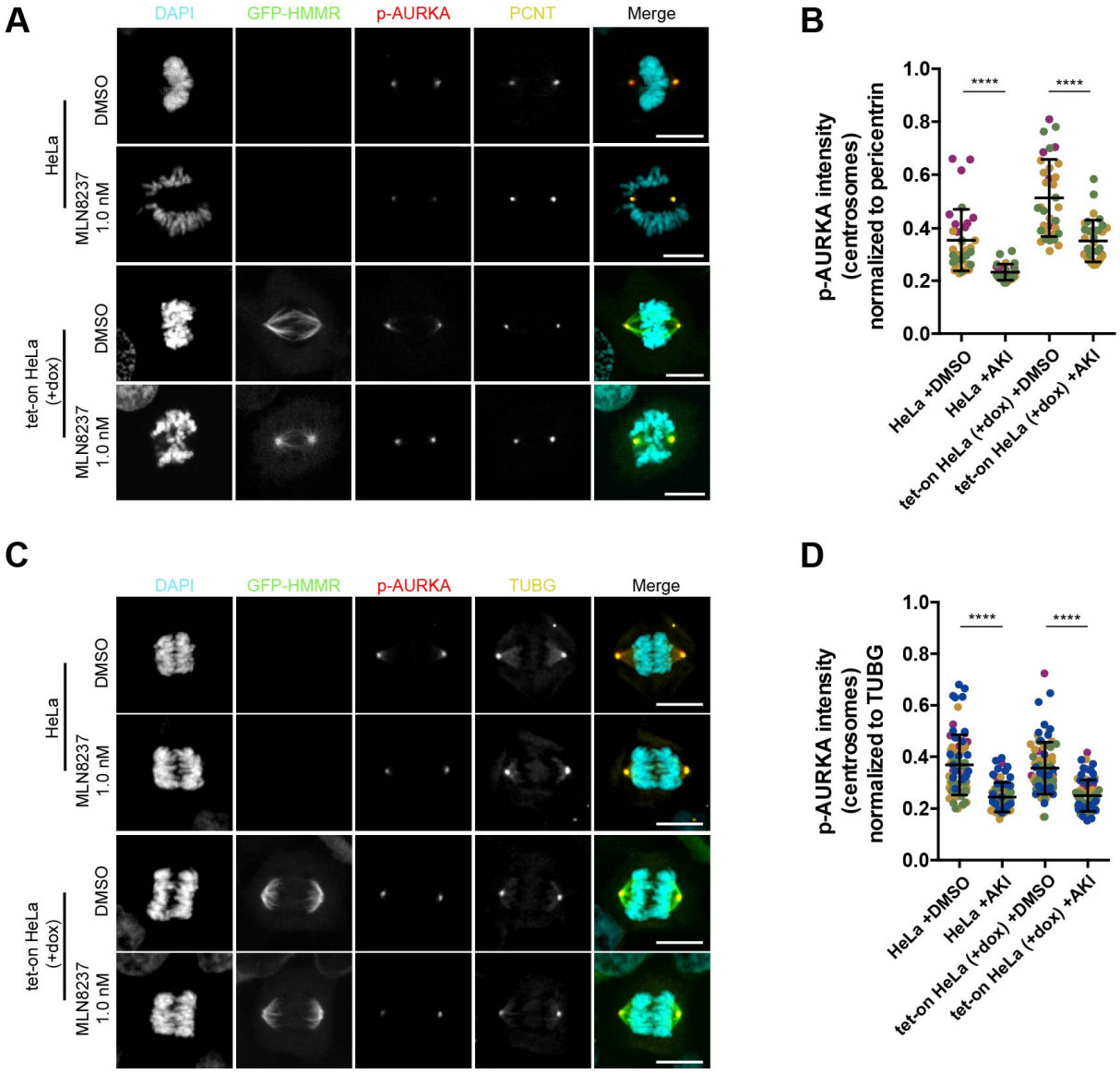

Figure 4.8 Treatment of 1 nM AKI decreases the level of p-Aurora A level at centrosomes.

A) Immunofluorescence analysis of phosphorylated Aurora A in prometaphase parental HeLa cells and tet-on HeLa cells (+dox) treated with DMSO or 1 nM MLN8237 for 2 hours prior to fixation. Centrosomes were marked by anti-pericentrin antibody. Scale bar = 10 μm**.**

B) Level of phosphorylated Aurora A at centrosomes during prometaphase. Centrosomes were marked by anti-pericentrin antibody (Mean ± SD, n= 33 (HeLa+DMSO), 28 (HeLa+AKI), 34 (+dox+DMSO), 34 (+dox+AKI) cells, ****P<0.0001, paired t-test).

C) Immunofluorescence analysis of phosphorylated Aurora A in anaphase parental HeLa cells and tet-on HeLa cells (+dox) treated with DMSO or 1 nM MLN8237 for 2 hours prior to fixation. Centrosomes were marked by anti-γ-tubulin antibody. Scale bar = 10 μm**.**

D) Level of phosphorylated Aurora A at centrosomes during anaphase. Centrosomes were marked by anti-γ-tubulin antibody (Mean ± SD, n=69 cells per group, ****P<0.0001, paired t-test).

4.2.6 Aurora A inhibition is not sufficient to rescue spindle position

Aurora A regulates spindle position and orientation through TPX2 and NuMA (Gallini et al., 2016; Polverino et al., 2021). While asymmetric membrane elongation is a mechanism in cells to correct spindle position during anaphase, that reduced anaphase blebbing and partial rescue of daughter cell-size ratio in AKI treated cells might be a result of corrected spindle position instead of effects on cortical stability. To address this question, I analyzed spindle position and orientation in cells treated with 1.0 nM AKI from movies collected by live-cell imaging microscope. For spindle position, I examined the spindle position as indicated in Figure 4.9A using the frame immediate before anaphase whereas for spindle orientation, I calculated the angle resulting from the difference of spindle orientation as cells entered metaphase and immediate before anaphase (Figure 4.9B). The analysis shows that there was no significant difference in terms of spindle position but might have an effect on spindle orientation in GFP-HMMR overexpressing group (Figure 4.9C). Since asymmetric membrane elongation occurs in response to off-centered spindle and spindle position was not affected by AKI treatment, the rescued blebbing and daughter cell-size was not a result of corrected spindle position.

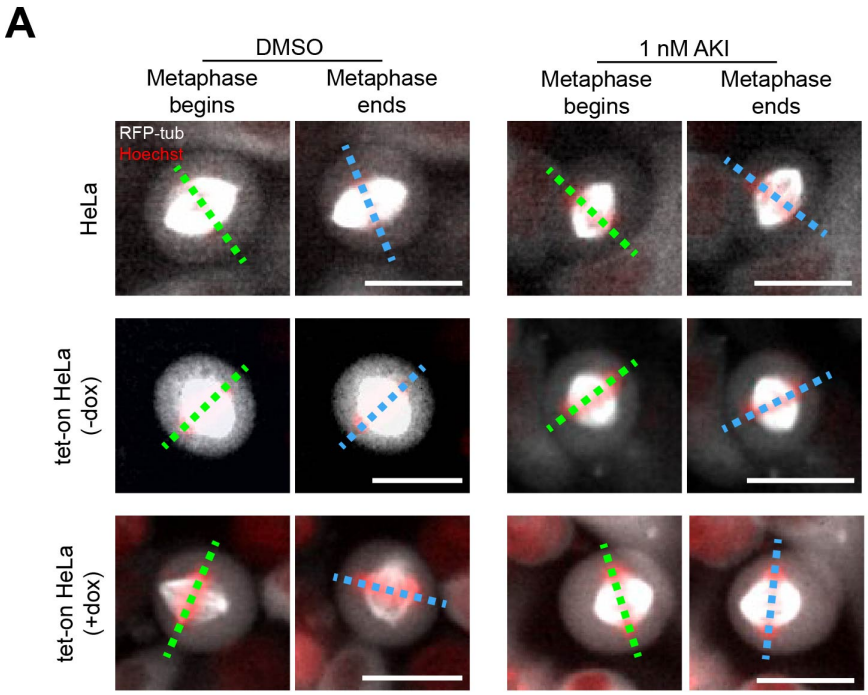
A
DMSO
1 nM AKI
Metaphase begins
Metaphase ends
Metaphase begins
Metaphase ends
RFP-tub
Hoechst
HeLa
tet-on HeLa (-dox)
tet-on HeLa (+dox)

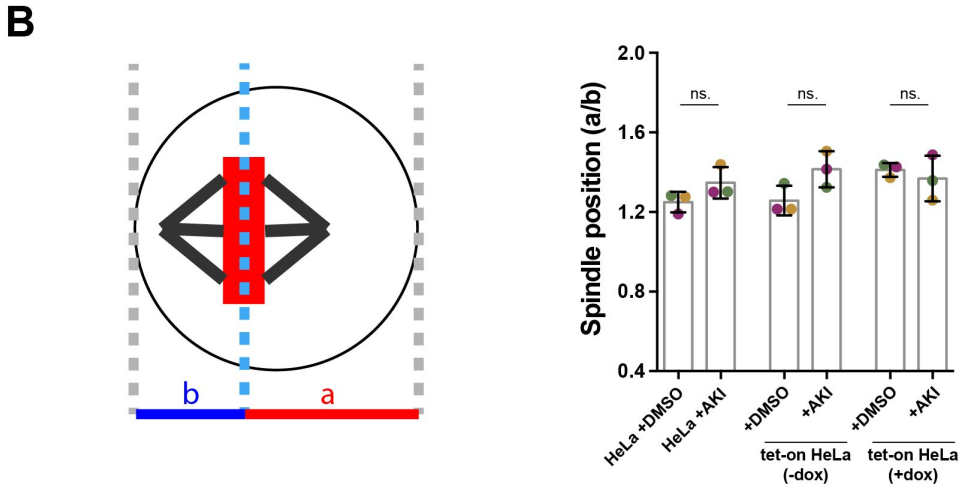
B
b
a
Spindle position (a/b)
2.0
1.6
1.2
0.8
0.4
ns.
ns.
ns.
HeLa +DMSO
HeLa +AKI
+DMSO
+AKI
+DMSO
+AKI
tet-on HeLa (-dox)
tet-on HeLa (+dox)

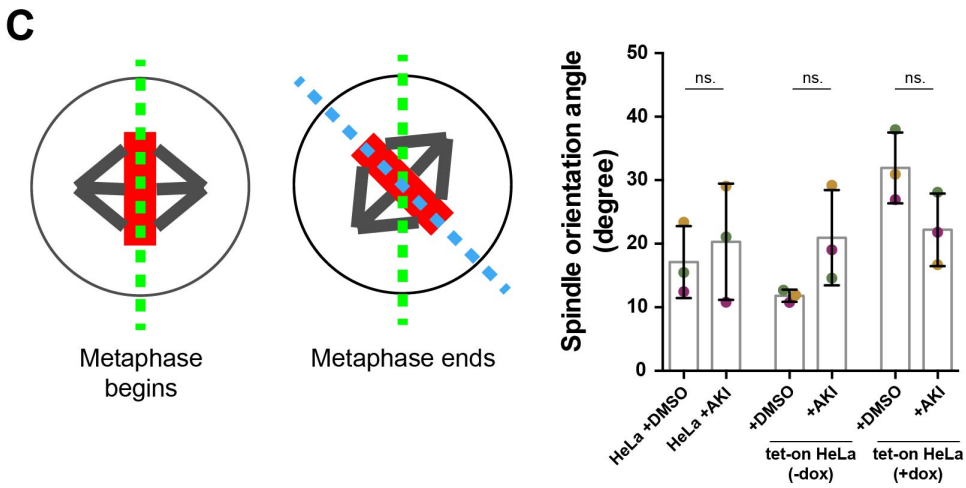
C
Metaphase begins
Metaphase ends
Spindle orientation angle (degree)
50
40
30
20
10
0
ns.
ns.
ns.
HeLa +DMSO
HeLa +AKI
+DMSO
+AKI
+DMSO
+AKI
tet-on HeLa (-dox)
tet-on HeLa (+dox)

Figure 4.9 Low-dose inhibition of Aurora A does not affect spindle position of GFP-HMMR overexpressing cells.

A) Live-cell images of HeLa, tet-on HeLa (-dox), tet-on HeLa (+dox) expressing RFP-tubulin. Scale bar = 10 μm**.** Metaphase plate in the beginning frame is highlighted with green dash line and in the end frame is highlighted with blue dash line.

B) A cartoon presenting how spindle position was quantified (Left). Quantitative analysis of spindle position of HeLa, tet-on HeLa (-dox), tet-on HeLa (+dox) treated with DMSO or 1 nM AKI before cells entering anaphase (Mean ± SD, n= 3 experiments, colour-coded, DMSO vs. AKI, P=0.14 (HeLa), P=0.23 (tet-on HeLa (-dox)), P=0.65 (tet-on HeLa (+dox)), paired t-test).

C) A cartoon presenting how spindle orientation was quantified (Left). Quantitative analysis of spindle orientation of HeLa, tet-on HeLa (-dox), tet-on HeLa (+dox) treated with DMSO or 1 nM AKI (Mean ± SD, n= 3 experiments, colour-coded, DMSO vs. AKI, P=0.32 (HeLa), P=0.18 (tet-on HeLa (-dox)), P=0.066 (tet-on HeLa (+dox)), paired t-test).

4.2.7 Inhibition of Aurora A activity regulates cortical localization of ARP2/3 complex in GFP-HMMR overexpressing cells

I found augmented frequency of anaphase blebbing (Figure 3.3), loss of daughter cell-size control (Figure 3.4), with concurrent ARPC2 spindle accumulation and attenuated cortical retention (Figure 3.13), in GFP-HMMR overexpressing tet-on HeLa cells. Because low-dose inhibition of Aurora A reduced membrane blebbing in anaphase and recovered daughter cell size ratios (Figure 4.3), I next examined the effect of AKI on the cortical localization of ARPC2 in cells overexpressing GFP-HMMR. I treated these cells with 1 nM AKI for 2 hours and visualized ARPC2 subcellular localization using confocal microscopy (Figure 4.10). Treatment with a low dose of AKI in parental HeLa cells did not significantly alter the localization of ARPC2 (Figure 4.10B,C), suggesting that Aurora A may not be necessary for this localization. In GFP-HMMR overexpressing tet-on HeLa cells (+dox), however, inhibition of Aurora A slightly increased the cortical localization of ARPC2 and significantly reduced the abnormal spindle pole localization (Figure 4.10C). These observations suggest that, in the context of hyperactive Aurora A activity induced via GFP-HMMR overexpression, low dose AKI treatment is sufficient to dampen ectopic localization of ARPC2 to the spindle. This change in localization of ARP2/3 complexes may block the induction of abnormal membrane blebbing phenotypes observed in GFP-HMMR overexpressing tet-on HeLa cells (+dox).

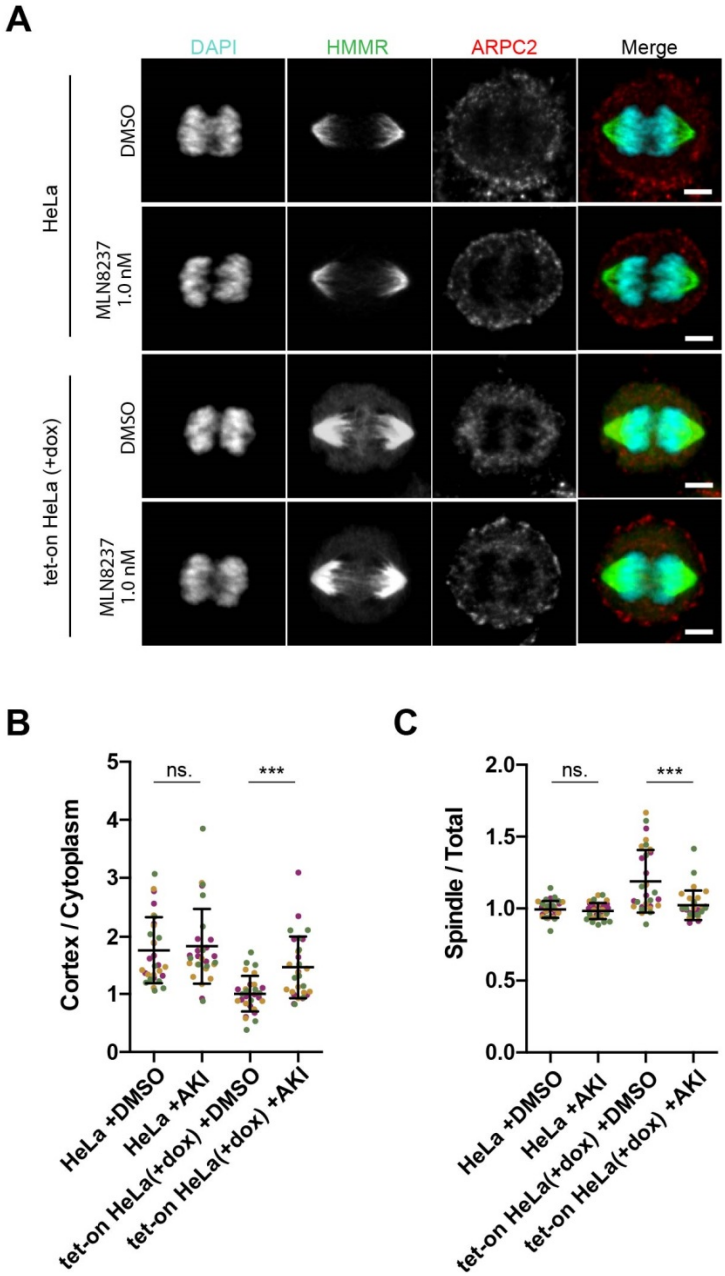

Figure 4.10 Reduction of Aurora A activity partially restores ARP2/3 cortical retention in GFP-HMMR-overexpressing cells.

A) Immunofluorescence analysis of HMMR (Green) and ARPC2 (Red) in GFP-HMMR overexpressing tet-on HeLa cells treated with 1 nM Aurora A inhibitor (MLN8237). Scale bar=5 µm.

B) Cortical enrichment of ARP2/3 complexes in cells treated with 1.0 nM AKI (Mean ± SD, n=30 cells per group, P=0.63 (HeLa), ***P=0.0004 (tet-on HeLa (+dox), paired t-test).

C) Spindle enrichment of ARP2/3 complexes in cells treated with 1.0 nM AKI. Ratio was calculated using mean intensity (Integrated Intensity/Area) (Mean ± SD n=30 cells per group, P=0.5364 (HeLa), ***P=0.0007 (tet-on HeLa (+dox), paired t-test).

4.2.8 The level of active Aurora A at centrosomes is higher in Aurora A overexpressing HeLa cells

My prior results suggested that hyperactive Aurora A activity, induced via GFP-HMMR overexpression, augments the ARP2/3 complexes at the spindle. I also observed lower abundance of the ARP2/3 complexes at the cortex and induced abnormal membrane blebbing phenotypes in GFP-HMMR overexpressing tet-on HeLa cells (+dox). To investigate whether the elevated expression of Aurora A alone is sufficient to engender similar phenotypes, I transduced HeLa cells with a lentivirus plasmid expressing GFP-AURKA or GFP as a control. Once I generated these cells, I first measured the level of Aurora kinase expression in prometaphase, metaphase and anaphase cells (Figure 4.11). Using immunofluorescence analysis, I detected increasing levels of Aurora A at the centrosome and throughout the cell as GFP-expressing cells progressed from prometaphase through anaphase (Figure 4.11B,C). The intensity of Aurora A was significantly elevated in all phases of mitosis for cells expressing GFP-AURKA (Figure 4.11B,C).

I next measured the intensity of p-Aurora A (Thr288) using immunofluorescence analysis. Similarly, the intensity of p-Aurora A (Thr288) increased from prometaphase to metaphase, but decreased in anaphase, in GFP-transduced cells (Figure 4.12). I observed an increased intensity of p-Aurora A (Thr288) at centrosomes in GFP-AURKA expressing cells (Figure 4.12B). However, the total abundance of p-Aurora A (Thr288) did not change (Figure 4.12C).

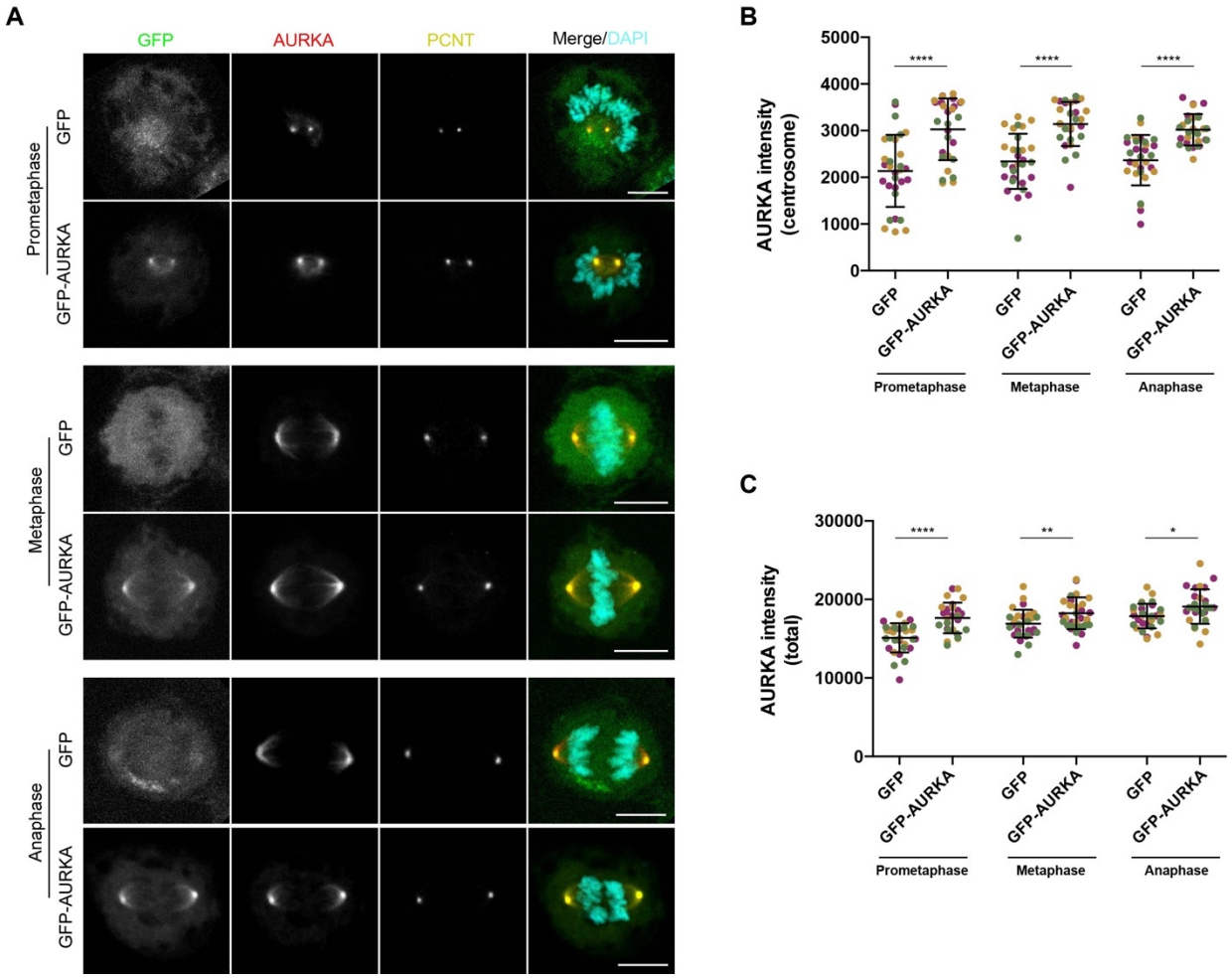

Figure 4.11 Aurora A level at centrosomes in GFP-AURKA overexpressing HeLa cells.

A) Immunofluorescence analysis of Aurora A and pericentrin in HeLa cells expressing GFP or GFP-AURKA at different mitotic phases. Scale bar=10 µm.

B) Quantitative analysis of Aurora A level at centrosomes in GFP or GFP-AURKA expressing HeLa cells at different mitotic phases (Mean ± SD, Prometaphase: n= 30 (GFP), 28 (GFP-AURKA) cells; Metaphase: n= 30 (GFP), 30 (GFP-AURKA) cells; Anaphase: n= 30 (GFP), 28 (GFP-AURKA) cells, ****P<0.0001, unpaired t-test).

C) Quantitative analysis of total Aurora A levels in GFP or GFP-AURKA expressing HeLa cells at different mitotic phases (Mean ± SD, Prometaphase: n= 30 (GFP), 28 (GFP-AURKA) cells, ****P<0.0001; Metaphase: n= 30 (GFP), 30 (GFP-AURKA) cells, **P=0.0002; Anaphase: n= 30 (GFP), 28 (GFP-AURKA) cells, *P=0.0174, unpaired t-test).

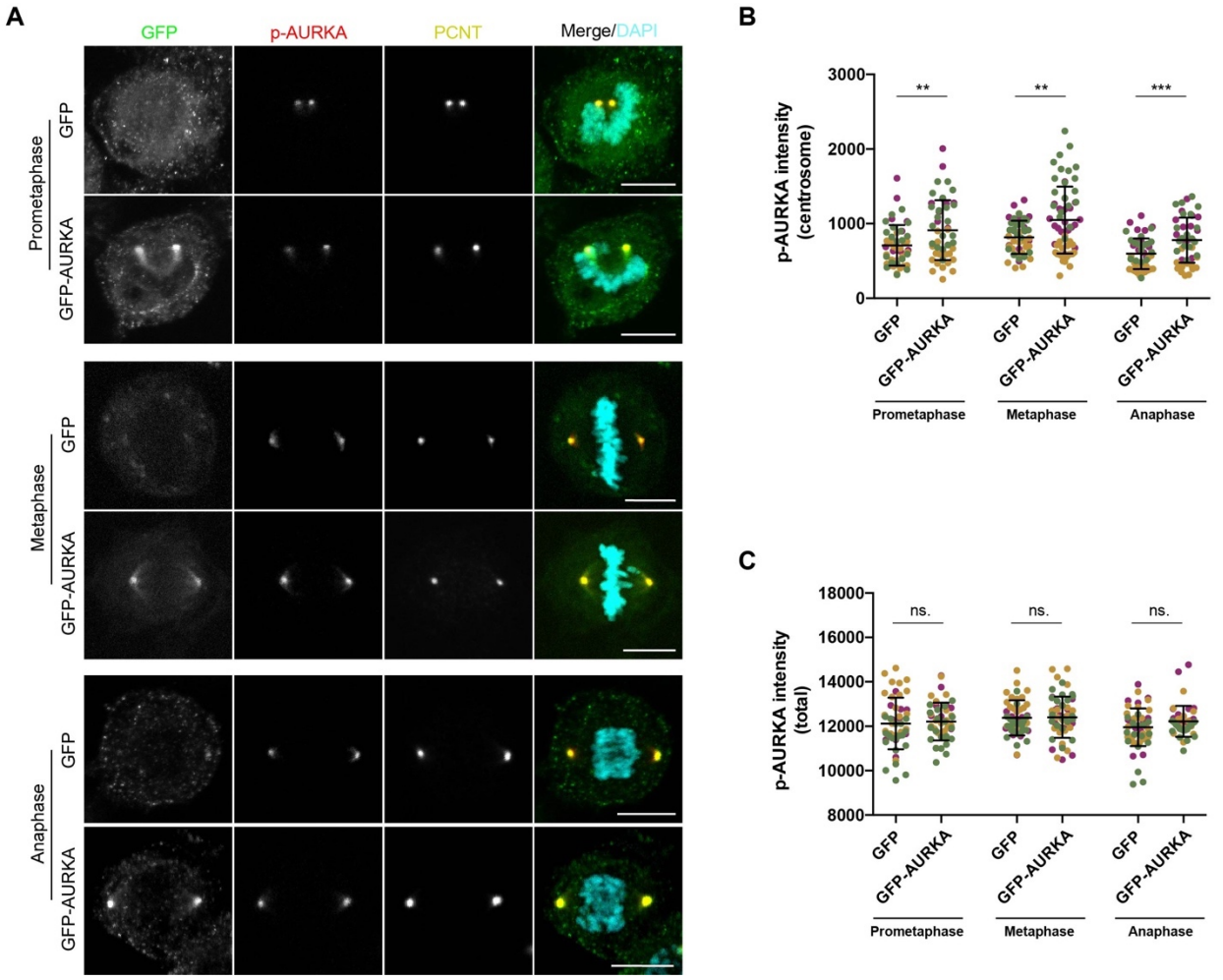

Figure 4.12 Phosphorylated Aurora A is higher at centrosomes in GFP-AURKA overexpressing HeLa cells.

A) Immunofluorescence analysis of p-Aurora A (Thr288) and pericentrin in HeLa cells expressing GFP and GFP-AURKA at different mitotic phases. Scale bar=10 µm.

B) Quantitative analysis of p-AURKA at centrosomes in GFP and GFP-AURKA expressing HeLa cells at different mitotic phases (Mean ± SD, Prometaphase: n=50 (GFP), 49 (GFP-AURKA) cells, **P=0.0041; Metaphase: n=48 (GFP), 60 (GFP-AURKA) cells, **P=0.0013; Anaphase: n=49 (GFP), 35 (GFP-AURKA) cells, ***P=0.0008, unpaired t-test).

C) Quantitative analysis of total p-AURKA in GFP and GFP-AURKA expressing HeLa cells at different mitotic phases (Mean ± SD, Prometaphase: n=50 (GFP), 49 (GFP-AURKA) cells, P=0.66; Metaphase: n=48 (GFP), 60 (GFP-AURKA) cells, P=0.86; Anaphase: n=49 (GFP), 35 (GFP-AURKA) cells, P=0.097, unpaired t-test).

4.2.9 Aurora A overexpression has a limited impact on APRC2 localization

After determining the levels of Aurora A and p-Aurora A at centrosomes in GFP-AURKA expressing cells, I examined ARPC2 localization from prometaphase to anaphase by immunofluorescence (Figure 4.13A). I quantified the cortical localization and spindle enrichment of ARPC2, as described in previous sections. I measured an increased spindle enrichment and reduced cortical intensity for ARPC2 in GFP-AURKA overexpressing cells (Figure 4.13B,C). However, the decreased cortical ARPC2 level was not as pronounced as that observed in GFP-HMMR overexpressing cells; similarly, the increase of p-Aurora A level at centrosomes was not as distinct as those in GFP-HMMR overexpressing cells (section 4.2.8).

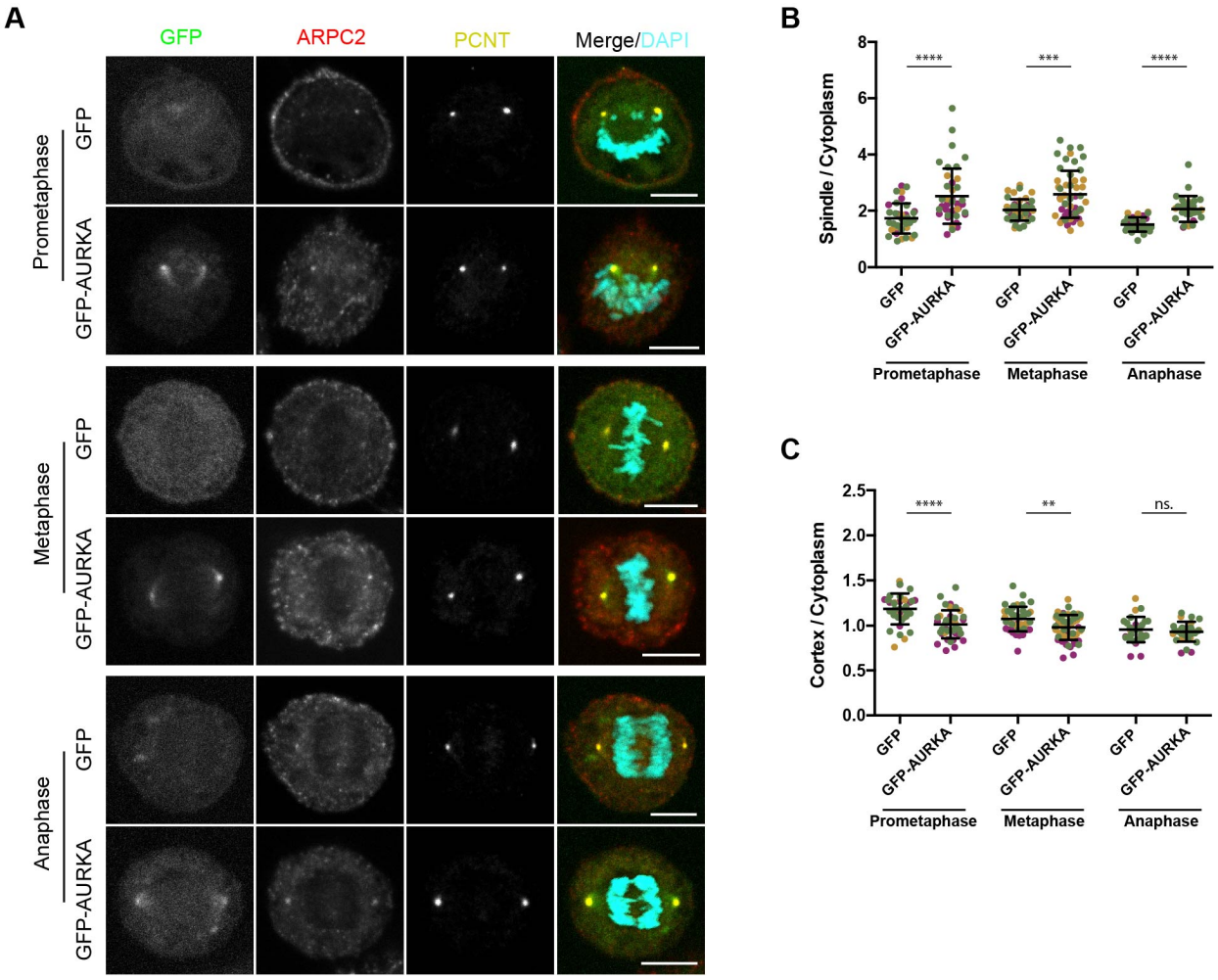

Figure 4.13 GFP-AURKA expressing cells presented potential cortical ARPC2 loss.

A) Immunofluorescence analysis of HeLa cells expressing GFP and GFP-AURKA probing ARPC2 and pericentrin at difference mitotic phases. Scale bar=10 µm.

B) Quantitative analysis of ARP2/3 complex spindle enrichment (Mean ± SD, Prometaphase: n=35 (GFP), 39 (GFP-AURKA) cells, ****P<0.0001; Metaphase: n=42 (GFP), 53 (GFP-AURKA) cells, ***P=0.0001; Anaphase: n=29 (GFP), 28 (GFP-AURKA) cells, ****P<0.0001, unpaired t-test).

C) Quantitative analysis of ARP2/3 complex cortical localization (Mean ± SD, Prometaphase: n=35 (GFP), 39 (GFP-AURKA) cells, ****P<0.0001; Metaphase: n=42 (GFP), 53 (GFP-AURKA) cells, **P=0.0012; Anaphase: n=29 (GFP), 28 (GFP-AURKA) cells, P=0.48, unpaired t-test).

4.2.10 Aurora A overexpression increases blebbing frequency and induces an unequal daughter cell-size

I next examined the effect of Aurora A overexpression on the frequency of membrane blebbing and daughter cell-size control. To approach this question, I followed GFP-AURKA and GFP expressing cells using live-cell imaging as described in section 3.2.2 and 3.2.3. In general, cells expressing GFP-AURKA showed a similar trend as those expressing GFP-HMMR, including a higher frequency of blebbing with larger bleb sizes and loss of daughter cell-size control (Figure 4.14A-C). However, the difference between GFP-AURKA overexpression and control was modest compared to the results in GFP-HMMR overexpressing cells. For example, it is worth noting the anaphase bleb size in GFP-AURKA expressing cells (~1.6% of cell size) was less pronounced than those in GFP-HMMR overexpressing cells (~10% of cell size) (Figure 4.14D). The more modest phenotypes that I observed in GFP-AURKA expressing cells correlates with the more limited increase in p-Aurora A intensity in GFP-AURKA expressing cells than in GFP-HMMR overexpressing cells.

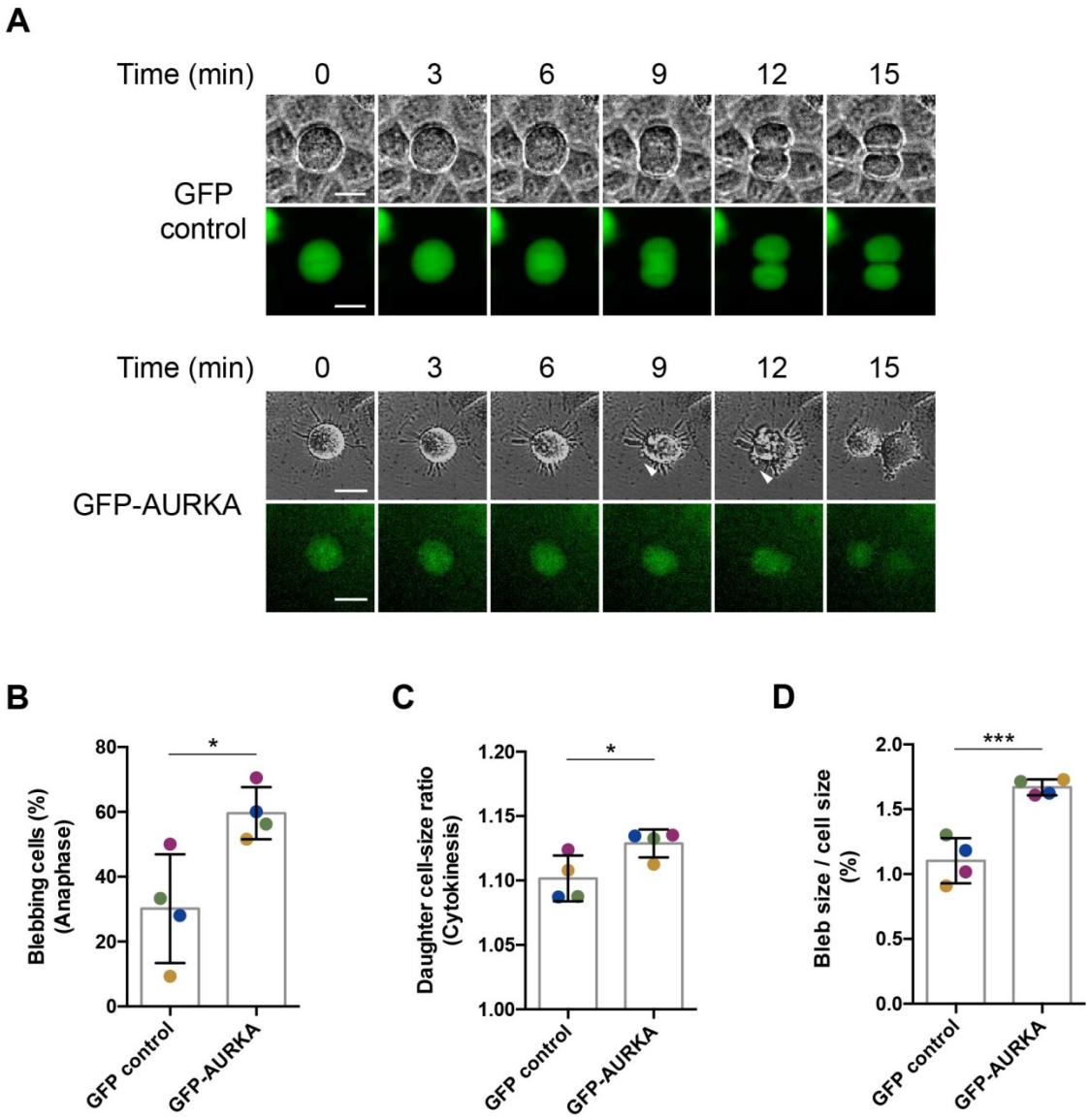

Figure 4.14 GFP-AURKA overexpressing HeLa cells showed similar trend in blebbing and daughter cell-size as in GFP-HMMR overexpressing cells.

A) Living cell images of mitotic HeLa cells transduced with lentivirus plasmid expressing GFP or GFP-AURKA followed by time-lapse microscopy. Images were taken at 3 minutes/ frame. Membrane blebs are highlighted with white arrowheads (Green channel = GFP; Grey channel = Transmitted light 50%). Scale bar=20 µm.

B) Quantification of anaphase membrane blebbing events in GFP-AURKA overexpressing HeLa cells (Mean ± SD, n=4 experiments, colour-coded, *P= 0.019, unpaired t-test).

C) Quantification of daughter cell ratio in GFP-AURKA overexpressing HeLa cells. (Mean ± SD, n=4 experiments, colour-coded, *P= 0.043, unpaired t-test).

D) Quantitation of bleb size in GFP-AURKA overexpressing HeLa cells (Mean ± SD, n=4 experiments, colour-coded, ***P= 0.0009, unpaired t-test).

I next analyzed spindle position and orientation between GFP-AURKA and GFP expressing cells as described in section 4.2.6 (Figure 4.15A). Similar to GFP-HMMR overexpressing HeLa cells, GFP-AURKA expressing cells also showed consistent level of off-centred spindle and spindle mis-orientation (Figure 4.15B,C). This result suggests that the increase in the level of p-AURKA at centrosomes (Figure 4.12B) was associated with spindle mis-positioning and mis-orientation.

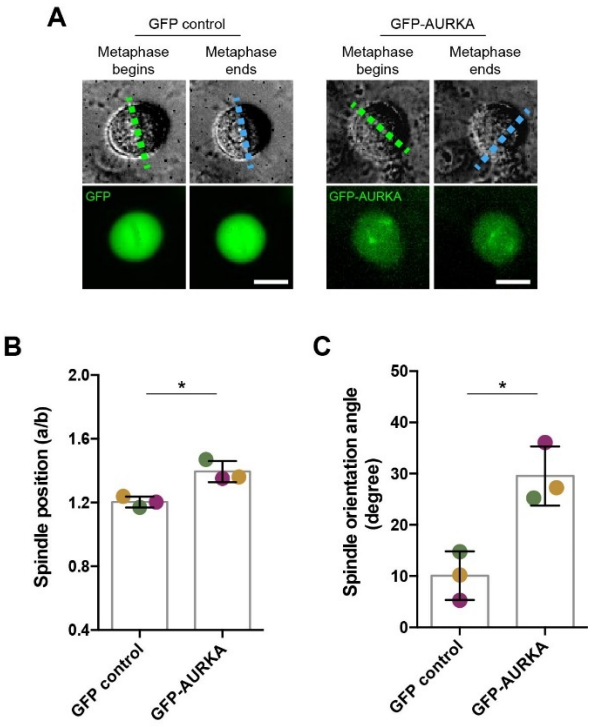

Figure 4.15 GFP-AURKA overexpressing HeLa cells showed off-centre spindle and mis-orientation as in GFP-HMMR overexpressing cells.

A) Live-cell images of GFP-AURKA and GFP expressing HeLa cells. Scale bar = 10 µm**.** Metaphase plate in the beginning frame is highlighted with green dash line and in the end frame is highlighted with blue dash line.

B) Quantitative analysis of spindle position of GFP-AURKA and GFP expressing HeLa cells before cells entering anaphase (Mean ± SD, n= 3 experiments, colour-coded, *P=0.011, unpaired t-test).

C) Quantitative analysis of spindle orientation of GFP-AURKA and GFP expressing HeLa cells (Mean ± SD, n= 3 experiments, colour-coded, *P=0.011, unpaired t-test).

4.3 Key findings

1. Cortical EB1 density is not increased in GFP-HMMR overexpressing cells suggesting premature polar relaxation is not the cause for ARPC2 mis-localization.
2. Phosphorylated Aurora A (Thr288) is augmented in GFP-HMMR overexpressing cells, and inhibition of Aurora A partially rescues the localization of ARPC2, reduces membrane blebbing frequency, and improves daughter cell size control.
3. Overexpression of GFP-AURKA partially, but not completely, recapitulates the alterations in ARPC2 localization, blebbing, and daughter cell-size related phenotypes observed in GFP-HMMR overexpressing cells.

4.4 Discussion

In Chapter 3, I found that HeLa cells expressing GFP-HMMR showed a mis-localization of the ARP2/3 component ARPC2, and pronounced membrane blebbing, which aggravated the daughter cell size ratio. IP-MS revealed a potential interaction between HMMR and ARP2/3 complex, but I was unable to confirm a direct interaction that may explain the observed mis-localization. Here, I investigated potential HMMR-mediated mechanisms that may explain the observed changes to ARP2/3 complex localization and cortical blebbing.

First, I examined the possibility that GFP-HMMR overexpression may induce a premature polar relaxation, which enables successful cytokinesis during cell division (Glotzer, 2004). In this model, astral microtubules reach the polar cortex and aid to reduce tension in the area by removing cortical proteins (Glotzer, 2004; Chapa-Y-Lazo *et al.*, 2020; Chen *et al.*, 2021a). The removed proteins from the cortex are mostly actin-regulating proteins that contribute to cortical stiffness and contractility (Glotzer, 2004; Chapa-Y-Lazo *et al.*, 2020; Chen

et al., 2021a). I hypothesized that overexpression of HMMR may lead to a higher density of astral microtubules and thus induce premature cortical relaxation. However, my analysis of cortical EB1 density indicates a reduced level of astral microtubules in metaphase and anaphase, rather than the predicted higher density. This observation is surprising given that I also found an elevated level of active Aurora A at spindle poles in GFP-HMMR overexpressing cells. I would expect elevated Aurora A activity would promote astral microtubule density and stability. To reconcile these observations, I propose that the reduced levels of astral microtubules are likely related to the dramatic spindle rotation that is also observed in GFP-HMMR overexpressing cells. It is also possible that higher active Aurora A leads to centrosome dysfunction and thus reduced astral microtubule stability. Also, the ARP2/3 complex accumulation at mitotic spindle may contribute to the effect on spindle microtubules. The reduction of astral microtubule stability as well as disrupted actin cell cortex in GFP-HMMR overexpressing cells could result in spindle rotation due to less connection between the spindle and the cortex. That is, the constantly rotating mitotic spindle may be a cause, or consequence, of the dramatic reduction in astral microtubule densities.

The change in ARPC2 localization is not likely a result of increased astral microtubule densities and so I tested a second hypothesis: GFP-HMMR overexpression induces a mitotic kinase mediated mechanism. During cell division, HMMR mainly localizes to the spindle poles, where it recruits multiple proteins, such as TPX2 and CHICA, which regulate the mitotic kinases Aurora A, PLK1 and CK1α (Chen *et al.*, 2014; Connell *et al.*, 2017; Fulcher *et al.*, 2019). These kinases regulate important cell division pathways, especially for spindle orientation and positioning (Chen *et al.*, 2014; Kiyomitsu, 2015; Connell *et al.*, 2017; Fulcher *et al.*, 2019). Thus,

I performed an inhibitor drug screen to determine whether the inhibition of these kinases may reduce the phenotypes I observed in HMMR-overexpressing tet-on HeLa cells.

I found that the inhibition of Aurora A partially restored daughter cell size control and reduced the spindle localization of cortical ARPC2. Although the measurements were not significantly different from DMSO control-treated cells, I found similar trends for the rescue of daughter cell size control when cells were treated with inhibitors against PLK1 or CK1α (section 4.2.4). This is perhaps not surprising given the strong interconnection of these mitotic kinase pathways in the control of mitotic microtubule growth, stability and orientation (Macurek *et al.*, 2008; Chen *et al.*, 2014; Joukov and De Nicolo, 2018; Fulcher *et al.*, 2019; Wellard *et al.*, 2021; He *et al.*, 2022).

We do not yet know how the abnormal activation of Aurora A may dysregulate the localization of the ARP2/3 complex. Aurora A is a serine/threonine kinase (Giet and Prigent, 1999; Kufer *et al.*, 2002) and ARP3 contains 13 putative phosphorylation sites based on discovery proteomics mass spectrometry analysis according to the database of PhosphoSitePlus. Serine and threonine phosphorylation was identified in all components of ARP2/3 complex, including ARP2, ARP3, ARPC11, ARPC1B, ARPC2, ARPC3, ARPC4 and ARPC5, through quantitative phosphoproteomics in mitotic cells (Kettenbach *et al.*, 2013). These phosphorylation events modify the activity of the complex (Pizarro-Cerdá *et al.*, 2017). Moreover, Aurora A interacts with the ARP2/3 complex and with ARPC1B (Mitsushima *et al.*, 2010) and phosphorylates Thr21 of ARPC1B (Molli *et al.*, 2010). Indeed, ARPC1B localizes to the centrosomes and activates Aurora A (Molli *et al.*, 2010). Thus, it is possible that the augmented activation of Aurora A at mitotic centrosomes, via the overexpression of HMMR, leads to the

ectopic localization of ARPC2 through its direct phosphorylation, or that of other components of the ARP2/3 complex.

Although we do not know how Aurora A may modify the localization of ARPC2, other work definitively demonstrates that Aurora A regulates the actin cytoskeleton during mitosis. Centrosome-associated Aurora A inhibits cortical actomyosin in order to promote symmetry breaking in *C. elegans* (Zhao *et al.*, 2019). In *Drosophila*, active Aurora A regulates actin-related processes by phosphorylating Rho-kinase (Berdnik and Knoblich, 2002; Moon and Matsuzaki, 2013). Also, Aurora A interacts with LIM domain kinase 1 (LIMK1) and LIM domain containing protein Ajuba, which facilitate the rearrangement of actin (Hirota *et al.*, 2003; Ritchey *et al.*, 2012). Overexpression of Aurora A also activates cofilin, an actin depolymerizing protein (Wang *et al.*, 2010). Thus, Aurora A may be critical for the regulation of actin cytoskeleton during mitosis.

Here, I demonstrate the overexpression of HMMR can hyperactivate Aurora A at the centrosome, induce the mis-localization of ARPC2, and promote abnormal membrane blebbing; these abnormal processes can be partially phenocopied by overexpression of Aurora A. In metaphase, a large pool of ARP2/3 complex is retained at the cell cortex to promote the round shape of the mitotic cell. My results suggest that as cells enter anaphase and the spindle is displaced from the centre, a gradient of HMMR and Aurora A at the spindle pole proximal to the cell cortex can recruit and phosphorylate components of ARP2/3 complex, which releases them from the cell cortex. This would enable the elongation of the anaphase cell membrane or facilitate asymmetric membrane elongation. Further investigation is needed to give more insights to the pathway.

Caveats – In Chapter 4, all the experiments were conducted in HeLa cells with the same caveats outlined in Chapter 3. Similar to tet-on HeLa cells that express GFP-HMMR, GFP-AURKA expression in HeLa cells was a non-physiological overexpression and the GFP tag may alter function although it did not alter localization. Although not addressed specifically in this thesis, other cell lines or samples with elevated Aurora A expression should be considered for validation.

Another major caveat for my findings is my use of small molecule inhibitors. Although I optimized doses by measuring cytotoxicity (and reducing doses up to 1000-fold) and confirmed target inhibition, target specificity is still a concern. To determine the correct dose of MLN8237, I performed a dose response from 50 μM to 5 pM and determined the IC50 dose to be ~41 nM. I then used 1 nM MLN8237 for my experiments. In another study that used a cell free assay measuring Aurora A Threonine 288 (Thr288) autophosphorylation and Serine10 (Ser10) phosphorylation of histone H3, respectively (Manfredi *et al.*, 2011), the inhibitory concentration for MLN8237 was 1.2 nM against Aurora A activity and 396.5 nM against Aurora B activity. In cell-based assays, the IC50 for Aurora A (IC50 = 6.7 nM) was more than 200-fold lower than for Aurora B (IC50 = 1,534 nM) and no significant effect was observed for 205 other kinases in cell-based assays (Manfredi *et al.*, 2011). Thus, I am confident that my observed effects using 1 nM MLN8237 were specific for the inhibition of Aurora A activity. Also, I should perform immunofluorescence to examine the inhibitory effect of other kinase inhibitors on the target. For the PLK1 inhibitor, BI2536, treatment of 0.1 nM was sufficient to reduce p-PLK1 (Thr210) in MCF10A cells (He *et al.*, 2022). It is important to note that it is challenging to confirm the small molecule inhibition effect by siRNA or shRNA depletion; knockdown of mitotic kinases often

prevents cell division or induces apoptosis (Liu and Erikson, 2003; Zhang *et al.*, 2011; Lu *et al.*, 2014).

Moreover, I used ARPC2 for immunofluorescent analysis to indicate ARP2/3 complex as it was used in another study (Farina *et al.*, 2019). A caveat of probing ARP2/3 complex is that the ARP2/3 complex components are not always regulated together. Thus, repeated experiments probing for other components of ARP2/3 complex can be performed to examine if HMMR overexpression affects the localization of certain ARP2/3 components instead of the entire complex.

Future studies – In Chapter 4, it is interesting that overexpression of GFP-AURKA was not sufficient to significantly elevate total p-Aurora A levels. Yet, p-Aurora A levels at centrosomes were significantly higher in the presence of GFP-HMMR overexpression. During cell division, overexpression of HMMR facilitates TPX2 localization and the phosphorylation of Aurora A (Chen *et al.*, 2014; Scrofani *et al.*, 2015). Consistently, I observed elevated p-Aurora A levels at centrosomes in GFP-HMMR expressing cells. In GFP-AURKA cells, however, I hypothesize that HMMR and TPX2 levels are unchanged, which limits their localization to centrosomes and, as a consequence, restricts p-Aurora A level at centrosomes and total p-Aurora A level. To address this question, I suggest to first examine the level of spindle TPX2 in both GFP-HMMR and GFP-AURKA overexpressing cells to determine if TPX2 level is elevated only in cells with HMMR overexpression. If TPX2 levels at the spindle are elevated in GFP-HMMR overexpressing cells, we can knockdown TPX2 by siRNA to rescue the hyperactive p-AURKA at centrosomes and the daughter cell-size relevant phenotypes.

Significance – In Chapter 4, my research shows that altered expression of HMMR activates Aurora A and inhibition of Aurora A is sufficient to partially reduce membrane blebbing events and rescue the control of daughter cell size. Ectopic expression of GFP-AURKA phenocopies many, but not all, of the phenotypes induced by overexpression of GFP-HMMR and the levels of p-Aurora A at the centrosome appears to be a critical determinant for the localization of the ARP2/3 complex and the ultimate loss of daughter cell size control.

Chapter 5: Overexpression of HMMR affects phenotypes related to daughter cell-size control *ex vivo* and *in vivo*

5.1 Rationale and hypothesis

Regulated cell division, including the control of mitotic spindle orientation and daughter cell size, is critical for tissue homeostasis and development (Cabernard and Doe, 2009; Morin and Bellaïche, 2011; Kiyomitsu, 2015; di Pietro *et al.*, 2016; Hu and Jasper, 2019). In the previous chapters, I investigated phenotypes during cell division in GFP-HMMR overexpressing HeLa cells. HeLa cells are a standard experimental model for the study of cell division, but there are multiple caveats associated with the study of an immortal, polyploid cancer cell line grown on tissue culture plastic. Thus, it is necessary to validate my prior findings in other models for HMMR overexpression.

The *Drosophila* neuroblast is one of the best described *in vivo* models for an asymmetric cell division (Chia *et al.*, 2008; Zhong and Chia, 2008; Chang *et al.*, 2011; Roth *et al.*, 2015). During embryogenesis of *Drosophila*, neuroblasts delaminate from the neuroectoderm and undergo mitosis (Yu *et al.*, 2006). In prophase, the centrosomes separate along the epithelium laterally followed by a 90° spindle rotation in metaphase, aligning the apical-basal axis (Yu *et al.*, 2006). During cytokinesis, a neuroblast divides into two daughter cells with different sizes and cell fate determinants, such as Miranda (Mira), which facilitates asymmetric localization of cell-fate regulating key proteins and mRNAs (Yu *et al.*, 2006; Chang *et al.*, 2011). The larger daughter cell remains a neuroblast and continues dividing whereas the smaller ganglion mother cell (GMC) divides to produce two neurons or glia (Yu *et al.*, 2006).

HMMR shares structural and sequence similarities with Miranda (Chang *et al.*, 2011; He *et al.*, 2020). Interestingly, Miranda is only encoded in the order Diptera while *Hmmr* is encoded

in all other insect orders and in vertebrates (He *et al.*, 2020). During cell division, Miranda mostly localizes to the cortical area, although Miranda also localizes to the centrosomes (Schuldt *et al.*, 1998; Mollinari *et al.*, 2002; Atwood and Prehoda, 2009). However, it has not yet been examined if HMMR and Miranda have orthologous functions during asymmetric cell division. We speculated that *Drosophila* neuroblasts, which have a null background for *Hmmr*, may present an interesting opportunity to examine HMMR overexpression in a genetically tractable and easily manipulated model system.

Transgenic mouse models are an excellent mammalian system to dissect gene function *in vivo* or *ex vivo*. In human populations, *HMMR* was identified as a low penetrance breast cancer susceptibility gene and, subsequently, an *HMMR* polymorphism (termed rs299290) is associated with elevated expression and modifies the risk of developing breast cancer in female *BRCA1* mutation carriers (Pujana *et al.*, 2007; Maxwell *et al.*, 2011). Indeed, HMMR abundance is regulated through ubiquitination by BRCA1/BARD1 (Joukov *et al.*, 2006; Pujana *et al.*, 2007) leading to its elevated expression in *BRCA1*-deficient cells (Li *et al.*, 2016). The Pujana Lab generated a new mouse model in which human *HMMR* is expressed under the control of beta-lactoglobulin-Cre in combination with floxed *Brca1*, termed BLG-Cre $Tp53^{+/-}$; $Brca1^{fl/fl}$; $HMMR^{Tg/Tg}$ mice (Mateo, He, Mei *et al.*, 2022). Primary mammary epithelial cells were isolated from these animals and transduced with lenti-Cre to drive HMMR overexpression in the presence of *Brca1* mutation. These cells provide a model to examine the effects of HMMR overexpression on primary mouse mammary cell division *ex vivo*.

As mentioned above, *HMMR* rs299290 is associated with elevated *HMMR* expression in mammary tissues (Mateo, He, Mei *et al.*, 2022). Thus, the study of cells expressing *HMMR* rs299290 allows for the measurement of physiological increases in *HMMR* expression. Such

cells can be isolated from mammary tissues donated from human females or these cells can be created through the use of a variety of genome editing technologies. *HMMR* rs299290 cells provide a model to examine the effects of physiological levels of HMMR overexpression on cell division.

In this chapter, I inspect the mitotic phenotypes of a variety of experimental models with elevated HMMR expression, in order to validate my findings from the study of GFP-HMMR overexpressing tet-on HeLa cells (+dox).

5.2 Results

5.2.1 Ectopic expression of human HMMR in *Drosophila* neuroblasts induces large membrane blebbing during cell division

In Chapter 3, I found that GFP-HMMR-overexpressing tet-on HeLa cells (+ dox) displayed pronounced membrane blebbing that followed mis-oriented mitotic spindles. I was interested in whether similar processes occur in tissues from model organisms. Dr. Marisa Connell, a prior postdoctoral fellow in the Maxwell Lab, created a number of *Drosophila* lines, including lines expressing *UAS-GFP-Hmmr*, *UAS-Hmmr* and *UAS-Cherry-Jupiter*; Jupiter is a microtubule binding protein and serves as an marker of mitotic spindle poles (Karpova *et al.*, 2006). Dr. Connell had collected embryos and imaged living neuroblast cells as they underwent asymmetric cell division *in situ*, and I examined those movies for the occurrence of asymmetric membrane blebbing.

In neuroblasts expressing *UAS-GFP-Hmmr* GFP-HMMR localized to the spindle poles in *Drosophila* (Figure 5.1A) as it is known to do in mammalian cells. Moreover, HMMR-expressing neuroblasts showed a significantly increased frequency of membrane blebbing during

anaphase compared with control neuroblasts (Figure 5.1C), which was similar to the blebbing frequency observed in GFP-HMMR-overexpressing HeLa cells (Chapter 3). I also quantified the bleb size relative to the cell size at the same time point during anaphase (Figure 5.1B,D). Statistical analysis showed no significant difference between bleb size in control neuroblasts and HMMR-expressing neuroblast cells *in situ*. However, some HMMR expressing neuroblasts presented with large membrane blebs that are phenotypically similar to those I observed in GFP-HMMR-overexpressing HeLa cells. Moreover, the size of GMC was often smaller in HMMR-expressing neuroblasts compared to control, although this phenotype was difficult to measure given the positioning of GMC daughter cells. Finally, it is important to note that these HMMR transgenic flies did not suffer gross phenotypic defects in neurodevelopment nor changes in lifespan (personal communication, M. Connell, Maxwell Lab). In conclusion, HMMR overexpression in *Drosophila* neural progenitors *in vivo* is associated with more pronounced anaphase membrane blebbing and larger bleb sizes in cells undergoing asymmetric cell division, which is consistent with my observations in GFP-HMMR overexpressing tet-on HeLa cells (+dox).

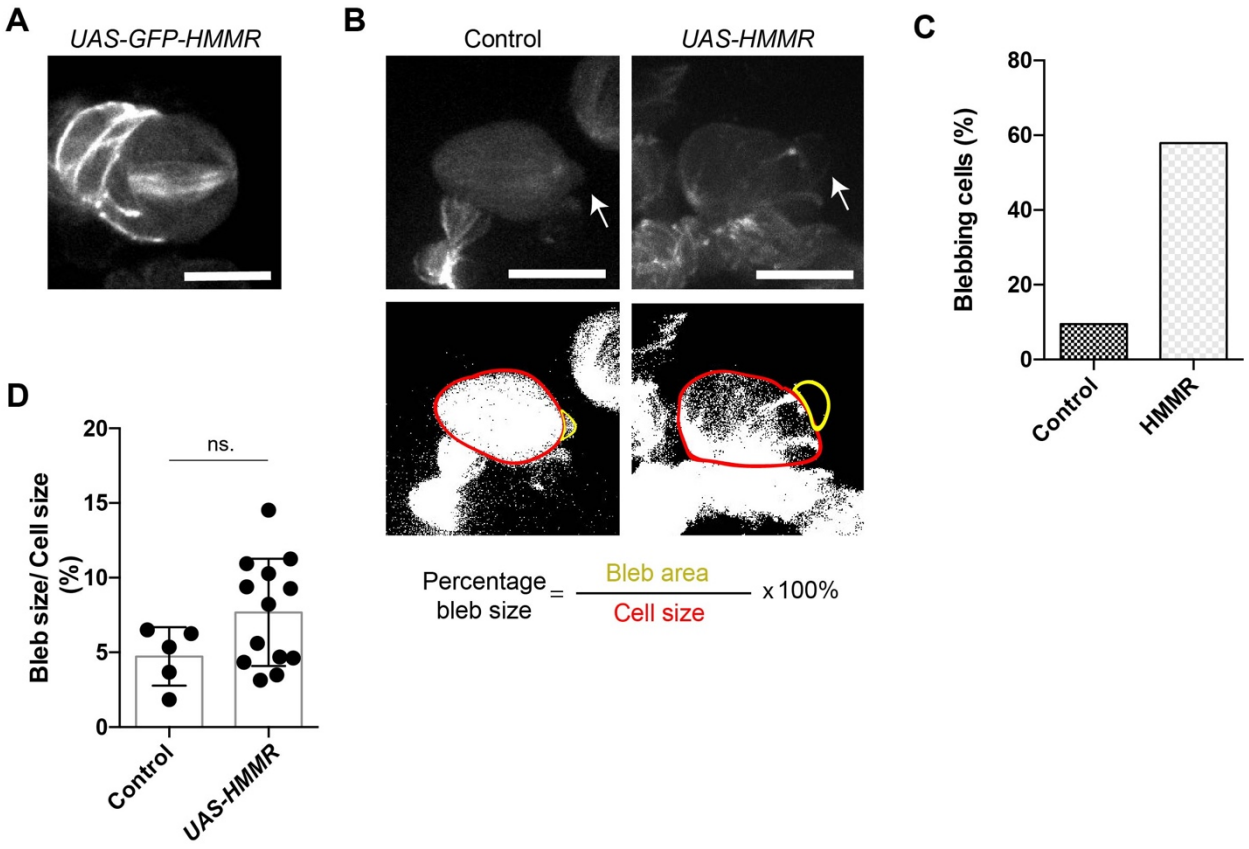

Figure 5.1 *Drosophila* neuroblasts expressing human HMMR undergo frequent and large membrane blebbing.

A) Expression of *UAS-GFP-Hmmr* in neuroblast cell division. Scale bar=10 μm.

B) Expression of *UAS-Cherry-Jupiter* and *UAS-Hmmr* induced membrane blebbing in neuroblast cell division. Arrows indicates cortical blebbing. Scale bar=20 μm. Bleb size was quantified by the largest bleb size (yellow) divided by the cell size (red).

C) Membrane blebbing frequency of neuroblasts expressing *UAS-Cherry-Jupiter* and *UAS-Hmmr* under the wor-Gal4 promoter (Mean, n=21 (Control), 19 (HMMR)).

D) Cortical bleb size in neuroblasts with *UAS-Cherry-Jupiter* and *UAS-Hmmr* under the wor-Gal4 promoter (Mean ± SD, n= 5 (WT), 13 (HMMR), ns., P=0.11, unpaired t-test).

5.2.2 Primary mammary epithelial cells isolated from *Trp53*$^{+/-}$; *Brca1*$^{fl/fl}$; *HMMR*$^{Tg/Tg}$ mice exhibit higher blebbing frequency in anaphase and different daughter cell size

HMMR is a low penetrance breast cancer susceptibility gene, which modifies breast cancer risk in *BRCA1* mutation carriers (Pujana *et al.*, 2007; Maxwell *et al.*, 2011). Analysis in mutation carriers identified *HMMR* rs299290 as a polymorphism associated with disease progression in *BRCA1* but not *BRCA2* mutation carriers (Maxwell *et al.*, 2011). Moreover, *HMMR* rs299290 is an expression quantitative trait loci associated with elevated *HMMR* expression in several tissues, including normal breast (Mateo, He, Mei *et al.*, 2022). Yet, it remains unclear how elevated HMMR expression mechanistically affects tumorigenesis in a *BRCA1* mutation background.

To approach this question, Dr. Miquel Àngel Pujana's laboratory (Catalan institute of Oncology, Barcelona, Spain) generated a mouse model with *Cre-loxP*-mediated expression of the full-length human HMMR under control of a mammary-specific promoter. The human *HMMR* coding sequence (NM_001142556, ENST00000393915) was cloned in the *Rosa26* locus, downstream of the *loxP-STOP-loxP* cassette. B-lactoglobulin promoter-Cre (*Blg-Cre*) was engineered in the mice to control the Cre expression, and thus induce human HMMR. Moreover, the mice with Cre-driven human HMMR expression were crossed with other mice with a Tp53 heterozygous (*Trp53*+/-) and *Brca1* floxed background. The resultant mice (*Blg-Cre Trp53*$^{+/-}$ *Brca1*$^{fl/fl}$ *HMMR*$^{Tg/Tg}$) have Cre-driven loss of BRCA1 and elevated expression of HMMR in the mammary gland following two rounds of pregnancy. The parental *Blg-Cre Trp53*$^{+/-}$ *Brca1*$^{fl/fl}$ mice develop mammary tumors that phenocopy the breast cancer subtypes that arise in human female carriers of *BRCA1* mutations (Molyneux *et al.*, 2010).

The initial analysis of mammary tissues isolated from *Blg-Cre Trp53*$^{+/-}$ *Brca1*$^{fl/fl}$ *HMMR*$^{Tg/Tg}$ mice revealed a moderate increased in HMMR expression, which was associated with higher penetrance of *Brca1*-mutant mammary tumors (Mateo, He, Mei *et al.*, 2022). The Pujana Lab provided our lab with tissue to examine the mitotic phenotypes of the primary mammary cells. I isolated the mammary epithelial cells (MECs) from mammary glands of the virgin six-week-old *Blg-Cre Trp53*$^{+/-}$ *Brca1*$^{fl/fl}$ *HMMR*$^{Tg/Tg}$ mice provided by the Pujana Lab. I thawed the frozen mouse mammary tissues and resected them for processing and partial dissociation to obtain single-cell suspensions. I then cultured the isolated cells and transduced them with lentiviruses expressing either EGFP or EGFP-Cre, to drive recombination events. Dr. Zhengcheng He (Maxwell Lab) sorted the GFP-positive cells 24 hours post-transduction and confirmed the Cre-induced HMMR overexpression (Mateo, He, Mei *et al.*, 2022).

Next, I seeded the sorted cells for live-cell imaging (Figure 5.2A). To determine the effect of HMMR overexpression, I isolated and examined MECs from *Blg-Cre Trp53*$^{+/-}$ *Brca1*$^{fl/fl}$ in parallel. It is important to note that MECs from all four experimental groups are TP53 heterozygous. The two control groups (GFP-transduced), and the GFP-Cre – transduced *Brca1* floxed cells, presented similar mitotic cell morphology with about 15-30% blebbing frequency in anaphase and a daughter cell size ratio of 1.1-1.15 (Figure 5.2B,C). GFP-Cre – transduced *Brca1* floxed *HMMR*$^{Tg/Tg}$ cells, however, displayed higher blebbing frequency during anaphase and higher daughter cell-size difference (Figure 5.2B,C), which are consistent phenotypes with other HMMR overexpression models. Moreover, some *HMMR*$^{Tg/Tg}$ cells did not round up properly during metaphase and remained an irregular shape for the entire cell division process. These results confirm HMMR overexpression is sufficient to cause cell shape changes and aberrant blebbing in primary murine mitotic cells.

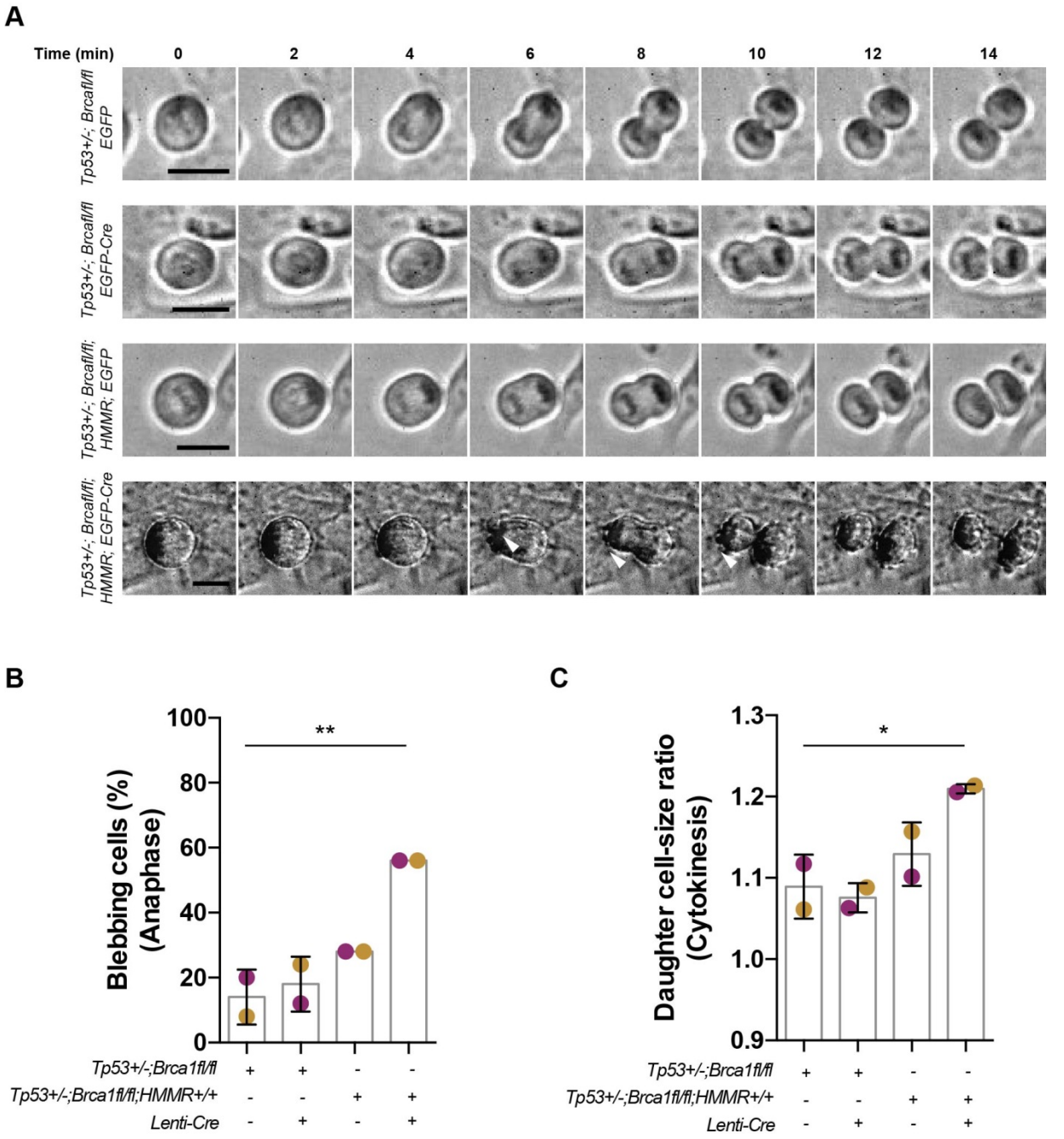

Figure 5.2 Cre-driven human HMMR overexpressed MECs with frequent anaphase blebbing and loss of daughter cell-size control.

A) Live-cell imaging of mitotic progression of BLG-Cre *Brca1*$^{f/f}$ *Trp53*$^{+/-}$ and BLG-Cre *Brca1*$^{f/f}$ *Trp53*$^{+/-}$ *HMMR*$^{Tg/Tg}$ cells transduced with GFP or GFP-Cre. Transmitted light channel, 2 min/frame. Membrane blebbing was highlighted with white arrows. Scale bar=10 μm.

B) Quantitative analysis of blebbing frequency in anaphase (Mean ± SD, n=2 experiments, colour-coded, **P=0.0072, one-way ANOVA).

C) Quantitative analysis of daughter cell-size ratio in cytokinesis (Mean ± SD, n=2 experiments, colour-coded, *P=0.033, one-way ANOVA).

5.2.3 Primary mammary epithelial cells isolated from *Trp53*$^{+/-}$; *Brca1*$^{fl/fl}$; *HMMR*$^{Tg/Tg}$ mice show attenuated cortical ARPC2 retention and a larger nucleus size

I next performed immunofluorescence analysis for ARPC2 in BLG-Cre *Brca1*$^{f/f}$ *Trp53*$^{+/-}$ and BLG-Cre *Brca1*$^{f/f}$ *Trp53*$^{+/-}$ *HMMR*$^{Tg/Tg}$ cells transduced with either GFP or GFP-Cre (Figure 5.3A,B). There is no significant difference across the groups in terms of total level (Figure 5.3C). However, I observed a loss of cortical ARPC2 in GFP-Cre transduced BLG-Cre *Brca1*$^{f/f}$ *Trp53*$^{+/-}$ *HMMR*$^{Tg/Tg}$ MECs but no significant localization of ARPC2 at the spindle (Figure 5.3D-F).

I also measured the nucleus size as it remains proportional to cell size even with altered DNA content or cell volume (Huber and Gerace, 2007). I found a wide range of nucleus sizes in GFP-Cre transduced BLG-Cre *Brca1*$^{f/f}$ *Trp53*$^{+/-}$ *HMMR*$^{Tg/Tg}$ cells, which were generally larger than in the control groups (Figure 5.4). Although cell size is affected by cell growth and cell cycle, the size of daughter cells post mitosis may also influence the general cell size. In addition, GFP-Cre-transduced BLG-Cre *Brca1*$^{f/f}$ *Trp53*$^{+/-}$ *HMMR*$^{Tg/Tg}$ cells also exhibited high genomic instability, as indicated by an elevated frequency of micronuclei and nuclear budding (Mateo, He, Mei *et al.*, 2022). In general, GFP-Cre-transduced BLG-Cre *Brca1*$^{f/f}$ *Trp53*$^{+/-}$ *HMMR*$^{Tg/Tg}$ cells showed similar phenotypes as those found in GFP-HMMR-overexpressing HeLa cells.

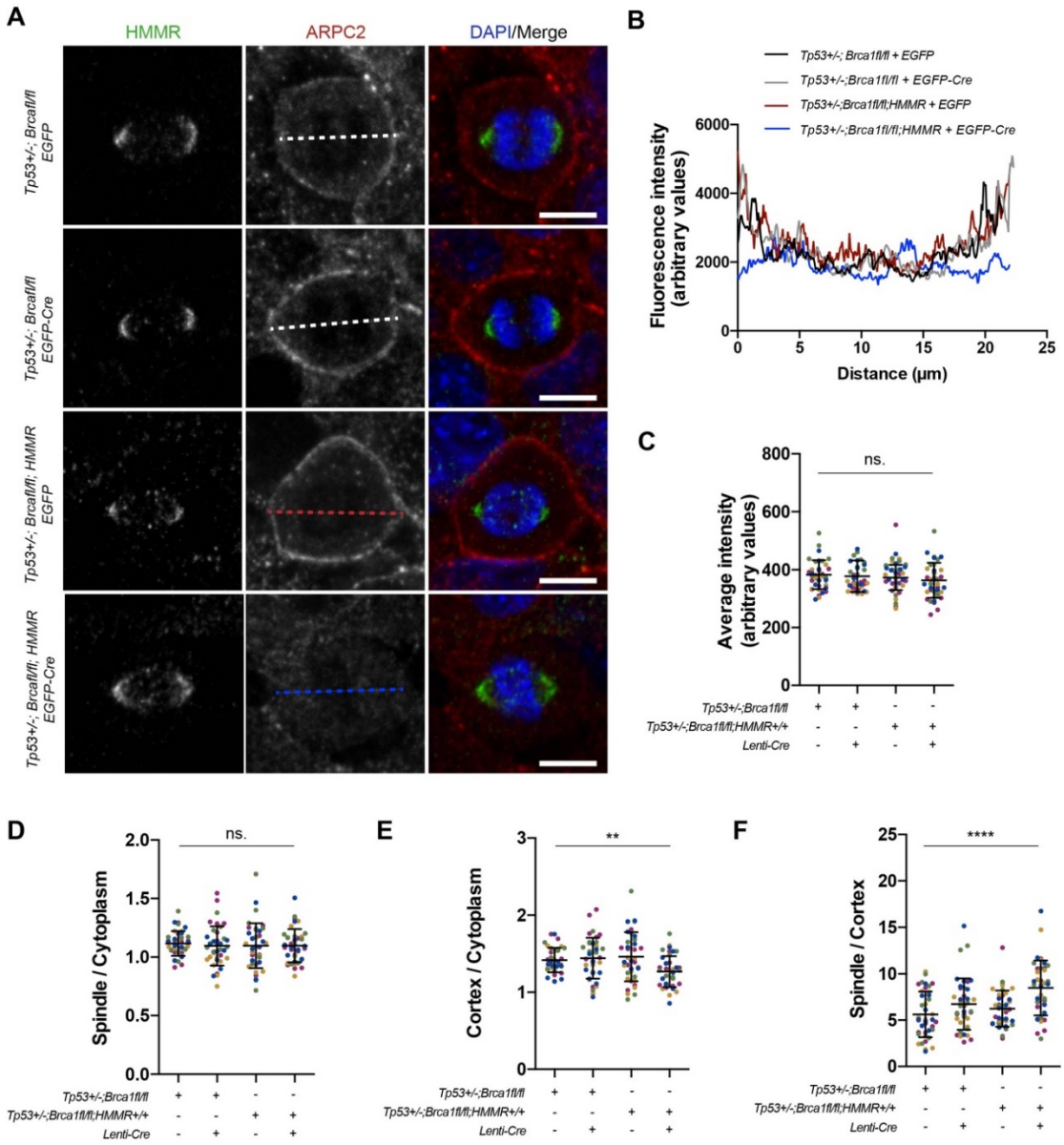

Figure 5.3 Intracellular localization of ARP2/3 complex in *HMMR*$^{Tg/Tg}$ MECs.

A) Immunofluorescence analysis of ARPC2 localization in *HMMR*$^{Tg/Tg}$ cells and control groups. Scale bar=10 µm.

B) A plot profile measuring fluorescence intensity across the anaphase cells shown by the dash lines in panel A.

C) Total abundance of ARPC2 in anaphase cells (Mean ± SD, n= 40 cells per group, P=0.41, one-way ANOVA).

D) Spindle enrichment of ARPC2 in mammary epithelial cells transduced with EGFP or EGFP-Cre lentivirus (Mean ± SD, n= 40 cells per group, P=0.92, one-way ANOVA).

E) Cortical enrichment of ARPC2 in mammary epithelial cells transduced with EGFP or EGFP-Cre lentivirus (Mean ± SD, n= 40 cells per group, **P=0.0020, one-way ANOVA).

F) ARPC2 spindle pole vs. cortical enrichment in mammary epithelial cells transduced with EGFP or EGFP-Cre lentivirus (Mean ± SD, n= 40 cells per group, ****P<0.0001, one-way ANOVA).

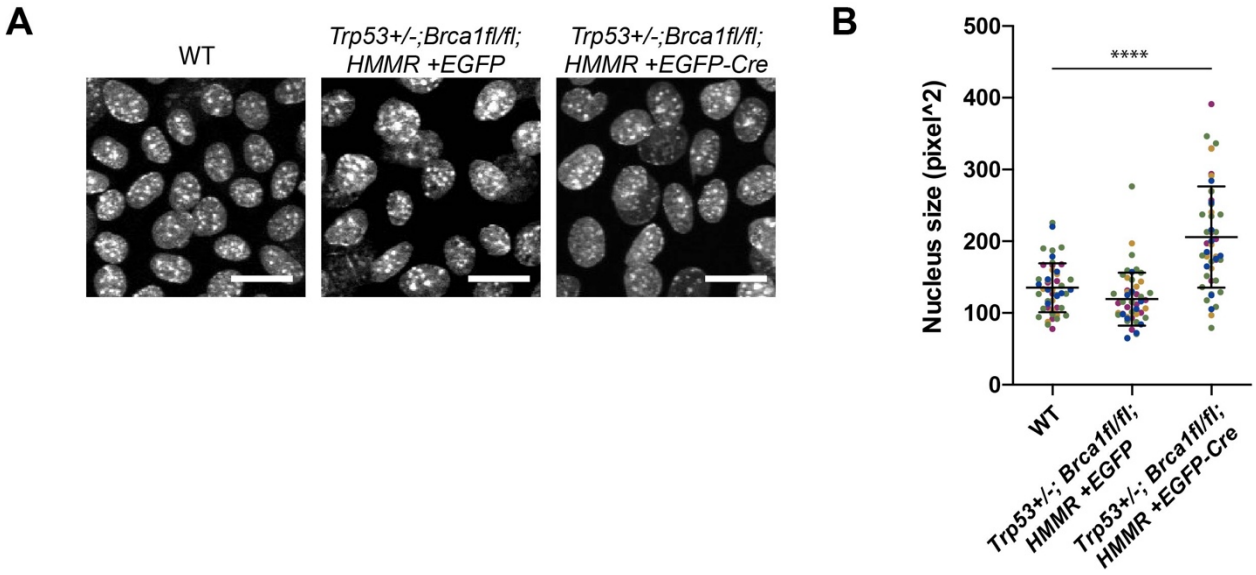

Figure 5.4 Mammary epithelial cells isolated from mice with genetic background simulating the breast cancer with a polymorphism associated with HMMR overexpression.

A) Immunofluorescence images of mammary epithelial cells isolated from C57BL/6J mice (left) and *Trp53*$^{+/-}$ *Brca1*$^{fl/fl}$ *HMMR*$^{Tg/Tg}$ *EGFP* (middle), *Trp53*$^{+/-}$ *Brca1*$^{fl/fl}$ *HMMR*$^{Tg/Tg}$ *EGFP-Cre* (right). Scale bar = 20 µm.

B) Quantitation of the nucleus size of mammary epithelial cells described in panel A (Mean ± SD, n= 4 experiments, colour-coded, ****P< 0.0001, one-way ANOVA).

5.2.4 Cortical ARP2/3 complex is reduced in *Trp53$^{+/-}$; Brca1$^{fl/fl}$; HMMR$^{Tg/Tg}$* MECs

To examine the consequence for HMMR overexpression *in situ*, I processed paraffin embedded mammary gland tissues dissected from 10- to 11-month-old BLG-Cre *Trp53$^{+/-}$ Brca1$^{fl/fl}$* mice and BLG-Cre *Trp53$^{+/-}$ Brca1$^{fl/fl}$ HMMR$^{Tg/Tg}$* mice that had undergone two pregnancies. We chose to dissect mammary tissue that was contralateral to incident tumours, without evidence of tumors, to study the premalignant state. Using immunofluorescence, I confirmed elevated expression of HMMR in BLG-Cre *Trp53$^{+/-}$ Brca1$^{fl/fl}$ HMMR$^{Tg/Tg}$* mice (Mateo, He, Mei *et al.*, 2022). Then, I performed immunofluorescence analysis of ARPC2 localization (Figure 5.5A). MECs in dissected mammary tissues *in situ* are denser, with few mitotic cells, making it challenging to identify intracellular ARPC2 localization. To do so, I measured the cortical intensity of ARPC2 within 1 μm width around the cortex (due to the tightly packed cells in tissues) and included all mitotic stages prior to telophase/cytokinesis in the analysis. The quantitative result revealed a significant reduction in ARPC2 cortical intensity in BLG-Cre *Trp53$^{+/-}$ Brca1$^{fl/fl}$ HMMR$^{Tg/Tg}$* mice (Figure 5.5B). This result was expected and aligned with the results observed in *ex vivo* cultured GFP-Cre-transduced BLG-Cre *Brca1$^{f/f}$ Trp53$^{+/-}$ HMMR$^{Tg/Tg}$* cells.

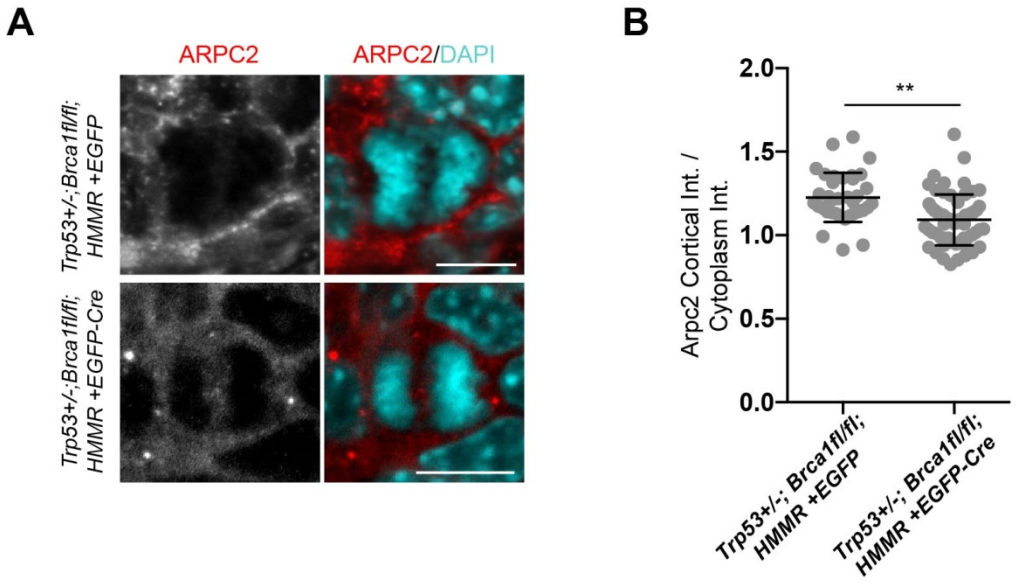

Figure 5.5 Cortical ARPC2 intensity in HMMR overexpressing murine mammary tissue.

A) Immunofluorescence analysis of ARPC2 localization in mammary tissue of BLG-Cre *Trp53*$^{+/-}$ *Brca1*$^{fl/fl}$ and BLG-Cre *Trp53*$^{+/-}$ *Brca1*$^{fl/fl}$ *HMMR*$^{Tg/Tg}$ mice. Scale bar = 10 µm.

B) Quantitative analysis of cortical ARPC2 level in mammary tissue of BLG-Cre *Trp53*$^{+/-}$ *Brca1*$^{fl/fl}$ and BLG-Cre *Trp53*$^{+/-}$ *Brca1*$^{fl/fl}$ *HMMR*$^{Tg/Tg}$ mice (Mean ± SD, n= 36 (*Trp53*$^{+/-}$ *Brca1*$^{fl/fl}$), 60 (*Trp53*$^{+/-}$ *Brca1*$^{fl/fl}$ *HMMR*$^{Tg/Tg}$), **P= 0.029, unpaired t-test).

5.2.5 Generation of rs299290 SNP in MCF10A cells using gene editing tools

In previous sections, I examined immortal cancer cells as well as primary *Drosophila* neuroblasts, or primary MECs isolated from transgenic mice, with genetically-driven abnormal expression of human HMMR. *HMMR* rs299290 is an expression quantitative trait loci associated with elevated physiological *HMMR* expression in several tissues, including normal breast (Mateo, He, Mei *et al.*, 2022). Thus, I aimed to generate and study *HMMR* rs299290 in the non-tumorigenic immortal RFP-TUBA1B MCF10A human mammary cells using gene editing tools.

The general workflow of gene editing is: i) use digestion and ligation method to insert the desired components into the delivering plasmids followed by cloning; ii) transfect the plasmid(s) encoding the required components such as enzyme, gRNA and template into the cell line for editing; iii) culture the cells and do single-cell sorting; iv) grow clones to confluence, split and collect DNA; and, v) sequence the targeting region using Sanger sequencing method.

Successful editing by CRISPR-Cas9 relies on the choice of gRNA based on the protospacer adjacent motif (PAM) sequence, about 3 bp downstream from the targeting site (Jiang and Doudna, 2017). However, there are only two candidate gRNA available according to the PAM sites surrounding the rs299290 site and the CRISPR targets database on UCSC Genome Browser (Kent *et al.*, 2002). In addition to the target site, I also designed a silent mutation to disrupt the PAM in order to avoid repetitive editing due to existing PAM site (Figure 5.6 highlighted in green).

For the first attempt, I chose a high efficiency scoring gRNA for the CRISPR design (Hsu *et al.*, 2013; Bae *et al.*, 2014; Moreno-Mateos *et al.*, 2015; Doench *et al.*, 2016; Haeussler *et al.*, 2016) and used lipofectamine3000 (Thermo Fisher Scientific) to deliver the plasmids. Yet, I detected neither the edited PAM site nor the desired mutation in the cells (Figure 5.6A). For the

second CRISPR-Cas9 attempt, I chose the second gRNA provided in UCSC Genome Browser database (Kent *et al.*, 2002). Although the second PAM site is proximal to the targeting site, the efficiency score was low and no desired editing detected (Figure 5.6B).

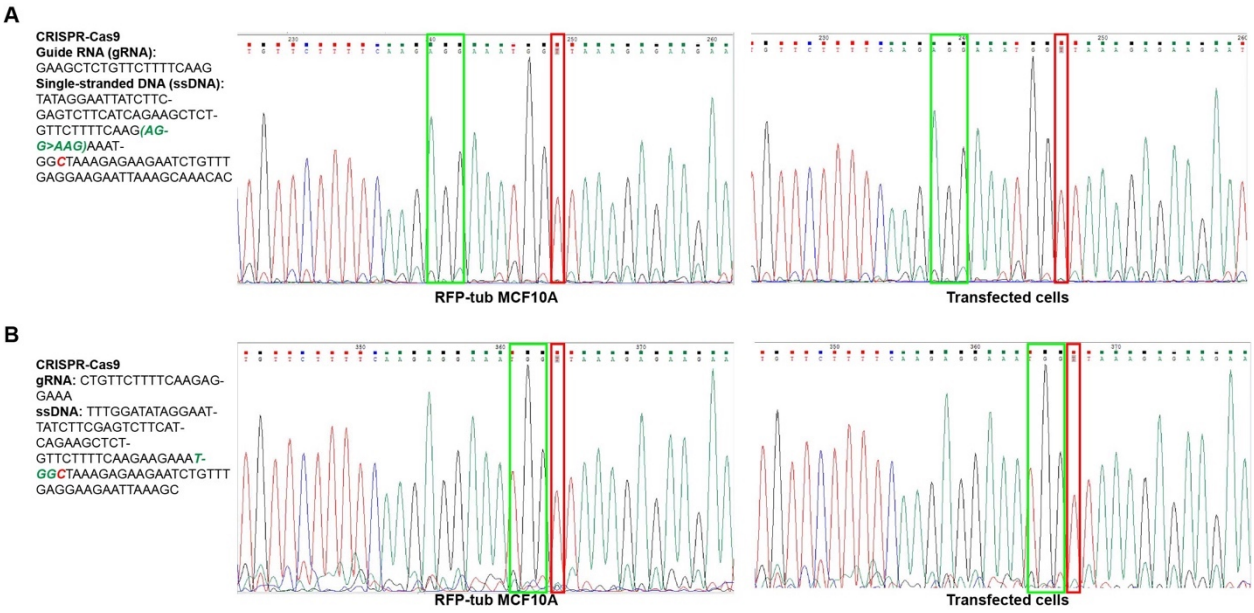

Figure 5.6 Gene editing designs to generate rs299290 SNP in MCF10A cells part I.
First attempts of gene editing using different CRISPR-Cas9 with the designed sequences for each component. Target site is highlighted in red and outlined in the Sanger sequencing result. PAM sequence is highlighted in green with labelled PAM disruption and outlined in green box in the Transfected cells indicate RFP-tub MCF10A cells transfected with gene editing plasmids containing the designed components.

Due to my lack of success with the traditional CRISPR-Cas9 approach, I then decided to utilize Prime editing. Prime editing is a more advanced method where Cas9 is fused to a reverse transcriptase, along with a 3' RTT after the sgRNA, enabling the reverse transcriptase to transcribe according to the template and increasing accuracy for the repair (Anzalone *et al.*, 2019). I attempted three different designs by altering the position of targeting site in extension template and changing the distance of ngRNA from the targeting site (Figure 5.7).

For the first attempt, I chose a design combination from the design webtool (Hsu *et al.*, 2021) but I did not detect the desired mutation or disrupted PAM sequence in the edited cells (Figure 5.7A). Then, I optimized the design by modifying the position of the target site in the 3'RTT and adding a "G" in front of the spacer since the U6 promoter must begin with a "G" (Anzalone *et al.*, 2019) (Figure 5.7B). In the third attempt, I chose another PAM site but again no desired mutation was identified (Figure 5.7C).

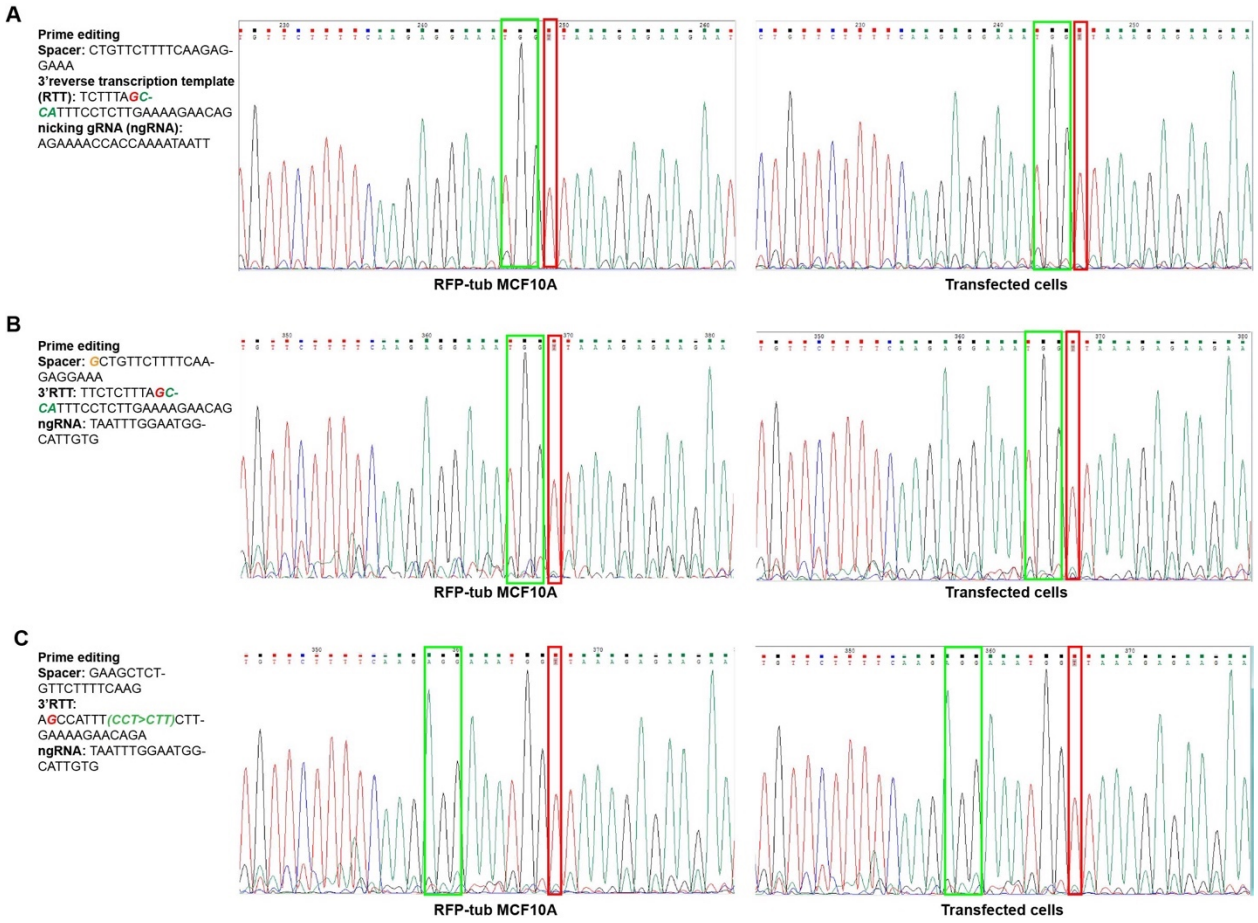

Figure 5.7 Gene editing designs to generate rs299290 SNP in MCF10A cells part II. Multiple attempts of gene editing using Prime editing with the designed sequences for each component. Target site is highlighted in red and outlined in the Sanger sequencing result. PAM sequence is highlighted in green with labelled PAM disruption and outlined in green box in the Sanger sequencing graph. Sequence with orange highlighted "G" is added for U6 promoter. Transfected cells indicate RFP-tub MCF10A cells transfected with gene editing plasmids containing the designed components.

The challenge of Prime editing design is the U6 promoter, which drives Pol III RNA polymerase for transcription, and terminates when it encounters consecutive Ts in the sequence (Anzalone *et al.*, 2019). Due to the limited PAM around the rs299290 targeting site, I had to include the group of four consecutive Ts in the spacer gRNA. So, to try to circumvent this, I also performed PRIME-Del, which is Precise genomic deletion using paired Prime editing, to tackle (Choi *et al.*, 2022).

My plan was to first perform a precise deletion to remove the 4Ts and surrounding sequence, followed by an accurate insertion by Prime editing. In this case, the design for gRNA would no longer be limited to the PAM around rs299290. The PRIME-Del software (Choi *et al.*, 2022) provided one set of oligos, but, after performing the edit, I did not identify the deletion in the resulting colonies (Figure 5.8A).

My subsequent plan was to *in vitro* transcribe Prime editing components and then deliver the RNA components into the cells. In this case, I only modified the PAM site and the target site. To further improve the efficiency, I added a 3'pseudoknot structure with a linker after 3'RTT to stabilize RNA, as described (Nelson *et al.*, 2021) (Figure 5.8B). The pseudoknot prevents RNA degradation and is small enough to not interrupt pegRNA function (Nelson *et al.*, 2021). I co-expressed an engineered dominant negative of a DNA mismatch repair gene *MLH1* (MLH1dn) to reduce the effect of DNA mismatch repair on Prime editing efficiency (Chen *et al.*, 2021b). Thus, I performed *in vitro* transcription on the pegRNA, Prime editor (PE) and MLH1dn plasmids, followed by nucleofection to deliver the RNA components.

The Sanger sequencing result from the bulk edited cells revealed an unexpected result. I identified a small peak (~10%) for the disrupted PAM (GAG>GAA) but no sign of targeted mutation (Figure 5.8B). The result was surprising because I expected PAM disruption and target

edit would occur together since they are both within 3'RTT for onsite reverse transcription simultaneously. Yet, the target site was near the end of the template which might be degraded before transcription despite the addition of RNA stabilizing components. In future experiment, an alternative design of Prime editing with a centered target site in 3'RTT should be considered.

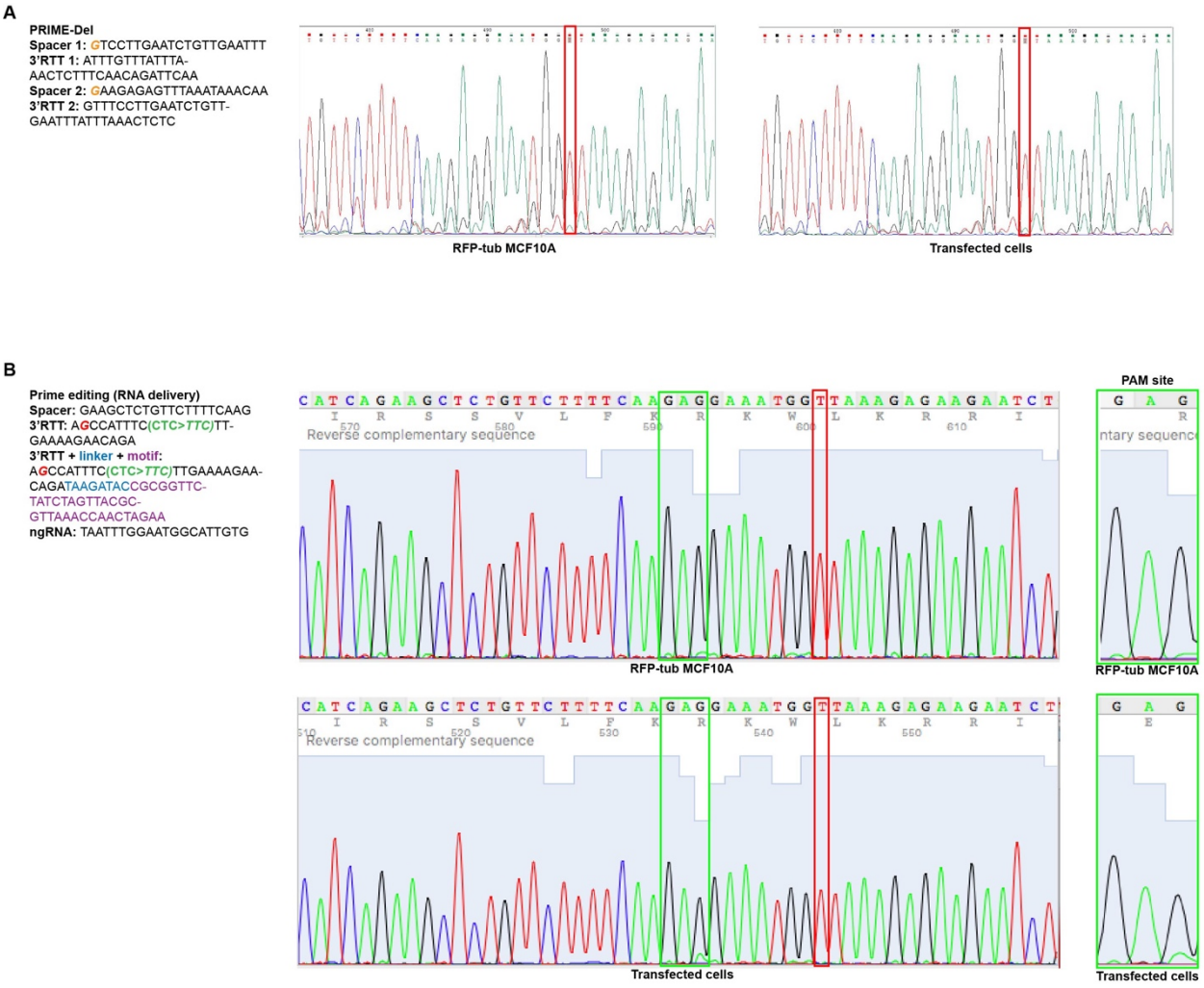

Figure 5.8 Gene editing designs to generate rs299290 SNP in MCF10A cells part III. Multiple attempts of gene editing using PRIME-Del and Prime editing with RNA delivery designed sequences for each component. Target site is highlighted in red and outlined in the Sanger sequencing result. PAM sequence is highlighted in green with labelled PAM disruption and outlined in green box in the Sanger sequencing graph. Sequence with orange highlighted "G" is added for U6 promoter. Linker and pseudoknot motif for RNA stability are highlighted in blue and purple, respectively. Transfected cells indicate RFP-tub MCF10A cells transfected with gene editing plasmids containing the designed components.

5.2.6 Primary mammary epithelial cells isolated from *BRCA1* mutation carriers present with elevated blebbing, daughter cell-size differences and ARPC2 mis-localization.

While I was optimizing the generation of *HMMR* rs299290 in immortal MCF10A cells, I investigated other physiological systems with elevated expression of HMMR. The expression of HMMR is regulated through the cell cycle, increasing prior to mitosis (Maxwell *et al.*, 2003), and is transcriptionally regulated via TP53 (Sohr and Engeland, 2008) and post-translationally regulated by BRCA1/BARD1 (Pujana *et al.*, 2007). Via ubiquitination, the BRCA1-BARD1 complex facilitates degradation of HMMR (Pujana *et al.*, 2007; Maxwell *et al.*, 2011) and the silencing of BRCA1 leads to the elevated expression of HMMR (Maxwell *et al.*, 2011; Li *et al.*, 2016; He *et al.*, 2017). In this section, I inspected these phenotypes in primary MECs isolated from human *BRCA1* mutation carriers.

Primary mammary epithelial cells were isolated from *BRCA1* mutation carriers (n=3) or age-matched non-carriers (n=3), followed by fluorescent-activated cell sorting to isolate luminal progenitor cells (LPs), as described (Mateo, He, Mei *et al.*, 2022). I cultured the LPs on collagen-coated plates for further analysis. It is important to note that each patient or donor sample showed varying levels of proliferation and, for the *BRCA1* mutation carriers, one sample (which happened to also carry a *HMMR* rs299290 polymorphism) contributed the majority of cell division events *ex vivo*.

First, I used immunofluorescence analysis to measure the HMMR expression levels in LPs and found significantly higher levels of expression in MECs isolated from *BRCA1* mutation carriers (Figure 5.9A,B). I also measured ARPC2 localization, and my analysis suggested a loss of cortical ARPC2 in *BRCA1* mutation carriers, as indicated by an increased spindle/cortex ratio (Figure 5.9C).

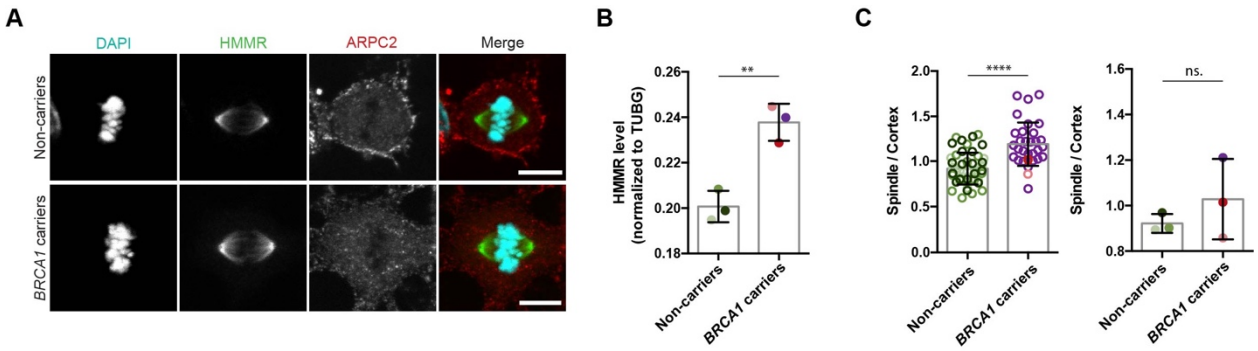

Figure 5.9 LPs from BRCA1 mutation carriers showed elevated HMMR level and loss of cortical ARPC2.

A) Immunofluorescence analysis of mitotic LPs isolated from *BRCA1* mutation carriers (n=3) and non-carriers (n=3). Scale bar=10 µm.

B) HMMR level in mitotic LPs isolated from *BRCA1* mutation carriers (n=3) and non-carriers (n=3) (Mean ± SD, n= 3 (non-carriers), 3 (*BRCA1* carriers), colour-coded for each donor, **P=0.0006, unpaired t-test).

C) Quantitative analysis of ARPC2 localization in mitotic LPs isolated from *BRCA1* mutation carriers (n=3) and non-carriers (n=3) (Mean ± SD, n= 48 (non-carriers), 31 (*BRCA1* carriers), ****P<0.0001, unpaired t-test) (Left). An average analysis of ARPC2 localization in mitotic LPs for each donor (Mean ± SD, n=3 (non-carriers), 3 (*BRCA1* carriers), ns., P=0.37, unpaired t-test)

In collaboration with Dr. Zhengcheng He, I imaged LP cell divisions on coated micropattern plates taking images every 10 min using live-cell imaging microscopy (Figure 5.10A). This was not ideal to capture anaphase and was designed to capture the cell division axis. Thus, I analysed membrane blebbing during cytokinesis since cytokinetic blebbing also reflects perturbation of the cortex (Dorn and Maddox, 2011). Membrane blebbing events were more frequent in LPs from *BRCA1* mutation carriers, although the mean frequency was not significantly different from LPs isolated from non-carrier control samples (Figure 5.10B,C). The trend was most pronounced between LPs isolated from non-carriers and LPs isolated from a BRCA1 mutation carrier that also encoded *HMMR* rs299290, although the difference was not statistically significant (Figure 5.10B,C).

My analysis of primary mammary cells with physiologically elevated levels of HMMR, through mutation of *BRCA1* and/or expression of the eQTL *HMMR* rs299290, was limited by the availability of primary samples and the heterogeneous proliferation capacity of primary MECs across patient samples. However, my analysis reveals mitotic phenotypes consistent with those I identified in immortal cancer cells as well as primary *Drosophila* neuroblasts or primary MECs isolated from transgenic mice with genetically-driven abnormal expression of human HMMR.

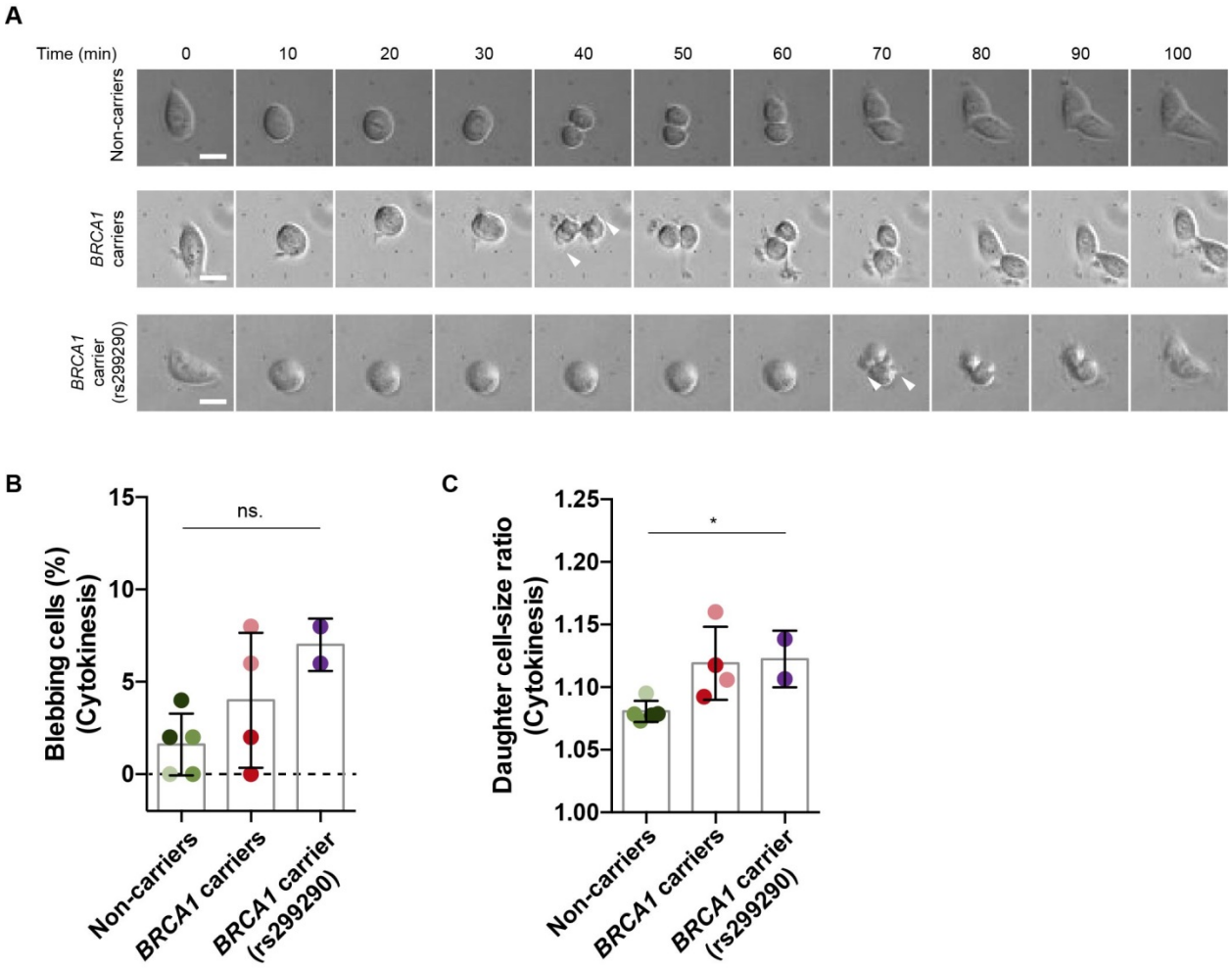

Figure 5.10 LPs from BRCA1 mutation carriers exhibited increased membrane blebbing and daughter cell-size ratio.

A) Live-cell imaging of LP cell division from MECs isolated from *BRCA1* mutation carriers (n=2), *BRCA1* mutation carrier with rs299290 (n=1) and non-carriers (n=3). Membrane blebbing is highlighted with white arrows. Scale bar=10 μm.

B) Proportion of cytokinesis blebbing cells from *BRCA1* carriers, *BRCA1* carrier with rs299290 and non-carriers (Mean ± SD, n=2 experiments, one-way ANOVA).

C) Daughter cell-size ratio of LPs during cytokinesis from *BRCA1* carriers, *BRCA1* carrier with rs299290 and non-carriers (Mean ± SD, n=2 experiments, *P=0.037, one-way ANOVA).

5.3 Key findings

1. HMMR expression in *Drosophila* neuroblasts induces frequent and pronounced anaphase membrane blebbing during asymmetric cell division *in vivo*.
2. BLG-Cre $Trp53^{+/-}$ $Brca1^{f/f}$ $HMMR^{Tg/Tg}$ MECs present higher anaphase blebbing frequency and daughter cell-size difference than BLG-Cre $Trp53^{+/-}$ $Brca1^{fl/fl}$ MECs.
3. Both *ex vivo* cultured mitotic MECs and mitotic MECs in mammary tissue section from BLG-Cre $Trp53^{+/-}$ $Brca1^{f/f}$ $HMMR^{Tg/Tg}$ mice reveal decreased cortical ARP2/3 complex localization.
4. LPs from *BRCA1* mutation carriers show elevated HMMR expression and exhibit frequent anaphase blebbing and higher daughter cell-size ratio.
5. LPs of *BRCA1* mutation carrier with rs299290 SNP show attenuated cortical ARP2/3 complex during mitosis.

5.4 Discussion

In this chapter, I investigated the phenotypes related to daughter cell-size control in several different models. I utilized *Drosophila* neuroblasts expressing GFP-HMMR, or HMMR, to determine whether the ectopic expression of HMMR is sufficient to augment anaphase membrane blebbing *in vivo*. In *Drosophila* neuroblasts, GFP-HMMR localized to the mitotic spindle during cell division and HMMR expressing cells showed significantly higher membrane blebbing events. Consistent with the result observed in GFP-HMMR-overexpressing HeLa cells, HMMR expressing neuroblasts presented blebs with larger size than those in control group, suggesting the same pathways may be affected. As mentioned before, spindle position during anaphase can affect cellular boundary of the two daughter cells and result in different relative amount of cytoplasmic content (Kiyomitsu, 2015). Thus, abnormal membrane blebbing during

cell division may also affect developmental process in *Drosophila* neuroblasts expressing HMMR however no gross pathologies nor shortened live span was observed in these flies (personal communication, Dr. Marisa Connell, Maxwell Lab).

I also investigated the link between HMMR overexpression and tumorigenesis. Many factors, such as lifestyle, diet, environments and other genetic variants, can contribute to the penetrance of *BRCA1* mutant breast cancer (Howell *et al.*, 2014). Moreover, a polymorphism of HMMR, rs299290, is linked to the risk of developing breast cancer in the presence of *BRCA1* mutation (Pujana *et al.*, 2007; Maxwell *et al.*, 2011). Yet, the mechanism by which HMMR affects the progression of tumorigenesis in *BRCA1* mutants remains unclear. In previous chapters, my findings demonstrated that elevated HMMR expression can lead to aberrant anaphase blebbing and different daughter cell-size, resulting in chromosome mis-segregation and micronuclei formation. Because genome instability increases the risk of tumorigenesis (Tubbs and Nussenzweig, 2017), it is significant to examine if elevated HMMR expression also modifies cell division integrity in a mouse model for hereditary *BRCA1* mutant breast cancer.

My analysis of primary MECs isolated from BLG-Cre $Trp53^{+/-}$ $Brca1^{fl/fl}$ $HMMR^{Tg/Tg}$ mice showed a reduction in the cortical ARP2/3 complex, which is consistent with my findings *in vitro* wherein the frequency of anaphase blebbing and daughter cell-size ratio were significantly higher. Similarly, primary LPs isolated from *BRCA1* mutation carriers presented with an elevated blebbing frequency and daughter cell-size ratio with reduced cortical ARP2/3 localization; however, *BRCA1* mutation LPs with rs299290-C did not show a more pronounced effect. It is important to note the degree of HMMR expression was only moderately increased in *BRCA1* mutation LPs and BLG-Cre $Trp53^{+/-}$ $Brca1^{f/f}$ $HMMR^{Tg/Tg}$ MECs, whereas the HMMR level was about 1.7 times higher in GFP-HMMR expressing HeLa cells (Figure 3.1A).

Caveats – The analysis of *Drosophila* neuroblasts in section 5.2.1 was retrospective. The experiments were conducted by Dr. Marisa Connell in the past and the flies were no longer available. Thus, the number of experiments was limited. Although more repeats of the *Drosophila* experiment would be supportive to the conclusion, analysis of *ex vivo* $Trp53^{+/-}$; $Brca1^{fl/fl}$; $HMMR^{Tg/Tg}$ MECs and LPs of *BRCA1* mutation carriers showed consistent blebbing phenotypes.

For *ex vivo* analysis of human LPs, the number of donor samples was limited. It is challenging to compare and draw conclusions for the difference between samples of BRCA1 mutation carriers with and without rs299290 SNP since only one sample was available with the HMMR rs299290 SNP. Another caveat is the non-equal contribution of patient samples to the dataset of *BRCA1* mutant cells. Due to limited number of mitotic cells obtained for immunofluorescence analysis, the majority of mitotic cells analyzed in the *BRCA1* mutation carrier group were from LPs with rs299290-C. The level of HMMR expression in mutants with and without rs299290 SNP was challenging to compare because the presence of a *BRCA1* mutation is documented to elevate the HMMR expression at the posttranslational level. It would be beneficial to evaluate the effect of rs299290 on HMMR expression level without the *BRCA1* mutation.

Although rs299290-C is a valine-to-alanine benign missense variant of HMMR, we cannot rule out the possibility that this genetic variant may function with other trans-acting variants (Cheung and Spielman, 2009). Trans-acting variants of a target gene are more difficult to identify because no pattern of variant localization relative to the target gene was identified and each trans-activating variant imposes smaller effects on the target gene (Cheung and Spielman, 2009). Thus, further investigation on this SNP is required to draw a final conclusion.

Future studies – As mentioned in the previous section, the investigation of rs299290 SNP independent of *BRCA1* mutation is significant to uncover the effect of this mutation on cell division: whether it is sufficient to disrupt mitotic events or it aggravates mitotic phenotypes in *BRCA1* mutation background. Therefore, I propose to further optimize the gene editing design to obtain MCF10A cells with rs299290-C mutation. Many potential factors could contribute to the low editing efficiency, for example, RNA stability and counterproductive secondary structure of RNA (Nelson *et al.*, 2021). In the last attempt of Prime editing with RNA delivery, I identified an edited PAM site but no desired editing on the target site (Figure 5.8B). Although a pseudoknot and MLH1dn were included to improve RNA stability, the target site was located at the end of 3'RTT and therefore it is plausible that the target site on the RNA was degraded. For future design, I propose to design a 3'RTT with a centred target site as well as a new ngRNA that is more proximal to the target site, facilitating the editing on the opposite strand. Base editing is also an alternative approach but the limited PAM sites around the target may still be a challenge.

Significance – In Chapter 5, my research showed that altered expression of HMMR in primary cells *in vivo* and *ex vivo* dysregulates asymmetric membrane elongation and the cortical localization of the ARP2/3 complex. I also found consistent results through my examination of physiological levels of elevated HMMR expression, as documented in mammary cells isolated from *BRCA1* mutation carriers with and without germline expression of *HMMR* rs299290. I also found that elevated HMMR expression correlates with the mis-localization of components of the ARP2/3 complex, which potentially disrupts cortical stability during mitosis.

Chapter 6: Discussion and conclusions

6.1 Summary and working models

The findings from my thesis provide insight into the molecular control of daughter cell sizes following cell division. The focus of my study is HMMR, the hyaluronan-mediated motility receptor, which is a microtubule-associated protein that regulates multiple pathways during mitosis (Dunsch *et al.*, 2012; Chen *et al.*, 2014; Connell *et al.*, 2017). HMMR was first considered as an extracellular receptor for a glycosaminoglycan, hyaluronan, which induces cell motility (Turley *et al.*, 1987). However, later studies discovered intracellular roles of HMMR, including interactions with the cytoskeleton (Assmann *et al.*, 1998, 1999; Hofmann *et al.*, 1998a), spindle integrity (Maxwell *et al.*, 2003, 2005), anastral spindle assembly (Groen *et al.*, 2004; Joukov *et al.*, 2006) and regulation of several kinases that are critical for cell division (Chen *et al.*, 2014; Connell *et al.*, 2017; Fulcher *et al.*, 2019).

HMMR is critical for spindle orientation and positioning pathways, regulating cortical proteins either directly or indirectly. During cell division, spindle position is regulated by two main pathways: 1) cortical dynein pulling forces and 2) asymmetric membrane elongation (Kiyomitsu, 2015). HMMR regulates cortical dynein by interacting with CHICA and DYNLL1 directly or through regulation of Ran-GTP and PLK1 activity at the spindle poles (Dunsch *et al.*, 2012; Chen *et al.*, 2014; Connell *et al.*, 2017).

Here, my findings indicate that a HMMR-mediated pathway can regulate cortical stability to adjust the cellular boundary and daughter cell size during cell division (Figure 6.1A). Ectopic overexpression of HMMR hyperactivates Aurora A leading to the abnormal recruitment of the ARP2/3 complex away from the cortex and to the spindle; these results suggest that during anaphase, HMMR promotion of Aurora A activity may recruit a small pool of nearby ARP2/3

complex to the spindle poles, reducing cortical retention to potentially lower actin branching efficiency and facilitate asymmetric membrane elongation and changes of cell shape (Figure 6.1B). This pathway may also be active when the mitotic spindle is off-centre during anaphase, to enable membrane elongation or blebbing on one side of the cortex to correct the cellular boundary of the eventual two daughter cells.

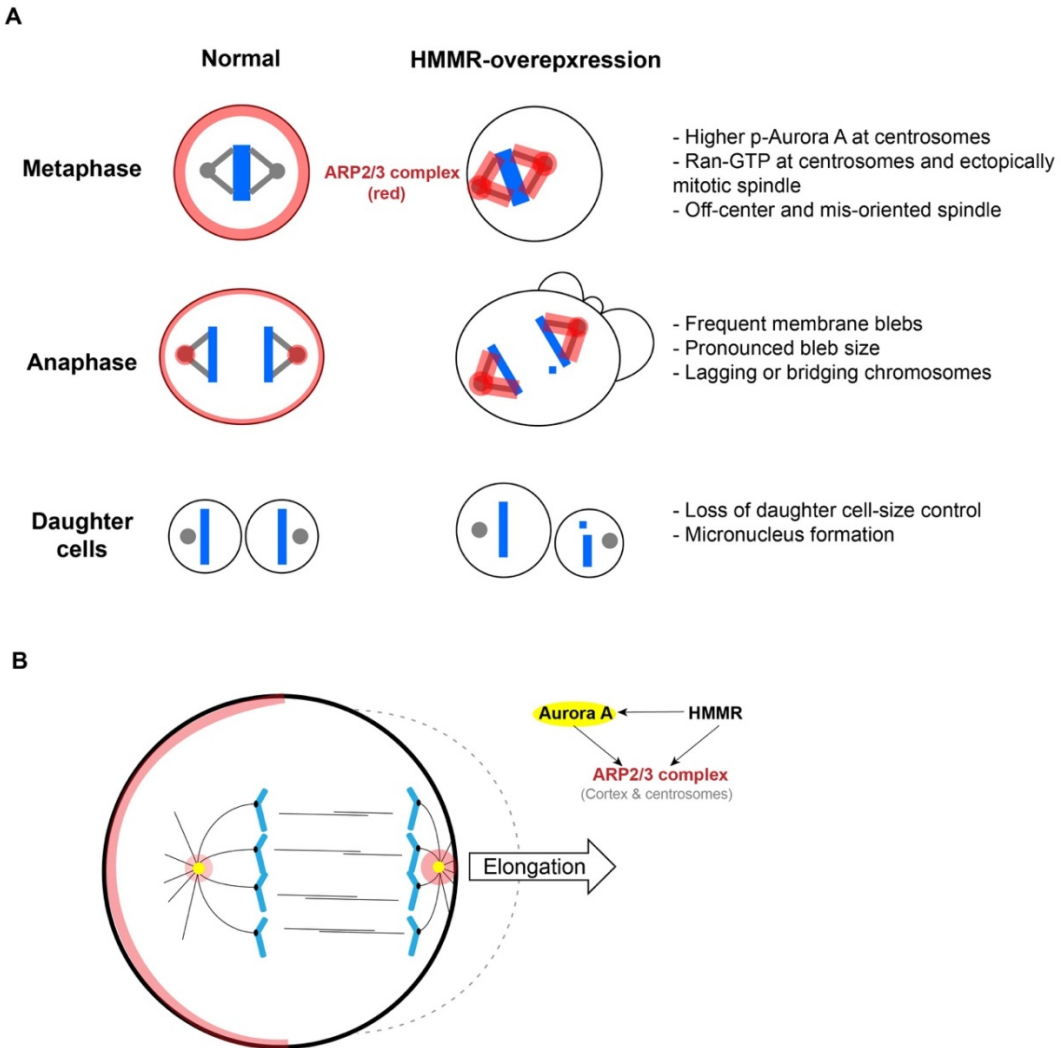

Figure 6.1 HMMR-mediated pathways that regulate anaphase asymmetric membrane blebbing and daughter cell size.

A) Summary of results observed from HMMR-overexpressing models.

B) As cells enter anaphase, a pool of ARP2/3 complex concentrates at the spindle poles to facilitate mitotic exit by altering cortex stability. When the mitotic spindle is displaced from the centre, HMMR on the spindle pole proximal to the cell cortex recruits cortical ARP2/3 complex to the spindle pole, where ARP2/3 complex may be phosphorylated by active Aurora A to inhibit its cortical retention.

6.2 Optimal HMMR levels are required for correct asymmetric membrane elongation during cell division

HMMR is involved in multiple pathways during mitosis and the maintenance of optimal levels of HMMR is critical. For example, BRCA1/BARD1 facilitates the degradation of HMMR to regulate TPX2 concentration on the spindle poles (Joukov *et al.*, 2006; Chen *et al.*, 2014), which is essential for activation of Aurora A and the recruitment of spindle assembly factors (SAFs) (Wittmann *et al.*, 2000). Both silencing and overexpression of HMMR leads to mitotic spindle defects such as multipolar spindles and consequent chromosome mis-segregation (Chen *et al.*, 2014; He *et al.*, 2020), which can result in genomic instability and tumorigenesis (Telmer *et al.*, 2011).

Optimal HMMR levels are also important for effective asymmetric membrane elongation because the absence of HMMR in HMMR-silenced cells leads to constantly rotating and moving spindles (Connell *et al.*, 2017). These kinetic spindles may reduce the time needed for asymmetric membrane blebbing to generate cytosolic flow in response to spindle proximity. On the other hand, in GFP-HMMR-overexpressing HeLa cells, small protrusions occur in metaphase to anaphase and the presence of pronounced bleb size both suggest reduced cortical-membrane attachment strength (Roh-Johnson and Goldstein, 2009; Beckham *et al.*, 2014).

Although non-apoptotic membrane blebbing has been reported to occur in mitotic cells in different cell lines, very few studies provide mechanistic insight into membrane blebbing as a mechanism to adjust the cellular boundary (Laster and Mackenzie, 1996; Boucrot and Kirchhausen, 2007; Khajah and Luqmani, 2016). Membrane blebbing appears more frequently from anaphase onset till cytokinesis compared to other mitotic phases as the amount of plasma membrane also increases rapidly during this period to facilitate the generation of daughter cells

(Boucrot and Kirchhausen, 2007). Here, my results suggest that the increased membrane blebbing during anaphase and cytokinesis may be not only a rapid method to increase the surface area of the cell, but also a regulated process that the position or direction of the blebs, the size of the blebs and the timing of blebbing are tightly controlled.

6.3 HMMR may play a role in the crosstalk between filament systems during mitosis

HMMR regulates spindle orientation and position through control of cortical protein localization during mitosis (Dunsch *et al.*, 2012; Chen *et al.*, 2014; Connell *et al.*, 2017). HMMR also affects spindle assembly and integrity through TPX2 and Aurora A, which regulate the recruitment of spindle assembly factors and motor proteins that move along microtubules (Chen *et al.*, 2014, 2018). These findings address the effect of HMMR on microtubule regulation during cell division. Here, my study sheds light on the link between HMMR and the actin network.

Although HMMR does not contain canonical actin-binding motifs, it shares similar sequence and structures with tropomyosin, which stabilizes filamentous actin (Ayscough, 1998). HMMR interacts with polymerized actin using standard *in vitro* binding assays (Assmann *et al.*, 1999). Also, HMMR-regulated Aurora A plays a role in actin cytoskeleton organization by phosphorylating actin-regulatory proteins (Berdnik and Knoblich, 2002; Hirota *et al.*, 2003; Wang *et al.*, 2010; Ritchey *et al.*, 2012; Moon and Matsuzaki, 2013; Zhao *et al.*, 2019). In this study, we identified a novel set of actin-binding proteins as potential binding partners of HMMR during mitosis and I specifically focused on the ARP2/3 complex. Similar to other Aurora A substrates that regulate actin, ARP2/3 complex may be phosphorylated by Aurora A at the spindle pole to modify its actin branching ability. The ARP2/3 complex plays a role in assembling spindle actin at the spindle and aberrant spindle actin is associated with impaired

mitotic spindle formation, resulting in disorganized chromosome segregation (Plessner *et al.*, 2019). This result is consistent with my observation of induced bridging and lagging chromosomes during anaphase and cytokinesis in GFP-HMMR overexpressing cells. Also, cytoskeletal structures change around the spindle poles as cells enter anaphase (Farina *et al.*, 2019). During anaphase, the intensity of microtubules decreases while actin filaments begin to form around the centrosomes and this change of cytoskeletal structures in the cells may facilitate mitotic exit (Farina *et al.*, 2019).

The changes in the ARP2/3 complex localization at cortex and spindle in cells with increased HMMR levels is associated with anaphase blebbing events, which are regulated by actomyosin and cortical stability. HMMR interacts with both microtubules and actin filaments and potentially regulates actin-regulating protein such as the ARP2/3 complex. Hence, HMMR may contribute to this crosstalk between the two filament systems during mitosis.

6.4 Aberrant daughter cell-size related phenotypes associated with HMMR overexpression might accelerate tumorigenesis

The effect of HMMR overexpression *in vivo* was examined in *Drosophila* neuroblasts expressing human HMMR and in transgenic mouse mammary epithelial cells following Cre-driven recombination events *in situ* and *ex vivo*. Consistent with the results I found in HeLa cells, the abnormal expression of HMMR in *Drosophila* neuroblasts induced membrane blebbing events that displayed greater bleb size compared with control. Nevertheless, the expression of HMMR, or GFP-HMMR, in neuroblasts did not result in gross abnormal phenotypes in these flies. Ectopic expression of HMMR in mouse mammary epithelial cells, however, did have a pronounced effect on *Brca1*-related tumorigenesis (Mateo, He, Mei *et al.*, 2022).

HMMR expression is linked to progression of disease and decreased survival rate in different cancers (Wang *et al.*, 1998; Yamada *et al.*, 1999; Li *et al.*, 2000; Rein *et al.*, 2003; Gust *et al.*, 2009; Shigeishi *et al.*, 2014) and is considered as a sign for poor prognosis (Hall *et al.*, 1995; Akiyama *et al.*, 2001; Zlobec and Lugli, 2008; Gust *et al.*, 2009; Ishigami *et al.*, 2011). *HMMR* is a breast cancer susceptibility gene (Pujana *et al.*, 2007), and haplotypes associated with either elevated *HMMR* expression or reduced *HMMR* expression both correlate with elevated risk for developing breast cancer in *BRCA1* mutation carriers (Pujana *et al.*, 2007). However, it was unclear how HMMR might play a role in tumorigenesis of BRCA1-associated cancers.

I found that abnormal blebbing during anaphase in HMMR-overexpressing cells was associated with bridging and lagging chromosomes, resulting in the formation of micronuclei. In the *Blg-Cre; $HMMR^{Tg/Tg}$; $Brca1^{f/f}$; $Trp53^{+/-}$* mouse model, we detected an increased number of cells with micronuclei, which was associated with activated cGAS-STING pathway and non-canonical NF- κB to recruit tumor-associated macrophages (TAMs) (Mateo, He, Mei *et al.*, 2022). Premalignant *Blg-Cre; $HMMR^{Tg/Tg}$; $Brca1^{f/f}$; $Trp53^{+/-}$* mouse tissue showed a higher level of CD45-positive cells as well as cells that express TAM markers, including CD68, F4/80, and VCAM1 (Mateo, He, Mei *et al.*, 2022). Collectively, these results suggest that HMMR overexpression induces mitotic instability that aggravates pro-tumorigenic processes, resulting in greater tumorigenesis in mammary tissues.

Our recent study focussed on the proinflammatory signals induced by mitotic instability in HMMR-overexpressing cells (Mateo, He, Mei *et al.*, 2022). In addition, I found a dramatic effect on daughter cell sizes. Similarly, Mu *et al.* found heterogenous cell sizes in a carcinoma cell-line with the smaller cells being more prone to metastasis (Mu *et al.*, 2017). As well, the

smaller colorectal cancer cells show higher levels of YAP1 which controls cell size and growth (Tumaneng *et al.*, 2012; Mu *et al.*, 2017). Finally, different level of cytoplasmic content can affect cell behaviour (Kiyomitsu, 2015). Thus, the loss of daughter cell size control, induced via elevated expression of HMMR, may also augment tumorigenesis.

6.5 HMMR is a centrosome protein rather than an extracellular receptor

HMMR is a controversial protein due to its potential intracellular and extracellular functions. As mentioned in the introduction, HMMR was first identified from murine cells as part of a hyaluronan receptor complex (Hardwick *et al.*, 1992). However, early studies used reagents that identified proteins smaller than full-length HMMR (Hofmann *et al.*, 1998a). Later studies identified full-length HMMR and the gene product was intracellular; thus, it was also named IHABP (Hofmann *et al.*, 1998b; Fieber *et al.*, 1999). In this thesis, my research focuses on the role of HMMR during cell division, when HMMR expression is elevated (Sohr and Engeland, 2008; Ly *et al.*, 2017).

To examine the correlation between HMMR and cell proliferation across different non-cancerous tissues, I compared expression level of HMMR and a set of proliferation markers, including PCNA, Ki67 and MCM2 (Whitfield *et al.*, 2006). I re-analysed data from NCBI GEO public database that is processed by Gene Expression database of Normal and Tumour tissues 2 (GENT2) (Park *et al.*, 2019) to examine the trend between the expression level of HMMR and the proliferation markers (Figure 6.2A). I observed a modest association between elevated expression of HMMR and proliferation markers. Individual tissue sample analysis also showed positive correlation between HMMR and the proliferation markers except MCM2 in bladder and PCNA in adipose, adrenal gland, bladder, pharynx and prostate (Figure 6.2B). In addition,

similar analysis from RNA-seq data collected by the Genotype-Tissue Expression (GTEx) project across normal tissues and the data was first processed by Expression atlas, as described (Papatheodorou *et al.*, 2018). Gene expression data from RNA-seq also suggests a correlation between HMMR and the selected proliferation markers in tissues with HMMR expression >1 TPM (Figure 6.2C). Although HMMR expression level varies in some tissue types between the two datasets, higher expression of HMMR and proliferation markers in testis are consistent.

In addition to the correlation with proliferation markers, I also extracted data for a set of mitotic markers (TPX2, AURKA, CCNB1, PLK1, BUB1) which show high expression during cell division (Whitfield *et al.*, 2002) and I repeated the analysis as described for Figure 6.2. Compare to data of proliferation markers, gene expression of mitotic markers shows a higher correlation with higher HMMR expression (Figure 6.3A) with positive correlation across most tissue types (Figure 6.3B) in both datasets (Figure 6.3C). This gene expression analysis emphasizes the role of HMMR in proliferation and cell division in human tissues.

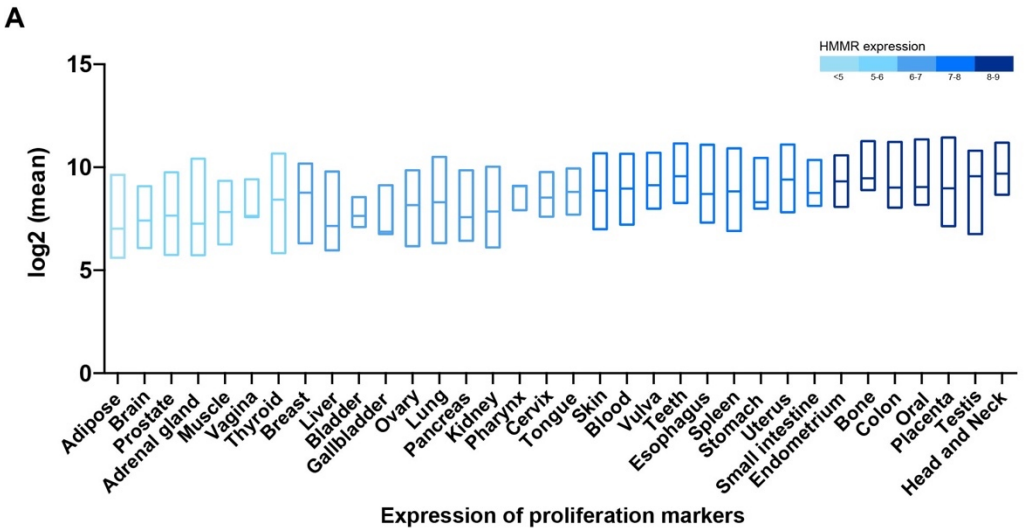
A
HMMR expression
<5
5-6
6-7
7-8
8-9
log2 (mean)
15
10
5
0
Adipose
Brain
Prostate
Adrenal gland
Muscle
Vagina
Thyroid
Breast
Liver
Bladder
Gallbladder
Ovary
Lung
Pancreas
Kidney
Pharynx
Cervix
Tongue
Skin
Blood
Vulva
Teeth
Esophagus
Spleen
Stomach
Uterus
Small intestine
Endometrium
Bone
Colon
Oral
Placenta
Testis
Head and Neck
Expression of proliferation markers

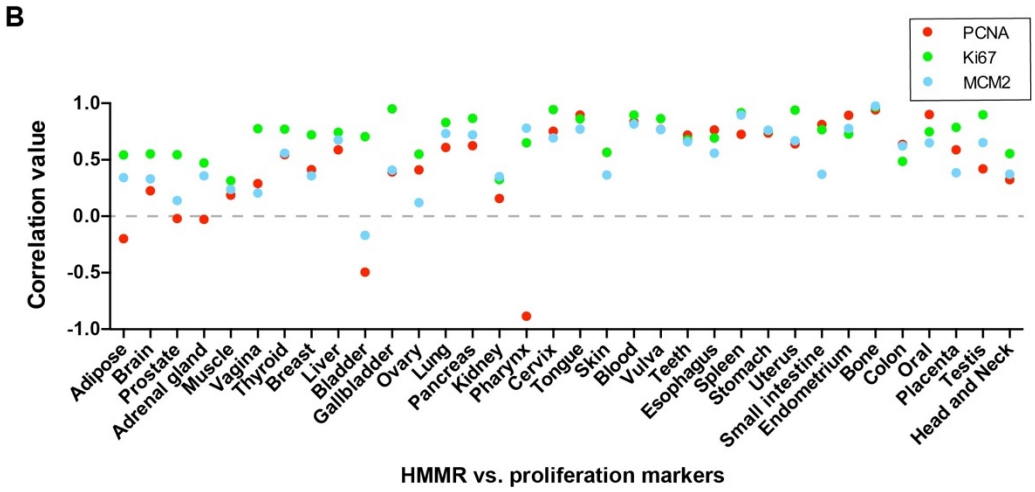
B
PCNA
Ki67
MCM2
Correlation value
1.0
0.5
0.0
-0.5
-1.0
Adipose
Brain
Prostate
Adrenal gland
Muscle
Vagina
Thyroid
Breast
Liver
Bladder
Gallbladder
Ovary
Lung
Pancreas
Kidney
Pharynx
Cervix
Tongue
Skin
Blood
Vulva
Teeth
Esophagus
Spleen
Stomach
Uterus
Small intestine
Endometrium
Bone
Colon
Oral
Placenta
Testis
Head and Neck
HMMR vs. proliferation markers

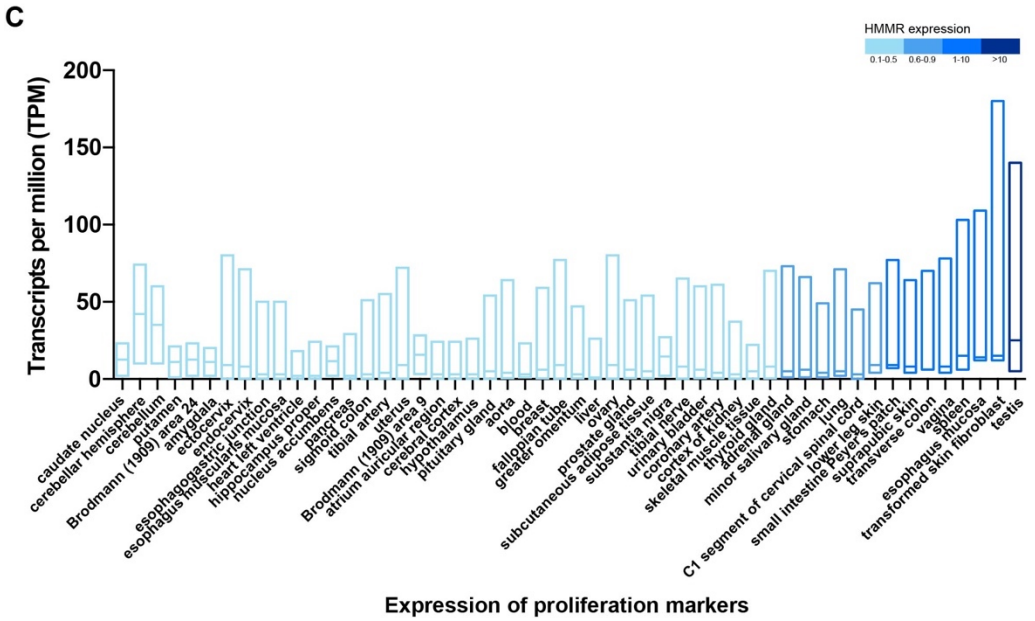
C
HMMR expression
0.1-0.5
0.6-0.9
1-10
>10
Transcripts per million (TPM)
200
150
100
50
0
caudate nucleus
cerebellar hemisphere
cerebellum
putamen
Brodmann (1909) area 24
amygdala
ectocervix
endocervix
esophagogastric junction
esophagus muscularis mucosa
heart left ventricle
hippocampus proper
nucleus accumbens
pancreas
sigmoid colon
tibial artery
Brodmann (1909) area 9
uterus
atrium auricular region
cerebral cortex
hypothalamus
pituitary gland
aorta
blood
breast
fallopian tube
greater omentum
liver
ovary
prostate gland
subcutaneous adipose tissue
substantia nigra
tibial nerve
urinary bladder
coronary artery
cortex of kidney
skeletal muscle tissue
thyroid gland
adrenal gland
minor salivary gland
stomach
lung
C1 segment of cervical spinal cord
lower leg skin
small intestine Peyer's patch
suprapubic skin
transverse colon
vagina
spleen
esophagus mucosa
transformed skin fibroblast
testis
Expression of proliferation markers

Figure 6.2 Correlation between HMMR and proliferation markers across different normal human tissues.

A) Gene expression of proliferation markers including PCNA, Ki67 and MCM2 across normal human tissues. Expression data was generated by U133Plus2 microarray platform from NCBI GEO database and the data is further processed with the MAS5 algorithm, as described (Park *et al.*, 2019). Mean expression of the three proliferation markers in each tissue type was calculated respectively and plotted for each tissue type. Expression level of HMMR is categorized and colour-coded.

B) Correlation value between HMMR and each proliferation markers (PCNA, Ki67, MCM2) across normal human tissues. Expression data was generated by U133Plus2 microarray platform from NCBI GEO database and the data is further processed with the MAS5 algorithm, as described (Park *et al.*, 2019).

C) Gene expression of proliferation markers including PCNA, Ki67 and MCM2 across normal human tissues. Tissue-specific gene expression data was generated by RNA-seq from 52 human tissue samples from the Genotype-Tissue Expression (GTEx) project and expression values as TPM for each sample was calculated by Expression atlas, as described (Papatheodorou *et al.*, 2018). Expression level shown in transcripts per million (TPM). Expression level of HMMR is categorized and colour-coded.

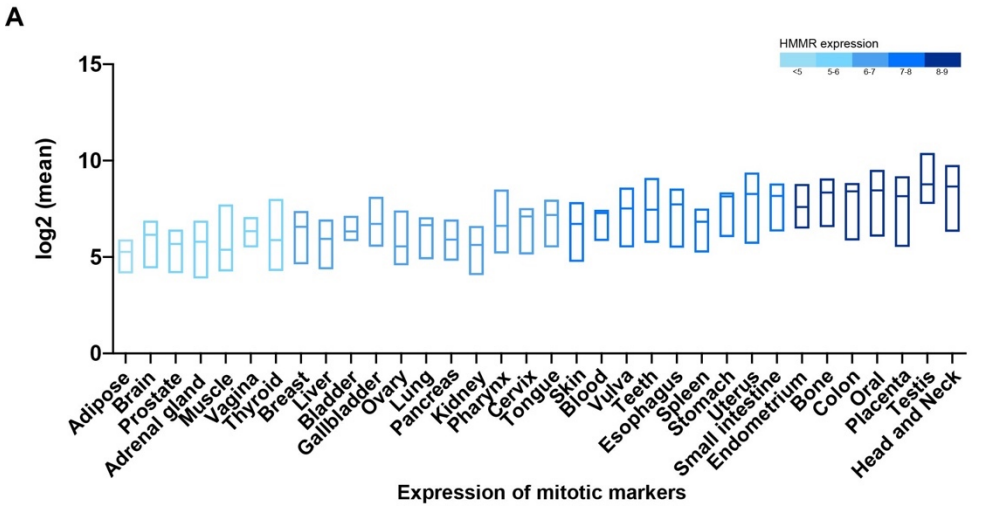
A
HMMR expression
<5
5-6
6-7
7-8
8-9
log2 (mean)
15
10
5
0
Adipose
Brain
Prostate
Adrenal gland
Muscle
Vagina
Thyroid
Breast
Liver
Bladder
Gallbladder
Ovary
Lung
Pancreas
Kidney
Pharynx
Cervix
Tongue
Skin
Blood
Vulva
Teeth
Esophagus
Spleen
Stomach
Uterus
Small intestine
Endometrium
Bone
Colon
Oral
Placenta
Testis
Head and Neck
Expression of mitotic markers

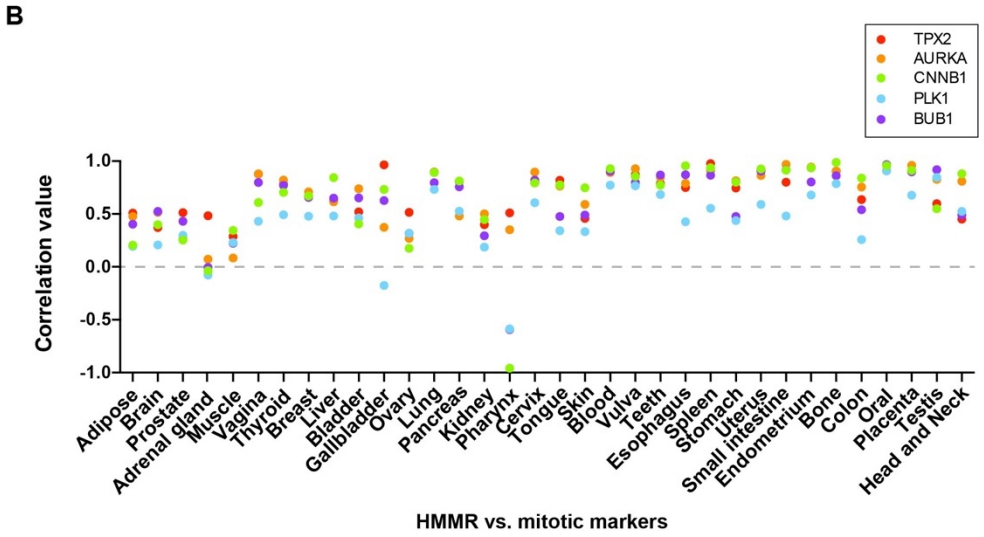
B
TPX2
AURKA
CNNB1
PLK1
BUB1
Correlation value
1.0
0.5
0.0
-0.5
-1.0
Adipose
Brain
Prostate
Adrenal gland
Muscle
Vagina
Thyroid
Breast
Liver
Bladder
Gallbladder
Ovary
Lung
Pancreas
Kidney
Pharynx
Cervix
Tongue
Skin
Blood
Vulva
Teeth
Esophagus
Spleen
Stomach
Uterus
Small intestine
Endometrium
Bone
Colon
Oral
Placenta
Testis
Head and Neck
HMMR vs. mitotic markers

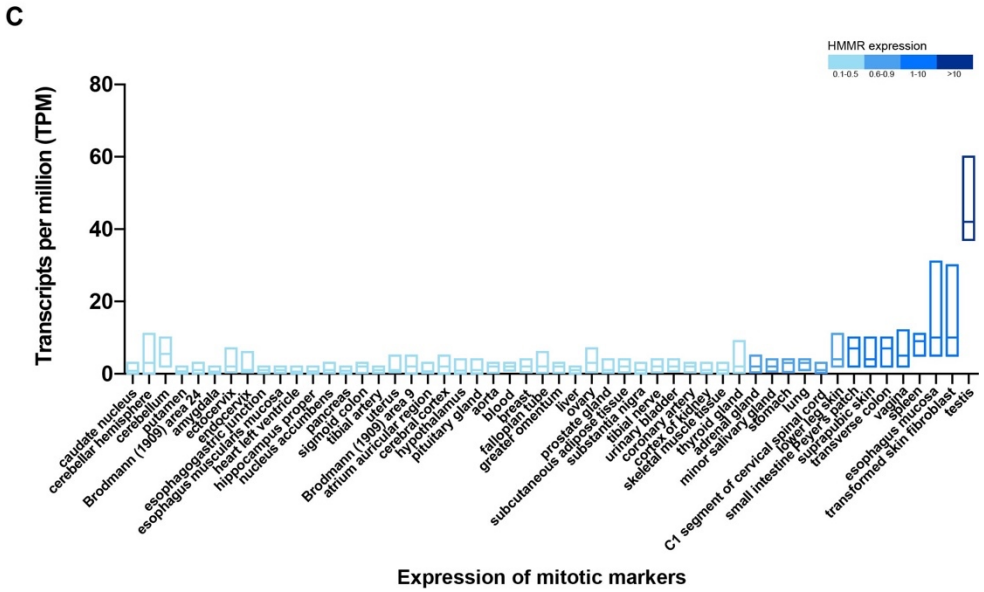
C
HMMR expression
0.1-0.5
0.6-0.9
1-10
>10
Transcripts per million (TPM)
80
60
40
20
0
caudate nucleus
cerebellar hemisphere
cerebellum
putamen 24
amygdala
ectocervix
endocervix
esophagogastric junction
esophagus mucosa
esophagus muscularis
heart left ventricle
hippocampus proper
nucleus accumbens
pancreas
sigmoid colon
tibial artery
uterus
Brodmann (1909) area 9
atrium auricular region
cerebral cortex
hypothalamus
pituitary gland
aorta
blood
breast
fallopian tube
greater omentum
liver
ovary
prostate gland
subcutaneous adipose tissue
substantia nigra
tibial nerve
urinary bladder
coronary artery
cortex of kidney
skeletal muscle tissue
thyroid gland
adrenal gland
minor salivary gland
stomach
lung
C1 segment of cervical spinal cord
lower leg skin
Peyer's patch
small intestine terminal ileum
suprapubic skin
transverse colon
vagina
spleen
esophagus mucosa
transformed skin fibroblast
testis
Expression of mitotic markers

Figure 6.3 Correlation between HMMR and mitotic markers across different normal human tissues.

A) Gene expression of mitotic markers including TPX2, AURKA, CCNB1, PLK1 and BUB1 across normal human tissues. Expression data was generated by U133Plus2 microarray platform from NCBI GEO database and the data is further processed with the MAS5 algorithm, as described (Park *et al.*, 2019). Mean expression of the three proliferation markers in each tissue type was calculated respectively and plotted for each tissue type. Expression level of HMMR is categorized and colour-coded.

B) Correlation value between HMMR and each mitotic marker (TPX2, AURKA, CCNB1, PLK1, BUB1) across normal human tissues. Expression data was generated by U133Plus2 microarray platform from NCBI GEO database and the data is further processed with the MAS5 algorithm, as described (Park *et al.*, 2019).

C) Gene expression of mitotic markers including TPX2, AURKA, CCNB1, PLK1 and BUB1 across normal human tissues. Tissue-specific gene expression data was generated by RNA-seq from 52 human tissue samples from the Genotype-Tissue Expression (GTEx) project and expression values as TPM for each sample was calculated by Expression atlas, as described (Papatheodorou *et al.*, 2018). Expression level shown in transcripts per million (TPM). Expression level of HMMR is categorized and colour-coded.

6.6 Limitations in the scope of this thesis

In my thesis, I propose an HMMR-mediated pathway that regulates daughter cell-size ratio by modifying localization of ARP2/3 complex through Aurora A. It is worth discussing that HMMR also regulates other pathways that contribute to spindle positioning and potentially cortical actomyosin localization simultaneously during cell division.

First, HMMR regulates Ran-GTP localization to the centrosomes in a PLK1-dependent manner (Connell *et al.*, 2017). Chromosome-derived Ran-GTP strips off cortical anillin locally when spindles approach to one side of the cortex and thus induces asymmetric membrane elongation (Kiyomitsu and Cheeseman, 2013). In GFP-HMMR-overexpressing HeLa cells, Ran localizes to the mitotic spindles ectopically along with loss of cortical NuMA localization, which phenocopied results observed in cells expressing constitutively active Ran (Connell *et al.*, 2017). Although HMMR is not essential for Ran localization at chromosomes which removes cortical NuMA and dynein at midzone during anaphase, I cannot exclude a potential effect on cortical

actomyosin from ectopic Ran localized at centrosomes in GFP-HMMR overexpressing cells (Kiyomitsu and Cheeseman, 2012; Connell *et al.*, 2017).

Second, I propose that the HMMR-Aurora A-ARP2/3 complex axis regulates cortical stability or actin structure that potentially leads to pronounced membrane blebbing phenotypes in anaphase. It is important to keep in mind that Aurora A interacts with several other actin related proteins which may also affect cortical stability (Berdnik and Knoblich, 2002; Hirota *et al.*, 2003; Wang *et al.*, 2010; Ritchey *et al.*, 2012; Moon and Matsuzaki, 2013; Chen *et al.*, 2014; Zhao *et al.*, 2019).

Third, HMMR modifies multiple proteins that regulate spindle positioning and orientation, including Aurora A (Chen *et al.*, 2014), PLK1 (Nousiainen *et al.*, 2006; Chen *et al.*, 2014), CK1α (Fulcher *et al.*, 2019), and CHICA-DYNLL1 (Dunsch *et al.*, 2012). As a result, overexpression of HMMR leads to a rotating spindle and can recruit proteins to the centrosomes, spindle and chromosomes in close proximity to the cortex randomly. For example, PP1 at the kinetochore dephosphorylates erzin/radixin/moesin proteins as the chromosomes are close to the polar cortex, inducing clearing of cortical actin (Rodrigues *et al.*, 2015). These pathways may also contribute to the regulation of cortical actin and thus affecting membrane blebbing events. Therefore, multiple pathways may contribute to asymmetric membrane blebbing or cortical stiffness regulation simultaneously during anaphase, and the relative contribution of the proposed HMMR-Aurora A-ARP2/3 complex pathway, warrants further study.

6.7 Suggested future studies

6.7.1 How are actin and microtubule structures changing during cell division in HMMR overexpressing cells?

In this thesis, I propose that cortical instability is associated with mis-localization of ARP2/3 complex. However, I have not yet examined the effect of HMMR overexpression or ARP2/3 complex localization on the cytoskeleton during cell division.

The actin cytoskeleton is critical for the regulation of mitotic cell shape and cortical tension (Chugh *et al.*, 2017). Compared to interphase cells, mitotic cells show lower cortical thickness and higher cortical tension (Chugh *et al.*, 2017). Although many studies focus on the role of myosin on cortical tension, mechanical changes by modification of actin filaments also contribute to cortical stability (Taubenberger *et al.*, 2020). For example, an amorphous cluster of actin filaments revolves along the cell cortex from prometaphase to anaphase and fuses into the contractile ring (Mitsushima *et al.*, 2010). This revolving cloud of actin structures depends on rapid depolymerization and polymerization along the cell cortex and the ARP2/3 complex is essential for the formation and movement of the actin cluster (Mitsushima *et al.*, 2010).

I found that cortical ARPC2 was reduced in GFP-HMMR overexpressing cells that had increased blebbing frequency. Therefore, I hypothesize that GFP-HMMR overexpressing cells may display aberrant cortex thickness and disrupted revolving actin clusters. Indeed, the distribution of the actin network was abnormal in GFP-HMMR overexpressing tet-on HeLa cells (Figure 3.6). In these cells, reduced cortical ARP2/3 complex may affect actin turnover and structure, thus altering cortex integrity (Charras *et al.*, 2005). To test this, atomic force microscopy can be used to measure cortical tension and I expect a decrease of membrane tension in GFP-HMMR overexpressing cells compare to parental and non-induced HeLa (-dox) cells. In

addition, live cell imaging using Life-Act to visualize actin filaments, or by expressing GFP-Utrch that binds to actin filaments, can detect the revolving actin cluster in parental and HMMR overexpressing cells. Finally, the decoupling of the cortex and membrane promotes blebbing (Beckham *et al.*, 2014), and I would evaluate cortex-membrane coupling through localization of myosin regulatory light-chain and the PH domain of phospholipase C (PLC), respectively. In GFP-HMMR overexpressing cells, I expect to observe reduced co-localization of the cell cortex and membrane.

The actin and microtubule cytoskeletons influence each other during cell division (Farina *et al.*, 2019). As mentioned in section 6.3, a decrease in microtubule density around centrosomes correlates with an increase in ARP2/3 complex when cells enter anaphase (Farina *et al.*, 2019). Inhibition of the ARP2/3 complex reduces spindle actin assembly and results in mitotic defects, such as chromosome mis-segregation, promoting micronuclei formation (Plessner *et al.*, 2019). Since I found that a pool of ARP2/3 complex was prematurely accumulating around the spindle poles prior to anaphase, I would examine actin and microtubule density around centrosomes from prometaphase to anaphase. An elevated level of ARP2/3 complex concentrated at the mitotic spindle, instead of inhibition or depletion, may also disrupt astral spindle assembly of microtubules and feed into the pronounced spindle rotation phenotypes I observed during mitosis in GFP-HMMR overexpressing tet-on HeLa cells.

6.7.2 How is the ARP2/3 complex recruited to the spindle poles?

In this study, I found that HMMR overexpression reduced the cortical localization of ARP2/3 complex during mitosis and that this effect was reversible through the inhibition of Aurora A. Accumulation of the ARP2/3 complex at the spindle poles, which normally occurs as

cells enter anaphase (Farina *et al.*, 2019), and the activity of Aurora A (Thr288) were both increased in GFP-HMMR-overexpressing cells. Consistently, GFP-AURKA expressing cells showed similar but relatively muted alterations to ARPC2 and downstream events; in fact, GFP-AURKA expressing cells did not result in higher p-Aurora A measured at spindle poles. It is possible that TPX2 might be the limiting factor in this pathway; that is, overexpression of HMMR may activate Aurora A more efficiently through the correct localization of TPX2, whereas overexpression of GFP-AURKA may require additional localization of TPX2 for optimal activation. To test this, we can transduce HeLa cells with lentivirus plasmid expressing GFP-TPX2 and determine if p-Aurora A level at centrosomes is elevated as observed in GFP-HMMR overexpressing cells. To investigate the movement of ARP2/3 complex in living cells, wild-type ARP2/3 components fused to RFP could be imaged in the corresponding component-depleted cells while inducing GFP-HMMR or GFP-TPX2 expression. Moreover, I suggest to use AdPROM to rescue the potential phenotypes in GFP-TPX2 overexpressing cells.

The mechanism by which active Aurora A promotes the spindle pole localization of ARPC2 is not known. Multiple potential S/T phosphorylation sites in components of the ARP2/3 complex were identified in Chapter 4. Among the seven subunits, I would focus future experiments on examining the phosphorylation sites of ARP3, ARPC2 and ARPC1B. ARP3 is highlighted in the IP-MS data analysis in section 3.2.8. Aurora A phosphorylates Thr21 of ARPC1B (Molli *et al.*, 2010). To study the effect of Thr21 phosphorylation on ARP2/3 complex localization, I would generate phosphomimetic mutants of the subunits separately or in combination by mutating serine and threonine to aspartic acid and glutamic acid in HeLa cells (Chen and Cole, 2015). In this case, we can track the localization of ARP2/3 complex using live

cell imaging or immunofluorescence and determine if phosphorylation of these components would resemble the results in GFP-HMMR overexpressing cells.

6.7.3 How does *HMMR* rs299290 affect cell division?

In Chapter 5, I examined luminal progenitor cells isolated from *BRCA1* mutation carriers and evaluated the mitotic phenotypes relevant to daughter cell size control. Among the three *BRCA1* mutation carriers, the luminal progenitor cells from a carrier with HMMR rs299290 expressed elevated levels of HMMR compared to control groups. Due to the limited number of mitotic cells from the other carrier samples, it remained unclear if *BRCA1* mutated cells with *HMMR* rs299290 expressed a higher level of HMMR than other *BRCA1* mutant cells. Moreover, the exclusive effect of *HMMR* rs299290 without *BRCA1* mutation is unknown. We are still not sure yet to what degree *HMMR* rs299290 solely can affect cell division process.

To investigate this, I intended to generate rs299290 T>C substitution using gene editing methods, including CRISPR-Cas9, Prime editing, PRIME-Del and Prime editing with mRNA delivery. Due to sequence complexity for efficient gene editing, we are still in the process of optimizing editing design and method. Once clonal MCF10A cells with rs299290 SNP are generated, I propose to examine the HMMR expression level in order to determine if rs299290 SNP without BRCA1 mutation can lead to elevated HMMR level. Next, I would investigate whether *HMMR* rs299290 affects daughter cell-size relevant phenotypes, including spindle position, anaphase blebbing frequency, bleb size and ARP2/3 complex localization.

HMMR rs299290 is an eQTL for *HMMR* and a missense valine-to-alanine change (amino acid 368), which falls within the defined CHICA binding region (amino acid 365-546) (Maxwell *et al.*, 2011; Dunsch *et al.*, 2012). HMMR interacts with CHICA and forms a complex with

DYNLL1 to regulate cortical dynein localization (Dunsch *et al.*, 2012). I hypothesize the rs299290 T>C substitution may attenuate the interaction between HMMR and CHICA and, thus, lower the level of DYNLL1 on the spindles. As a result, cortical localization of dynein may not be regulated in response to spindle position, which may cause more frequent membrane blebbing in order to correct the daughter cell-size ratio. I propose to investigate the interaction between rs299290 T>C HMMR and CHICA by performing reciprocal immunoprecipitation and evaluating the localization of cortical dynein, using DHC-GFP, with respect to spindle position. Together, these studies will determine whether *HMMR* rs299290 increases the absolute expression of HMMR and alters the critical HMMR-CHICA interaction, which is needed to control intrinsic spindle positioning pathways.

6.8 Final remarks

This study identified a HMMR-Aurora A kinase mediated pathway that affects the localization of ARPC2 and induces abnormal asymmetric membrane elongation events. This molecular axis may be critical for the normal regulation of daughter cell sizes through rapid membrane blebbing during anaphase. This pathway was identified through the *in vitro* study of immortal cancer cells but was also found to influence membrane blebbing events in *Drosophila* neuroblasts, transgenic mouse models, and primary samples isolated from *BRCA1* mutation carriers.

Bibliography

Adey, A., Burton, J. N., Kitzman, J. O., Hiatt, J. B., Lewis, A. P., Martin, B. K., Qiu, R., Lee, C., and Shendure, J. (2013). The haplotype-resolved genome and epigenome of the aneuploid HeLa cancer cell line. Nature *500*, 207–211.

Adikusuma, F. *et al.* (2021). Optimized nickase- and nuclease-based prime editing in human and mouse cells. Nucleic Acids Res. *49*, 10785–10795.

Agarwal, P., and Zaidel-Bar, R. (2019). Principles of Actomyosin Regulation In Vivo. Trends Cell Biol. *29*, 150–163.

Akiyama, Y., Jung, S., Salhia, B., Lee, S., Hubbard, S., Taylor, M., Mainprize, T., Akaishi, K., Van Furth, W., and Rutka, J. T. (2001). Hyaluronate receptors mediating glioma cell migration and proliferation. J. Neurooncol. *53*, 115–127.

Alam, M. S. (2018). Proximity Ligation Assay (PLA). Curr Protoc Immunol. *123*, e58.

Anzalone, A. V. *et al.* (2019). Search-and-replace genome editing without double-strand breaks or donor DNA. Nature *576*, 149–157.

Assmann, V., Gillett, C. E., Poulsom, R., Ryder, K., Hart, I. R., and Hanby, A. M. (2001). The pattern of expression of the microtubule-binding protein RHAMM/IHABP in mammary carcinoma suggests a role in the invasive behaviour of tumour cells. J. Pathol. *195*, 191–196.

Assmann, V., Jenkinson, D., Marshall, J. F., and Hart, I. R. (1999). The intracellular hyaluronan receptor RHAMM/IHABP interacts with microtubules and actin filaments. J. Cell Sci. *112*, 3943–3954.

Assmann, V., Marshall, J. F., Fieber, C., Hofmann, M., and Hart, I. R. (1998). The human hyaluronan receptor RHAMM is expressed as an intracellular protein in breast cancer cells. J. Cell Sci. *111 (Pt 1*, 1685–1694.

Atwood, S. X., and Prehoda, K. E. (2009). Article aPKC Phosphorylates Miranda to Polarize Fate Determinants during Neuroblast Asymmetric Cell Division. Curr. Biol. *19*, 723–729.

Ayscough, K. R. (1998). In vivo functions of actin-binding proteins. Curr. Opin. Cell Biol. *10*, 102–111.

Badirou, I., Pan, J., Legrand, C., Wang, A., Lordier, L., Boukour, S., Roy, A., Vainchenker, W., and Chang, Y. (2014). Carboxyl-terminal-dependent recruitment of nonmuscle myosin II to megakaryocyte contractile ring during polyploidization. Blood *124*, 2564–2568.

Bae, S., Kweon, J., Kim, H. S., and Kim, J. S. (2014). Microhomology-based choice of Cas9 nuclease target sites. Nat. Methods *11*, 705–706.

Baird, M. A., Billington, N., Wang, A., Adelstein, R. S., Sellers, J. R., Fischer, R. S., and Waterman, C. M. (2017). Local pulsatile contractions are an intrinsic property of the myosin 2A motor in the cortical cytoskeleton of adherent cells. Mol. Biol. Cell *28*, 240–251.

Bakhoum, S. F. *et al.* (2018). Chromosomal instability drives metastasis through a cytosolic DNA response. Nature *553*, 467–472.

Barros, T. P., Kinoshita, K., Hyman, A. A., and Raff, J. W. (2005). Aurora A activates D-TACC-Msps complexes exclusively at centrosomes to stabilize centrosomal microtubules. J. Cell Biol. *170*, 1039–1046.

Bateman, A. (2019). UniProt: A worldwide hub of protein knowledge. Nucleic Acids Res. *47*, D506–D515.

Bayliss, R., Sardon, T., Vernos, I., and Conti, E. (2003). Structural basis of Aurora-A activation

by TPX2 at the mitotic spindle. Mol. Cell *12*, 851–862.
Beach, J. R., and Egelhoff, T. T. (2009). Myosin II recruitment during cytokinesis independent of centralspindlin-mediated phosphorylation. J. Biol. Chem. *284*, 27377–27383.
Beach, J. R., Shao, L., Remmert, K., Li, D., Betzig, E., and Hammer, J. A. (2014). Nonmuscle myosin II isoforms coassemble in living cells. Curr. Biol. *24*, 1160–1166.
Beaudet, D., Akhshi, T., Phillipp, J., Law, C., and Piekny, A. (2017). Active Ran regulates anillin function during cytokinesis. Mol. Biol. Cell *28*, 3517–3531.
Beckham, Y., Vasquez, R. J., Stricker, J., Sayegh, K., Campillo, C., and Gardel, M. L. (2014). Arp2/3 inhibition induces amoeboid-like protrusions in MCF10A epithelial cells by reduced cytoskeletal-membrane coupling and focal adhesion assembly. PLoS One *9*, e100943.
Berdnik, D., and Knoblich, J. A. (2002). Drosophila Aurora-A is required for centrosome maturation and actin-dependent asymmetric protein localization during mitosis. Curr. Biol. *12*, 640–647.
Bereiter-Hahn, J., Luck, M., Miebach, T., Stelzer, H. K., and Voth, M. (1990). Spreading of trypsinized cells: Cytoskeletal dynamics and energy requirements. J. Cell Sci. *96*, 171–188.
Bergert, M., Chandradoss, S. D., Desai, R. A., and Paluch, E. (2012). Cell mechanics control rapid transitions between blebs and lamellipodia during migration. Proc. Natl. Acad. Sci. U. S. A. *109*, 14434–14439.
Berglind, H., Pawitan, Y., Kato, S., Ishioka, C., and Soussi, T. (2008). Analysis of p53 mutation status in human cancer cell lines: A paradigm for cell line cross-contamination. Cancer Biol. Ther. *7*, 699–708.
Biro, M., Romeo, Y., Kroschwald, S., Bovellan, M., Boden, A., Tcherkezian, J., Roux, P. P., Charras, G., and Paluch, E. K. (2013). Cell cortex composition and homeostasis resolved by integrating proteomics and quantitative imaging. Cytoskeleton *70*, 741–754.
Bischoff, J. R. *et al.* (1998). A homologue of Drosophila aurora kinase is oncogenic and amplified in human colorectal cancers. EMBO J. *17*, 3052–3065.
Blanco, I. *et al.* (2015). Assessing associations between the AURKA-HMMR-TPX2-TUBG1 functional module and breast cancer risk in BRCA1/2 mutation carriers. PLoS One *10*, 1–18.
Bompard, G., Rabeharivelo, G., and Morin, N. (2008). Inhibition of cytokinesis by wiskostatin does not rely on N-WASP/Arp2/3 complex pathway. BMC Cell Biol. *9*, 1–14.
Boucrot, E., and Kirchhausen, T. (2007). Endosomal recycling controls plasma membrane area during mitosis. Proc. Natl. Acad. Sci. U. S. A. *104*, 7939–7944.
Bovellan, M. *et al.* (2014). Cellular control of cortical actin nucleation. Curr. Biol. *24*, 1628–1635.
Brownlee, C., and Heald, R. (2019). Importin α Partitioning to the Plasma Membrane Regulates Intracellular Scaling. Cell *176*, 805-815.e8.
Burgess, D. R., and Chang, F. (2005). Site selection for the cleavage furrow at cytokinesis. Trends Cell Biol. *15*, 156–162.
Cabernard, C., and Doe, C. Q. (2009). Apical/Basal Spindle Orientation Is Required for Neuroblast Homeostasis and Neuronal Differentiation in Drosophila. Dev. Cell *17*, 134–141.
Carmena, M., Ruchaud, S., and Earnshaw, W. C. (2009). Making the Auroras glow: regulation of Aurora A and B kinase function by interacting proteins. Curr. Opin. Cell Biol. *21*, 796–

805.
Castro, A., Vigneron, S., Bernis, C., Labbé, J. C., Prigent, C., and Lorca, T. (2002). The D-Box-activating domain (DAD) is a new proteolysis signal that stimulates the silent D-Box sequence of Aurora-A. EMBO Rep. *3*, 1209–1214.
Cazales, M., Schmitt, E., Montembault, E., Dozier, C., Prigent, C., and Ducommun, B. (2005). CDC25B phosphorylation by Aurora-A occurs at the G2/M transition and is inhibited by DNA damage. Cell Cycle *4*, 1233–1238.
Chang, C. W., Nashchekin, D., Wheatley, L., Irion, U., Dahlgaard, K., Montague, T. G., Hall, J., and St. Johnston, D. (2011). Anterior-posterior axis specification in drosophila oocytes: Identification of novel bicoid and oskar mRNA localization factors. Genetics *188*, 883–896.
Chapa-Y-Lazo, B., Hamanaka, M., Wray, A., Balasubramanian, M. K., and Mishima, M. (2020). Polar relaxation by dynein-mediated removal of cortical myosin II. J. Cell Biol. *219*.
Charras, G. T. (2008). A short history of blebbing. J. Microsc. *231*, 466–478.
Charras, G. T., Coughlin, M., Mitchison, T. J., and Mahadevan, L. (2008). Life and times of a cellular bleb. Biophys. J. *94*, 1836–1853.
Charras, G. T., Hu, C. K., Coughlin, M., and Mitchison, T. J. (2006). Reassembly of contractile actin cortex in cell blebs. J. Cell Biol. *175*, 477–490.
Charras, G. T., Yarrow, J. C., Horton, M. A., Mahadevan, L., and Mitchison, T. J. (2005). Non-equilibration of hydrostatic pressure in blebbing cells. Nature *435*, 365–369.
Chen, A., Ulloa Severino, L., Panagiotou, T. C., Moraes, T. F., Yuen, D. A., Lavoie, B. D., and Wilde, A. (2021a). Inhibition of polar actin assembly by astral microtubules is required for cytokinesis. Nat. Commun. *12*, 1–13.
Chen, H., Connell, M., Mei, L., Reid, G. S. D., and Maxwell, C. A. (2018). The nonmotor adaptor HMMR dampens Eg5-mediated forces to preserve the kinetics and integrity of chromosome segregation. Mol. Biol. Cell *29*, 786–796.
Chen, H., Mohan, P., Jiang, J., Nemirovsky, O., He, D., Fleisch, M. C., Niederacher, D., Pilarski, L. M., Lim, C. J., and Maxwell, C. A. (2014). Spatial regulation of Aurora A activity during mitotic spindle assembly requires RHAMM to correctly localize TPX2. Cell Cycle *13*, 2248–2261.
Chen, P. J. *et al.* (2021b). Enhanced prime editing systems by manipulating cellular determinants of editing outcomes. Cell *184*, 5635-5652.e29.
Chen, S. S., Chang, P. C., Cheng, Y. W., Tang, F. M., and Lin, Y. S. (2002). Suppression of the STK15 oncogenic activity requires a transactivation-independent p53 function. EMBO J. *21*, 4491–4499.
Chen, Z., and Cole, P. A. (2015). Synthetic Approaches to Protein Phosphorylation. Curr Opin Chem Biol *28*, 115–122.
Cheung, V. G., and Spielman, R. S. (2009). Genetics of human gene expression: Mapping DNA variants that influence gene expression. Nat. Rev. Genet. *10*, 595–604.
Chia, W., Somers, W. G., and Wang, H. (2008). Drosophila neuroblast asymmetric divisions: Cell cycle regulators, asymmetric protein localization, and tumorigenesis. J. Cell Biol. *180*, 267–272.
Chikina, A. S., Svitkina, T. M., and Alexandrova, A. Y. (2019). Time-resolved ultrastructure of the cortical actin cytoskeleton in dynamic membrane blebs. J. Cell Biol. *218*, 445–454.
Choi, J., Chen, W., Suiter, C. C., Lee, C., Chardon, F. M., Yang, W., Leith, A., Daza, R. M., Martin, B., and Shendure, J. (2022). Precise genomic deletions using paired prime editing.

Nat. Biotechnol. *40*, 218–226.
Chugh, P., Clark, A. G., Smith, M. B., Cassani, D. A. D., Dierkes, K., Ragab, A., Roux, P. P., Charras, G., Salbreux, G., and Paluch, E. K. (2017). Actin cortex architecture regulates cell surface tension. Nat. Cell Biol. *19*, 689–697.
Connell, M. *et al.* (2017). HMMR acts in the PLK1-dependent spindle positioning pathway and supports neural development. Elife *6*, 1–27.
Crainie, M., Belch, A. R., Mant, M. J., and Pilarski, L. M. (1999). Overexpression of the receptor for hyaluronan-mediated motility (RHAMM) characterizes the malignant clone in multiple myeloma: identification of three distinct RHAMM variants. Blood *93*, 1684–1696.
Crane, R., Kloepfer, A., and Ruderman, J. V. (2004). Requirements for the destruction of human Aurora-A. J. Cell Sci. *117*, 5975–5983.
Dalton, C. M., and Carroll, J. (2013). Biased inheritance of mitochondria during asymmetric cell division in the mouse oocyte. J. Cell Sci. *126*, 2955–2964.
Dey, S. K., Singh, R. K., Chattoraj, S., Saha, S., Das, A., Bhattacharyya, K., Sengupta, K., Sen, S., and Jana, S. S. (2017). Differential role of nonmuscle myosin II isoforms during blebbing of MCF-7 cells. Mol. Biol. Cell *28*, 1034–1042.
Dodson, C. A., and Bayliss, R. (2012). Activation of Aurora-A kinase by protein partner binding and phosphorylation are independent and synergistic. J. Biol. Chem. *287*, 1150–1157.
Dodson, C. A., Kosmopoulou, M., Richards, M. W., Atrash, B., Bavetsias, V., Blagg, J., and Bayliss, R. (2010). Crystal structure of an Aurora-A mutant that mimics Aurora-B bound to MLN8054: insights into selectivity and drug design. Biochem. J. *427*, 551.
Doench, J. G. *et al.* (2016). Optimized sgRNA design to maximize activity and minimize off-target effects of CRISPR-Cas9. Nat. Biotechnol. *34*, 184–191.
Dorn, J. F., and Maddox, A. S. (2011). Cytokinesis : Cells Go Back and Forth about Division. Curr. Biol. *21*, R848–R850.
Du, Y.-C. N., Chou, C.-K., Klimstra, D. S., and Varmus, H. (2011). Receptor for hyaluronan-mediated motility isoform B promotes liver metastasis in a mouse model of multistep tumorigenesis and a tail vein assay for metastasis. Proc. Natl. Acad. Sci. *108*, 16753–16758.
Dunsch, A. K., Hammond, D., Lloyd, J., Schermelleh, L., Gruneberg, U., and Barr, F. A. (2012). Dynein light chain 1 and a spindle-associated adaptor promote dynein asymmetry and spindle orientation. J. Cell Biol. *198*, 1039–1054.
Eibes, S., Gallisà-Suñé, N., Rosas-Salvans, M., Martínez-Delgado, P., Vernos, I., and Roig, J. (2018). Nek9 Phosphorylation Defines a New Role for TPX2 in Eg5-Dependent Centrosome Separation before Nuclear Envelope Breakdown. Curr. Biol. *28*, 121-129.e4.
Eirew, P., Stingl, J., Raouf, A., Turashvili, G., Aparicio, S., Emerman, J. T., and Eaves, C. J. (2008). A method for quantifying normal human mammary epithelial stem cells with in vivo regenerative ability. Nat. Med. *14*, 1384–1389.
Entwistle, J., Zhang, S., Yang, B., Wong, C., Li, Q., Hall, C. L., A, J., Mowat, M., Greenberg, A. H., and Turley, E. A. (1995). Characterization of the murine gene encoding the hyaluronan receptor RHAMM. Gene *163*, 233–238.
Even-Ram, S., Doyle, A. D., Conti, M. A., Matsumoto, K., Adelstein, R. S., and Yamada, K. M. (2007). Myosin IIA regulates cell motility and actomyosin-microtubule crosstalk. Nat. Cell Biol. *9*, 299–309.
Eyers, P. A., Churchill, M. E. A., and Maller, J. L. (2005). The Aurora A and Aurora B Protein

Kinases A Single Amino Acid Difference Controls Intrinsic Activity and Activation by TPX2. Cell Cycle *4*, 784–789.
Eyers, P. A., Erikson, E., Chen, L. G., and Maller, J. L. (2003). A Novel Mechanism for Activation of the Protein Kinase Aurora A. Curr. Biol. *13*, 654–658.
Farina, F. *et al.* (2019). Local actin nucleation tunes centrosomal microtubule nucleation during passage through mitosis. EMBO J. *38*, e99843.
Fieber, C., Plug, R., Sleeman, J., Dall, P., Ponta, H., and Hofmann, M. (1999). Characterisation of the murine gene encoding the intracellular hyaluronan receptor IHABP (RHAMM). Gene *226*, 41–50.
Forester, C. M., Maddox, J., Louis, J. V., Goris, J., and Virshup, D. M. (2007). Control of mitotic exit by PP2A regulation of Cdc25C and Cdk1. Proc. Natl. Acad. Sci. U. S. A. *104*, 19867–19872.
Fulcher, L. J. *et al.* (2019). FAM 83D directs protein kinase CK 1α to the mitotic spindle for proper spindle positioning. EMBO Rep. *20*, e47495.
Fulcher, L. J., Hutchinson, L. D., Macartney, T. J., Turnbull, C., and Sapkota, G. P. (2017). Targeting Endogenous proteins for degradation through the affinity-directed protein missile system. Open Biol. *7*.
Fulcher, L. J., Macartney, T., Bozatzi, P., Hornberger, A., Rojas-Fernandez, A., and Sapkota, G. P. (2016). An affinity-directed protein missile system for targeted proteolysis. Open Biol. *6*.
Funkhouser, C. M., Sknepnek, R., Shimi, T., Goldman, A. E., Goldman, R. D., and De La Cruz, M. O. (2013). Mechanical model of blebbing in nuclear lamin meshworks. Proc. Natl. Acad. Sci. U. S. A. *110*, 3248–3253.
Fuse, N., Hisata, K., Katzen, A. L., and Matsuzaki, F. (2003). Heterotrimeric G Proteins Regulate Daughter Cell Size Asymmetry in Drosophila Neuroblast Divisions. Curr. Biol. *13*, 947–954.
Garzon-Coral, C., Fantana, H. A., and Howard, J. (2016). A force-generating machinery maintains the spindle at the cell center during mitosis. Science (80-.). *352*, 1124–1127.
Gautreau, A. M., Fregoso, F. E., Simanov, G., and Dominguez, R. (2022). Nucleation, stabilization, and disassembly of branched actin networks. Trends Cell Biol. *32*, 421–432.
Ghavami, S., Chitayat, S., Hashemi, M., Eshraghi, M., Chazin, W. J., Halayko, A. J., and Kerkhoff, C. (2009). S100A8/A9: A Janus-faced molecule in cancer therapy and tumorgenesis. Eur. J. Pharmacol. *625*, 73–83.
Giet, R., McLean, D., Descamps, S., Lee, M. J., Raff, J. W., Prigent, C., and Glover, D. M. (2002). Drosophila Aurora A kinase is required to localize D-TACC to centrosomes and to regulate astral microtubules. J. Cell Biol. *156*, 437–451.
Giet, R., and Prigent, C. (1999). Aurora/Ipl1 p-related kinases, a new oncogenic family of mitotic serine-threonine kinases. J. Cell Sci. *112*, 3591–3601.
Giet, R., Uzbekov, R., Cubizolles, F., Le Guellec, K., and Prigent, C. (1999). The Xenopus laevis aurora-related protein kinase pEg2 associates with and phosphorylates the kinesin-related protein XlEg5. J. Biol. Chem. *274*, 15005–15013.
Ginzberg, M. B., Kafri, R., and Kirschner, M. (2015). On Being the Right Size. Science (80-.). *348*, 1–10.
Giubettini, M., Asteriti, I. A., Scrofani, J., De Luca, M., Lindon, C., Lavia, P., and Guarguaglini, G. (2011). Control of Aurora-A stability through interaction with TPX2. J. Cell Sci. *124*, 113–122.

Glotzer, M. (2004). Cleavage furrow positioning. J. Cell Biol. *164*, 347–351.
Glover, D. M., Leibowitz, M. H., McLean, D. A., and Parry, H. (1995). Mutations in aurora prevent centrosome separation leading to the formation of monopolar spindles. Cell *81*, 95–105.
Goley, E. D., and Welch, M. D. (2006). The ARP2/3 complex: An actin nucleator comes of age. Nat. Rev. Mol. Cell Biol. *7*, 713–726.
Gores, G. J., Herman, B., and Lemasters, J. J. (1990). Plasma membrane bleb formation and rupture: A common feature of hepatocellular injury. Hepatology *11*, 690–698.
Gournier, H., Goley, E. D., Niederstrasser, H., Trinh, T., and Welch, M. D. (2001). Reconstitution of human Arp2/3 complex reveals critical roles of individual subunits in complex structure and activity. Mol. Cell *8*, 1041–1052.
Groen, A. C., Cameron, L. A., Coughlin, M., Miyamoto, D. T., Timothy J. Mitchison, and Ohi, and R. (2004). XRHAMM Functions in Ran-Dependent Microtubule Nucleation and Pole Formation during Anastral Spindle Assembly. Curr. Biol. *14*, 1801–1811.
Grosstessner-Hain, K. *et al.* (2011). Quantitative Phospho-proteomics to Investigate the Polo-like Kinase 1-Dependent Phospho-proteome. Mol. Cell. Proteomics *10*, M111.008540.
Gust, K. M. *et al.* (2009). RHAMM (CD168) is overexpressed at the protein level and may constitute an immunogenic antigen in advanced prostate cancer disease. Neoplasia *11*, 956–963.
Habib, S. J., and Acebrón, S. P. (2022). Wnt signalling in cell division : from mechanisms to tissue engineering. Trends Cell Biol., 1–14.
Haeussler, M. *et al.* (2016). Evaluation of off-target and on-target scoring algorithms and integration into the guide RNA selection tool CRISPOR. Genome Biol. *17*, 1–12.
Hall, C. L. *et al.* (1995). Overexpression of the hyaluronan receptor RHAMM is transforming and is also required for H-ras transformation. Cell *82*, 19–28.
Hara, Y., and Kimura, A. (2011). Cell-size-dependent control of organelle sizes during development. In: Cell Cycle in Development, 93–108.
Hardwick, C., Hoare, K., Owens, R., Hohn, H. P., Hook, M., Moore, D., Cripps, V., Austen, L., Nance, D. M., and Turley, E. A. (1992). Molecular cloning of a novel hyaluronan receptor that mediates tumor cell motility. J. Cell Biol. *117*, 1343–1350.
He, Z. *et al.* (2017). BRCA1 controls the cell division axis and governs ploidy and phenotype in human mammary cells. Oncotarget *8*, 32461–32475.
He, Z. *et al.* (2022). Pathogenic BRCA1 variants disrupt PLK1-regulation of mitotic spindle orientation. Nat. Commun. *13*.
He, Z., Mei, L., Connell, M., and Maxwell, C. A. (2020). Hyaluronan Mediated Motility Receptor (HMMR) Mitosis , and Meiosis Regulator Rather than a Hyaluronan Receptor. Cells *9*, 819.
Heng, Y.-W., and Koh, C.-G. (2010). Actin cytoskeleton dynamics and the cell division cycle. Int. J. Biochem. Cell Biol. *42*, 1622–1633.
Hickson, G. R. X., Echard, A., and O'Farrell, P. H. (2006). Rho-kinase controls cell shape changes during cytokinesis. Curr. Biol. *16*, 359–370.
Hirota, T., Kunitoku, N., Sasayama, T., Marumoto, T., Zhang, D., Nitta, M., Hatakeyama, K., and Saya, H. (2003). Aurora-A and an interacting activator, the LIM protein Ajuba, are required for mitotic commitment in human cells. Cell *114*, 585–598.
Hofmann, M., Assmann, V., Fieber, C., Sleeman, J. P., Moll, J., Ponta, H., Hart, I. R., and Herrlich, P. (1998a). Problems with RHAMM: a new link between surface adhesion and

oncogenesis? Cell *95*, 591–592; author reply 592-593.
Hofmann, M., Fieber, C., Assmann, V., Göttlicher, M., Sleeman, J., Plug, R., Howells, N., von Stein, O., Ponta, H., and Herrlich, P. (1998b). Identification of IHABP, a 95 kDa intracellular hyaluronate binding protein. J. Cell Sci. *111*, 1673–1684.
Hou, Y. *et al.* (2018). Non-canonical NF-κB Antagonizes STING Sensor-Mediated DNA Sensing in Radiotherapy. Immunity *49*, 490-503.e4.
Howell, A., Anderson, A. S., Clarke, R. B., Duffy, S. W., Evans, D. G., Garcia-Closas, M., Gescher, A. J., Key, T. J., Saxton, J. M., and Harvie, M. N. (2014). Risk determination and prevention of breast cancer. Breast Cancer Res. *16*, 1–19.
Hsu, J. Y. *et al.* (2021). PrimeDesign software for rapid and simplified design of prime editing guide RNAs. Nat. Commun. *12*, 8–13.
Hsu, P. D. *et al.* (2013). DNA targeting specificity of RNA-guided Cas9 nucleases. Nat. Biotechnol. *31*, 827–832.
Hu, D. J. K., and Jasper, H. (2019). Control of Intestinal Cell Fate by Dynamic Mitotic Spindle Repositioning Influences Epithelial Homeostasis and Longevity. Cell Rep. *28*, 2807-2823.e5.
Huber, M. D., and Gerace, L. (2007). The size-wise nucleus: Nuclear volume control in eukaryotes. J. Cell Biol. *179*, 583–584.
Ichikawa, M., Williams, R., Wang, L., Vogl, T., and Srikrishna, G. (2011). S100A8/A9 activate key genes and pathways in colon tumor progression. Mol Cancer Res. *9*, 133–148.
Ishigami, S. *et al.* (2011). Prognostic impact of CD168 expression in gastric cancer. BMC Cancer *11*, 106.
Jankele, R., Jelier, R., and Gönczy, P. (2021). Physically asymmetric division of the c. Elegans zygote ensures invariably successful embryogenesis. Elife *10*, 1–66.
Jiang, F., and Doudna, J. A. (2017). CRISPR – Cas9 Structures and Mechanisms. Annu. Rev. Biophys. *46*, 505–529.
Joukov, V., Groen, A. C., Prokhorova, T., Gerson, R., White, E., Rodriguez, A., Walter, J. C., and Livingston, D. M. (2006). The BRCA1/BARD1 Heterodimer Modulates Ran-Dependent Mitotic Spindle Assembly. Cell *127*, 539–552.
Joukov, V., and De Nicolo, A. (2018). Aurora-PLK1 cascades as key signaling modules in the regulation of mitosis. Sci. Signal. *11*, 1–26.
Kardon, J. R., and Vale, R. D. (2009). Regulators of the cytoplasmic dynein motor. Nat. Rev. Mol. Cell Biol. *10*, 854–865.
Karpova, N., Bobinnec, Y., Fouix, S., Huitorel, P., and Debec, A. (2006). Jupiter, a new Drosophila protein associated with microtubules. Cell Motil. Cytoskeleton *63*, 301–312.
Katayama, H., Sasai, K., Kawai, H., Yuan, Z. M., Bondaruk, J., Suzuki, F., Fujii, S., Arlinghaus, R. B., Czerniak, B. A., and Sen, S. (2004). Phosphorylation by aurora kinase A induces Mdm2-mediated destabilization and inhibition of p53. Nat. Genet. *36*, 55–62.
Katayama, H., Zhou, H., Li, Q., Tatsuka, M., and Sen, S. (2001). Interaction and Feedback Regulation between STK15/BTAK/Aurora-A Kinase and Protein Phosphatase 1 through Mitotic Cell Division Cycle. J. Biol. Chem. *276*, 46219–46224.
Kelkar, M., Bohec, P., and Charras, G. (2020). Mechanics of the cellular actin cortex: from signalling to shape change. Curr. Opin. Cell Biol. *66*, 69–78.
Kent, W. J., Sugnet, C. W., Furey, T. S., Roskin, K. M., Pringle, T. H., Zahler, A. M., and Haussler, and D. (2002). The Human Genome Browser at UCSC. Genome Res. *12*, 996–1006.

Kettenbach, A. N., Schweppe, D. K., Faherty, B. K., Pechenick, D., Pletnev, A. A., and Gerber, S. A. (2013). Quantitative phosphoproteomics identifies substrates and functional modules of Aurora and Polo-like kinase activities in mitotic cells. Sci Signal. *4*.

Khajah, M. A., and Luqmani, Y. A. (2016). Involvement of Membrane Blebbing in Immunological Disorders and Cancer. Med. Princ. Pract. *25*, 18–27.

Khammanivong, A., Wang, C., Sorenson, B. S., Ross, K. F., and Herzberg, M. C. (2013). S100A8/A9 (Calprotectin) Negatively Regulates G2/M Cell Cycle Progression and Growth of Squamous Cell Carcinoma. PLoS One *8*, 1–12.

Khoo, L. T., and Chen, L. (2018). Role of the cGAS–STING pathway in cancer development and oncotherapeutic approaches. EMBO Rep. *19*.

Kinoshita, K., Noetzel, T. L., Pelletier, L., Mechtler, K., Drechsel, D. N., Schwager, A., Lee, M., Raff, J. W., and Hyman, A. A. (2005). Aurora A phosphorylation of TACC3/maskin is required for centrosome-dependent microtubule assembly in mitosis. J. Cell Biol. *170*, 1047–1055.

Kiyomitsu, T. (2015). Mechanisms of daughter cell-size control during cell division. Trends Cell Biol. *25*, 286–295.

Kiyomitsu, T., and Cheeseman, I. M. (2012). Chromosome- and spindle-pole-derived signals generate an intrinsic code for spindle position and orientation. Nat. Cell Biol. *14*, 311–317.

Kiyomitsu, T., and Cheeseman, I. M. (2013). Cortical dynein and asymmetric membrane elongation coordinately position the spindle in anaphase. Cell *154*, 391–402.

Kovács, M., Tóth, J., Hetényi, C., Málnási-Csizmadia, A., and Seller, J. R. (2004). Mechanism of blebbistatin inhibition of myosin II. J. Biol. Chem. *279*, 35557–35563.

Kriegstein, A. R., and Noctor, S. C. (2004). Patterns of neuronal migration in the embryonic cortex. Trends Neurosci. *27*, 392–399.

Kufer, T. A., Silljé, H. H. W., Körner, R., Gruss, O. J., Meraldi, P., and Nigg, E. A. (2002). Human TPX2 is required for targeting Aurora-A kinase to the spindle. J. Cell Biol. Rep. *158*, 617–623.

Kunda, P., and Baum, B. (2009). The actin cytoskeleton in spindle assembly and positioning. Trends Cell Biol. *19*, 174–179.

Landry, J. J. M. *et al.* (2013). The genomic and transcriptomic landscape of a hela cell line. G3 Genes, Genomes, Genet. *3*, 1213–1224.

Lane, J. D., Allan, V. J., and Woodman, P. G. (2005). Active relocation of chromatin and endoplasmic reticulum into blebs in late apoptotic cells. J. Cell Sci. *118*, 4059–4071.

Lara-Gonzalez, P., Pines, J., and Desai, A. (2021). Spindle assembly checkpoint activation and silencing at kinetochores. Semin. Cell Dev. Biol. *117*, 86–98.

Laster, S. M., and Mackenzie, J. M. (1996). Bleb formation and F-actin distribution during mitosis and tumor necrosis factor-induced apoptosis. Microsc. Res. Tech. *34*, 272–280.

Lee, J. Y., and Spicer, A. P. (2000). Hyaluronan: A multifunctional, megaDalton, stealth molecule. Curr. Opin. Cell Biol. *12*, 581–586.

Lee, Y.-J., and Keng, P. C. (2005). Studying the Effects of Actin Cytoskeletal Destabilization on Cell Cycle by Cofilin Overexpression. Mol. Biotechnol. *31*, 001–010.

Lens, S. M. A., Voest, E. E., and Medema, R. H. (2010). Shared and separate functions of polo-like kinases and aurora kinases in cancer. Nat. Rev. Cancer *10*, 825–841.

Li, H. *et al.* (2015). RHAMM deficiency disrupts folliculogenesis resulting in female hypofertility. Biol. Open *4*, 562–571.

Li, H. *et al.* (2016). Impaired planar germ cell division in the testis, caused by dissociation of RHAMM from the spindle, results in hypofertility and seminoma. Cancer Res. *76*, 6382–6395.
Li, H., Guo, L., Li, J. W., Liu, N., Qi, R., and Liu, J. (2000). Expression of hyaluronan receptors CD44 and RHAMM in stomach cancers: relevance with tumor progression. Int. J. Oncol. *17*, 927–932.
Li, H., Kroll, T., Moll, J., Frappart, L., Herrlich, P., Heuer, H., and Ploubidou, A. (2017). Spindle Misorientation of Cerebral and Cerebellar Progenitors Is a Mechanistic Cause of Megalencephaly. Stem Cell Reports *9*, 1071–1080.
Li, J., Ji, X., and Wang, H. (2018). Targeting Long Noncoding RNA HMMR-AS1 Suppresses and Radiosensitizes Glioblastoma. Neoplasia (United States) *20*, 456–466.
Line, A., Slucka, Z., Stengrevics, A., Silina, K., Li, G., and Rees, R. C. (2002). Characterisation of tumour-associated antigens in colon cancer. Cancer Immunol. Immunother. *51*, 574–582.
Liu, H. *et al.* (2018). Nuclear cGAS suppresses DNA repair and promotes tumorigenesis. Nature *563*, 131–136.
Liu, W., Ma, J., Cheng, Y., Zhang, H., Luo, W., and Zhang, H. (2016). HMMR antisense RNA 1, a novel long noncoding RNA, regulates the progression of basal-like breast cancer cells. Breast Cancer Targets Ther. *8*, 223–229.
Liu, X., and Erikson, R. L. (2003). Polo-like kinase (Plk)1 depletion induces apoptosis in cancer cells. Proc. Natl. Acad. Sci. U. S. A. *100*, 5789–5794.
Liu, Z., Ho, C. H., and Grinnell, F. (2014). The different roles of myosin IIA and myosin IIB in contraction of 3D collagen matrices by human fibroblasts. Exp. Cell Res. *326*, 295–306.
London, N., and Biggins, S. (2014). Signalling dynamics in the spindle checkpoint response. Nat. Rev. Mol. Cell Biol. *15*, 735–747.
Lu, Y., Liu, Y., Jiang, J., Xi, Z., Zhong, N., Shi, S., Wang, J., and Wei, X. (2014). Knocking down the expression of Aurora-A gene inhibits cell proliferation and induces G2/M phase arrest in human small cell lung cancer cells. Oncol. Rep. *32*, 243–249.
De Luca, M., Lavia, P., and Guarguaglini, G. (2006). A functional interplay between Aurora-A, Plk1 and TPX2 at spindle poles: Plk1 controls centrosomal localization of Aurora-A and TPX2 spindle association. Cell Cycle *5*, 296–303.
Ly, T., Whigham, A., Clarke, R., Brenes-Murillo, A. J., Estes, B., Madhessian, D., Lundberg, E., Wadsworth, P., and Lamond, A. I. (2017). Proteomic analysis of cell cycle progression in asynchronous cultures, including mitotic subphases, using PRIMMUS. Elife *6*.
Ma, X., and Adelstein, R. S. (2014). The role of vertebrate nonmuscle Myosin II in development and human disease. Bioarchitecture *4*, 88–102.
Ma, X., Kovacs, M., Conti, M. A., Wang, A., Zhang, Y., Sellers, J. R., and Adelstein, R. S. (2012). Nonmuscle myosin II exerts tension but does not translocate actin in vertebrate cytokinesis. Proc. Natl. Acad. Sci. *109*, 4509–4514.
Mackenzie, K. J. *et al.* (2017). cGAS surveillance of micronuclei links genome instability to innate immunity. Nature *548*, 461–465.
Macurek, L., Lindqvist, A., Lim, D., Lampson, M. A., Klompmaker, R., Freire, R., Clouin, C., Taylor, S. S., Yaffe, M. B., and Medema, R. H. (2008). Polo-like kinase-1 is activated by aurora A to promote checkpoint recovery. Nature *455*, 119–123.
Maliga, Z. *et al.* (2013). A genomic toolkit to investigate kinesin and myosin motor function in cells. Nat. Cell Biol. *15*, 325–334.

Manfredi, M. G. *et al.* (2011). Characterization of alisertib (MLN8237), an investigational small-molecule inhibitor of Aurora A kinase using novel in vivo pharmacodynamic assays. Clin. Cancer Res. *17*, 7614–7624.
Mantripragada, K. K., Spurlock, G., Kluwe, L., Chuzhanova, N., Ferner, R. E., Frayling, I. M., Dumanski, J. P., Guha, A., Mautner, V., and Upadhyaya, M. (2008). High-resolution DNA copy number profiling of malignant peripheral nerve sheath tumors using targeted microarray-based comparative genomic hybridization. Clin. Cancer Res. *14*, 1015–1024.
Margolis, S. S. *et al.* (2006). Role for the PP2A/B56δ Phosphatase in Regulating 14-3-3 Release from Cdc25 to Control Mitosis. Cell *127*, 759–773.
Marumoto, T., Zhang, D., and Saya, H. (2005). Aurora-A - A guardian of poles. Nat. Rev. Cancer *5*, 42–50.
Mateo, F. *et al.* (2022). Modification of BRCA1-associated breast cancer risk by HMMR overexpression. Nat. Commun. *13*, 1–16.
Maxwell, C. A. *et al.* (2004). RHAMM expression and isoform balance predict aggressive disease and poor survival in multiple myeloma. Blood *104*, 1151–1158.
Maxwell, C. A. *et al.* (2011). Interplay between BRCA1 and RHAMM Regulates Epithelial Apicobasal Polarization and May Influence Risk of Breast Cancer. PLoS Biol. *9*, e1001199.
Maxwell, C. A., Keats, J. J., Belch, A. R., Pilarski, L. M., and Reiman, T. (2005). Receptor for hyaluronan-mediated motility correlates with centrosome abnormalities in multiple myeloma and maintains mitotic integrity. Cancer Res. *65*, 850–860.
Maxwell, C. A., Keats, J. J., Crainie, M., Sun, X., Yen, T., Shibuya, E., Hendzel, M., Chan, G., and Pilarski, L. M. (2003). RHAMM Is a Centrosomal Protein That Interacts with Dynein and Maintains Spindle Pole Stability. Mol. Biol. Cell *14*, 2262–2276.
McNally, F. J. (2013). Mechanisms of spindle positioning. J. Cell Biol. *200*, 131–140.
Mellacheruvu, D. *et al.* (2013). The CRAPome: A contaminant repository for affinity purification-mass spectrometry data. Nat. Methods *10*, 730–736.
Mitsushima, M., Aoki, K., Ebisuya, M., Matsumura, S., Yamamoto, T., Matsuda, M., Toyoshima, F., and Nishida, E. (2010). Revolving movement of a dynamic cluster of actin filaments during mitosis. J. Cell Biol. *191*, 453–462.
Mohan, P. *et al.* (2013). Genomic imbalance of HMMR/RHAMM regulates the sensitivity and response of malignant peripheral nerve sheath tumour cells to aurora kinase inhibition. Oncotarget *4*, 80–93.
Molli, P. R. *et al.* (2010). Arpc1b, a centrosomal protein, is both an activator and substrate of Aurora A. J. Cell Biol. *190*, 101–114.
Mollinari, C., Lange, B., and González, C. (2002). Miranda , a protein involved in neuroblast asymmetric division , is associated with embryonic centrosomes of Drosophila melanogaster. Biol Cell. *94*, 1–13.
Molyneux, G. *et al.* (2010). BRCA1 basal-like breast cancers originate from luminal epithelial progenitors and not from basal stem cells. Cell Stem Cell *7*, 403–417.
Mondet, J., Chevalier, S., and Mossuz, P. (2021). Pathogenic Roles of S100A8 and S100A9 Proteins in Acute Myeloid and Lymphoid Leukemia: Clinical and Therapeutic Impacts Julie. Molecules *26*, 1323.
Moon, W., and Matsuzaki, F. (2013). Aurora A kinase negatively regulates Rho-kinase by phosphorylation in vivo. Biochem. Biophys. Res. Commun. *435*, 610–615.
Moreno-Mateos, M. A., Vejnar, C. E., Beaudoin, J. D., Fernandez, J. P., Mis, E. K., Khokha, M.

K., and Giraldez, A. J. (2015). CRISPRscan: Designing highly efficient sgRNAs for CRISPR-Cas9 targeting in vivo. Nat. Methods *12*, 982–988.
Mori, D. *et al.* (2007). NDEL1 phosphorylation by Aurora-A kinase is essential for centrosomal maturation, separation, and TACC3 recruitment. Mol. Cell. Biol. *27*, 352–367.
Morin, X., and Bellaïche, Y. (2011). Mitotic Spindle Orientation in Asymmetric and Symmetric Cell Divisions during Animal Development. Dev. Cell *21*, 102–119.
Morrison, S. J., and Kimble, J. (2006). Asymmetric and symmetric stem-cell divisions in development and cancer. Nature *441*, 1068–1074.
Moulding, D. A. *et al.* (2007). Unregulated actin polymerization by WASp causes defects of mitosis and cytokinesis in X-linked neutropenia. J. Exp. Med. *204*, 2213–2224.
Mu, L., Huang, K., Hu, Y., Yan, C., Li, X., Tao, D., Gong, J., and Qin, J. (2017). Small-sized colorectal cancer cells harbor metastatic tumorinitiating cells. Oncotarget *8*, 107907–107919.
Murrell, M., Oakes, P. W., Lenz, M., and Gardel, M. L. (2015). Forcing cells into shape: The mechanics of actomyosin contractility. Nat. Rev. Mol. Cell Biol. *16*, 486–498.
Nehlig, A., Molina, A., Rodrigues-Ferreira, S., Honoré, S., and Nahmias, C. (2017). Regulation of end-binding protein EB1 in the control of microtubule dynamics. Cell. Mol. Life Sci. *74*, 2381–2393.
Nelson, J. W. *et al.* (2021). Engineered pegRNAs improve prime editing efficiency. Nat. Biotechnol. *40*, 402–410.
Ng, K. W., Marshall, E. A., Bell, J. C., and Lam, W. L. (2018). cGAS–STING and Cancer: Dichotomous Roles in Tumor Immunity and Development. Trends Immunol. *39*, 44–54.
Nousiainen, M., Silljé, H. H. W., Sauer, G., Nigg, E. A., and Körner, R. (2006). Phosphoproteome analysis of the human mitotic spindle. Proc. Natl. Acad. Sci. USA *103*, 5391–5396.
Ou, G., and Scholey, J. M. (2022). Motor Cooperation During Mitosis and Ciliogenesis. Annu. Rev. Cell Dev. Biol. *38*, 1–26.
Ou, G., Stuurman, N., Ambrosio, M. D., Vale, R. D., Ou, G., Stuurman, N., Ambrosio, M. D., and Valej, R. D. (2010). Polarized Myosin Produces Unequal-Size Daughters During Asymmetric Cell Division. Sci. New Ser. *330*, 677–680.
Ouderkirk, J. L., and Krendel, M. (2014). Non-muscle myosins in tumor progression, cancer cell invasion, and metastasis. Cytoskeleton *71*, 447–463.
Pacquelet, A., Jousseaume, M., Etienne, J., and Michaux, G. (2019). Simultaneous Regulation of Cytokinetic Furrow and Nucleus Positions by Cortical Tension Contributes to Proper DNA Segregation during Late Mitosis. Curr. Biol. *29*, 3766-3777.e4.
Paluch, E., Piel, M., Prost, J., Bornens, M., and Sykes, C. (2005). Cortical actomyosin breakage triggers shape oscillations in cells and cell fragments. Biophys. J. *89*, 724–733.
Paluch, E., Sykes, C., Prost, J., and Bornens, M. (2006). Dynamic modes of the cortical actomyosin gel during cell locomotion and division. Trends Cell Biol. *16*, 5–10.
Papatheodorou, I. *et al.* (2018). Expression Atlas: Gene and protein expression across multiple studies and organisms. Nucleic Acids Res. *46*, D246–D251.
Park, S. J., Yoon, B. H., Kim, S. K., and Kim, S. Y. (2019). GENT2: An updated gene expression database for normal and tumor tissues. BMC Med. Genomics *12*, 1–8.
Peukes, J., and Betz, T. (2014). Direct measurement of the cortical tension during the growth of membrane blebs. Biophys. J. *107*, 1810–1820.
di Pietro, F., Echard, A., and Morin, X. (2016). Regulation of mitotic spindle orientation: an

integrated view. EMBO Rep. *17*, 1106–1130.
Pizarro-Cerdá, J., Chorev, D. S., Geiger, B., and Cossart, P. (2017). The Diverse Family of Arp2/3 Complexes. Trends Cell Biol. *27*, 93–100.
Plessner, M., Knerr, J., and Grosse, R. (2019). Centrosomal Actin Assembly Is Required for Proper Mitotic Spindle Formation and Chromosome Congression. IScience *15*, 274–281.
Pollard, T. D., and Borisy, G. G. (2003). Cellular Motility Driven by Assembly and Disassembly of Actin Filaments. Cell *112*, 453–465.
Prager, A., Hagenlocher, C., Ott, T., Schambony, A., and Feistel, K. (2017). hmmr mediates anterior neural tube closure and morphogenesis in the frog Xenopus. Dev. Biol. *430*, 188–201.
Pujana, M. A. *et al.* (2007). Network modeling links breast cancer susceptibility and centrosome dysfunction. Nat. Genet. *39*, 1338–1349.
Rafii, S., and Lyden, D. (2006). S100 chemokines mediate bookmarking of premetastatic niches. Nat. Cell Biol. *8*, 1321–1323.
Rannou, Y., Troadec, M. B., Petretti, C., Hans, F., Dutertre, S., Dimitrov, S., and Prigent, C. (2008). Localization of aurora A and aurora B kinases during interphase: Role of the N-terminal domain. Cell Cycle *7*, 3012–3020.
Rappsilber, J., Ishihama, Y., and Mann, M. (2003). Stop And Go Extraction tips for matrix-assisted laser desorption/ionization, nanoelectrospray, and LC/MS sample pretreatment in proteomics. Anal. Chem. *75*, 663–670.
Rein, D. T., Roehrig, K., Schöndorf, T., Lazar, a, Fleisch, M., Niederacher, D., Bender, H. G., and Dall, P. (2003). Expression of the hyaluronan receptor RHAMM in endometrial carcinomas suggests a role in tumour progression and metastasis. J. Cancer Res. Clin. Oncol. *129*, 161–164.
Ridley, A. J. (2015). Rho GTPase signalling in cell migration. Curr. Opin. Cell Biol. *36*, 103–112.
Ritchey, L., and Chakrabarti, R. (2014). Aurora A kinase modulates actin cytoskeleton through phosphorylation of Cofilin: Implication in the mitotic process. Biochim. Biophys. Acta - Mol. Cell Res. *1843*, 2719–2729.
Ritchey, L., Ottman, R., Roumanos, M., and Chakrabarti, R. (2012). A functional cooperativity between Aurora A kinase and LIM kinase1: Implication in the mitotic proce. Cell Cycle *11*, 296–309.
Robinson, R. C., Turbedsky, K., Kaiser, D. A., Marchand, J., Higgs, H. N., Choe, S., and Pollard, T. D. (2001). Crystal Structure of Arp2 / 3 Complex. Science (80-.). *294*, 1679–1685.
Rodnick-Smith, M., Liu, S. L., Balzer, C. J., Luan, Q., and Nolen, B. J. (2016). Identification of an ATP-controlled allosteric switch that controls actin filament nucleation by Arp2/3 complex. Nat. Commun. *7*, 1–13.
Rodrigues, N. T. L., Lekomtsev, S., Jananji, S., Kriston-Vizi, J., Hickson, G. R. X., and Baum, B. (2015). Kinetochore-localized PP1-Sds22 couples chromosome segregation to polar relaxation. Nature *524*, 489–492.
Roghi, C., Giet, R., Uzbekov, R., Morin, N., Chartrain, I., Le Guellec, R., Couturier, A., Dorée, M., Philippe, M., and Prigent, C. (1998). The Xenopus protein kinase pEg2 associates with the centrosome in a cell cycle-dependent manner, binds to the spindle microtubules and is involved in bipolar mitotic spindle assembly. J. Cell Sci. *111*, 557–572.
Roh-Johnson, M., and Goldstein, B. (2009). In vivo roles for Arp2/3 in cortical actin organization during C. elegans gastrulation. J. Cell Sci. *122*, 3983–3993.

Roman, B. I., Verhasselt, S., and Stevens, C. V. (2018). Medicinal Chemistry and Use of Myosin II Inhibitor (S)-Blebbistatin and Its Derivatives. J. Med. Chem. *61*, 9410–9428.

Rosa, A., Vlassaks, E., Pichaud, F., and Baum, B. (2015). Ect2/Pbl Acts via Rho and Polarity Proteins to Direct the Assembly of an Isotropic Actomyosin Cortex upon Mitotic Entry. Dev. Cell *32*, 604–616.

Rosenblatt, J., Cramer, L. P., Baum, B., and McGee, K. M. (2004). Myosin II-dependent cortical movement is required for centrosome separation and positioning during mitotic spindle assembly. Cell *117*, 361–372.

Roth, M., Roubinet, C., Ifflander, N., Ferrand, A., and Cabernard, C. (2015). Asymmetrically dividing Drosophila neuroblasts utilize two spatially and temporally independent cytokinesis pathways. Nat. Commun. *6*, Ariticle number: 6551.

Rotty, J. D., Wu, C., Haynes, E. M., Suarez, C., Winkelman, J. D., Johnson, H. E., Haugh, J. M., Kovar, D. R., and Bear, J. E. (2015). Profilin-1 Serves as a gatekeeper for actin assembly by Arp2/3-Dependent and - Independent pathways. Dev. Cell *32*, 54–67.

Rouiller, I., Xu, X. P., Amann, K. J., Egile, C., Nickell, S., Nicastro, D., Li, R., Pollard, T. D., Volkmann, N., and Hanein, D. (2008). The structural basis of actin filament branching by the Arp2/3 complex. J. Cell Biol. *180*, 887–895.

Roy, A., Lordier, L., Mazzi, S., Chang, Y., Lapierre, V., Larghero, J., Debili, N., Raslova, H., and Vainchenker, W. (2016). Activity of nonmuscle myosin II isoforms determines localization at the cleavage furrow of megakaryocytes. Blood *128*, 3137–3145.

Sankaran, S., Crone, D. E., Palazzo, R. E., and Parvin, J. D. (2007). Aurora-A kinase regulates breast cancer-associated gene 1 inhibition of centrosome-dependent microtubule nucleation. Cancer Res. *67*, 11186–11194.

Sankaran, S., Starita, L. M., Groen, A. C., Ko, M. J., and Parvin, J. D. (2005). Centrosomal microtubule nucleation activity is inhibited by BRCA1-dependent ubiquitination. Mol. Cell. Biol. *25*, 8656–8668.

Sankaran, S., Starita, L. M., Simons, A. M., and Parvin, J. D. (2006). Identification of domains of BRCA1 critical for the ubiquitin-dependent inhibition of centrosome function. Cancer Res. *66*, 4100–4107.

Satinover, D. L., Leach, C. A., Stukenberg, P. T., and Brautigan, D. L. (2004). Activation of Aurora-A kinase by protein phosphatase inhibitor-2, a bifunctional signaling protein. Proc. Natl. Acad. Sci. U. S. A. *101*, 8625–8630.

Sauer, G., Körner, R., Hanisch, A., Ries, A., Nigg, E. A., and Silljé, H. H. W. (2005). Proteome Analysis of the Human Mitotic Spindle. Mol. Cell. Proteomics *4*, 35–43.

Scheffner, M., Werness, B. A., Huibregtse, J. M., Levine, A. J., and Howley, P. M. (1990). The E6 oncoprotein encoded by human papillomavirus types 16 and 18 promotes the degradation of p53. Cell *63*, 1129–1136.

Schell, C. *et al.* (2018). ARP3 Controls the Podocyte Architecture at the Kidney Filtration Barrier. Dev. Cell *47*, 741-757.e8.

Schnoor, M., Stradal, T. E., and Rottner, K. (2018). Cortactin: Cell Functions of A Multifaceted Actin-Binding Protein. Trends Cell Biol. *28*, 79–98.

Schuldt, A. J., Adams, J. H. J., Davidson, C. M., Micklem, D. R., Haseloff, J., Johnston, D. S., and Brand, A. H. (1998). Miranda mediates asymmetric protein and RNA localization in the developing nervous system. Genes Dev. *12*, 1847–1857.

Scrofani, J., Sardon, T., Meunier, S., and Vernos, I. (2015). Microtubule nucleation in mitosis by a RanGTP-dependent protein complex. Curr. Biol. *25*, 131–140.

Sedzinski, J., Biro, M., Oswald, A., Tinevez, J. Y., Salbreux, G., and Paluch, E. (2011). Polar actomyosin contractility destabilizes the position of the cytokinetic furrow. Nature *476*, 462–468.

Severson, A. F., Baillie, D. L., and Bowerman, B. (2002). A Formin Homology protein and a profilin are required for cytokinesis and Arp2/3-independent assembly of cortical microfilaments in C. elegans. Curr. Biol. *12*, 2066–2075.

Sheetz, M. P., and Dai, J. (1996). Modulation of membrane dynamics and cell motility by membrane tension. Trends Cell Biol. *6*, 85–89.

Shigeishi, H., Higashikawa, K., and Takechi, M. (2014). Role of receptor for hyaluronan-mediated motility (RHAMM) in human head and neck cancers. J. Cancer Res. Clin. Oncol. *140*, 1629–1640.

Shutova, M. S., and Svitkina, T. M. (2018). Common and Specific Functions of Nonmuscle Myosin II Paralogs in Cells. Biochem. *83*, 1459–1468.

Smith, A. S., Nowak, R. B., Zhou, S., Giannetto, M., Gokhin, D. S., Papoin, J., Ghiran, I. C., Blanc, L., Wan, J., and Fowler, V. M. (2018). Myosin IIA interacts with the spectrin-actin membrane skeleton to control red blood cell membrane curvature and deformability. Proc. Natl. Acad. Sci. U. S. A. *115*, E4377–E4385.

Smutny, M., Cox, H. L., Leerberg, J. M., Kovacs, E. M., Conti, M. A., Ferguson, C., Hamilton, N. A., Parton, R. G., Adelstein, R. S., and Yap, A. S. (2010). Myosin II isoforms identify distinct functional modules that support integrity of the epithelial zonula adherens. Nat. Cell Biol. *12*, 696–702.

Sohr, S., and Engeland, K. (2008). RHAMM is differentially expressed in the cell cycle and downregulated by the tumor suppressor p53. Cell Cycle *7*, 3448–3460.

Song, L., and Rape, M. (2010). Regulated Degradation of Spindle Assembly Factors by the Anaphase-Promoting Complex. Mol. Cell *38*, 369–382.

Sorce, B. *et al.* (2015). Mitotic cells contract actomyosin cortex and generate pressure to round against or escape epithelial confinement. Nat. Commun. *6*, 8872.

Spicer, a P., Roller, M. L., Camper, S. a, McPherson, J. D., Wasmuth, J. J., Hakim, S., Wang, C., Turley, E. a, and McDonald, J. a (1995). The human and mouse receptors for hyaluronan-mediated motility, RHAMM, genes (HMMR) map to human chromosome 5q33.2-qter and mouse chromosome 11. Genomics *30*, 115–117.

Spira, F., Cuylen-Haering, S., Mehta, S., Samwer, M., Reversat, A., Verma, A., Oldenbourg, R., Sixt, M., and Gerlich, D. W. (2017). Cytokinesis in vertebrate cells initiates by contraction of an equatorial actomyosin network composed of randomly oriented filaments. Elife *6*, e30867.

Straight, A. F., Cheung, A., Limouze, J., Chen, I., Westwood, N. J., Sellers, J. R., and Mitchison, T. J. (2003). Dissecting temporal and spatial control of cytokinesis with a myosin II inhibitor. Science (80-.). *299*, 1743–1747.

Straight, A. F., Field, C. M., and Mitchison, T. J. (2005). Anillin binds nonmuscle myosin II and regulates the contractile ring. Mol. Biol. Cell *16*, 193–201.

Sun, S. C., Wang, Z. B., Xu, Y. N., Lee, S. E., Cui, X. S., and Kim, N. H. (2011). Arp2/3 complex regulates asymmetric division and cytokinesis in mouse oocytes. PLoS One *6*.

Sun, T., and Hevner, R. F. (2014). Growth and folding of the mammalian cerebral cortex: from molecules to malformations. Nat. Rev. Neurosci. *15*, 217–232.

Sung, Y., Tzur, A., Ph, S., Choi, W., Li, V., Dasari, R. R., Yaqoob, Z., and Kirschner, M. W. (2013). Size homeostasis in adherent cells studied by synthetic phase microscopy. Proc.

Natl. Acad. Sci. U. S. A. *110*, 16687–16692.
Svitkina, T. M. (2020). Actin Cell Cortex: Structure and Molecular Organization. Trends Cell Biol. *30*, 556–565.
Svitkina, T. M., Verkhovsky, A. B., McQuade, K. M., and Borisy, G. G. (1997). Analysis of the actin-myosin II system in fish epidermal keratocytes: Mechanism of cell body translocation. J. Cell Biol. *139*, 397–415.
Taneja, N., and Burnette, D. T. (2019). Myosin IIA drives membrane bleb retraction. Mol. Biol. Cell *30*, 1051–1059.
Taubenberger, A. V., Baum, B., and Matthews, H. K. (2020). The Mechanics of Mitotic Cell Rounding. Front. Cell Dev. Biol. *8*, 1–16.
Taverna, E., Götz, M., and Huttner, W. B. (2014). The Cell Biology of Neurogenesis: Toward an Understanding of the Development and Evolution of the Neocortex.
Telmer, P. G., Tolg, C., McCarthy, J. B., and Turley, E. A. (2011). How does a protein with dual mitotic spindle and extracellular matrix receptor functions affect tumor susceptibility and progression? Commun. Integr. Biol. *4*, 182–185.
Terada, Y., Uetake, Y., and Kuriyama, R. (2003). Interaction of Aurora-A and centrosomin at the microtubule-nucleating site in Drosophila and mammalian cells. J. Cell Biol. *162*, 757–763.
Thompson, S. L., and Compton, D. A. (2011). Chromosome missegregation in human cells arises through specific types of kinetochore-microtubule attachment errors. Proc. Natl. Acad. Sci. U. S. A. *108*, 17974–17978.
Tinevez, J. Y., Schulze, U., Salbreux, G., Roensch, J., Joanny, J. F., and Paluch, E. (2009). Role of cortical tension in bleb growth. Proc. Natl. Acad. Sci. U. S. A. *106*, 18581–18586.
Tolg, C., Poon, R., Fodde, R., Turley, E. A., and Alman, A. (2003). Genetic deletion of receptor for hyaluronan-mediated motility (Rhamm) attenuates the formation of aggressive fibromatosis (desmoid tumor). Oncogene *22*, 6873–6882.
Tsai, M. Y., Wiese, C., Cao, K., Martin, O., Donovan, P., Ruderman, J., Prigent, C., and Zheng, Y. (2003). A Ran signalling pathway mediated by the mitotic kinase Aurora A in spindle assembly. Nat. Cell Biol. *5*, 242–248.
Tubbs, A., and Nussenzweig, A. (2017). Endogenous DNA Damage as a Source of Genomic Instability in Cancer. Cell *168*, 644–656.
Tumaneng, K., Schlegelmilch, K., Russell, R. C., Yimlamai, D., Basnet, H., Mahadevan, N., Fitamant, J., Bardeesy, N., Camargo, F. D., and Guan, K. L. (2012). YAP mediates crosstalk between the Hippo and PI(3)K-TOR pathways by suppressing PTEN via miR-29. Nat. Cell Biol. *14*, 1322–1329.
Turley, E. A., Austen, L., Vandeligt, K., and Clary, C. (1991). Hyaluronan and a cell-associated hyaluronan binding protein regulate the locomotion of ras-transformed cells. J. Cell Biol. *112*, 1041–1047.
Turley, E. A., Moore, D., and Hayden, L. J. (1987). Characterization of hyaluronate binding proteins isolated from 3T3 and murine sarcoma virus transformed 3T3 cells. Biochemistry *26*, 2997–3005.
Tzur, A., Kafri, R., LeBleu, V. S., Lahav, G., and Kirschner, M. W. (2009). Cell Growth and Size Homeostasis in Proliferating Animal Cells. Science (80-.). *325*, 167–171.
Vasilescu, J., and Figeys, D. (2006). Mapping protein-protein interactions by mass spectrometry. Curr. Opin. Biotechnol. *17*, 394–399.
Verma, V., Mogilner, A., and Maresca, T. J. (2019). Classical and emerging regulatory

mechanisms of cytokinesis in animal cells. Biology (Basel). *8*, 55.
Vicente-Manzanares, M., Ma, X., Adelstein, R. S., and Horwitz, A. R. (2009). Non-muscle myosin II takes centre stage in cell adhesion and migration. Nat. Rev. Mol. Cell Biol. *10*, 778–790.
Walczak, C. E., Cai, S., and Khodjakov, A. (2010). Mechanisms of chromosome behaviour during mitosis. Nat Rev Mol Cell Biol *11*, 91–102.
Wang, C., Entwistle, J., Guangpei, H., Li, Q., and Turley, E. A. (1996). The characterization of a human RHAMM cDNA: Conservation of the hyaluronan-binding domains. Gene *174*, 299–306.
Wang, C., Thor, D., Moore, H., Zhao, Y., Kerschmann, R., Stern, R., Watson, P. H., and Turley, A. (1998). The Overexpression Regulates of RHAMM , ras Signaling , Protein Cancer Kinase a Hyaluronan-binding Correlates and with Overexpression Is a Significant Protein of Mitogen-activated Parameter in Breast Progression. Clin. Cancer Res. *4*, 567–576.
Wang, L. H. *et al.* (2010). The mitotic kinase aurora-A induces mammary cell migration and breast cancer metastasis by activating the cofilin-F-actin pathway. Cancer Res. *70*, 9118–9128.
Wang, Z., Wu, Y., Wang, H., Zhang, Y., Mei, L., and Fang, X. (2013). Interplay of mevalonate and Hippo pathways regulates RHAMM transcription via YAP to modulate breast cancer cell motility. PNAS *113*, E89-98.
Wellard, S. R., Zhang, Y., Shults, C., Zhao, X., McKay, M., Murray, S. A., and Jordan, P. W. (2021). Overlapping roles for PLK1 and Aurora A during meiotic centrosome biogenesis in mouse spermatocytes. EMBO Rep. *22*, 1–16.
Whitfield, M. L. *et al.* (2002). Human Cell Cycle and Their Expression in Tumors. Mol. Biol. Cell *13*, 1977–2000.
Whitfield, M. L., George, L. K., Grant, G. D., and Perou, C. M. (2006). Common markers of proliferation. Nat. Rev. Cancer *6*, 99–106.
Winder, S. J., and Ayscough, K. R. (2005). Actin-binding proteins. J. Cell Sci. *118*, 651–654.
Wittmann, T., Wilm, M., Karsenti, E., and Vernos, I. (2000). TPX2, a novel Xenopus MAP involved in spindle pole organization. J. Cell Biol. *149*, 1405–1418.
Wu, C. C., Yang, T. Y., Yu, C. T. R., Phan, L., Ivan, C., Sood, A. K., Hsu, S. L., and Lee, M. H. (2012). p53 negatively regulates Aurora A via both transcriptional and posttranslational regulation. Cell Cycle *11*, 3433–3442.
Wu, C., Haynes, E. M., Asokan, S. B., Simon, J. M., Sharpless, N. E., Baldwin, A. S., Davis, I. J., Johnson, G. L., and Bear, J. E. (2013). Loss of Arp2/3 induces an NF-κB-dependent, nonautonomous effect on chemotactic signaling. J. Cell Biol. Rep. *203*, 907–916.
Xu, X., Wang, X., Xiao, Z., Li, Y., and Wang, Y. (2011). Two TPX2-dependent switches control the activity of Aurora A. PLoS One *6*, e16757.
Yamada, Y., Itano, N., Narimatsu, H., Kudo, T., Hirohashi, S., Ochiai, a, Niimi, a, Ueda, M., and Kimata, K. (1999). Receptor for hyaluronan-mediated motility and CD44 expressions in colon cancer assessed by quantitative analysis using real-time reverse transcriptase-polymerase chain reaction. Jpn. J. Cancer Res. *90*, 987–992.
Yang, B., Yang, B. L., Savani, R. C., and Turley ', E. A. (1994). Identification of a common hyaluronan binding motif in the hyaluronan binding proteins RHAMM, CD4 and link protein. EMBO J. *1*, 286–296.
Yang, B., Zhang, L., and Turley, E. A. (1993). Identification of two hyaluronan-binding domains in the hyaluronan receptor RHAMM. J. Biol. Chem. *268*, 8617–8623.

Yang, Q., Zhang, X. F., Pollard, T. D., and Forscher, P. (2012). Arp2/3 complex-dependent actin networks constrain myosin II function in driving retrograde actin flow. J. Cell Biol. *197*, 939–956.

Yu, F., Kuo, C. T., and Jan, Y. N. (2006). Drosophila Neuroblast Asymmetric Cell Division: Recent Advances and Implications for Stem Cell Biology. Neuron *51*, 13–20.

Zeng, K., Bastos, R. N., Barr, F. A., and Gruneberg, U. (2010). Protein phosphatase 6 regulates mitotic spindle formation by controlling the T-loop phosphorylation state of Aurora A bound to its activator TPX2. J. Cell Biol. *191*, 1315–1332.

Zhang, H., Chen, X., Liu, B., and Zhou, L. (2011). Effects of stable knockdown of Aurora kinase a on proliferation, migration, chromosomal instability, and expression of focal adhesion kinase and matrix metalloproteinase-2 in HEp-2 cells. Mol. Cell. Biochem. *357*, 95–106.

Zhang, Y., Chen, X., Gueydan, C., and Han, J. (2018). Plasma membrane changes during programmed cell deaths. Cell Res. *28*, 9–21.

Zhao, P., Teng, X., Tantirimudalige, S. N., Nishikawa, M., Wohland, T., Toyama, Y., and Motegi, F. (2019). Aurora-A Breaks Symmetry in Contractile Actomyosin Networks Independently of Its Role in Centrosome Maturation. Dev. Cell *48*, 631-645.e6.

Zhong, W., and Chia, W. (2008). Neurogenesis and asymmetric cell division. Curr. Opin. Neurobiol. *18*, 4–11.

Zlobec, I., Baker, K., M.terracciano, L., and Lugli, A. (2008). RHAMM, p21 combined phenotype identifies microsatellite instability-high colorectal cancers with a highly adverse prognosis. Clin. Cancer Res. *14*, 3798–3806.

Zlobec, I., and Lugli, A. (2008). Prognostic and predictive factors in colorectal cancer. Postgrad. Med. J. *84*, 403–411.